

# Hydrogen-Bonded Small Molecules and Polymers in Organic Electronics

Présentée le 26 juin 2020

à la Faculté des sciences et techniques de l'ingénieur  
Laboratoire des matériaux organiques et macromoléculaires  
Programme doctoral en science et génie des matériaux

pour l'obtention du grade de Docteur ès Sciences

par

**Bilal ÖZEN**

Acceptée sur proposition du jury

Prof. A. Fontcuberta i Morral, présidente du jury  
Prof. H. Frauenrath, directeur de thèse  
Dr E. D. Glowacki, rapporteur  
Dr A. Bayer, rapporteur  
Prof. K. Sivula, rapporteur





To my family...



©2020 Hasan Halit Özen



# Acknowledgments

The moment of writing the acknowledgments made me think about how this journey has started and evolved in due of time. The work presented here would not have been possible without constant support, encouragement, and help from a great number of people, including my colleagues, collaborators, friends, and family.

First of all, I wanted to express my deepest gratitude to my supervisor, Prof. Holger Frauenrath. Not only he gave me the opportunity to pursue a PhD in his group, he also provided a necessary freedom, guidance and support throughout this work and beyond. Besides, I would like to thank my thesis committee: Prof. Anna Fontcuberta i Morral, Prof. Kevin Sivula, Dr. Eric Daniel Głowacki, and Dr. Andreas Bayer for their time in evaluating this work.

The work in such an interdisciplinary form has benefited greatly from subject-specific collaborators. Therefore, I would like to give my acknowledgments to my coworkers Dr. Nicolas Candau (LMOM, EPFL) for his help with 2D SAXS and WAXD measurements performed in Lille and Lyon; Jacques Morisod from the laboratory of Prof. Harm-anton Klok (LP, EPFL) for his help with GPC measurements; Dr. Rosario Scopelliti (ISIC, EPFL), Dr. Farzaneh Fadaei Tirani (ISIC, EPFL) and Dr. Kurt Schenk (LQM, EPFL) for numerous single-crystal X-ray measurements; Dr. Piotr de Silva from the laboratory of Prof. Clémence Corminbœuf (LCMD, EPFL) for DFT calculations; Cansel Temiz and Prof. Ferdinand Grozema from Delft University of Technology for microwave conductivity measurements; Dr. Andrzej Sienkiewicz from the laboratory of Prof. László Forró (LPMC, EPFL) for electrospinning set-up; Dr. Pascal Schouwink (EPFL, Sion) for preliminary results on temperature dependent WAXD. It was a real pleasure to work with you all.

I am deeply indepted to Dr. Christopher Plummer, for his contributions (AFM, SAED, WAXD simulation) to this work and particularly for reviewing and proofreading various drafts of manuscripts. A special thanks goes to my "Best Man", my friend, Dr. Julien Cretenoud, for being there whenever needed, for many fruitful discussions on different topics, but mostly for his sense of humor. I am grateful to his dedicated friendship over many years. Michel Schär should of course, not to be forgotten for the help and guidance during the first six months of my PhD.

## Acknowledgments

---

I believe that a friendly and positive work environment plays an important role in stress management during this period. In this regard, I was lucky enough to work with an exceptional group of researchers that contributed nice working atmosphere. Thus, I would like to thank all the current group members; Enzo, Reuben, Piotr, Yevhen, Matthieu, Daniel, Lucile, Michael, Oğuzhan, Shuichi as well as our recent alumni, that I was privileged to work with, even for short time. Thus my gratitude goes to Nicolas, Regina, Bjoern, Vincent, Thomas, Roman, Stephen, Damien, Su, Giuseppe, Dragana, Sylvain, Jan Gebers. Similarly, I would like to acknowledge the current and former members of the SUNMIL group for being a nice neighbor across the hallway.

Furthermore, I would like to acknowledge Sylvie Vaucher, Chrystelle Demierre, Anne Kolly and Dr. Shawn Koppenhoefer for their help with administrative and IT-related issues.

And last but most importantly, I would like to thank my whole family that backed me up with complete support in any way I can imagine through the years without hesitation. In particular, my wife Sinem and my two-years old son Hasan Halit, who stood by me every step of the way and supported me continuously since the day one. Without her patience, understanding, and infinite moral support of my son, this work could not have been accomplished in its current form. I'm very thankful to both of you for everything ..

*Lausanne, 5 Mai 2020*

B. Ö.

# Abstract

Organic semiconductors are important components for applications in different fields of technology, as their advantages include the possibility of low-temperature processing as well as low-cost, large-area manufacturing based on solution-based processes, compared with inorganic counterparts. These organic materials are based on  $\pi$ -conjugated molecules whose arrangements across different length scales in bulk materials are an important factor that determines their macroscopic optoelectronic properties. However, the control of their complex microstructure and morphology at the nanoscale remains challenging.

In the present thesis, we investigated the use of amide hydrogen bonding as an additional structural motif to control the arrangement of  $\pi$ -conjugated molecules in bulk across different length scales. In the first part, we prepared a series of hydrogen-bonded, amide-functionalized oligothiophenes together with their non-hydrogen-bonded ester analogues and studied in detail the resulting structure-property relationships. Our results showed that hydrogen-bonded bithiophenes and quaterthiophenes induced a tighter packing of the molecules as compared to their non-hydrogen-bonded analogues, resulting in a larger  $\pi$ -overlap. Moreover, hydrogen bonding provided an additional driving force for a preferred formation of layered structures resulting in crystalline thin films with large domain sizes. Both of these factors resulted in an excellent performance of the thin films in field-effect transistors that is on par with that of single-crystals of related quaterthiophene derivatives.

In the second part, we extended the scope to polymer semiconductors. To this end, we designed and synthesized a series of polyamides that make use of bithiophene and perylene bisimide cores as model repeat units to provide optoelectronic functionality. We have studied in detail the synergistic interplay of hydrogen bonding and  $\pi$ - $\pi$  interactions and their role for the resulting materials' microstructure. As a result, we found that these materials exhibited microscopic structures similar to those of industrial-grade polyamides, providing comparable thermoplastic properties. In addition, these materials showed significant charge carrier mobility. This study may, therefore, pave the way towards polyamide-based semiconductors, with a synergistic interplay of interchain hydrogen bonding and  $\pi$ - $\pi$  stacking rendering them suitable for applications in which both mechanical and optoelectronic properties play an important role.

## Keywords

Semiaromatic polyamide • hydrogen bonding • organic semiconductors • organic field-effect transistors • oligothiophene • perylene bisimide • structure-property relationships



# Zusammenfassung

Organische Halbleitermaterialien sind wichtige Komponenten für Anwendungen in verschiedenen Technologiefeldern, da sie sich im Vergleich zu anorganischen Materialien besser zur Verarbeitung bei niedrigen Temperaturen sowie die für kostengünstige grossflächige Herstellung auf der Basis lösungsbasierter Prozesse eignen. Diese organischen Materialien basieren auf  $\pi$ -konjugierten Molekülen, deren Anordnung im Material auf verschiedenen Längenskalen ein wichtiger Faktor ist, der ihre makroskopischen optoelektronischen Eigenschaften bestimmt. Die Kontrolle ihrer Mikrostruktur und nanoskopischen Morphologie bleibt jedoch eine Herausforderung.

In der vorliegenden Arbeit untersuchten wir die Verwendung von Wasserstoffbrücken-Bindungen zwischen Amid-Gruppen als zusätzliches Strukturmotiv zur Steuerung der Anordnung von  $\pi$ -konjugierten Molekülen im Festkörper über verschiedene Längenskalen hinweg. Im ersten Teil haben wir eine Reihe von Wasserstoffbrücken-gebundenen, amid-funktionalisierten Oligothiophenen hergestellt und die resultierenden Struktur-Eigenschafts-Beziehungen im Detail untersucht. Unsere Ergebnisse zeigten, dass Wasserstoffbrücken-gebundene Bithiophene und Quaterthiophene eine dichtere Packung der Moleküle im Vergleich zu nicht Derivaten ohne Wasserstoffbrücken-Bindungen induzierten, was zu stärkeren  $\pi$ -Wechselwirkungen führte. Darüber hinaus bot die Wasserstoffbrücken-Bindung eine zusätzliche Triebkraft für eine bevorzugte Bildung von Schichtstrukturen, was zu Dünnschichten mit grossen kristallinen Domänen führte. Beide Faktoren resultierten in einer hervorragenden Leistung der Dünnschichten in Feldeffekttransistoren, die der von Einkristallen verwandter Quaterthiophenderivate entspricht.

Im zweiten Teil haben wir unseren Anwendungsbereich auf Polymerhalbleiter erweitert. Zu diesem Zweck haben wir eine Reihe von Polyamiden synthetisiert, die Bithiophene oder Perylenbisimide als Wiederholungseinheiten verwenden, um so eine optoelektronische Funktion bereitzustellen. Wir haben das synergistische Zusammenspiel von Wasserstoffbrücken und  $\pi$ - $\pi$  Wechselwirkungen sowie ihre Rolle für die Mikrostruktur der resultierenden Materialien im Detail untersucht. Wir stellten fest, dass diese Materialien ähnliche mikroskopische Strukturen wie industriell verwendete Polyamide aufwiesen, und auch vergleichbare thermoplastische Eigenschaften lieferten. Zusätzlich zeigten diese Materialien eine signifikante Ladungsträgermobilität. Diese Studie zeigt daher einen Weg zu Halbleitern basierend auf Polyamiden, die durch ein synergistisches Zusammenspiel von Wasserstoffbrücken und  $\pi$ - $\pi$  Wechselwirkungen für Anwendungen geeignet sind, bei denen sowohl mechanische als auch optoelektronische Eigenschaften eine wichtige Rolle spielen.

## Stichwörter

Semiaromatisches Polyamid • Wasserstoffbrückenbindung • Organische Halbleiter • Organische Feldeffekttransistoren • Oligothiophene • Perylenbisimide • Struktur-Eigenschafts-Beziehungen





# Résumé

Les semi-conducteurs organiques jouent un rôle important dans différents domaines technologiques puisqu'il est aisé de les fabriquer à grande échelle en utilisant des procédés en solution à faible coût et à basse température, ce qui n'est pas le cas de leurs homologues inorganiques. Ces matériaux organiques sont basés sur des molécules  $\pi$ -conjuguées dont l'arrangement à différentes échelles est un facteur important qui détermine leurs propriétés optoélectroniques à l'échelle macroscopique. Néanmoins, le contrôle de leur microstructure et de leur morphologie à l'échelle nanométrique reste un grand défi. Dans la présente thèse, nous avons étudié l'utilisation des liaisons hydrogène entre groupements amides comme motif structurel additionnel permettant de contrôler à différentes échelles l'arrangement des molécules  $\pi$ -conjuguées.

Dans la première partie, nous avons donc synthétisé une série d'oligothiophènes modifiés avec des groupements amides et les avons comparés à des analogues de type esters. En étudiant les relations entre structure et propriétés, nous avons pu démontrer que les bithiophènes et les quaterthiophènes fonctionnalisés amide, et donc ayant la capacité de faire des ponts hydrogène intermoléculaires, induisaient un arrangement plus compact des molécules, entraînant par la même occasion un plus grand chevauchement des orbitales  $\pi$ . Nous avons également réalisé que les liaisons hydrogène promouvaient la formation de structures à couches résultant en des films minces possédant de grands domaines cristallins. En combinant ces deux facteurs, d'excellentes performances ont été obtenues sur des films minces de transistors à effet de champ, comparables à celles de monocristaux de certains dérivés de quaterthiophènes apparentés.

Dans la deuxième partie, la portée de notre étude a été étendue aux polymères semi-conducteurs. Nous avons ainsi conçu et synthétisé une série de polyamides contenant des noyaux aromatiques de bithiophène ou de pérylène bisimide afin de leur fournir une fonction optoélectronique. Le but ici était d'étudier la synergie entre liaisons hydrogène et interactions  $\pi$ - $\pi$  ainsi que le rôle joué par ces interactions non-covalentes dans la microstructure des matériaux fabriqués. Nous avons ainsi constaté, d'une part, qu'ils présentaient des structures microscopiques et des propriétés comparables à celles des polyamides thermoplastiques industriels et, d'autre part, qu'ils possédaient une bonne mobilité des porteurs de charge. Cette étude pourrait donc ouvrir la voie à des semi-conducteurs à base de polyamides qui pourraient être utiles dans des applications où propriétés mécaniques et propriétés optoélectroniques jouent un rôle important.

## Mots clés

Polyamide semi-aromatique • liaison hydrogène • semi-conducteurs organiques • transistors à effet de champ organiques • oligothiophènes • pérylène bisimide • relations structure-propriétés



# Table of Contents

<b>Acknowledgments</b>	<b>i</b>
<b>Abstract (English/Deutsch/Français)</b>	<b>iii</b>
<b>List of Abbreviations</b>	<b>xi</b>
<b>1 General Introduction</b>	<b>1</b>
1.1 Motivation . . . . .	1
1.2 Structure-Property Relationships in Organic Semiconductors . . . . .	3
1.2.1 Charge Transport on Different Length Scales . . . . .	3
1.2.2 Disorder in Polymer Semiconductors . . . . .	10
1.3 Hydrogen Bonding: From Self-Assembly to Materials . . . . .	13
1.3.1 The Nature of Hydrogen Bonding . . . . .	13
1.3.2 The Role of Hydrogen Bonding in Organic Electronics . . . . .	17
1.4 The Amide Motif in Polymers: Polyamides . . . . .	23
1.4.1 General Features and Nomenclature of Polyamides . . . . .	23
1.4.2 Synthesis Approaches . . . . .	24
1.4.3 Crystallinity and Typical Crystal Morphology . . . . .	26
1.4.4 Properties and Applications of Polyamides . . . . .	33
1.5 Scope and Outline of this Thesis . . . . .	34
<b>2 Bithiophenes with Hydrogen-Bonded Substituents</b>	<b>39</b>
2.1 Introduction . . . . .	40
2.2 Results and Discussion . . . . .	42
2.2.1 Synthesis of the Bithiophene Diesters and Bithiophene Diamides . . . . .	42
2.2.2 Single-Crystal X-Ray Structures . . . . .	43
2.2.3 Compatibility of $\pi$ -Interactions and Amide Hydrogen Bonding . . . . .	49
2.2.4 Thermal and Spectroscopic Properties . . . . .	55
2.3 Conclusions . . . . .	56
<b>3 OFET Performance of a Hydrogen-Bonded Quaterthiophene</b>	<b>59</b>
3.1 Introduction . . . . .	60
3.2 Results and Discussion . . . . .	61
3.2.1 Synthesis of Non-Hydrogen-Bonded Quaterthiophene . . . . .	61
3.2.2 Single-Crystal X-Ray Structure . . . . .	62
3.2.3 DFT Computations of Electron Overlap Effects . . . . .	66
3.2.4 Thin Film Morphology . . . . .	67
3.2.5 Organic Field-Effect Transistors . . . . .	68
3.3 Conclusions . . . . .	70
	ix

## Table of Contents

---

<b>4 Engineering Polymers from Bithiophene-Containing Polyamides</b>	<b>75</b>
4.1 Introduction . . . . .	76
4.2 Results and Discussion . . . . .	77
4.2.1 Synthesis of Bithiophene-Containing Semiaromatic Polyamides . . . . .	77
4.2.2 Structural Characterization . . . . .	82
4.2.3 Mechanical Characterization . . . . .	87
4.2.4 Optoelectronic Properties . . . . .	88
4.3 Conclusions . . . . .	90
<b>5 Semiaromatic Polyamides Containing Perylene Bisimide Repeat Units</b>	<b>93</b>
5.1 Introduction . . . . .	94
5.2 Results and Discussion . . . . .	95
5.2.1 Synthesis of Perylene Bisimide-Containing Semiaromatic Polyamides . . . . .	95
5.2.2 Crystalline Morphology of the Polyamides . . . . .	98
5.2.3 Thermomechanical Properties of the Polyamides . . . . .	100
5.2.4 Optoelectronic Properties of the Polyamides . . . . .	101
5.3 Conclusions . . . . .	103
<b>6 Conclusions and Outlook</b>	<b>107</b>
<b>7 Experimental Part</b>	<b>113</b>
7.1 Instrumentation and Methods . . . . .	113
7.2 Synthesis Procedures and Analytical Data for Compounds . . . . .	121
7.2.1 Bithiophenes with Hydrogen-Bonded Substituents . . . . .	121
7.2.2 OFET Performance of a Hydrogen-Bonded Quaterthiophene . . . . .	126
7.2.3 Engineering Polymers from Bithiophene-Containing Polyamides . . . . .	126
7.2.4 Semiaromatic Polyamides Containing Perylene Bisimide Repeat Units . . . . .	128
<b>8 Bibliography</b>	<b>135</b>
<b>9 Appendix</b>	<b>153</b>
9.1 Crystallographic and Refinement Data . . . . .	153
9.2 NMR Spectra . . . . .	172
9.2.1 Bithiophenes with Hydrogen-Bonded Substituents . . . . .	172
9.2.2 OFET Performance of a Hydrogen-Bonded Quaterthiophene . . . . .	185
9.2.3 Engineering Polymers from Bithiophene-Containing Polyamides . . . . .	186
9.2.4 Semiaromatic Polyamides Containing Perylene Bisimide Repeat Units . . . . .	190
<b>List of Figures</b>	<b>199</b>
<b>List of Tables</b>	<b>213</b>
<b>List of Schemes</b>	<b>217</b>
<b>Curriculum Vitae</b>	<b>219</b>

# List of Abbreviations

$\delta$	chemical shift (NMR spectroscopy)
$\lambda$	wavelength
$\sigma$	conductivity
$\theta$	scattering angle
$^{13}\text{C NMR}$	carbon nuclear magnetic resonance
$^1\text{H NMR}$	proton nuclear magnetic resonance
$R_f$	retention factor
$E$	elastic modulus
$G$	shear modulus
$H$	hardness
$I_{\text{DS}}$	drain current (FET device)
$J$	coupling constant (NMR spectroscopy)
$L$	channel length (FET device)
$L$	lamellar long period (in SAXS)
$M_n$	number-average molecular weight
$M_w$	weight-average molecular weight
$P_n$	degradation onset temperature
$T_c$	crystallization temperature
$T_d$	degradation onset temperature
$T_g$	glass temperature

## List of Abbreviations

---

$T_m$	melting temperature
$V_D$	drain voltage (FET device)
$V_G$	gate voltage (FET device)
$V_T$	threshold voltage (FET device)
$W$	channel width (FET device)
$c$	concentration
$l$	crystalline lamellar thickness (in SAXS)
$m/z$	mass-to-charge ratio (mass spectrometry)
$\bar{D}$	dispersity
1D	one-dimensional
2D	two-dimensional
AFM	atomic force microscopy
anal.	analysis
APCI	atmospheric-pressure chemical ionization
APPI	atomic pressure photoionization (mass spectrometry)
ATR	attenuated total reflection (IR spectroscopy)
calcd	calculated
C	coulomb
cm	centimeter
COSY	correlation spectroscopy (NMR experiment)
CSD	cambridge structural database
DCM	dichloromethane
d	day
d	duplet (NMR spectroscopy)
DFT	density functional theory
DIC	<i>N,N'</i> -diisopropylcarbodiimide
DIPEA	<i>N,N'</i> -diisopropylethylamine

DMF	<i>N,N'</i> -dimethylformamide
DMSO	dimethylsulfoxide
DORI	density overlap region indicator
dppf	1,1'-bis(diphenylphosphino)ferrocene
EDCI	1-ethyl-3(3-dimethylaminopropyl)carbodiimide
EI	electron impact ionization (mass spectrometry)
equiv.	equivalents
ESI	electrospray ionization (mass spectrometry)
FET	field-effect transistor
FT	fourier transform
FWHM	full width at half maximum
g	gram
HFIP	1,1,1,3,3,3-hexafluoro-2-propanol
h	hour
HMBC	heteronuclear multiple bond correlation (NMR experiment)
HMPA	hexamethylphosphoramide
HOBt	1-hydroxybenzotriazole
HOMO	highest occupied molecular orbital
HRMS	high resolution mass spectrometry
HSQC	heteronuclear single quantum correlation (NMR experiment)
HV	high vacuum
Hz	hertz
IR	infrared
K	kelvin
kV	kilovolt
L	liter
LUMO	lowest unoccupied molecular orbital

## List of Abbreviations

---

m.p.	melting point
MALDI	matrix assisted laser desorption ionization (mass spectrometry)
mbar	millibar
MD	molecular dynamics
MeOH	methanol
MHz	megahertz
min	minute
mL	milliliter
M	molar
m	multiplet (NMR spectroscopy)
mm	millimeter
mN	millinewton
MS	mass spectrometry
ms	millisecond
nA	nanoampere
nm	nanometer
NMP	<i>N</i> -methyl-2-pyrrolidone
NMR	nuclear magnetic resonance
N	newton
OFET	organic field-effect transistor
OLED	organic light-emitting diode
OSC	organic solar cell
OTS	octadecyltrichlorosilane
PBI	perylene bisimide
p	quintet (NMR spectroscopy)
ppm	parts per million (NMR spectroscopy)
PR-TRMC	pulse-radiolysis time-resolved microwave conductivity



q	quartet (NMR spectroscopy)
RFID	radio-frequency identification tag
SAED	selected-area electron diffraction
SAXS	small-angle X-ray diffraction
SEM	scanning electron microscopy
s	singlet (NMR spectroscopy)
T2	bithiophene
T4	quaterthiophene
TEM	transmission electron microscopy
TFA	trifluoroacetic acid
TGA	thermogravimetric analysis
THF	tetrahydrofuran
TLC	thin layer chromatography
TOF	time of flight (mass spectrometry)
t	triplet (NMR spectroscopy)
UV-vis	ultraviolet-visible
vdW	van der Waals
WAXD	wide-angle X-ray diffraction
wt%	weight percent
XRD	X-ray diffraction
°C	degree celsius
Å	angstrom
μl	microliter
μm	micrometer



# **General Introduction**





# 1 General Introduction

## 1.1 Motivation

Over the last few decades, electronics and information technology have undergone very rapid development. Up to now, the increase in complexity and downsizing of semiconductor devices has followed Moore's law (Figure 1.1).<sup>1,2</sup> Almost all electronic devices are currently based on inorganic materials such as silicon, the processing of which requires considerable amounts of energy, and noble and rare-earth metals whose prices have shown dramatic increases during the last decade.<sup>3,4</sup> Furthermore, the technical feasibility of further miniaturization is expected to reach a limit within the next twenty years. Alternative technologies must therefore be developed.

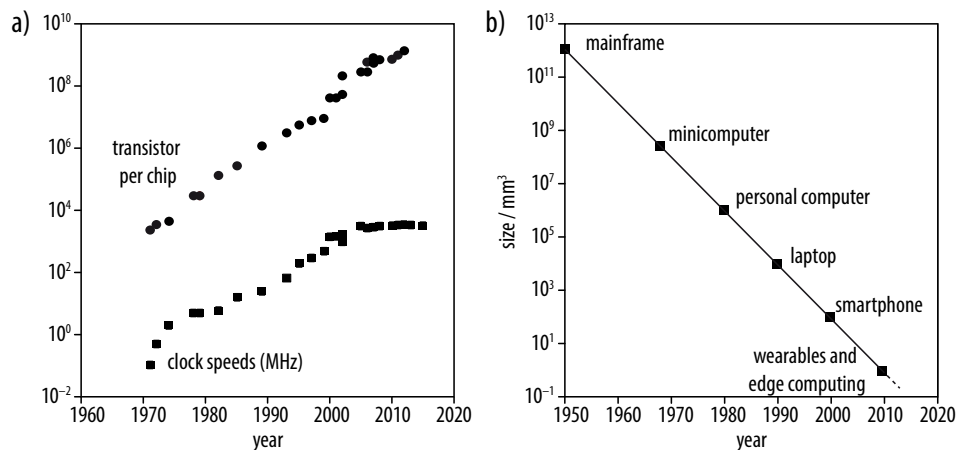


**Figure 1.1.** *a)* In the course of last five decades, the number of transistors per chip has doubled every two years in line with Moore's law, while the increase in clock speed (how fast a microprocessor executes commands) slowed after 2004 because of the need to limit heat generation. *b)* Computers increase their performance and become smaller in size. Consequently, a new class of instruments has emerged about once every ten years. Figure adapted from ref. [5].

In this context, organic and polymer semiconductors have emerged as a promising class of materials in many fields of technology, including field-effect transistors (FETs).<sup>6,7</sup> Compared with conventional inorganic semiconductors, organic and polymer semiconductors have the advantage of low density, ease of processing into thin films, and potential low-cost for large area applications. Semiconducting polymers also show favorable thermomechanical properties owing to their ability to form continuous entangled network structures.<sup>8–10</sup> Furthermore, an effectively unlimited number of potentially active organic materials may be prepared and their functionality tailored by proper molecular design.

Organic semiconductor materials generally consist of  $\pi$ -conjugated molecules that assemble through supramolecular interactions, including the  $\pi$ -interactions that are at the origin of the optoelectronic properties of these materials. Consequently, the final characteristics of such materials are dependent not only on the intrinsic features of their constituent building blocks, but also on their arrangement at different length scales. However, control of their complex morphology at the micro- and nanoscale remains challenging. In this regard, non-covalent interactions have recently become of prime interest for obtaining novel  $\pi$ -conjugated architectures, owing to their ability to tune the solid-state arrangement of the molecules.<sup>11</sup> In addition, it has recently been recognized that careful tailoring of disorder and defects in otherwise partially ordered materials can play an important role in their macroscopic properties.<sup>12–15</sup> Therefore, new approaches to manipulating the intricate balance between short-range order and overall disorder are now highly sought after for the development of mechanically durable, novel high-performance materials for organic electronics.

Based on the above context, the aim of the current thesis project was to investigate the use of amide hydrogen bonding as a non-covalent interaction and a structure-directing motif for the control of structure formation at different length scales in organic and polymer semiconductors. In the first part of the project, we studied the effect of the terminal amide hydrogen bonding on the structural elements required for efficient  $\pi$ -overlap. We then built on this experience in the second part of the project, where we focused mainly on polyamides comprising  $\pi$ -conjugated segments, materials that are expected to combine the beneficial thermomechanical properties of a polyamide with the optoelectronic performance of a  $\pi$ -conjugated core.

In the following, a brief overview of charge transport at different length scales in organic semiconductors will provide a general understanding of how their structure and properties may correlate (Section 1.2). Then, further discussion is devoted to the nature of hydrogen bonding and its applications in the organic electronics literature (Section 1.3). Finally, an overview of the synthesis, structure and applications of the most important aliphatic and semiaromatic polyamides (Section 1.4) will allow us to place the data obtained in the course of the thesis within a broader perspective.

## 1.2 Structure-Property Relationships in Organic Semiconductors

Over the last decades, organic semiconductors processed from solution at low temperatures have received tremendous attention as promising candidates for future “plastic electronics” applications such as flexible displays,<sup>16,17</sup> radio-frequency identification tags (RFID),<sup>18</sup> and logic circuits.<sup>19–21</sup> Due to this great commercial interest, significant progress has been made in organic semiconductors, especially in FET devices, with field-effect mobilities,  $\mu$ , reaching values of more than  $1 \text{ cm}^2 \text{ V}^{-1} \text{ s}^{-1}$  (Figure 1.2), which exceed the important benchmark provided by the mobilities observed in amorphous silicon.<sup>22–24</sup> Designing and developing high-performance organic semiconductors is non-trivial, however, because the current understanding of their charge transport mechanisms is still not comprehensive. In view of the importance of this technology, considerable recent effort has therefore been devoted to correlating and explaining structure-property relationships in conjugated polymers.<sup>12,25–28</sup>

The aim of this section is to explore the current state-of-the-art with regard to charge transport properties in organic semiconductors. Because of its particular relevance, special focus will be placed on charge transport on different length scales, followed by a literature survey of the current generation of high mobility polymers.

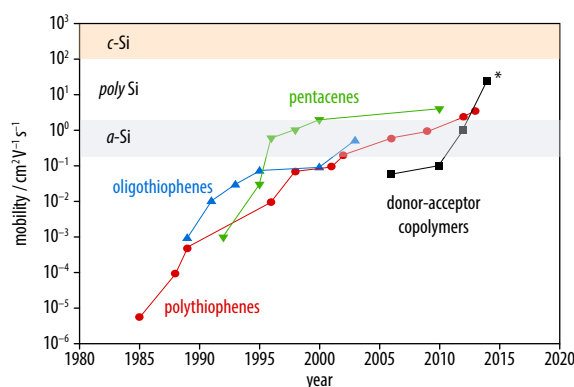


**Figure 1.2.** Progress in organic semiconductor performance over a thirty-year period. Charge carrier mobility has improved by more than six orders of magnitude, exceeding the performance of amorphous silicon. The recent dramatic increase in the performance of donor-acceptor based systems is especially promising for future applications (\* A special technique was used to align the material). Figure adapted from ref. [13].

### 1.2.1 Charge Transport on Different Length Scales

Organic semiconductors are a class of materials comprising  $\pi$ -conjugated small molecules or polymers with a backbone of  $sp^2$ -hybridized carbon atoms. The in-plane overlap of the two adjacent  $sp^2$ -hybridized orbitals forms a stable interatomic  $\sigma$ -bond, while the remaining  $p_z$  orbitals overlap laterally, leading to a  $\pi$ -bond, and hence overall a double bond between the adjacent atoms (Figure 1.3a). Systems with an alternating sequence of single and double

bonds are called  $\pi$ -conjugated systems. The electrons in such  $\pi$ -conjugated systems are to some extent delocalized among the carbon atoms, which enables charge transport within the molecule. Because of the large overlap between  $sp^2$ -hybridized atoms, the absolute energy of the electrons in  $\sigma$ -bonds is lower than in  $\pi$ -bonds, which therefore become the frontier orbitals of the molecule (Figure 1.3*b*). These frontier orbitals, that is, the highest occupied (HOMO) and the lowest unoccupied molecular orbitals (LUMO), participate actively in charge transfer, oxidation, reduction, and charge injection processes.<sup>29</sup> Moreover, they are of particular interest for charge transport, and their characteristics such as the band gap and bandwidth play a fundamental role in the optical and electronic properties of a material. In an organic crystal, intermolecular interactions induce additional energy splitting and generate the corresponding HOMO and LUMO energy bands, which are sometimes also referred to as the valence and conduction bands, respectively, by analogy to inorganic semiconductors (Figure 1.3*c*).

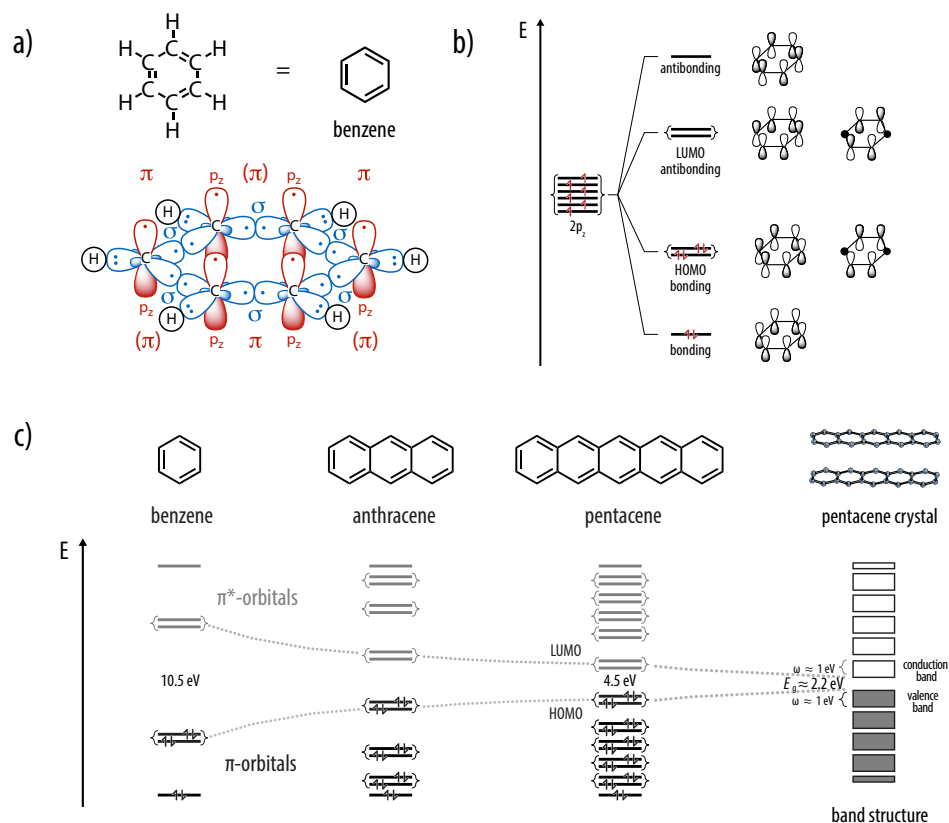


**Figure 1.3.** Schematic representation of *a*) the bonds ( $\sigma$  and  $\pi$ ) and orbitals ( $sp^2$  and  $p_z$  – coloured by blue and red, respectively), and the chemical structure of a benzene molecule and its *b*) molecular orbital diagram, illustrating the HOMO and LUMO energy levels along with the corresponding  $p_z$  orbital representation. *c*) Molecular orbital diagrams of benzene, anthracene, pentacene and pentacene crystals. From benzene to pentacene, the HOMO–LUMO energy gap decreases with increasing extension of the  $\pi$ -system. A band-like structure is generated in case of an organic crystal (e.g. pentacene) by further splitting of initial energy levels due to intermolecular (quadrupolar and dispersive) interactions.



## 1.2. Structure-Property Relationships in Organic Semiconductors

Inorganic semiconductors are nevertheless different from organic semiconductors in many respects, particularly with regard to charge transport. In an inorganic semiconductor crystal, atoms are connected via covalent bonds. This allows strong electronic interactions between atomic orbitals, resulting in the formation of well-defined energy bands with bandwidths of the order of a few eV.<sup>30</sup> By contrast, organic semiconductor crystals are held together by rather weak intermolecular van der Waals and electrostatic interactions, resulting in weak electronic interactions between the molecules, and the formation of narrow bands with bandwidths of less than 500 meV.<sup>31,32</sup> When charges are injected into periodic inorganic semiconductors, charge carriers are free to travel within well-defined energy bands. By contrast, charge injection leads to the perturbation of the electronic structure in organic semiconductors, leading to a bound state between the charge carrier and the molecule, called as polaron.<sup>29,33,34</sup> As a result, charge carriers may be transported through delocalization in combination with hopping, upon the presence of an electrical field.

The microstructure of the organic semiconductors features variations in structural order that has an enormous impact on the charge transport properties.<sup>35</sup> This is even more critical in the case of polymer semiconductors, as they have a complex multiscale morphology, typically incorporating more or less ordered amorphous and crystalline regions. Therefore, charge transport in such systems may be considered to be made up of three separate contributions, namely intramolecular, intermolecular, and interdomain transport (Figure 1.4).<sup>26</sup> In the following paragraphs, the parameters that may affect charge transport in a polymer semiconductor at different length scales will be discussed in more detail.

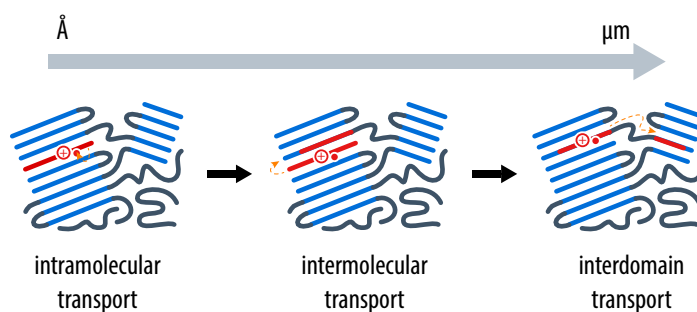


**Figure 1.4.** Schematic illustration of intra-, intermolecular, and interdomain transport across different length scales.

Intramolecular transport in a polymer semiconductor takes place via extended states, which mainly depend on the rigidity, planarity and degree of dynamic disorder on the molecular level.<sup>27,33</sup> For optimum charge carrier delocalization, orbital overlap should be optimized. Therefore  $\pi$ -conjugated segments need to be as flat and rigid as possible, resulting in an increase in the effective conjugation length. By contrast, a decrease in the effective conjugation length due to kinks, chain twisting or an increase in dynamic disorder, leads to more localized charge carriers, which significantly hampers intramolecular charge transport.<sup>36</sup>

The importance of the molecular rigidity and degree of disorder along a polymer backbone for the overall charge transport has been demonstrated in both computational and experimental studies.<sup>13,37–39</sup> For instance, Venkateshvaran et al. reported the beneficial effect of backbone rigidity for efficient charge transport in an indacenothiophene-benzothiadiazole (**IDTBT**) copolymer (Figure 1.5).<sup>40</sup> Interestingly, this copolymer shows excellent transport properties but little long-range crystalline order<sup>41,42</sup> compared with poly-3-hexylthiophene<sup>43</sup> (**P3HT**) and poly(2,5-bis(3-alkylthiophen-2-yl)thieno(3,2-b)thiophene)<sup>12</sup> (**PBTTT**). A combination of quantum chemical and molecular dynamics (MD) calculations suggested that **IDTBT** has a rigid torsion-free backbone (Figure 1.5*b*). This was further confirmed by pressure-dependent Raman spectroscopy (Figure 1.5*c*) of as-deposited **IDTBT** films, which indicate a planar conformation that allows side chain disorder to be accommodated but at the same time promoting efficient transport of charge carriers along the polymer backbone. On the basis of their results, Venkateshvaran et al.<sup>40</sup> proposed various strategies for the design of high-performance semiconductors able to retain similar backbone rigidity. They envisaged a reduced number of torsion-sensitive substituents, that is, extended  $\pi$ -conjugated segments with long side chains on either side permit space filling without introducing backbone torsion and disrupting close  $\pi$ - $\pi$  contacts. Moreover, they proposed that the ideal material should have deep gas-phase torsion potential minima ideally close to 0°, 180° or both (Figure 1.5*d*), again favouring a planar conformation.

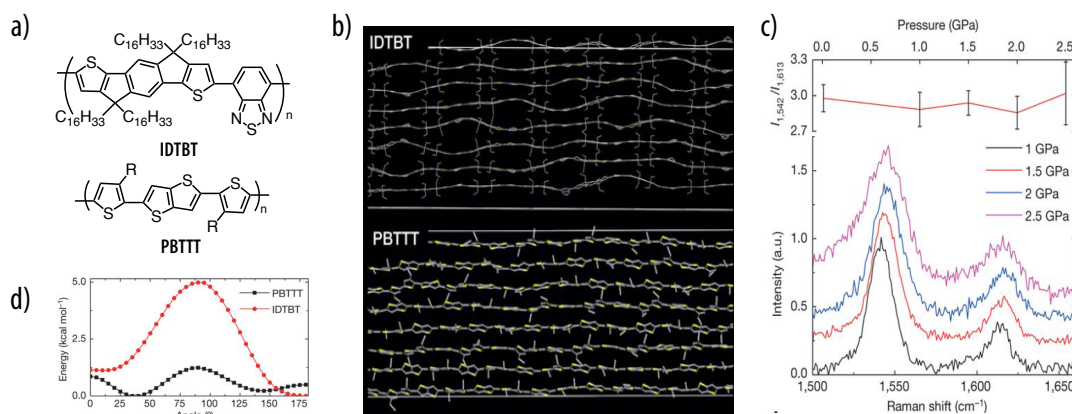


**Figure 1.5.** Venkateshvaran et al. investigated the benefits of structural resilience for charge transport properties. *a*) Chemical structure of the **IDTBT** copolymer that was the focus of the work and the reference semicrystalline  $\pi$ -conjugated polymer system **PBTTT** ( $R = C_{12}H_{25}$ ). *b*) Molecular modeling of the backbone conformation of **IDTBT** and **PBTTT** (side chains and hydrogens omitted for clarity). *c*) The polymer backbone may be planarized under pressure if it exhibits significant torsion in as-deposited films. Thus, pressure-dependent Raman spectroscopy measurements were performed on **IDTBT** films. It was found that Raman intensity ratio between 1542 cm<sup>-1</sup> (ring stretching mode for **BT**) and 1613 cm<sup>-1</sup> (ring stretching mode for **IDT**) was independent of pressure, indicating a planar backbone. *d*) Calculated gas-phase torsion energies for **IDTBT** and **PBTTT**. For planar structures the potential minima are close to 0°, 180° or both. Figure reproduced from ref. [40].

## 1.2. Structure-Property Relationships in Organic Semiconductors

Alternatively, various processing techniques can also enable an efficient intramolecular charge transport in semiconducting polymers.<sup>44</sup> In this context, an interesting example is provided by the work of Heeger et al., who investigated the effect of macroscopic alignment on charge carrier mobility in the poly[4-(4,4- dihexadecyl-4H-cyclopenta[1,2-*b*:5,4-*b'*]dithiophen-2-yl)-alt-[1,2,5]thiadiazolo[3,4-*c*]pyridine] (**PCDTPT**) (Figure 1.6).<sup>45</sup> The authors found that the performance of these donor-acceptor-type regio-regular polymers **PCDTPT** was insensitive to molecular weight when they were aligned using nano-grooved substrates. The aligned films showed FET mobilities as high as  $23.7 \text{ cm}^2 \text{ V}^{-1} \text{ s}^{-1}$ , which is almost one order of magnitude higher than for devices without orientation (Figure 1.6*b*). Moreover, activation energies as low as  $\sim 33 \text{ meV}$  were obtained from temperature-dependent FET measurements (Figure 1.6*c*), which the authors attributed to a low density of deep trap states in the polymer. However, the optical properties were anisotropic, and the obtained mobilities were higher along the alignment direction.<sup>46</sup> The authors concluded that the long-range alignment of the polymer backbone obtained by proper processing resulted in enhanced intramolecular charge transport, explaining the high charge carrier mobilities.

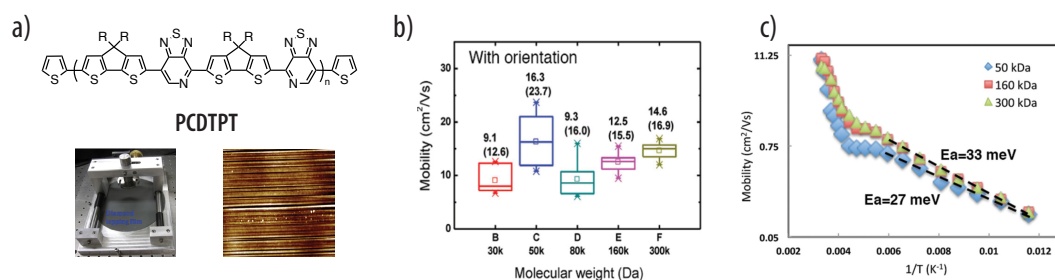


**Figure 1.6.** Heeger et al. studied the field effect transistor performance of **PCDTPT** with different molecular weights. *a*) Top: chemical structure of **PCDTPT** ( $R = C_{16}H_{33}$ ); bottom left: scratching machine for nano-grooved  $SiO_2$ ; bottom right: resulting  $SiO_2$  after scratching. *b*) The mobility value and the value in parentheses represent mean and maximum values obtained from devices fabricated by slow drying. *c*) Temperature-dependent mobility values of 50, 160, 300 kDa materials. Figure reproduced from ref. [45].

The examples presented so far underline the importance of the chain backbone for intramolecular charge transport. However, optimization of the chain backbone may not be enough to improve the overall charge transport if intermolecular charge transport is the rate-limiting process. As illustrated previously (Figure 1.3), a periodic arrangement of  $\pi$ -conjugated segments may lead to significant overlap of  $\pi$ -orbitals between neighbouring molecules, generating a band-like structure. The resulting electronic coupling allows for charge transport from one molecule to another, mainly through hopping or tunneling mechanisms. The coupling constant  $J$ , which is a measure of the intermolecular interaction between adjacent molecules, depends strongly on overlap of  $\pi$ -segments and hence on the overall packing of polymer chains.<sup>30,31,47–50</sup> Moreover, to optimize  $J$  and therefore promote intermolecular transport, the static and dynamic disorder of the polymer chains should be kept to a minimum.

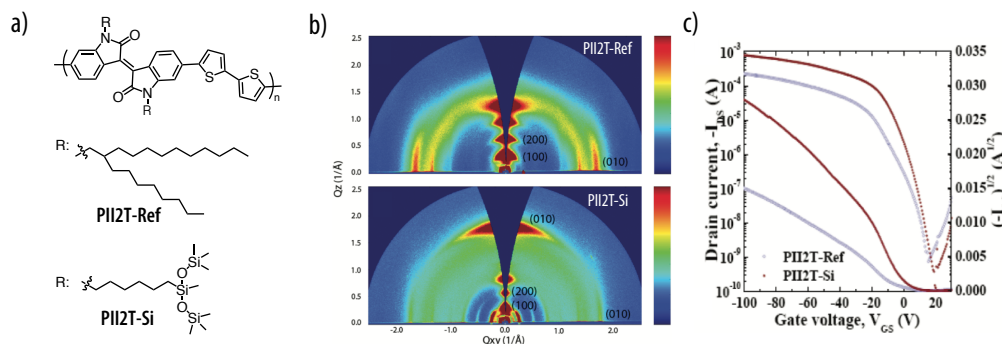


**Figure 1.7.** Mei et al. introduced siloxane-terminated side chains into an isoindigo-based semiconducting polymer and investigated the resulting structure-property relationships. *a*) Chemical structure of the isoindigo based polymer, where R stands for siloxane terminated side chains (**PII2T-Si**) or for a branched alkyl chain as a reference (**PII2T-Ref**). *b*) 2D grazing incidence X-ray scattering (GIXS) patterns of annealed **PII2T-Ref** and annealed **PII2T-Si**. *c*) Representative transfer curves for **PII2T-Ref** and **PII2T-Si**. Average hole mobilities up to  $2.0 \text{ cm}^2 \text{ V}^{-1} \text{ s}^{-1}$  were found for **PII2T-Si**, which is six times higher than **PII2T-Ref**. Figure adapted from ref. [22].

Side chain engineering is one of the most widely used techniques to facilitate enhanced electronic coupling between neighboring chains.<sup>51–54</sup> For instance, Mei et al. demonstrated the influence of branched versus linear siloxane-terminated side chains in an isoindigo-based semiconducting polymer (Figure 1.7).<sup>22</sup> The siloxane-terminated side chains decrease the steric hinderance between adjacent polymer backbones leading to an almost 5% reduction in the  $\pi$ -stacking distance to  $3.58 \text{ \AA}$ , as evidenced by GIXS (Figure 1.7*b*). This resulted in enhanced electronic coupling, yielding average hole mobilities of up to  $2.0 \text{ cm}^2 \text{ V}^{-1} \text{ s}^{-1}$ , which is six times higher than for the branched reference compound (Figure 1.7*c*). The beneficial effects of side chain engineering have also been observed in diketopyrrolopyrrole (**DPP**)-based polymer systems (Figure 1.8). By systematically shifting the side chain branching point away from the polymer backbone, close intermolecular  $\pi$ - $\pi$  contacts were increasingly favored (Figure 1.8*b*).<sup>52</sup> This was found to give hole mobilities of up to  $12 \text{ cm}^2 \text{ V}^{-1} \text{ s}^{-1}$  after an optimized thermal annealing procedure (Figure 1.8*c*). The same idea of shifting the side chain branching point away from the polymer backbone has recently been employed in cyclopentadithiophene-benzothiadiazole copolymers.<sup>54</sup> This led to a systematic decrease of  $\pi$ -stacking distance from  $3.8$  to  $3.55 \text{ \AA}$ , but substantially increase in the resulting FET mobilities from  $0.0001$  to  $0.4 \text{ cm}^2 \text{ V}^{-1} \text{ s}^{-1}$ .

Conjugated semicrystalline polymers are not well ordered in the solid-state, but neither are they fully amorphous. In such systems, intramolecular and intermolecular charge transport occurs within local crystalline regions, while on a macroscopic scale, charge carriers must travel through a heterogenous morphology with ordered aggregates embedded in more disordered regions. Thus the interdomain transport plays a significant role in the macroscopic electronic properties of polymer semiconductors. The chain disorder includes kinks and folds, thus exhibits limited conjugation length, and a wider HOMO–LUMO gap than in the ordered aggregates, which results in a predominant localization of the charge carriers within

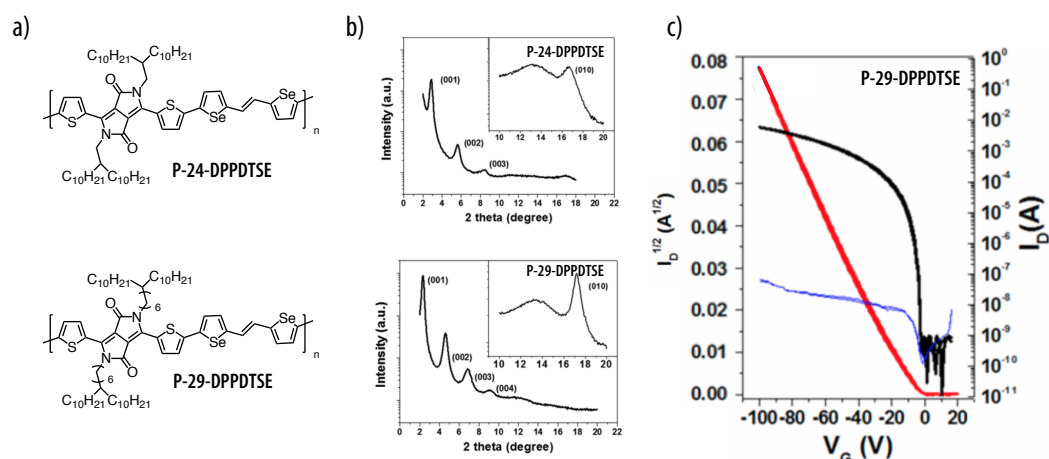


**Figure 1.8.** Kang et al. designed DPP-based polymers with a side chain branching point far from the polymer backbone and reported their photophysical and structural features as well as their device performance. *a*) Chemical structure of **P-24-DPPDTSE** (reference compound) and **P-29-DPPDTSE**. *b*) Out-of-plane diffraction spectra of **P-24-DPPDTSE** and **P-29-DPPDTSE**. Inset: the corresponding in-plane diffraction patterns. *c*) Representative transfer curve for **P-29-DPPDTSE**. Figure adapted from ref. [52].

the ordered aggregates. Consequently, interdomain transport occurs from ordered aggregates to another via disordered polymer segments of the material. It was recently suggested by Salleo et al., that short-range intermolecular aggregation should be beneficial for charge transport in  $\pi$ -conjugated polymers.<sup>12</sup> This hypothesis was confirmed experimentally by measuring the electroluminescence spectra of blends composed of controlled amounts of **RR-P3HT** and **RRa-P3HT** (Figure 1.9).<sup>12</sup> The electroluminescence spectra of the blends at different current densities were similar to those of pure regioregular **P3HT**, indicating that charges were moving and recombining within the crystalline regions of the film (Figure 1.9*b,c*). This finding was in line with results for local mobility<sup>55</sup> and conductive atomic force microscopy (AFM) measurements,<sup>56</sup> indicating that mobility is determined by the transport of charges from one small ordered aggregate to another via bridging polymer chains. One of the key requirements for designing high performance polymers is hence not to increase the degree of crystallinity but rather to increase the fraction of interconnected short range ordered aggregates so as to ensure sufficient intermolecular charge transfer.<sup>12,57</sup>

To summarize, charge transport in polymer semiconductors is a complex phenomenon that depends strongly on their organization at different length scales. Consequently, high-performance semiconducting polymers require the presence of interconnected small aggregates and sufficient interchain electronic coupling. At the same time, the structure of the backbone needs to be highly tolerant of structural disorder. In the next section, selected examples of state-of-the-art high mobility “semi-amorphous or near-amorphous” polymers will be reviewed.

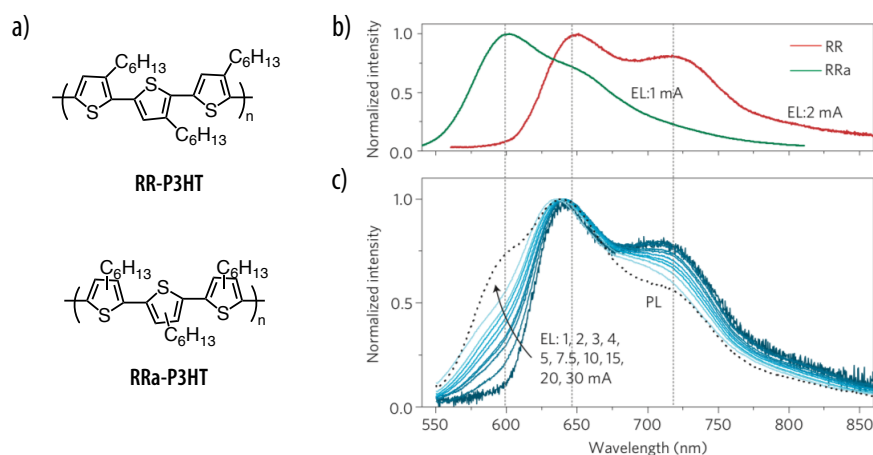


**Figure 1.9.** Noriega et al. carried out a systematic study on the relationship between microstructure and electrical properties in polymer semiconductors. *a*) Chemical structure of regioregular (**RR**) and regiorandom (**RRa**) **P3HT**. *b*) Electroluminescence spectra of films made from pure **RR**- and pure **RRa**-**P3HT**. *c*) Photoluminescence (dotted) and electroluminescence spectra of the blend films containing 90% **RRa**-**P3HT** and 10% **RR**-**P3HT**. Unlike the photoluminescence spectra, the electroluminescence spectra only exhibited emissions from **RR**-**P3HT** on application of a certain current. This finding showed that charges move and recombine in the more ordered regions of the blend. Figure reproduced from ref. [12].

### 1.2.2 Disorder in Polymer Semiconductors

As described in the previous sections, typical polymer semiconductors are semicrystalline and feature varying degrees of structural disorder that affect their electronic properties. The correlation between molecular parameters such as chemical structure and molecular weight, order at different length scales, and electronic properties such as charge carrier mobility is far from trivial. In **P3HT** as a prototypical example, charge carrier mobilities have been found to increase rapidly with increasing molecular weight, despite the simultaneous decrease in long-range order.<sup>25,58</sup> This has been attributed to an improved connection of crystalline domains via amorphous polymer segments. Beyond the entanglement molecular weight of the polymer, however, the crystallites are sufficiently connected, and the charge carrier mobility saturates or even decreases, as further increases in molecular weight merely contribute to overall structural disorder.<sup>12,59</sup> Further investigations have revealed that the size of the individual crystallites in polymer semiconductors is in fact not critical, because the free mean path of charge carriers transverse to the polymer chains is typically of the order of few nanometers.<sup>12,60</sup> Consequently, large domain sizes are less relevant to efficient charge transport than short-range correlations between the polymer chains.<sup>12</sup> This is one of the reasons for the high charge carrier mobilities observed in so-called semi-amorphous or near-amorphous polymer semiconductors developed in recent years. Selected examples will be discussed in the following paragraphs.

One of the first instances of high-mobility donor-acceptor polymers is a copolymer of cyclopentadithiophene and benzodithiazole (**CDT-BTZ**) described by Müllen and coworkers (Figure 1.10).<sup>61</sup> Charge carrier mobilities of up to  $0.17 \text{ cm}^2 \text{ V}^{-1} \text{ s}^{-1}$  were observed in drop-cast



thin films of this polymer on an hexamethyldisilazane (HMDS) treated  $\text{SiO}_2$  substrate and up to  $1.4 \text{ cm}^2 \text{ V}^{-1} \text{ s}^{-1}$  in dip-coated thin films of higher molecular weight.<sup>62</sup> The authors improved the charge carrier mobility to  $3.3 \text{ cm}^2 \text{ V}^{-1} \text{ s}^{-1}$  by further increasing the molecular weight and optimizing the thin film morphology and crystallinity.<sup>63</sup> Even though X-ray diffraction indicated more pronounced order than in lower molecular weight **CDT-BTZ** polymers (Figure 1.10*b*), the disorder remained significantly higher than in semicrystalline polymers as in the case of **P3HT**.<sup>64–66</sup> This indicates **CDT-BTZ** to be a high-mobility polymer with a lack of long-range order.

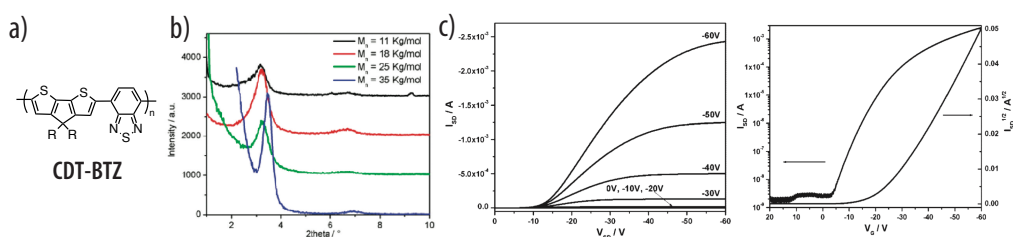


**Figure 1.10.** Müllen et al. described an alternating copolymer **CDT-BTZ**. *a*) Chemical structure of **CDT-BTZ** ( $\text{R} = \text{C}_{16}\text{H}_{33}$ ). *b*) X-ray diffraction patterns from **CDT-BTZ** with different molecular weight. *c*) Output and transfer characteristics for drop-cast annealed thin films **CDT-BTZ** with the highest  $M_n = 35 \text{ kg/mol}$ . Figure reproduced from ref. [63].

In another example, the donor-acceptor polymer naphthalenediimide-bithiophene (**PNDI2OD-T2**) was found to show mobilities of up to  $0.85 \text{ cm}^2 \text{ V}^{-1} \text{ s}^{-1}$  in spin-coated thin films with top-gate bottom-contact (TGBC) architecture after optimizing the choice of the dielectric.<sup>20</sup> The lack of peaks in X-ray diffraction patterns indicated significant macroscopic disorder.<sup>14</sup> However a fiber-like film morphology and exothermic/endothermic phase transitions in differential scanning calorimetry (DSC) scans revealed the presence of crystalline aggregates.<sup>20,67</sup> The same behavior has also been observed in structurally analogous rylene-based copolymers.<sup>68</sup>

Similarly, Zhang et al. studied the molecular origin of the high field-effect mobility observed in an indacenodithiophene-benzothiadiazole (**C<sub>16</sub>IDT-BT**) copolymer (Figure 1.11).<sup>42</sup> Building on previous work,<sup>41</sup> they increased the FET mobility to  $3.6 \text{ cm}^2 \text{ V}^{-1} \text{ s}^{-1}$  by increasing the molecular weight. In addition, temperature-dependent mobility measurements revealed a small activation energy of 61 meV, indicating a low degree of energetic disorder in this polymer (Figure 1.11*b*). However, a detailed study of the orientational order of the entire film revealed significant local molecular order, as opposed to long-range crystalline order (Figure 1.11*c*).

McCulloch and coworkers investigated structure-property relationships in copolymers containing thieno[3,2-*b*]thiophene (**TT**) and **DPP**.<sup>69</sup> These polymers exhibited hole mobilities of up to  $2 \text{ cm}^2 \text{ V}^{-1} \text{ s}^{-1}$  in FET devices and power conversion efficiencies of up to 5.4% with  $\text{PC}_{71}\text{BM}$  in organic photovoltaic devices. Surprisingly, X-ray diffraction and DSC provided no evidence of crystallinity, but optical absorption spectra indicated aggregation in the solid-state. Chung et al. observed similar behavior in a new alternating copolymer composed of dithieno[2,3-

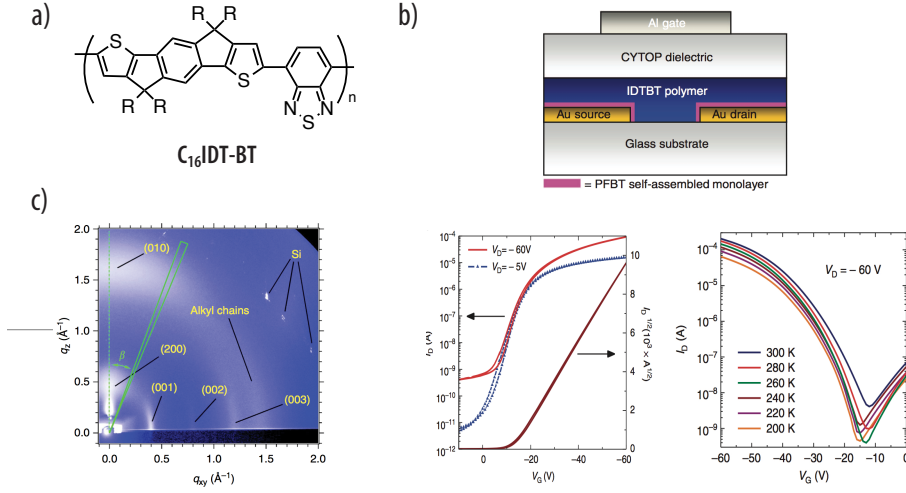


**Figure 1.11.** Zhang et al. studied the molecular origin of high field-effect mobility in a  $C_{16}IDT-BT$  copolymer. *a*) Chemical structure of  $C_{16}IDT-BT$  ( $R = C_{16}H_{33}$ ). *b*) Top: the top-gate bottom-contact device configuration (TGBC) with the channel length  $50 \mu m$  and width  $1 mm$ ; bottom left: transfer curves in the linear and saturation regimes; bottom right: transfer curves from temperature-dependent transistor measurements. *c*) GIXS profile for  $C_{16}IDT-BT$ , where broad arc patterns indicate a lack of longer-range crystalline order. Figure reproduced from ref. [42].

*d*;2',3'-*d'*]benzo[1,2-*b*;4,5-*b'*]dithiophene (**DTBDT**) and **DPP** units (Figure 1.12).<sup>70</sup> This polymer showed hole mobilities of up to  $2.7 cm^2 V^{-1} s^{-1}$  in spin-coated thin films on  $SiO_2$  substrates and activation energies for charge transport as low as  $\sim 40 meV$ , which is similar to those obtained from semicrystalline polymers (Figure 1.12*b*).<sup>12</sup> However, GIXS and AFM studies showed that PDPDBD consisted of disordered small polymer domains with ordered crystalline aggregates (Figure 1.12*c*).<sup>70</sup> A recent comparative study on the correlation between composition and charge transport in **DPP**-based random copolymers also showed that charge transport is influenced more by efficient intramolecular charge carrier delocalization than high degrees of long-range crystalline order.<sup>71</sup>

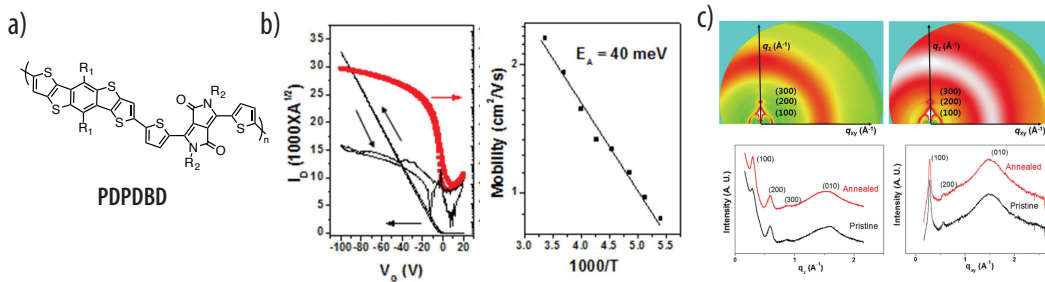


**Figure 1.12.** Chung et al. prepared a new alternating copolymer, **PDPDBD**, and investigated its electronic properties. *a*) Chemical structure of **PDPDBD** ( $R_1 = 2$ -ethylhexyl,  $R_2 = 2$ -decyltetradecyl). *b*) Transfer curve of a FET from annealed **PDPDBD** (left). Temperature-dependent transfer characteristics, where the mobility is plotted as a function of the inverse temperature (right). *c*) 2D GIXS profiles for pristine (top left) and annealed **PDPDBD** thin films (top right). Figure reproduced from ref. [70].



Interestingly, although all of these examples are associated with a low degree of order, they exhibit a strong ability to locally form highly ordered intermolecular aggregates, providing efficient charge transfer between polymer chains, while intramolecular transport is enhanced by their conformationally rigid polymer backbones. It is important to note that the order/disorder phenomena such as the ones described above are in fact not uniquely observed in polymer semiconductors. Crystalline regions in many other polymer systems are known to be highly disordered, to the extent that features commonly associated with three-dimensional crystalline order become difficult to identify. The presence of such disorder in polyamides will be discussed in more detail in Section 1.4.3.

## 1.3 Hydrogen Bonding: From Self-Assembly to Materials

A hydrogen bond,  $D-H\cdots A$ , where D stands for the donor and A stands for the acceptor, is a complex attractive interaction between a hydrogen atom H and an electron pair of an electronegative atom A. The hydrogen bond nevertheless acts as a strong bridge between D and A, and is of great importance for biochemical and physical processes and, in particular, supramolecular chemistry, where it acts as a structure-defining motif that controls and tailors the packing arrangements of molecules.<sup>72–76</sup> This section provides an overview of the characteristics of hydrogen bonding, including directionality and spectroscopic properties, with a particular focus on the applications of hydrogen-bonded molecules in the field of organic electronics.

### 1.3.1 The Nature of Hydrogen Bonding

Although the hydrogen bond was first described over 100 years ago, its definition became over time ambiguous due to the emergence of “weakly hydrogen-bonded” species with weak to moderate electronegativity of D and A, such as  $C-H\cdots O$  and  $C-H\cdots N$ .<sup>73,77</sup> Therefore, a comprehensive report on the hydrogen bond was commissioned by the International Union of Pure and Applied Chemistry (IUPAC) in 2011.<sup>78</sup> This report starts with the following definition of a hydrogen bond: “[The hydrogen bond] is an attractive interaction between a hydrogen atom from a molecule or a molecular fragment  $X-H$  in which X is more electronegative than H, and an atom or a group of atoms in the same or a different molecule, in which there is evidence of bond formation”. It continues with a number of complementary criteria and comments that will be discussed below, together with the techniques that may be used to demonstrate hydrogen bond formation.

Hydrogen bonding is generally weaker than covalent bonding, but significantly stronger than van der Waals interactions, with associated bond energies varying from 2 to 170 kJ/mol.<sup>72,79–81</sup> Its interaction energy may be divided into different components, including the electrostatic  $E_{ES}$ , polarization  $E_{PL}$ , charge transfer  $E_{CT}$ , and van der Waals (exchange repulsion  $E_{EX}$ , dispersion  $E_{DISP}$ ) interaction energies, each with a distinct dependence on distance,  $r$ , and angle.<sup>82</sup> Umeyama and coworkers investigated the origin of hydrogen bonding via an energy decom-

position study.<sup>83</sup> They found that all the above interactions ( $E_{ES}$ ,  $E_{PL}$ ,  $E_{CT}$ ) are important at relatively small distances, while at long distances,  $E_{ES}$  dominates, because its strength decreases with  $r^{-3}$ , that is, more slowly than the other energy terms. However, the contribution of the different energy terms also depends on the chemical nature of the D and A. In addition, strength (covalency), directionality, and cooperativity are key characteristics of hydrogen bonding and distinguish the hydrogen bond from other types of non-covalent interactions.<sup>84</sup>

The nature of hydrogen bonding has been described according to many different models. Surprisingly, all the early models considered strong hydrogen bonds to be “exceptions” and therefore neglected them in the theory. It was hence often thought that the simple electrostatic model (SEM) might be sufficient to describe complex systems containing hydrogen bonding interactions.<sup>85–87</sup> The observation of a large number of hydrogen-bonded complexes with different properties to those predicted on the basis of electrostatic interactions (bond distances and angles) has led to a new model that combines covalent interactions with electrostatic forces, known as the electrostatic-covalent hydrogen bond model (ECHBM).<sup>88,89</sup> According to this model, weak hydrogen bonds are mainly electrostatic in nature, while stronger hydrogen bonds result from a combination of electrostatic and covalent contributions, and become dominated by the covalent term as their strength increases.<sup>88</sup> The strength of a hydrogen bond is not always easy to predict from the nature of D and A. For example, water molecules in an acidic or basic medium have a hydrogen bond strength that is six times stronger than in neutral water.<sup>90</sup> This problem provided the starting point for new predictions of hydrogen bond strength from molecular characteristics.

It is known that a hydrogen bond can be formulated as an acid-base reaction where the hydrogen is transferred to and forms a covalent bond with the acceptor, as well as a hydrogen bond with the donor. The acidic constant  $pK_a$  and proton affinity of the donor and acceptor hence play an important role in the strength of the hydrogen bond. According to Gilli and coworkers, the strength of the hydrogen bond increases continuously with the differences in  $pK_a$  values or proton affinities of D and A as long as these are close to zero.<sup>90</sup> In systems with strong hydrogen bonds, such as HF, dicarboxylic acid dimers and 1,8-bis(dimethylamino)naphthalene, the chemically equivalent structure occurs on hydrogen atom transfer to the acceptor, and the resulting  $\Delta pK_a$  is equal to zero. For hydrogen bonding between amine and carboxylic acid groups, on the other hand, the strong electrostatic interaction occurs between ammonium cation and the carboxylate anion by weak hydrogen bond formation.

The directionality of the hydrogen bond is important in that it strongly affects the molecular conformation of hydrogen-bonded systems. It may be explained in terms of a molecular orbital description of a hydrogen bond. The molecular orbital energy diagram for D–H comprises two energy levels corresponding to a  $\sigma$  orbital filled with two electrons, and an empty  $\sigma^*$  antibonding orbital. As it approaches an acceptor, a lone electron pair from the acceptor interacts with the empty D–H  $\sigma^*$  antibonding orbital. The direction of the  $\sigma$ -bonds and the corresponding  $\sigma^*$  orbital defines the position of the acceptor. Hence, hydrogen bond formation is only strong if the angle D–H...A is close to 180°. The more the bond deviates

from linearity, the less covalent character it will show. This is also confirmed by distance and D–H...A angle analysis of crystal structures taken from the CSD.<sup>91</sup> For strong O–H...O contacts with relatively short H...O distances, the angles are mostly between 170–180 ° (Figure 1.13a), whereas in the case of weak C–H...O contacts, the H...O distances are large and there is a far broader distribution in bond angles (Figure 1.13b).<sup>91</sup>

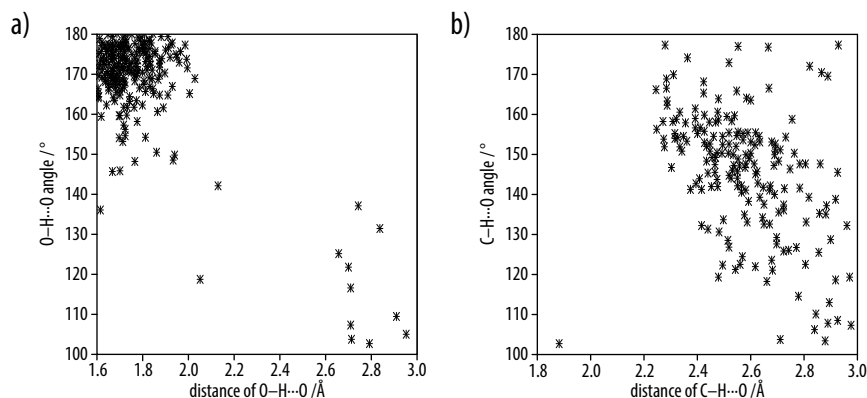


**Figure 1.13.** Scatter plots of the angle versus distance for a) O–H...O and b) C–H...O illustrating the angular preference of strong hydrogen bonds above 160 °. Figure adapted from ref. [91].

Particular combinations of hydrogen bonds may be more stable overall than the sum of the individual hydrogen bond energies. This phenomenon is known as cooperativity and is another important characteristic of hydrogen bonds.<sup>92</sup> Cooperativity may be grouped into two categories proposed by Jeffrey,<sup>93</sup> namely  $\sigma$ -bond and  $\pi$ -bond cooperativity. The former is also known as polarization assisted (enhanced) hydrogen bonding; the polarization of A–H is increased by additional hydrogen bonding, D–H...A–H...A, leading to enhancement of the H...A interaction. Polarization-assisted hydrogen bonding is typical of moderately strong hydrogen bonds that form chains or rings, such as the O–H...O–H bonds in alcohols, water and phenol crystals.<sup>82</sup> By contrast,  $\pi$ -bond cooperativity, also called as resonance-assisted hydrogen bonding (RAHB), occurs when the donor and acceptor of the hydrogen bond are connected to segments containing alternating single and double bonds and mainly dependent on the synergistic effect between hydrogen bond strengthening and  $\pi$ -delocalization through D and A.<sup>94</sup> Typical examples include the strong O–H...O interactions between dimers of carboxylic acid or  $\beta$ -diketone enols. RAHB is at the origin of the keto-enol tautomerism and is of vital importance in biochemistry via its role in DNA and the secondary structure of proteins, for example.<sup>95,96</sup> Hence, an excellent example of RAHB is an amide N–H group that becomes a stronger donor by accepting the oxygen atom of another amide group, resulting a hydrogen bond, N–H...O=C–N–H that has a zwitterionic resonance form. Beside of this resonance enhancement, the amides are acidic enough and  $\Delta pK_a$  value between amide NH ( $15 < pK_a < 17$ ) and the hypothetical OH ( $-2 < pK_a < 1$ ), that is the result of the hydrogen bond formation, is far from zero.<sup>90</sup> Thus amide hydrogen bonding is only moderate in strength, with energies of around 60 kJ/mol and strongly directional.<sup>91,97</sup> The mixture of electrostatic and covalent nature of amide hydrogen bonding is beneficial for its utilization as structure-directing motif.

## Chapter 1. General Introduction

On this basis, a classification of the hydrogen bond strength was proposed by Jeffrey<sup>98</sup> (Table 1.1). However, there are no well-defined limits between the different categories.

**Table 1.1:** Hydrogen bond strength can be divided into three categories, namely strong, moderate and weak based on their nature and geometrical parameters. Data adapted from ref. [98].

	Strong	Moderate	Weak
<b>interaction type</b>	strongly covalent	mostly electrostatic	electrostatic
<b>bond energy [kJ/mol]</b>	60–170	20–60	2–20
<b>H...A [Å]</b>	1.2–1.5	1.5–2.2	>2.2
<b>X...A [Å]</b>	2.2–2.5	2.5–3.2	>3.2
<b>directionality</b>	strong	moderate	weak
<b>bond angles [°]</b>	170–180	>130	>90

Evidence for hydrogen bonding and estimates of its strength may be obtained from both experimental and computational techniques.<sup>91</sup> Infrared (IR) spectroscopy is one of technique that is uniquely sensitive towards the formation of hydrogen bonds, which leads to significant changes in the vibrational energies of the associated groups. For example, upon formation of an N–H...O=C bond, the C=O and N–H bonds are weakened, resulting in a shift of the corresponding stretching vibration towards lower frequencies. More detailed peak analysis of the IR absorption peak shape and full width at half maximum (FWHM) shed light on the nature of the cooperativity and, hence, the strength of the hydrogen bond. For example, Coleman and coworkers used temperature-dependent IR spectroscopy to quantify the degree of hydrogen bonding in semicrystalline and amorphous polyamides and polyurethanes.<sup>99–101</sup> They found that the amide A mode was insensitive to conformational changes, and that its width reflected the distribution of hydrogen bond strengths, a narrower distribution leading to a smaller bandwidth. By contrast, the amide I band was sensitive to conformational changes mainly due to dipole-dipole interactions, so that ordered and disordered hydrogen bonds could be distinguished quantitatively.

<sup>1</sup>H NMR spectroscopy is another technique that may be useful for characterizing hydrogen bonding. Increasing the strength of the hydrogen bond interaction increases deshielding of the proton nuclei, leading to a downfield chemical shift.<sup>82,91,102</sup> This chemical shift may also be correlated with the length of the hydrogen bond. Gilli and coworkers investigated the relationship between crystallographic data and the <sup>1</sup>H NMR chemical shift of the  $\beta$ -diketone enol groups, which form intramolecular hydrogen bonds.<sup>103</sup> They prepared five new compounds containing  $\beta$ -diketone enol fragments and determined their structure from X-ray measurements (Figure 1.14a). Shortening of the intramolecular hydrogen bond length was found to be correlated with the downfield shift of the enolic proton signal  $\delta(\text{OH})$ , consistent with 42 other analog structures retrieved from the Cambridge Structural Database (CSD) (Figure 1.14b). Moreover, direct evidence of hydrogen bond formation may be obtained from correlation spectroscopy (COSY), as a result of scalar coupling between magnetically active nuclei on both sides of hydrogen bond.<sup>104–106</sup> The size of the scalar coupling is affected by the

geometrical arrangement of the magnetically active nuclei, and its detailed analysis therefore provides significant structural insight into hydrogen bond formation.<sup>107,108</sup>

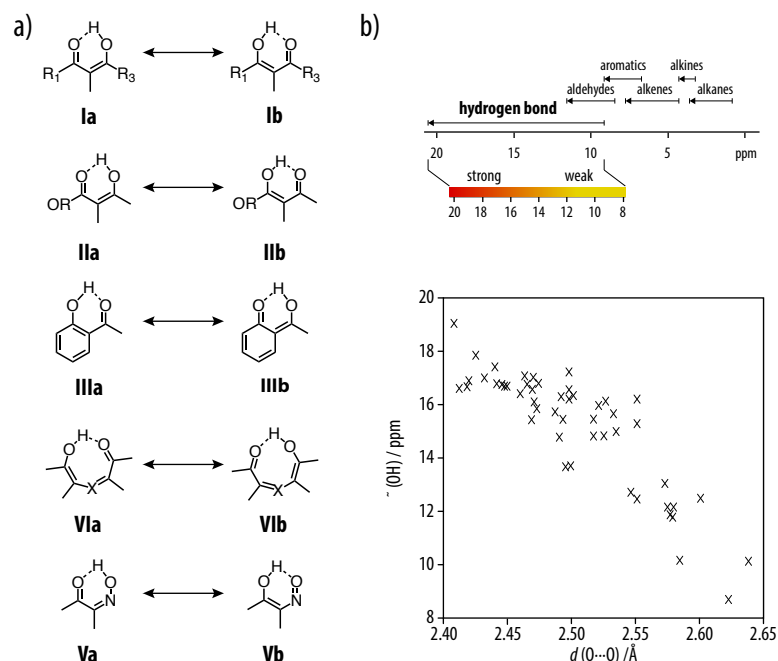


**Figure 1.14.** Gilli et al. examined the correlation between the intramolecular O–H...O hydrogen bond distance and  $^1\text{H}$  NMR chemical shifts of the enolic proton  $\delta(\text{OH})$  in  $\beta$ -diketone enols. *a)* Classification of different molecules with  $\text{O}=\text{C}-\text{C}=\text{C}-\text{OH}$   $\beta$ -diketone enol groups; **I**  $\beta$ -diketone enols, **II**  $\beta$ -ketoesters, **III** 2-hydroxybenzoketones, **IV**  $\delta$ -diketone enols, **V**  $\alpha$ -keto-oximes. *b)* Top: The range of  $^1\text{H}$  NMR chemical shifts correspond to hydrogen bonds with different strengths. Bottom: A plot of  $\delta(\text{OH})$  versus distance  $d(\text{O}\cdots\text{O})$  shows that shortening of the bond distance is strongly correlated with the downfield shift of the enolic proton. Figure reproduced from refs. [103,109].

In conclusion, it has become clear that hydrogen bonding does not correspond to one specific type of interaction with a certain energy and geometry. It exists in many different forms, depending on the chemical nature of the components. As a consequence, hydrogen bond interactions cover a wide range of geometries and bond energies. Crystallographic data combined with different characterization techniques, including vibrational spectroscopy and NMR, and numerical modeling has provided considerable insight into hydrogen bond formation in structurally complex molecules.

### 1.3.2 The Role of Hydrogen Bonding in Organic Electronics

Hydrogen bonding is ubiquitous in natural systems. For instance, hydrogen bonding connects complementary base pairs in a DNA double helix and is responsible for structure formation and functionality in proteins. Hydrogen-bonded templates are also well known to guide self-assembly at the molecular level in many synthetic systems with important consequences for crystal engineering and organic electronics, for example. The present section is aimed at

elucidating the role of hydrogen bonding in  $\pi$ -conjugated materials. Selected examples of the use of hydrogen-bonded templates as a tool for designing new functional materials will be presented in what follows.

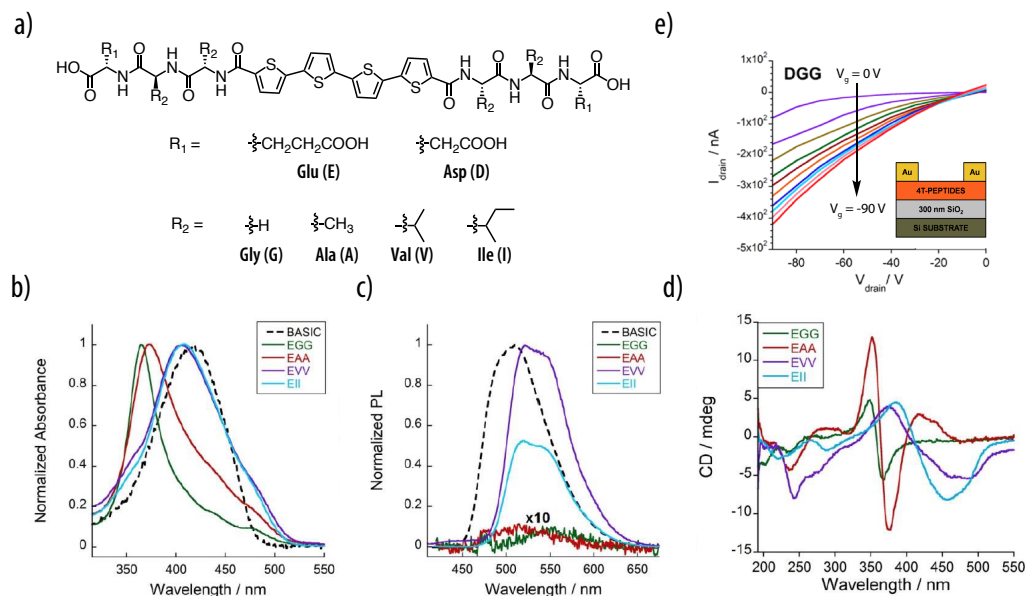


**Figure 1.15.** Tovar et al. prepared quaterthiophenes substituted with tripeptide segments and investigated their performance in OFET devices. *a*) Molecular structure of **T4- $\text{R}_1\text{R}_2\text{R}_2$**  where  $\text{R}_1$  and  $\text{R}_2$  are chosen from glutamic acid (Glu), aspartic acid (Asp) and glycine (G), alanine (A), valine (V), or isoleucine (I). Solution-phase *b*) absorption, *c*) fluorescence and *d*) CD spectra of **T4ER<sub>2</sub>R<sub>2</sub>** demonstrate that **AA** and **GG** substituted molecules have the highest intermolecular electronic coupling, leading to most blue-shifted absorption, quenched emission and strong bisignate CD signal with a negative Cotton effect. *e*) Output characteristics of OFET devices with the **T4-DGG** as semiconducting layer yielded mobilities as high as  $0.02 \text{ cm}^2 \text{ V}^{-1} \text{ s}^{-1}$ . Figure reproduced from ref. [110].

Hydrogen bonding has been widely used to promote solution-phase self-assembly of  $\pi$ -conjugated systems. Many well-defined one-dimensional nanostructures containing different  $\pi$ -conjugated cores have been prepared and analyzed using spectroscopic techniques.<sup>111–113</sup> However, these have rarely been implemented in electronic devices. Tovar and coworkers investigated the incorporation of an electron-rich quaterthiophene substituted with different oligopeptide segments as an active layer in the organic field-effect transistors (OFET). (Figure 1.15).<sup>110</sup> The different oligopeptide sequences were attached to the ends of quaterthiophenes using solid-state peptide synthesis and Pd-catalyzed cross-coupling reactions.<sup>114,115</sup> Reversible self-assembly by intermolecular hydrogen bonding resulted in the formation of one-dimensional nanostructures under acidic conditions, as evidenced by UV-vis, CD and fluorescence spectroscopy (Figure 1.15*b–d*). Devices fabricated from drop-cast specimens of **T4-DGG** exhibited mobilities as high as  $0.02 \text{ cm}^2 \text{ V}^{-1} \text{ s}^{-1}$ , performing better than previously reported peptide-oligothiophene nanostructures (Figure 1.15*e*).<sup>114,116–118</sup> However, with other oligopeptide segments **T4-EVV** or **T4-DVV**, the obtained mobility decreased drastically by about three orders of magnitude, and was even lower for **T4-EII** or **T4-DII**, for which no measurable mobilities were observed. The authors attributed these decreases to the bulkier

### 1.3. Hydrogen Bonding: From Self-Assembly to Materials

nature of isoleucine and valine residues, which may hinder the  $\pi$ -conjugation to a greater extent than glycine and alanine. Additionally, in a control experiment they demonstrated that the oligopeptides without a semiconducting core showed no conductivity.

In another example, Stupp and coworkers examined the use of self-assembly of a hairpin-shaped oligothiophene incorporated as a donor component in bulk heterojunction solar cell devices (Figure 1.16).<sup>119</sup> The self-assembly of the hairpin-shaped sexithiophene (**T6-M1**) in toluene resulted in voids along the resulting nanofiber axes. The authors claimed that this particular nanostructure could accommodate a molecule such as phenyl-C<sub>71</sub>-butyric acid methyl ester (PC<sub>71</sub>BM), and prevent it from phase-segregating on thermal annealing. This type of complex therefore facilitates efficient exciton splitting, while maintaining charge percolation domains. In order to back up this hypothesis, the device performance of self-assembled **T6-M1** was compared with that obtained with linear dihexylsexithiophene, which is not capable of forming hydrogen bonds. Devices prepared with **T6-M1** performed significantly better ( $\mu = 0.48\%$ ) than those fabricated with linear molecules ( $\mu = 0.09\%$ ).

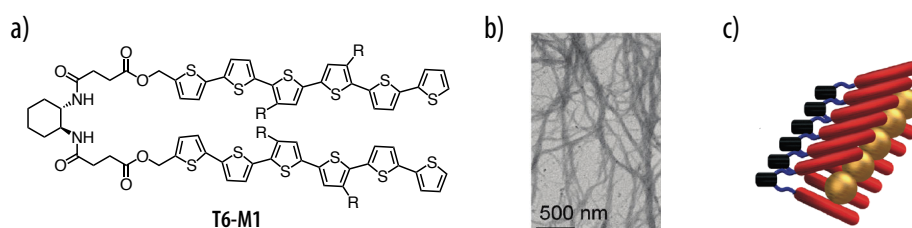


**Figure 1.16.** Stupp et al. employed a self-assembling hairpin-shaped **T6-M1** as a donor component in organic solar cells. *a*) Molecular structure of **T6-M1** (R = hexyl). *b*) Transmission electron microscopy (TEM) images of **T6-M1** showed bundles of nanofibers. *c*) Illustration of the nanostructural organization of **T6-M1** in the presence of PC<sub>71</sub>BM upon thermal annealing. Figure reproduced from refs. [116,119].

The main idea behind the incorporation of 1D nanostructures into devices is to gain insight into the resulting structure-property relationships, rather than to obtain high-performance semiconductors, because charge transport pathways are restricted to one dimension. During the last decade, many different hydrogen-bonded  $\pi$ -conjugated compounds have emerged and have been studied as charge-transport materials in OFETs.

One of the earliest hydrogen-bonded organic semiconductors was investigated by Würthner and coworkers.<sup>120</sup> They prepared octachloroperylene bisimide (**Cl<sub>8</sub>-PTCDI**) and investigated its performance in a field-effect transistor set-up (Figure 1.17). The crystal structure of this material exhibited a highly twisted perylene backbone with close face-to-face stacking of around 3.4 Å, resulting in a dense “brickwork” arrangement (Figure 1.17*b*). OFETs fabricated from this material exhibited electron transport mobilities of between 0.5 and 0.9 cm<sup>2</sup> V<sup>-1</sup> s<sup>-1</sup>, along with excellent  $I_{\text{on}}/I_{\text{off}}$  ratios of up to 10<sup>8</sup> in both air and an inert atmosphere, as well as a remarkable device stability (Figure 1.17*c*). For comparison, OFETs prepared from the related non-hydrogen-bonded octachloroperylene bisanhydride showed mobilities almost

five orders of magnitude lower. The authors attributed the improved performance of the hydrogen-bonded structure to enhanced charge percolation paths for electron transport.

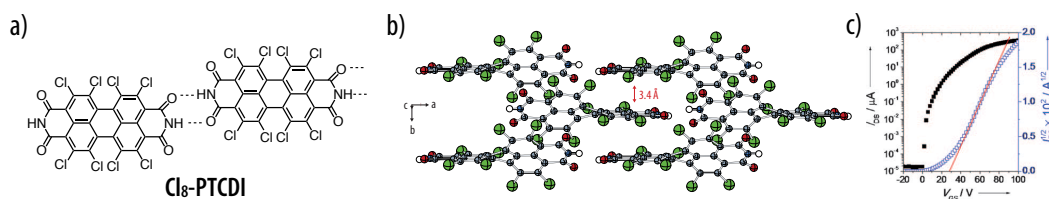


**Figure 1.17.** Würthner et al. demonstrated crystal engineering approach using hydrogen bonding, resulting an enhanced device performance together with remarkable device stability. *a)* Molecular structure of **Cl<sub>8</sub>-PTCDI** *b)* Single crystal X-ray structure analysis revealed a twisted perylene backbone with a “brickwork” arrangement. *c)* Transfer curve of an OFET from **Cl<sub>8</sub>-PTCDI** showing mobilities as high as  $0.9 \text{ cm}^2 \text{ V}^{-1} \text{ s}^{-1}$  with excellent  $I_{\text{on}}/I_{\text{off}}$  ratios up to  $10^8$  in air. Figure reproduced from ref. [120].

Further pioneering work was carried out by Głowacki and coworkers, who investigated the semiconductor behavior of commercially available low-cost hydrogen-bonded organic pigments, by employing them as an active layer in OFETs and organic light emitting diodes (OLED).<sup>121–128</sup> For example, they prepared OFETs from N–H...O=C hydrogen-bonded epindolidone and quinacridone, which can be regarded as heteroacene analogues of tetracene and pentacene, respectively (Figure 1.18*a*).<sup>122</sup> In a bottom-gate top-contact device configuration, mobilities of up to  $1.5 \text{ cm}^2 \text{ V}^{-1} \text{ s}^{-1}$  and  $0.1 \text{ cm}^2 \text{ V}^{-1} \text{ s}^{-1}$  were observed for these two compounds, respectively (Figure 1.18*b,c*). In addition, these heteroacene pigments showed enhanced device stability compared with their well-known non-hydrogen-bonded acene analogues (Figure 1.18*b,c*). The authors attributed this improved stability to the lowering of corresponding HOMO energy levels by inclusion of electronegative nitrogen and oxygen atoms in the  $\pi$ -conjugated system.

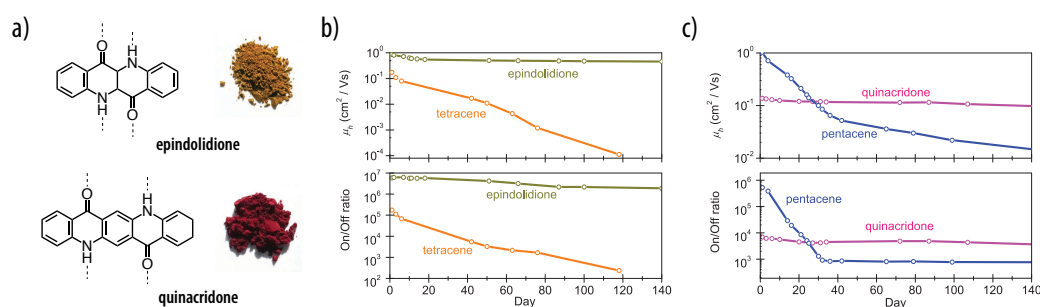


**Figure 1.18.** Głowacki et al. investigated the thin film transistor performance of organic pigments that had been widely used as toners for inkjet printing and were available at low-cost. *a)* Molecular structure of epindolidone and quinacridone. OFET devices fabricated from *b)* epindolidone and *c)* quinacridone resulted in mobilities of up to 1.5 and  $0.1 \text{ cm}^2 \text{ V}^{-1} \text{ s}^{-1}$  along with  $I_{\text{on}}/I_{\text{off}}$  ratios around  $10^7$  and  $10^4$ , respectively. Both were stable in air more than 140 days, as compared to their non-hydrogen-bonded acene analogues. Figure reproduced from ref. [122].

The previous examples involved the formation of hydrogen bond arrays within the plane of a  $\pi$ -conjugated system, which has been demonstrated to be useful in enhancing the  $\pi$ -interactions between the neighboring molecules, resulting in promising OFET characteristics.



In an alternative approach, organic molecules with hydrogen bonding donor and acceptor functions may be used to guide hetero-association through complementary hydrogen bonding perpendicular to the  $\pi$ -stacking axis. Perepichka and coworkers combined p-type and n-type organic semiconductors in this way by complementary hydrogen bonding (Figure 1.19).<sup>129</sup> They employed diphenyldipyrrolopyridine (**DP-P2P**), which forms triple hydrogen bonds with naphthalenetetracarboxydiimide (**NDI**). Single-crystal X-ray analysis revealed that **DP-P2P:NDI-8<sub>1</sub>** self-organized into segregated stacks connected by the short hydrogen bonds (Figure 1.19b). Changing the *N*-substituent on the **NDI** to cyclohexyl, however, resulted in mixed stacks of the two components. OFET devices based on the co-crystals of **DP-P2P:NDI-8<sub>1</sub>** and **DP-P2P:NDI-CyHex** showed ambipolar transport with hole and electron mobilities of 0.043 and 0.089 cm<sup>2</sup> V<sup>-1</sup> s<sup>-1</sup> and 0.0004, 0.22 cm<sup>2</sup> V<sup>-1</sup> s<sup>-1</sup>, respectively, while **DP-P2P:NDI-H<sub>2</sub>** was found to show only unipolar behavior with electron mobilities of 0.0003 cm<sup>2</sup> V<sup>-1</sup> s<sup>-1</sup> (Figure 1.19c).

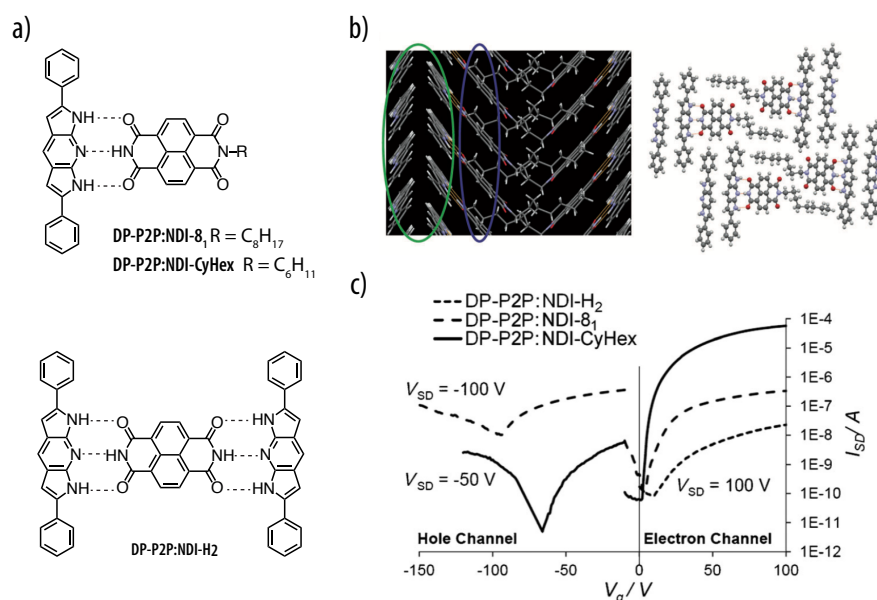


**Figure 1.19.** Perepichka et al. exploited co-assembly of hydrogen donor and acceptor molecules through complementary hydrogen bonding and investigated the resulting electronic properties of the cocrystals. *a*) Molecular structure of diphenyldipyrrolopyridine (**DP-P2P**), which co-assembled with naphthalenetetracarboxydiimides (**NDI**) via triple hydrogen bonds. *b*) The single crystal X-ray structure of **DP-P2P:NDI-8<sub>1</sub>** displayed an alternating arrangement of dimerized donor and acceptor columns, marked with green and purple circles, respectively *c*) Transfer characteristics of single co-crystal OFET devices demonstrated ambipolar transport for **DP-P2P:NDI-8<sub>1</sub>** and **DP-P2P:NDI-CyHex**, while only unipolar n-type transport was observed for **DP-P2P:NDI-H<sub>2</sub>**. Figure reproduced from ref. [129].

Several groups have also investigated the effect of hydrogen-bonded end groups on charge carrier mobility. For instance, Asha and coworkers studied structure-property relationships in different naphthalene diimide amide derivatives.<sup>130</sup> Similarly, Dautel and coworkers examined the role of hydrogen bonding in a hydroxyl end group functionalized benzothieno[3,2-*b*][1]benzothiophene (BTBT).<sup>131</sup> In both cases, hydrogen bonding induced self-organization in

the solid-state, but no significant improvements in hole and electron mobilities were observed. By contrast, an  $\alpha,\omega$ -hydroxypropyl-substituted sexithiophene was found to exhibit enhanced layer-by-layer thin film growth via interlayer hydrogen bonding.<sup>132</sup> Thus, field-effect mobilities of up to  $0.07 \text{ cm}^2 \text{ V}^{-1} \text{ s}^{-1}$  were observed, which were close to the highest mobility reported for  $\alpha$ -sexithiophene,<sup>133</sup> but still more than one order of magnitude lower than that of  $\alpha,\omega$ -dihexylsexithiophene.<sup>133</sup> Interestingly, these hydrogen-bonded thin films also showed improved stability towards atmospheric degradation.

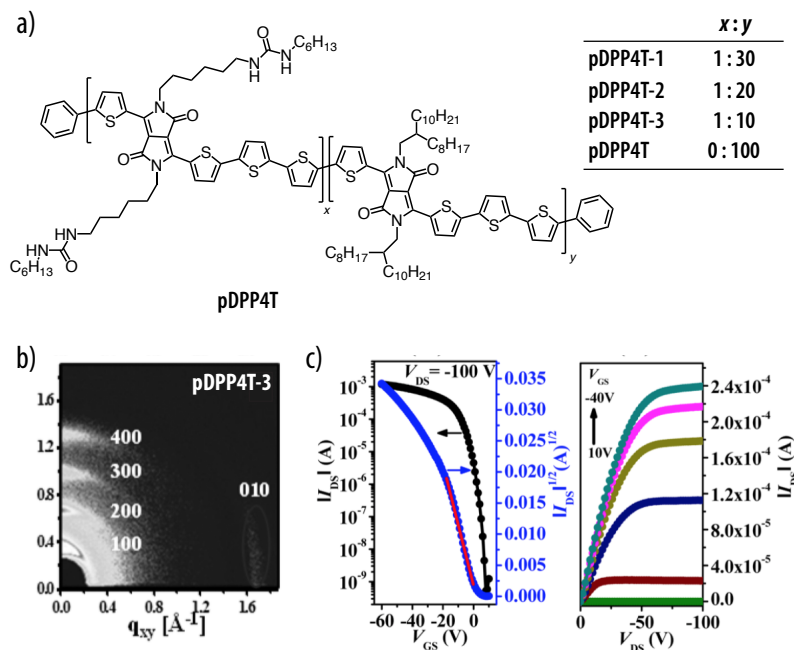


**Figure 1.20.** Zhang et al. investigated how urea-containing alkyl chains affect FET device performance. *a*) Molecular structure of diketopyrrolopyrrole-quaterthiophene (**DPP4T**) semiconducting polymer with urea-containing alkyl side chains in the molar ratios 1:30, 1:20, 1:10, 0:100. *b*) 2D GIXS profiles for annealed **pDPP4T-3** deposited on an OTS modified  $\text{Si}^+/\text{SiO}_2$  substrate exhibited a well-defined lamellar arrangement. *c*) Transfer and output curves from OFET devices fabricated from the thin films of **pDPP4T-3** using a bottom gate top contact configuration, after annealing. Figure reproduced from ref. [134].

Side chains in polymer semiconductors play a significant role in device performance.<sup>23,52</sup> However only a few examples of hydrogen-bonded side chains in polymer semiconductors have been reported to date.<sup>134,135</sup> For example, Zhang and coworkers prepared a series of diketopyrrolopyrrole-quaterthiophene conjugated polymers comprising varying molar ratios of urea-containing alkyl chains and branched alkyl chains in order to investigate the effect on the charge carrier mobility (Figure 1.20).<sup>134</sup> According to GIXS data (Figure 1.20*b*), the presence of the urea groups in the alkyl side chains was found to enhance the lamellar packing order in thin films as compared with **pDPP4T** without the hydrogen-bonded side chains. FET devices fabricated from **pDPP4T-3** by spin coating revealed hole mobilities of up to  $13.1 \text{ cm}^2 \text{ V}^{-1} \text{ s}^{-1}$  after thermal annealing, while **pDPP4T** showed hole mobilities of not more than  $3.4 \text{ cm}^2 \text{ V}^{-1} \text{ s}^{-1}$  (Figure 1.20*c*). This mobility is among the best reported to date. In the

same study, the urea containing alkyl side chain polymers were used as a donor component in the bulk heterojunction solar cell devices with PC<sub>71</sub>BM as an acceptor. These devices yielded higher power conversion efficiencies than for polymers lacking the urea groups in the side chains.

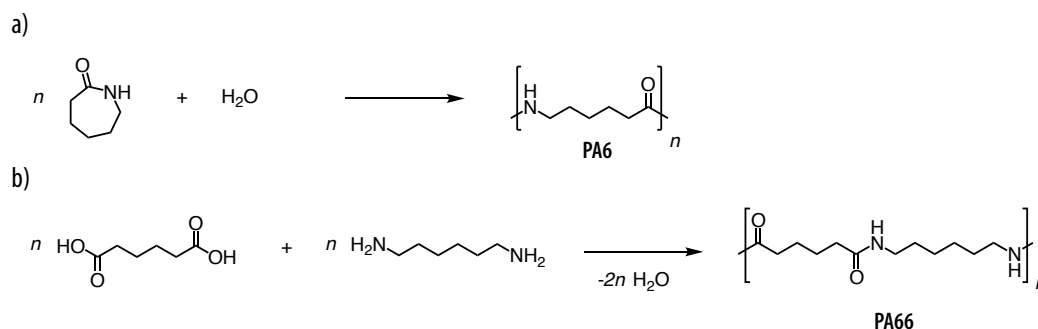
In conclusion, hydrogen bonding as an additional structure-directing element may be applied successfully in both p-type and n-type small molecule and polymer semiconductors for organic electronic applications. It may be used as a supramolecular motif either as part of the  $\pi$ -system or attached to the  $\pi$ -system. In both cases, it is clear that hydrogen bonding is a highly effective tool for molecular design, promoting self-assembly and guiding crystal packing and film morphologies, rendering beneficial effects for resulting device performance.

### 1.4 The Amide Motif in Polymers: Polyamides

Since the invention of the world's first synthetic fiber, Nylon-6,6 (or PA66) by W.H. Carothers and its first commercialization by DuPont in 1939,<sup>136</sup> many different types of polyamides have been developed with tailored properties for a wide range of applications, from clothes to automotive industry.<sup>137</sup> Understanding the chemical structure of polyamides and the nanoscopic arrangement of the chains is of great importance because they will greatly influence the aggregation and structure of its crystalline phase and thus determine the physical and mechanical properties. This section therefore gives a brief overview of the nomenclature of polyamides and the synthetic procedures most relevant to laboratory scale synthesis, followed by a discussion of their microstructure, morphology, and properties and as well as a presentation of selected applications.

#### 1.4.1 General Features and Nomenclature of Polyamides

Polyamides, also known as Nylons, are engineered thermoplastic materials that contain multiple amide groups along the polymer chain. They can be divided into two categories, namely naturally occurring (silk, wool) and synthetically produced (Kevlar<sup>®</sup>, Nylon 6) polyamides. The latter are produced either by ring opening polymerization of lactams (AB-type) or polycondensation reaction of two complementary monomers (AABB-type) (Scheme 1.1).<sup>138</sup> Ring opening polymerization only gives aliphatic polyamides, whereas polycondensation accounts for considerable more chemical diversity. The combination of an aliphatic or aromatic monomer with an aromatic monomer, for example, results in semiaromatic and fully aromatic polyamides, respectively. The nomenclature for aliphatic AB-type and AABB-type polyamides is as follows. The letters "PA" are followed by the number of the carbon atoms present in the repeating unit for AB-type polyamides, while for AABB-type polyamides, "PA" is followed first by the number of the carbon atoms in the diamine unit and then that in the diacid unit.

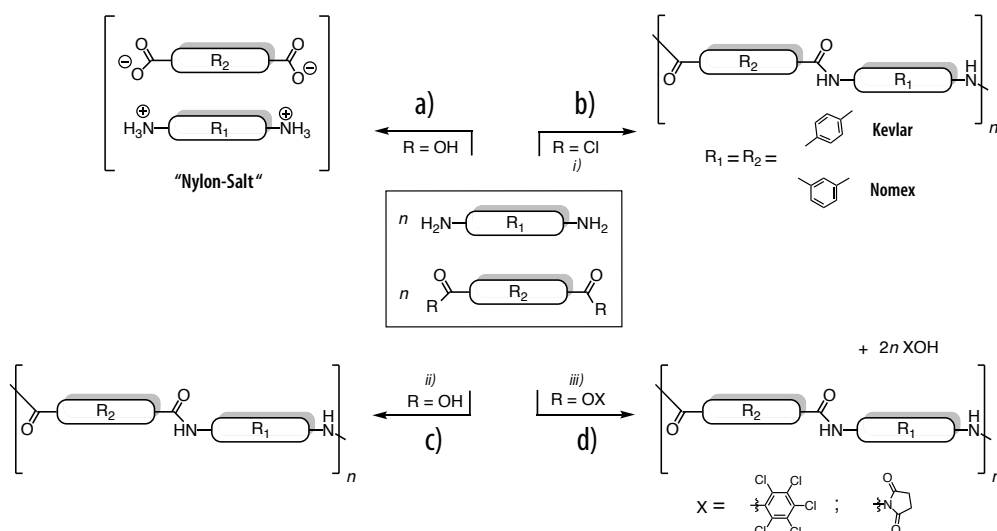


**Scheme 1.1.** Illustrative examples for the synthesis of AB- and AABBB-type polyamides. *a)* Generally aliphatic AB-type polyamides can be prepared by ring opening polymerization of lactams. For example, PA6 can be synthesized starting from  $\epsilon$ -caprolactam with water as a nucleophile. *b)* Synthetic scheme for the polycondensation of PA66 starting from adipic acid and hexamethylene diamine. This is a general scheme for AABBB-type polyamides that can be used for preparation of aliphatic, semiaromatic or fully aromatic polyamides.

### 1.4.2 Synthesis Approaches

Because polycondensation is an example of a step-growth polymerization, the use of equimolar amounts of the both monomers is crucial. Any deviation from equimolarity has a huge impact on the degree of polymerization and thus on the molecular weight, as shown by Carothers equation.<sup>139</sup> Therefore, industrial-grade AABBB-type polyamides are often synthesized starting with the formation of the diammonium dicarboxylate salt (“Nylon salt”), which allows for better control of the stoichiometric ratio of the monomers (Scheme 1.2*a*).<sup>140</sup> The Nylon salt is polycondensed at high temperature and pressure (up to 50 bars) in a water-based process using a high-pressure autoclave to create a supercritical water dispersion. Solid-state or melt post-polycondensation is then used to achieve the desired molecular weight.<sup>138,141</sup> However this method is not suitable for the industrial preparation of fully aromatic and certain semiaromatic polyamides, which tend to decompose before they melt.<sup>142</sup> There has therefore been an interest in developing alternative solution polycondensation techniques (Scheme 1.2*b–d*). The most widely used laboratory-scale methods will be reviewed in the following paragraphs.

The well-known ‘fully’ aromatic polyamides (or “aramids”), marketed under the tradenames Kevlar® and Nomex®, were first synthesized by workers from DuPont using low-temperature solution polycondensation of diacyl chlorides with diamines (Scheme 1.2*b*).<sup>143</sup> This process is suitable for many polyamides<sup>144–148</sup> and typically takes place in polar aprotic amide solvents such as *N*-methyl-2-pyrrolidone (NMP), hexamethylphosphoramide (HMPA), *N,N*-dimethylacetamide (DMAc), which scavenge the hydrogen chloride formed in the reaction.<sup>142</sup> Other polar solvents such as *N,N*-dimethylformamide (DMF) and dimethylsulfoxide (DMSO) cannot be used due to significant side reactions with acyl chloride monomers.<sup>142</sup> In some cases, triethylamine was used effectively as the base to scavenge the hydrogen chloride, along with an inorganic salt (LiCl, CaCl<sub>2</sub>) to facilitate solubility in the early stages of polycondensation, thus avoiding any premature precipitation.<sup>149</sup>



**Scheme 1.2.** General synthetic scheme of melt and solution-phase polycondensations. *a)* Melt polycondensation between two bifunctional monomers at high temperatures through “Nylon salt” formation, which enables control over the stoichiometry, is typically used for preparation of aliphatic polyamides. Solution-phase polycondensation, which is preferred for synthesis of semiaromatic and aromatic polyamides, can be divided into low-temperature or direct polycondensation carried out in either the presence or absence of phosphites and inorganic salts. For instance, *b)* Kevlar® and Nomex® were synthesized by low-temperature polycondensations starting from monomers *p*-phenylene diamine, terephthaloyl chloride and *m*-phenylene diamine isophthaloyl chloride, respectively. *Reagents and conditions:* *i)* triethylamine, inorganic salts ( $\text{LiCl}$ ,  $\text{CaCl}_2$ ), NMP,  $< 0^\circ\text{C}$ . *c)* The direct solution polycondensation of diacid and diamine monomers is carried out at higher temperatures using triphenyl phosphite (TPP). This polycondensation is also known as Yamazaki-Higashi polycondensations. *Reagents and conditions:* *ii)* TPP, inorganic salt ( $\text{LiCl}$ ,  $\text{CaCl}_2$ ), NMP/pyridine,  $120^\circ\text{C}$ . *d)* The active ester polycondensation route has the advantage that additional additives (inorganic salts, catalysts) are not required. *Reagents and conditions:* *iii)* HMPA or DMSO  $30\text{--}120^\circ\text{C}$ .

Although diacyl chlorides are readily synthesized from dicarboxylic acids using, for instance, thionyl chloride, the instability of diacyl chlorides towards hydrolysis makes them difficult to purify and store for longer periods of time. Alternative solution polycondensation approaches have therefore been sought. In 1974, Higashi and Yamazaki developed a novel method starting from the dicarboxylic acid and diamine monomers (Scheme 1.2c).<sup>150–152</sup> The reaction was carried out in NMP using triphenyl phosphite (TPP) with  $\text{LiCl}$  or  $\text{CaCl}_2$  and pyridine as activating agents at temperatures of  $80\text{--}120^\circ\text{C}$ . The authors stated that the formation of the polyamide proceeds via a pentacoordinated intermediate between TPP, pyridine and the dicarboxylic acid monomer that eventually breaks down to phenol and diphenylphosphite, under recycling of the pyridine.<sup>153,154</sup> One of the advantages of this route is that it uses the same starting monomers as the industrial process and can proceed at higher temperatures, reducing the overall reaction time. Polyamides prepared by this method are typically obtained in high yields and as high molecular weight polymers, but with the drawback of a by-product that is difficult to remove, necessitating several consecutive washing steps with hot MeOH.

Attempts to replace the TPP led to no significant improvement in the results.<sup>155</sup> This process is therefore preferred in its originally published form.

Katsarava et al.<sup>156,157</sup> used an alternative approach, active ester polycondensation, based on the work of Šebenda et al.<sup>158</sup> and Ohira et al.<sup>159</sup> Instead of using the dicarboxylic acid monomer, they prepared its active ester derivatives via esterification with pentachlorophenol<sup>157</sup> or *N*-hydroxysuccinimide (Scheme 1.2*d*).<sup>156</sup> The resulting active esters were then polycondensed with various diamines in HMPA medium at temperatures between 30 and 120 °C. Introduction of various additives (inorganic salts, catalysts) to the reaction mixture resulted in no significant change in polycondensation rate.<sup>156</sup> This approach is especially useful compared to other methods owing to its straightforward work-up by precipitation into water, followed by several washing steps in water and acetone. However, its main drawback is the use of the carcinogenic HMPA, which was later replaced with DMSO by Kricheldorf and coworkers.<sup>160</sup>

In conclusion, solution-phase polycondensation is a suitable method for laboratory scale synthesis without the need for high pressure and temperatures. However, the resulting molecular weights are typically not as high as those obtained at the industrial scale, due to precipitation from solution. Moreover, for solution phase polycondensation, the monomer concentration, reaction temperature, solvent(s) and the speed of the stirring must be adjusted for different monomers, which also influences the resulting molecular weight of the polyamide.

### 1.4.3 Crystallinity and Typical Crystal Morphology

Polymers are frequently classified according to whether they are fully amorphous or semicrystalline. Semicrystalline polyamides are generally composed of certain fraction of ordered, chain-folded, typically lamellar crystallites dispersed in a matrix of non-crystalline, “amorphous” material. These crystallites typically form spherical aggregates known as spherulites under quiescent crystallization conditions. The crystallization behavior of a polyamide has a huge impact on its physical and mechanical properties. In this subsection, we shall therefore review the typical crystal structure and morphology of commercially available polyamides.

The crystallization of polyamides is strongly influenced by hydrogen bonding between N–H and C=O groups in neighboring chains. Hence, many polyamides form two-dimensional hydrogen-bonded sheets that stack via van der Waals interactions to form three-dimensional crystals.<sup>161</sup> However, depending on the crystallization conditions and the stability and crystallization kinetics associated with other types of crystalline arrangements, polyamides may show a wide range of crystalline polymorphs.<sup>161</sup> Common commercial “even-even” AABB-type and “even” AB-type aliphatic polyamides such as PA66 and PA610, and PA6, respectively are found to crystallize predominantly in the so-called  $\alpha$  form, which consists of stacks of hydrogen-bonded sheets with the chains in an all-*trans* conformation. Fiber X-ray diffraction patterns show similar crystallographic unit cell parameters in all cases, with the exception of the *c* repeat distance;<sup>162,163</sup> for instance,  $a = 4.9 \text{ \AA}$ ,  $b = 5.4 \text{ \AA}$ ,  $c = 17.2 \text{ \AA}$ ,  $\alpha = 48.5^\circ$ ,  $\beta = 77^\circ$ ,

$\gamma = 63.5^\circ$  for PA66, or  $a = 4.95 \text{ \AA}$ ,  $b = 5.4 \text{ \AA}$ ,  $c = 22.4 \text{ \AA}$ ,  $\alpha = 49^\circ$ ,  $\beta = 76.5^\circ$ ,  $\gamma = 63.5^\circ$  for PA610 (Figure 1.21a). The  $\alpha$  structure in even-even aliphatic polyamides is associated with intense X-ray Bragg peaks corresponding to  $d$ -spacings of 4.4 and 3.8  $\text{\AA}$ , which correspond to the spacings between the chains in the hydrogen bonding direction and the distance between the hydrogen-bonded sheets, respectively (Figure 1.21b).<sup>164,165</sup> By contrast, even-odd, odd-even and odd-odd polyamides crystallize in the so called  $\gamma$  phase. The plane of the amide groups tilts away from that of the methylene groups to allow formation of intersheet hydrogen bonds, resulting in a reduction of the lattice parameter in chain length. Pleated sheet structures of this type typically show a pseudo-hexagonal packing with a characteristic single, strong  $hk0$  reflection. Pseudo-hexagonal packing is also seen in even AB-type polyamides such as PA12, with comparatively long methylene chains, in which hence the optimization of the interactions between the methylene groups becomes more important than hydrogen bonding for the overall crystal stability (Figure 1.21b).<sup>166</sup> Changing the crystallization conditions or varying external parameters such as the water content or applied strain may also result in changes in the crystalline phase of a polyamide.

For instance, the monoclinic  $\alpha$  structure of PA6, in which the all-*trans* hydrogen-bonded chains are antiparallel, is obtained preferentially from solution, while rapid crystallization from the melt may give rise to a pseudo-hexagonal phase that has been associated with parallel hydrogen-bonded chains with a distorted conformation (Figure 1.21c).<sup>161</sup> A reversible transformation between the  $\alpha$  phase and a pseudo-hexagonal phase may also be induced in many polyamides upon heating, known as the “Brill transition”. The temperature at which the structural transition takes place is called the “Brill temperature” ( $T_B$ ). This phenomenon was first reported for PA66<sup>170</sup> (Figure 1.21d), but has since been observed in various polyamides,<sup>167,171–175</sup> although it is still not fully understood, and neither its dependence on the thermal history, heating rate, or initial crystallization conditions. Similar modifications in structure may also be observed upon stretching.<sup>161</sup>

The supramolecular organization of the aliphatic polyamides has been widely studied using electron microscopy. It was found that the polyamide crystals typically feature re-entrant chain folding, so that the long polymer chains are accommodated in the crystal entity in a similar way to semicrystalline polyethylene. In this context, Dreyfuss and Keller investigated chain folding behavior of solution crystallized PA66 both wide-angle X-Ray diffraction and small-angle X-Ray scattering (WAXD and SAXS).<sup>176</sup> They observed a lamellar thickness of about 5.5 nm for PA66, corresponding to only 3.5 monomer repeat units, due to the more favorable folding of the diamine segments (Figure 1.21e). Similar chain-folded crystalline lamellae form spherulites by crystallization from melt, but chain folding has been argued to be less regular than for solution-crystallized polymers, comprising loose amorphous chain segments.<sup>177</sup>

The morphology of aramids is somewhat different to that of aliphatic polyamides. Several groups studied the structure and morphology of aramids, focusing on poly(*p*-phenylene terephthalamide) (PPTA or “Kevlar®”) fibers, which have superior mechanical properties.<sup>178</sup>

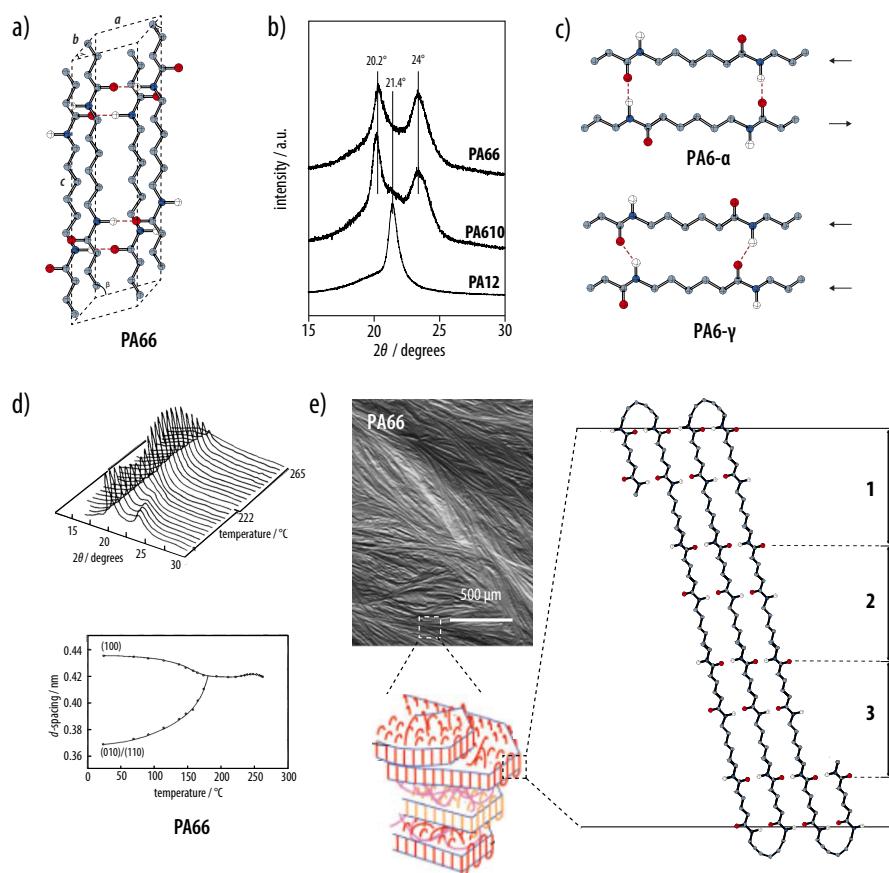


**Figure 1.21.** a) PA66 crystallizes in  $\alpha$  phase with the chains in an all-*trans* conformation, forming hydrogen-bonded sheets that are stacked along the  $b$ -axis. PA66 has a triclinic unit cell with lattice parameters  $a = 4.9 \text{ \AA}$ ,  $b = 5.4 \text{ \AA}$ ,  $c = 17.2 \text{ \AA}$ ,  $\alpha = 48.5^\circ$ ,  $\beta = 77^\circ$ ,  $\gamma = 63.5^\circ$ . b) Wide-angle X-Ray diffractograms of the “even-even” ABBB-type polyamides PA66 and PA610, and the “even” AB-type polyamide, PA12. The wide-angle X-Ray diffraction (WAXD) patterns shown for PA66 and PA610 are characteristic of the  $\alpha$  phase, with two intense Bragg peaks at  $20.2^\circ$  and  $24^\circ$  associated with intrachain distances within and between the hydrogen-bonded sheets, respectively. The WAXD pattern for PA12, on the other hand, shows only a single strong reflection characteristic of the  $\gamma$  phase. c) By altering the crystallization conditions, PA6 may form the  $\alpha$  or  $\gamma$  phase, with the hydrogen-bonded chains are antiparallel and parallel, respectively. d) WAXD patterns at different temperatures showing the transition to pseudo-hexagonal packing on heating the  $\alpha$  phase of PA66. The transition temperature is referred to as the Brill temperature. e) AFM amplitude image of semicrystalline PA66 showing chain-folded crystalline lamellae, which in turn aggregate to form spherulites. Figure adapted from refs. [162,166–169].

Northolt and Tadokoro and coworkers independently reported the crystal structure of PPTA determined from X-ray diffraction.<sup>179–181</sup> The diffraction pattern of fibers spun from an anisotropic solution indicated a monoclinic (pseudo-orthorhombic) unit cell containing two polymer chains (Figure 1.22a,b). Two years later, Takayanagi and coworkers found two crystal structures in PPTA fibers coagulated with different solvents.<sup>182</sup> The structure of Northolt and Tadokoro termed “modification I” was formed by coagulation of a PPTA solution in sulphuric acid using organic solvents such as acetone, ethanol, or methanol,



whereas a second polymorph, “modification II” (Figure 1.22c), was obtained with water as the coagulant, and also comprises two polymer chains per unit cell. Moreover, depending on the polymer concentration in sulfuric acid solution, modification II may transform irreversibly to modification I upon annealing.<sup>182,183</sup> WAXD of PPTA fibers suggested a very high degree of order in PPTA fibers with only a small fraction of amorphous phase, which was detected from the equatorial scans (Figure 1.22d).<sup>178,184</sup>

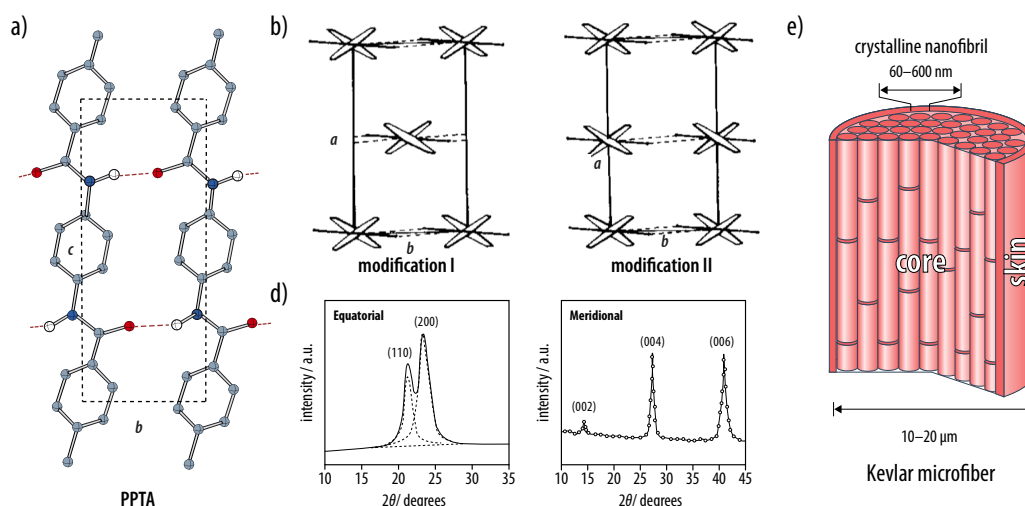


**Figure 1.22.** Crystal structure of poly(*p*-phenylene terephthalamide) (PPTA) based on X-ray diffraction studies. *a, b*) Northolt and Tadokoro proposed a monoclinic (pseudo-orthorhombic) unit cell with lattice parameters  $a = 7.87 \text{ \AA}$ ,  $b = 5.18 \text{ \AA}$ ,  $c = 12.9 \text{ \AA}$  and  $\gamma = 90^\circ$  containing two polymer chains. This structure is also known as modification I. *c*) Representation of a second PPTA polymorph viewed along the *c*-axis, known as modification II and may be obtained by using water as a coagulant. *d*) Equatorial and meridional WAXD scans of PPTA fibers. The presence of sharp Bragg peaks and the absence of a strong amorphous halo reflects the high crystallinity of the PPTA fibers. *e*) Schematic illustration of microfibrils and skin-core structure of PPTA fibers. Figure reproduced from refs. [178,179,182].

The detailed morphology of PPTA fibers has been investigated using different techniques. It is reported that a PPTA fiber consists of bundles of nanofibrils of about 600 nm in diameter, as evidenced by optical microscopy.<sup>184</sup> Using a combination of electron diffraction and electron microscope dark-field image techniques, Dobb et al. proposed the radially organized “pleated” sheet structure for PPTA fibers, which is superimposed onto the fibrillar structure along the fiber axis.<sup>185</sup> This periodic pleating has been confirmed to be a characteristic feature of oriented liquid crystalline polymers.<sup>186</sup> Furthermore, optical microscopy and scanning electron microscopy of normal and etched PPTA fibers have shown a clear differentiation of the skin and core parts of the PPTA fibers (Figure 1.22e). Panar et al. have postulated a structure in which fibrils located in the skin are axially oriented, whereas the fibrils in the core are partly disordered.<sup>184</sup>

Semiaromatic polyamides can be regarded as a compromise between aliphatic and aromatic polyamides with regard to their physical properties, although they may also show unique morphological properties. Considerable research has focused on semiaromatic polyamides

containing terephthaloyl and aliphatic segments. For instance, Rastogi and coworkers made a structural study of semiaromatic polyamides prepared by the solution-phase polycondensation of *p*-phenylene diamine with various aliphatic diacid chlorides containing 3, 4, 6 and 8 methylene units.<sup>187</sup> On the basis of quantitative WAXD analysis and molecular simulations, they found the polymer chain conformation and chain packing to depend on the number of methylene units in the polymer backbone. In spite of their semicrystalline nature, no melting transitions were observed for polyamides with fewer than 8 methylene segments.<sup>187</sup> The length of the aliphatic segment is, hence, a key design parameter for processable semiaromatic polyamides. An example of this is provided by the long aliphatic segments containing semiaromatic polyamide, poly(nonamethylene terephthalamide) (PA9T), commercialized as Genestar<sup>TM</sup>.<sup>188,189</sup> Recently, Tashiro et al. studied the thermally induced phase transition behavior of PA9T and proposed a crystal structure for this polymer (Figure 1.23).<sup>190</sup>

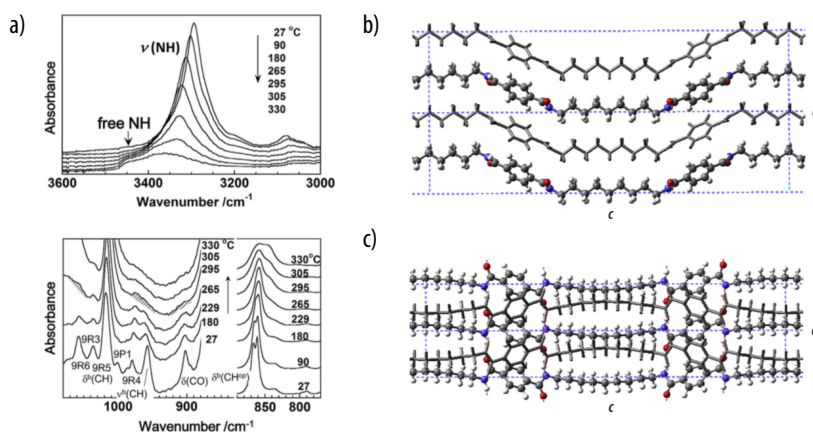


**Figure 1.23.** Tashiro et al. studied the crystal structure and phase transition behavior of semiaromatic PA9T. *a*) IR spectra of amide A (top) and methylene regions (bottom) of PA9T recorded from 27 to 330 °C. The sharp and strong N–H stretching mode became weaker and shifted towards higher wavenumbers with increasing temperature, indicating a decrease in the concentration of hydrogen-bonded amide groups and a weakening of the hydrogen bond strength with increasing temperature. In addition, IR bands associated with the methylene units became weaker and broader with increasing temperature, indicating increased conformational disorder. *b,c*) Suggested crystal structure of PA9T derived from 2D WAXD patterns and computer modeling. The diffraction patterns were indexed assuming a orthorhombic unit cell with lattice parameters  $a = 4.95 \text{ \AA}$ ,  $b = 8.39 \text{ \AA}$ ,  $c = 38.6 \text{ \AA}$ . Figure reproduced from ref. [190].

Combinations of temperature dependent WAXD, SAXS and IR techniques have shown two phase transitions at temperatures of about 190 °C and 270 °C, respectively (Figure 1.23*a*). In the first transition, the aliphatic segments became disordered and the strength of hydrogen bonding diminished, while in the second transition, disorder became even more pronounced and the hydrogen bonds fully broke. Tashiro et al. suggested the molecular chains to adopt all-*trans* conformations in the low temperature phase and to be organized into hydrogen-bonded sheets stacked along the *b*-axis, with the aromatic groups tilted out of plane resulting in local herringbone structures (Figure 1.23*b,c*), which is a common feature of many benzene-containing polyamides.<sup>180,187,191–195</sup>

By decreasing the length of the aliphatic segment in polyamides comprising terephthaloyl (T) repeat units, the melting point increases into a non-processable range. PA6T has a higher melting point (370 °C) than its degradation temperature (350 °C) and is thus not suitable for melt processing. One way to circumvent this problem is to introduce a kinked comonomer, such as an isophthalic (I) unit, at random locations in the PA6T chain backbone. Reducing the regularity of the polymer backbone results in melting points of around 315 °C for poly(hexamethylene terephthalamide-co-isophthalamide) PA6TI, containing 30 mol% I units.<sup>196</sup> This polyamide has exceptional mechanical properties, and is commercially available from EMS Grivory.<sup>197</sup> Recently, Frauenrath et al. reported the detailed structural characteristics of PA6TI (Figure 1.24).<sup>168,198,199</sup> By combining selected area electron diffraction (SAED) with WAXD analysis, they identified the crystalline phase with a triclinic unit cell containing a single PA6T chemical repeating unit (Figure 1.24b).

As in other even-even aliphatic polyamides, the crystal structure was composed of stacks of hydrogen-bonded sheets with the methylene segments in an all-*trans* conformation and in which the benzene rings are slightly tilted with respect to the amide groups, leading to optimized hydrogen bond and  $\pi$ - $\pi$  distances (Figure 1.24b). Moreover, SAXS analysis revealed the thickness of the crystalline lamellae to be about 2 nm, corresponding to only 1.5 times the crystallographic repeat distance along the chain axis (Figure 1.24c). The authors therefore suggested that the crystalline lamellae were composed of (T6T) sequences. AFM images confirmed the lamellae to form spherulites with fibrillar morphologies similar to those seen in aliphatic polyamides (Figure 1.24d).<sup>200</sup>

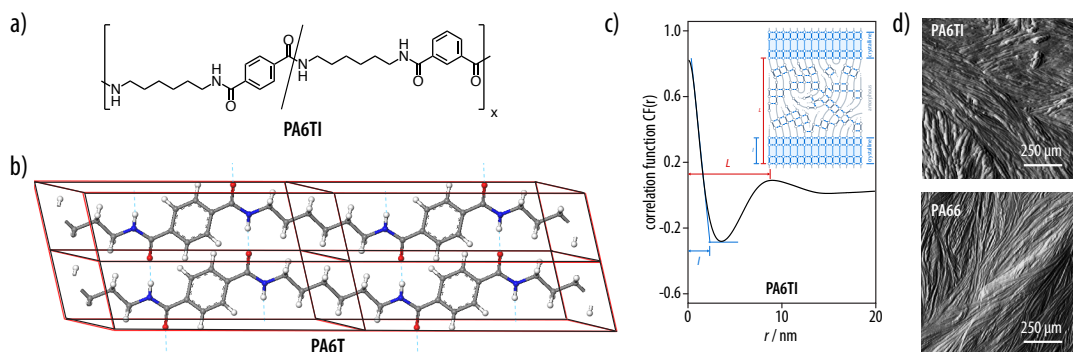


**Figure 1.24.** *a*) Chemical structure of semiaromatic polyamide poly(hexamethylene terephthalamide-co-isophthalamide) (PA6TI) prepared by the copolymerization of rigid terephthalic acid (T) and isophthalic acid (I) monomers with hexamethylene diamine. *b*) Crystal structure of PA6T determined from selected-area electron diffraction of an oriented PA6TI thin film. The observed reflections were indexed using triclinic unit cell with lattice parameters  $a = 5.02$  Å,  $b = 5.4$  Å,  $c = 16.4$  Å,  $\alpha = 50.5^\circ$ ,  $\beta = 79^\circ$ ,  $\gamma = 94^\circ$ . *c*) The 1D SAXS correlation function was used to estimate the lamellar thickness ( $l$ ) and long period ( $L$ ) of the PA6TI, under the assumption of two-phase model (insert). *d*) AFM amplitude images of PA6TI revealed well-defined spherulitic textures similar to those in aliphatic PA66. Figure reproduced from refs. [168,198,199].

Transamidation during high temperature processing is not only a powerful alternative method for the preparation of novel polyamide-based materials but also compatible with materials processing on the industrial scale.<sup>201–203</sup> Frauenrath et al. chose to combine the semiaromatic polyamide PA6TI with selected aliphatic polyamides (PA66, PA610 and PA12) (Figure 1.25).<sup>168</sup> Mass spectrometry, determination of the glass transition temperatures, melting temperatures and enthalpies, as well as atomic force microscopy showed melt extrusion of the even-even semiaromatic polyamide PA6TI with either of the even-even aliphatic polyamides PA66 or PA610 to result in homogeneous random copolymers with a microstructure similar to neat PA6TI (Figure 1.25a,b). By contrast, transamidation was shown to be less efficient in the case of PA6TI extruded with the aliphatic polyamide PA12 because of macroscopic phase separation (Figure 1.25c). The authors argued that the different hydrogen bonding patterns and the consequent low initial miscibility in this case severely limit the rate and extent of transamidation during extrusion.

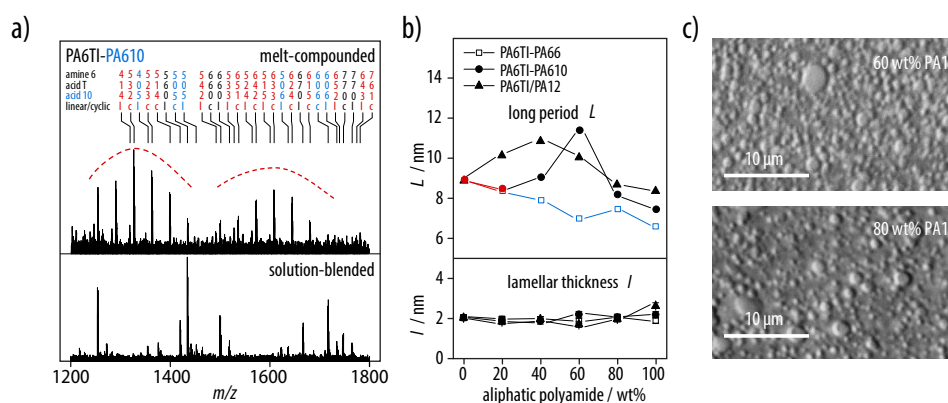


**Figure 1.25.** Frauenrath et al. reported the efficient formation of random copolymers by transamidation during melt compounding of semicrystalline semiaromatic polyamides and certain semicrystalline aliphatic polyamides. *a*) MALDI-TOF mass spectra of the PA6TI blended with 50 wt% PA610 in melt and in solution. The appearance of the new peaks (marked in red) in the melt-compounded spectra indicated efficient transamidation resulting in random copolymers *b*) Correlation lengths deduced from SAXS as a function of aliphatic polyamide reveal the lamellar thickness ( $l$ ) to be similar for almost all the materials, while the long period ( $L$ ) varies somewhat. *c*) Nomarski differential interference contrast images of the PA6TI-PA12 blends showed phase separated domains. Figure reproduced from ref. [168].

From the examples above, it is evident that the morphology of polyamides is quite complex, and governed mainly by intermolecular hydrogen bonding, that is transverse to the polymer chain axis. Varying the crystallization and processing conditions may enormously influence the morphology, including the crystalline form, crystallinity, and lamellar thickness. While fully aromatic aramids typically show a stiff rod-like polymer chain conformation and extended chain crystallites, aliphatic and semiaromatic polyamides form chain-folded crystalline lamellae composed of stacked hydrogen-bonded sheets that aggregate to form spherical entities called spherulites. In contrast to other flexible and semi-flexible polymers these crystalline lamellae may show thicknesses of as little as about 2 nm, corresponding

to only 1–1.5 crystallographic repeat units along the chain axis.<sup>198,199,204,205</sup> Consequently, the degree of order may vary substantially at a given nominal lamellar thickness, resulting in absence of a sharp transition between crystalline and the amorphous phase.

#### 1.4.4 Properties and Applications of Polyamides

Polyamides are one of the most versatile classes of “engineering polymers”, as they show excellent thermomechanical properties and have a correspondingly wide range of applications in almost every industrial sector, ranging from textiles and clothing to food packaging.<sup>137</sup> For example, the most common aliphatic polyamides, PA6 and PA66, which combine high strength, stiffness and ductility, are widely used in commercial fibers for carpets, clothing and seatbelts, as well as in high performance injection moldings for use in the automotive industry. Changing the chemical composition of the monomers (aliphatic or aromatic) is a common way to tune the thermomechanical properties of polyamides. In this regard, combinations of aliphatic monomers with suitable functionalities for polycondensation, lead to aliphatic polyamides with different amide densities, which has a paramount importance for moisture absorption and chemical resistance as well as thermomechanical properties.

**Table 1.2:** Thermomechanical properties of aliphatic, semiaromatic polyamides (poly(*m*-xylene adipamide) (MXD6), PA6TI) and aramids (Nomex<sup>®</sup>, Kevlar<sup>®</sup>) with steel as a reference. The values for the tensile strength ( $\sigma_{\max}$ ), stiffness ( $E$ ), and elongation at break ( $\epsilon_b$ ) may vary depending on processing conditions. Data from refs. [198,199,206–209]

Material	$\rho$ [g/cm <sup>3</sup> ]	$T_m$ [°C]	$\sigma_{\max}$ [MPa]	$E$ [GPa]	$\epsilon_b$ [%]
<b>Aliphatic PA</b>	1.13–1.35	166–315	50–100	1–5	30–200
<b>MXD6</b>	1.22	237	99	4.7	2.3
<b>PA6TI</b>	1.44	325	120–125	3.7–4.0	10
<b>Nomex</b>	1.38	>350 <sup>a</sup>	500–1400	11–22	10–30
<b>Kevlar</b>	1.4–1.5	>500 <sup>a</sup>	2800–3500	70–180	2–4
<b>Steel</b>	7.8–8.0	1400	1500	200	1

<sup>a</sup> Decomposition temperatures for Kevlar<sup>®</sup> and Nomex<sup>®</sup>

Aromatic repeating units, on the other hand, increase the chain rigidity, which results in better thermomechanical properties at higher temperatures. In case of the aramid, Kevlar<sup>®</sup>, the rigidity of the fully aromatic backbone, hydrogen bonding, tight packing between the polymer chains, and extensive  $\pi$ – $\pi$  stacking gives rise to specific tensile strengths greater than steel.<sup>207</sup> By using the corresponding *meta*-substituted diamine and diacyl chloride, a “kinked” aramid known as Nomex<sup>®</sup> can be obtained. The introduction of the kinked substituent reduces the overall crystallinity, leading to a decrease in strength and stiffness but increased ductility and flexibility compared to Kevlar<sup>®</sup>, but comparable chemical and heat resistance (Table 1.2) owing to the high dissociation energies of their C–C and C–N bonds (about 20% higher than in

aliphatic polyamides).<sup>210</sup> At the same time, strong hydrogen bonding and high chain rigidity translate into higher glass transition temperatures compared with aliphatic polyamides.<sup>211</sup>

The outstanding mechanical properties of Kevlar<sup>®</sup> make it in principle attractive for replacing metals. However, processability, efficiency, low-cost, and high throughput are crucial for industrial processes. High throughput typically requires melt processing, which rules out aramids for many applications.<sup>137</sup> Semiaromatic polyamides may be melt-processed and hence provide a viable alternative, and are considered to be promising candidates for the replacement of metals in advanced engineering applications, such as lightweight structural parts in the automotive and aerospace industries. However, a good balance between the proportions of aromatic and aliphatic segments is necessary in order to achieve tailorable mechanical properties, while keeping the processing window within a reasonable temperature range (200–300 °C) so as to avoid excessive degradation.

### 1.5 Scope and Outline of this Thesis

From the examples presented in the previous sections, it becomes evident that the balance of order and disorder across different length scales has a significant importance in the resulting macroscopic properties of a material. Therefore, the control of the disorder and defects in partially ordered polymer semiconductors has recently become of interest for obtaining novel, mechanically durable polymer semiconductors. In this regard, a promising approach is the use of hydrogen bonding motifs that promote specific non-covalent intermolecular interactions, due to their combination of moderate strength and directionality. Hydrogen bonding was successfully applied in many different examples in both small molecule organic and polymer semiconductors. However, there is still a lack of clear guidelines on how to design hydrogen-bonded organic semiconductors.

In the present thesis, we therefore aim to explore the use of amide hydrogen bonding sites incorporated in the substituents attached to  $\pi$ -conjugated chromophores as a means to guide the supramolecular arrangement of the chromophores in the solid-state, their crystallization, and the morphology of thin films from these materials, and their optoelectronic properties. To this end, two different classes of materials based on either small molecule organic or polymer semiconductors will be investigated in two complementary approaches: (*i*) incorporating terminal hydrogen bonding sites into terminal substituents of  $\pi$ -conjugated organic molecules, such as oligothiophenes (Chapters 2 and 3); (*ii*) incorporating p-type or n-type semiconducting cores, such as bithiophene (Chapter 4) and dicyanoperylene bisimide (Chapter 5), into a polyamide. We intend to address the following research questions:

- Which effect do the amide hydrogen bonding sites incorporated in the terminal substituents of calamitic  $\pi$ -conjugated molecules have on the solid-state organization and the optical properties of the molecules? Does a spacer, that separates the chromophore and the hydrogen bonding sites play a critical role? To address these questions, we

intend to develop detailed structure-property relationships by preparing two series of bithiophene derivatives with amide and ester functions in the terminal substituents, separated from the core with differently long alkyl spacers (Chapter 2).

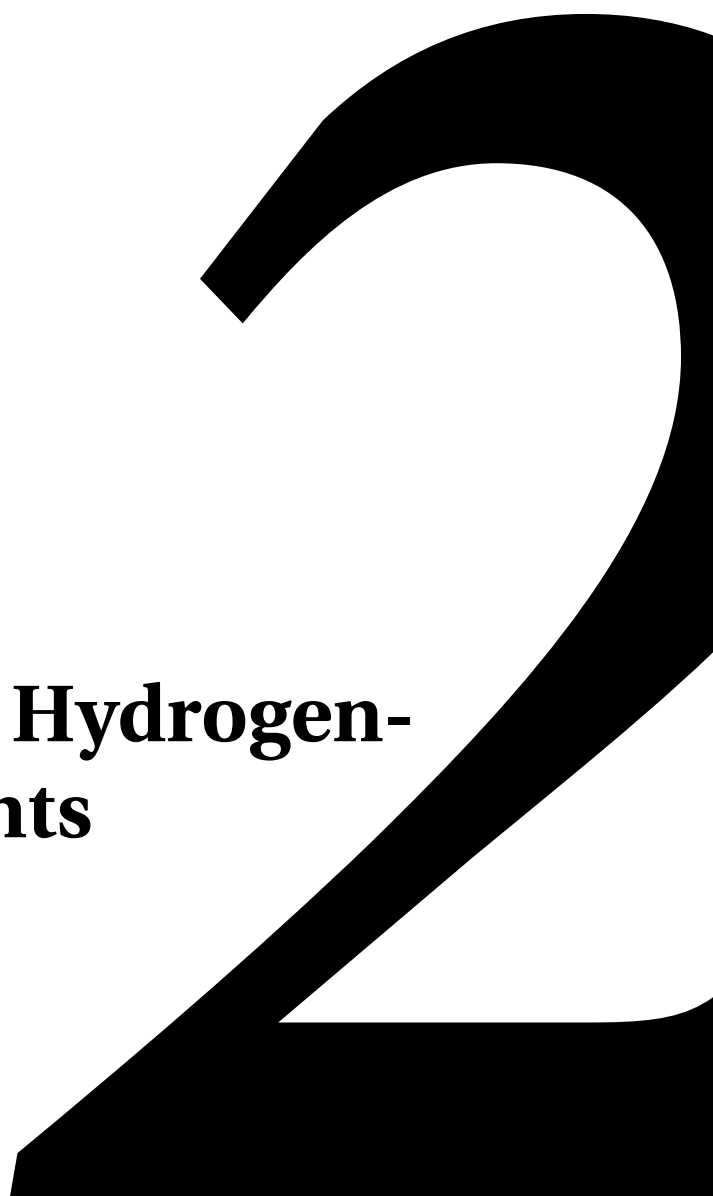
- What is the influence of the amide hydrogen bonding incorporated in the terminal substituents of calamitic  $\pi$ -conjugated molecules on the thin film growth and morphology as well as the macroscopic charge transport? To be able to address this question, we will focus on a quaterthiophene derivative, a core that has been well investigated in the literature, has an extended  $\pi$ -system for macroscopic charge transport, and is synthetically easily accessible. We will prepare derivatives with amide or ester functions in the terminal substituents and compare the solid-state organization and macroscopic charge transport behavior of the thin films (Chapter 3).
- Can we add optoelectronic functionality to polyamides by incorporating p-type or n-type  $\pi$ -conjugated segment repeat units into the polyamide, while maintaining the thermomechanical characteristics of typical engineering polyamides? To this end, we will synthesize semiaromatic polyamides containing bithiophene (Chapter 4) or dicyanoperylene bisimide (Chapter 5) repeat units and investigate their microstructure, thermomechanical characteristics, and optoelectronic properties in detail.

The results achieved during the present thesis will be presented in the style of a cumulative dissertation, including all supplementary information. Chapter 3 is a part of an article, that is published in *Chemistry – A European Journal*, while Chapter 4 corresponds to an article published in *Journal of Materials Chemistry C*. Furthermore Chapters 2 and 5 are drafts of two manuscripts that will be submitted to peer-reviewed journal in due course.





# **Bithiophenes with Hydrogen-Bonded Substituents**



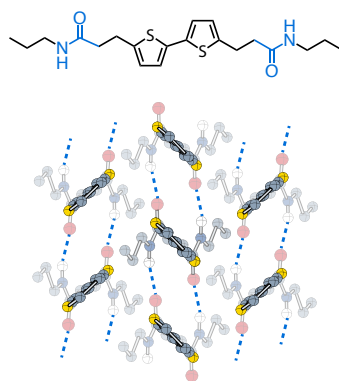
---

The results presented in this chapter are part of a manuscript in preparation. Özen, B.; Tirani, F. F.; Schenk K.; Scopelliti, R.; Frauenrath, H. "Structure-Property Relationships in Bithiophenes with Hydrogen-Bonded Substituents".

B.Ö. performed the chemical synthesis, thermal, spectroscopic characterization and prepared the crystals suitable for single-crystal X-ray measurements, which were solved and refined by F.F.T. and R.S. The calculation of pitch and roll angles was performed by K.S. together with F.F.T. and B.Ö.

## 2 Bithiophenes with Hydrogen-Bonded Substituents

The use of crystal engineering to control the supramolecular arrangement of  $\pi$ -conjugated molecules in the solid-state is of considerable interest for the development of novel organic electronic materials. In the present study, we investigated the effect of combining of two types of supramolecular interactions with different geometric requirements, amide hydrogen bonding and  $\pi$ -interactions, on the  $\pi$ -overlap between calamitic  $\pi$ -conjugated cores. To this end, we prepared two series of bithiophene diesters and diamides with methylene, ethylene, or propylene spacers between the bithiophene core and the functional groups in their terminal substituents. The hydrogen-bonded bithiophene diamides showed significantly denser packing of the bithiophene cores than the diesters and other known  $\alpha,\omega$ -disubstituted bithiophenes. The bithiophene packing density reach a maximum in the bithiophene diamide with an ethylene spacer, which featured the smallest longitudinal bithiophene displacement and infinite 1D arrays of electronically conjugated, parallel, and almost linear N–H $\cdots$ O=C hydrogen bonds. The synergistic hydrogen bonding and  $\pi$ -interactions were attributed to the favorable conformational mechanics of the ethylene spacer and resulted in H-type spectroscopic aggregates in solid-state absorption spectroscopy. These results demonstrate that the optoelectronic properties of  $\pi$ -conjugated materials in the solid-state may be tailored systematically via side chain engineering, and hence that this approach has significant potential for the design of organic and polymer semiconductors.



## 2.1 Introduction

Functional  $\pi$ -conjugated compounds, including both small molecules and polymers, have been widely used as organic semiconductor materials in organic field-effect transistors,<sup>6</sup> photovoltaics,<sup>212</sup> light-emitting diodes,<sup>213</sup> and other functional devices.<sup>214</sup> Molecular orientation and efficient intermolecular  $\pi$ -overlap at the supramolecular level are known to be highly important for the optoelectronic properties of such materials.<sup>215–217</sup> Molecular design strategies leading to improved control over their supramolecular arrangement in the solid-state should therefore be of considerable interest for the development of novel organic electronic materials.

Most investigations to date have focused on the use of non-functional substituents, such as alkyl residues. These serve both as solubilizing agents and to direct structure formation, guiding crystallization and molecular orientation in the solid-state.<sup>218–224</sup> When terminal  $\alpha, \omega$ -dialkyl substituents are introduced into calamitic (rod-like)  $\pi$ -conjugated compounds, the molecules typically organize into layered-herringbone (LHB) structures, which are known to result in favorable two-dimensional charge transport pathways.<sup>225</sup> This particular packing motif is observed in many prototypical high-performance organic semiconductor materials based, for example, on pentacene<sup>226</sup> or benzo[thieno[3,2-*b*]thiophene (BTBT) cores,<sup>224,227</sup> among others.<sup>228–230</sup>

Another strategy has been to explore the use of functional groups that provide additional non-covalent interactions, such as hydrogen bonding,<sup>231</sup> halogen interactions,<sup>232</sup> or other specific short contacts, as “conformational locks”.<sup>233</sup> Hydrogen bonding has proven to be particularly useful as a structure-directing interaction because of its directionality and short-range character.<sup>84</sup> Hydrogen bonding sites may be introduced into organic electronic materials in geometrically different ways. For instance, hydrogen bond donors and acceptors may be part of the  $\pi$ -conjugated cores themselves, resulting in hydrogen bonding within the planes defined by these cores. Examples include certain perylene bisimide,<sup>120</sup> epindolidone,<sup>128</sup> quinacridone,<sup>121</sup> azaphenacene,<sup>234</sup> ellipticine,<sup>235</sup> diketopyrrolopyrrole, or indigo<sup>236</sup> derivatives. Some of these small hydrogen-bonded molecules exhibit promising optoelectronic properties as compared with the corresponding non-hydrogen bonded analogues.

There has likewise been interest in the effect of end groups that give rise to terminal hydrogen bonding interactions aligned along the long axis of the  $\pi$ -conjugated cores, as in  $\alpha, \omega$ -dihydroxyl-substituted BTBT<sup>131</sup> and sexithiophene<sup>132</sup> derivatives, or  $\alpha, \omega$ -dicarboxylic acid-substituted quaterthiophenes.<sup>237</sup> In all of these cases, the molecules remain organized into lamellar structures, but with additional interlamellar hydrogen bonding. This may lead to improved performance in field-effect transistors or photovoltaic devices, as well as greater longevity under ambient conditions.

Hydrogen-bonding interactions aligned with the  $\pi$ - $\pi$  stacking direction have also frequently been used to promote supramolecular self-assembly in solutions of, for instance, oligothiophene<sup>110,113,118,119,238–243</sup> or perylene bisimide<sup>238,244–250</sup> derivatives, for example. The result-

ing one-dimensional nanostructures have been investigated as model systems for understanding charge transport mechanisms and, in some cases, have been employed as active materials in organic devices.<sup>110,119</sup> Hydrogen-bonded side chains have also proven to be of interest for polymer semiconductors,<sup>134,135</sup> whose the solid-state morphology may be modified by incorporating amide functions, resulting in improved performance in both field-effect transistors and photovoltaic devices compared with their non-hydrogen bonded counterparts. Similarly, introduction of  $\pi$ -conjugated segments into polyamides has recently been reported to provide materials that combine promising optoelectronic properties with mechanical properties comparable to those of structural polyamides.<sup>251</sup> Moreover, the use of hydrogen-bonded acetamide end groups was reported to induce tighter packing of quaterthiophene derivatives than in related quaterthiophene acetates, resulting in more efficient  $\pi$ -overlap and a stronger tendency to form well-ordered lamellar structures, and excellent performance in organic field-effect transistors.<sup>252</sup> However, systematic investigations of this type of hydrogen-bonded organic semiconductors have rarely been reported for crystalline materials of low molecular weight  $\pi$ -conjugated compounds.

Here, we investigated the influence of hydrogen-bonded substituents on the packing in two series of the bithiophene derivatives **1a–c** and **2a–c** with, respectively, ester and amide functions in the terminal substituents, separated from the core with alkyl spacers of different lengths (Figure 2.1). We thus introduced hydrogen-bonding interactions parallel to the crystalline layers of the calamitic  $\pi$ -conjugated molecules. From a detailed comparison of the single-crystal X-ray structures of these compounds and their optical properties, we conclude that hydrogen-bonded amide end groups result in an overall denser packing of the bithiophene cores than for the corresponding ester end groups, which is accompanied by smaller pitch angles, increased  $\pi$ -overlap, and stronger H-type coupling in their absorption spectra.

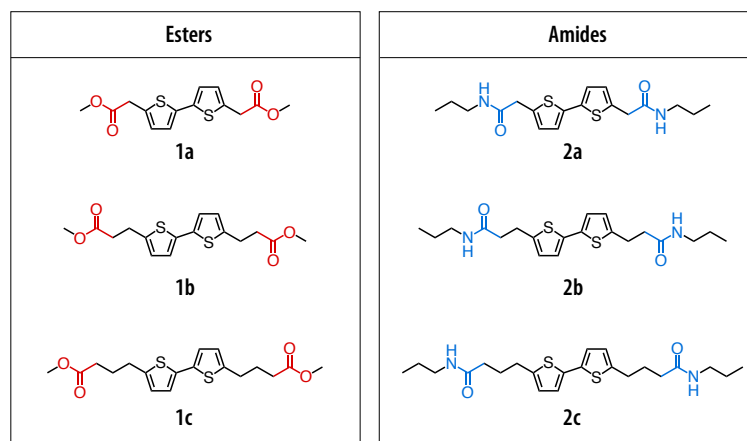
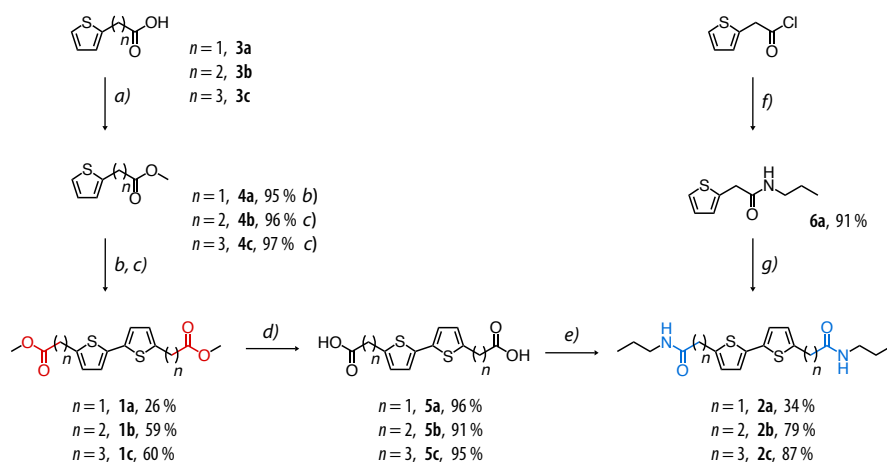


**Figure 2.1.** Structures of the bithiophene derivatives functionalized with ester or amide groups investigated in this work.

## 2.2 Results and Discussion

### 2.2.1 Synthesis of the Bithiophene Diesters and Bithiophene Diamides

The synthesis of the bithiophene diesters **1a–c** and the corresponding diamides **2a–c** with methylene, ethylene, propylene spacers between the bithiophene core and the amide or ester functionalities started from the thiophene-2-acetic **3a**, thiophene-2-propionic **3b**, and thiophene-2-butyric acids **3c**, respectively (Scheme 2.1). The bithiophene diesters **1a–c** were synthesized starting from the thiophene carboxylic acids **3a–c**, which were subjected to an acid-catalyzed esterification in refluxing MeOH to give the corresponding methyl esters **4a–c** in almost quantitative yields. A subsequent Pd-catalyzed oxidative homocoupling using AgF did not yield the desired product **1a**. We instead performed a Pd-catalyzed oxidative homocoupling using oxygen as the oxidant in DMSO/TFA at 60 °C following Wang et al.<sup>253</sup> Both reaction conditions gave the desired bithiophene diesters **1a–c** on multigram scales in yields of 26%, 59%, and 60%, respectively.



**Scheme 2.1.** Synthesis of bithiophene diesters **1a–c** and bithiophene diamides **2a–c**. *Reagents and conditions:* *a)* H<sub>2</sub>SO<sub>4</sub> (96%, cat.), MeOH, reflux, 8 h, 97% yield; *b)* Pd(OAc)<sub>2</sub>, TFA, DMSO, 60 °C, 48 h, 26% yield; *c)* AgF, (C<sub>6</sub>H<sub>5</sub>CN)<sub>2</sub>PdCl<sub>2</sub>, DMSO, 85 °C, 14 h, 60% yield; *d)* LiOH, THF/H<sub>2</sub>O, reflux, 8 h, 95% yield; *e)* EDCI, HOBt, DIPEA, propylamine, room temperature, 12 h, 87% yield; *f)* propylamine, 1 h, 91% yield; *g)* Pd(OAc)<sub>2</sub>, TFA, DMSO, 60 °C, 48 h, 34% yield.

The amide-functional bithiophenes **2b–c** were then prepared by saponification and subsequent amide coupling. The bithiophene diesters **1b–c** were saponified using LiOH by refluxing in a THF/water (1:1) mixture, which furnished the diacids **5b–c** in almost quantitative yields after acidification with 1 M HCl. Subsequent amide coupling reactions with propylamine using EDCI/HOBt as coupling promoters resulted in the corresponding bithiophene diamides in yields of 79% (**2b**) and 87% (**2c**). In the case of **2a**, however, even though it was confirmed by mass spectrometry, the product could not be isolated by either crystallization or column chromatography. As an alternative route, the reaction of 2-thiopheneacetyl chloride with propylamine furnished **6a** in 90% yield (Figure 2.2). This intermediate was then subjected

to Pd-catalyzed oxidative homocoupling oxygen as the oxidant in DMSO/TFA at 60 °C. The crude product was purified by Soxhlet extraction with dioxane for 12 h, and the bithiophene diamide **2a** was isolated as a yellow solid in a yield of 34%.

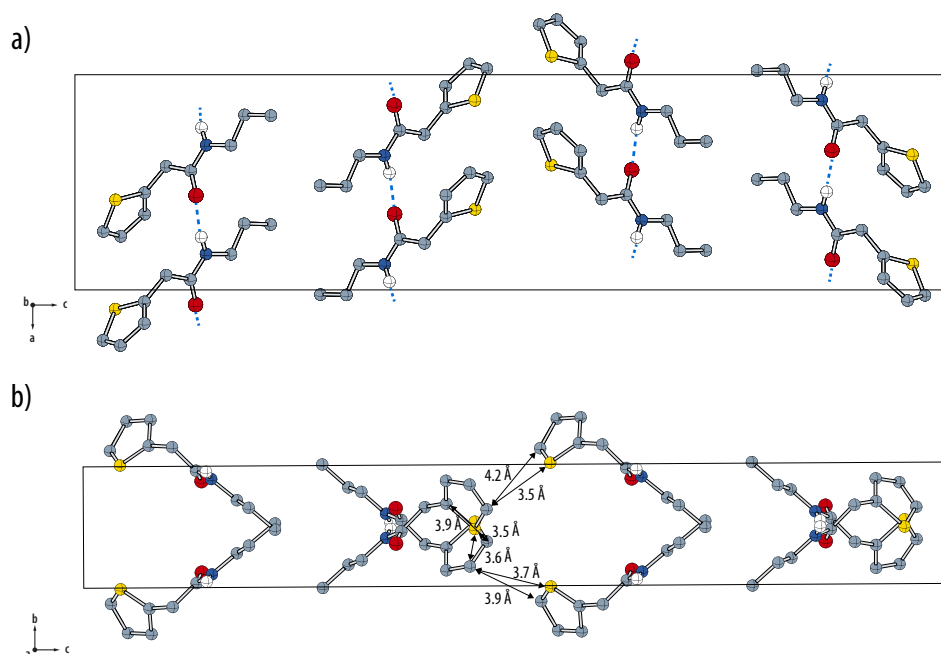


**Figure 2.2.** Ball-and-stick representations of the single-crystal X-ray structure of **6a** (CCDC 1951223). The crystal contained eight molecules of **6a** per orthorhombic unit cell  $Pca2_1$ , with the lattice parameters  $a = 9.48958(16)$  Å,  $b = 5.37710(10)$  Å,  $c = 38.1047(6)$  Å, and  $\alpha = \beta = \gamma = 90^\circ$ . *a, b*) Unit cell representation of **6a** along crystallographic *b*-axis and *a*-axis, respectively. Along the crystallographic *a*-axis, the adjacent thienyl cores arranged in edge-to-face arrangement, exhibiting intermolecular C...S and C...C close contacts of 3.460 and 3.923 Å within the close pairs, respectively. The amide groups in side chains organized almost orthogonal by an angle of  $86.9^\circ$  to the thienyl plane, with two different hydrogen bonding distances of 2.867 and 2.906 Å (all hydrogen atoms except those that participate in hydrogen bonding have been omitted for clarity).

### 2.2.2 Single-Crystal X-Ray Structures

Recrystallization of the bithiophene derivatives either by slow evaporation of a solution in dichloromethane (**1a** and **1c**) or ethyl acetate (**1b**), or by vapor diffusion of *n*-heptane into a dimethyl sulfoxide solution (**2a**) or a dioxane solution (**2b** and **2c**) gave single-crystals with sufficient quality for single-crystal X-ray structure analysis (Figure 2.3). A common feature of all six crystal structures was that the bithiophene cores were planar with the thiophene rings arranged in an anti-conformation, similar to other examples of oligothiophenes.<sup>219</sup> Moreover, the bithiophene cores were tightly arranged layers in parallel-displaced stacks or 2D herringbone layers, that is, packing patterns typical of extended  $\pi$ -conjugated systems (Table 2.1).

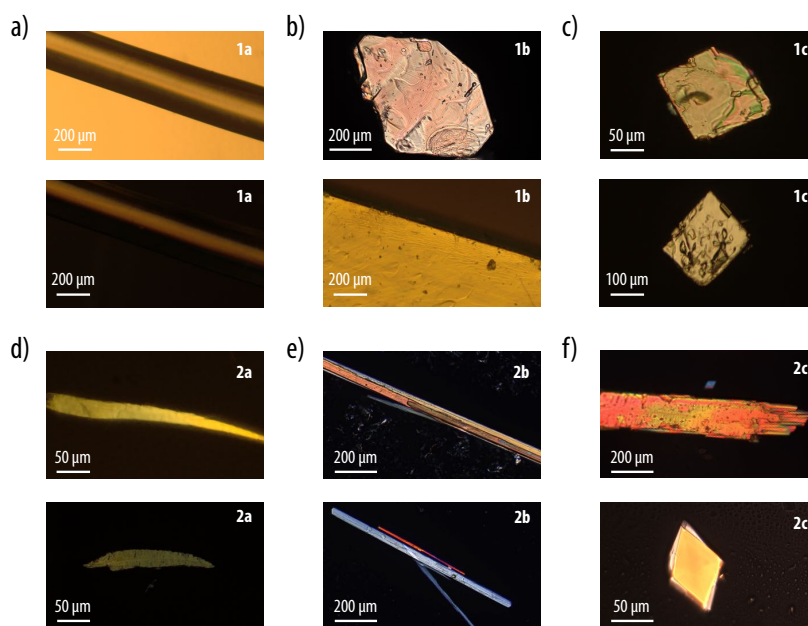


**Figure 2.3.** Representative polarized optical microscopy images of *a–c*) bithiophene diesters **1a–c**, and *d–f*) bithiophene diamides **2a–c** using polarized optical under cross polarizers.

The bithiophene diester **1a** crystallized with the space group  $P\bar{1}$  and one molecule in the unit cell. The lattice parameters were  $a = 5.6993(3)$  Å,  $b = 8.0985(4)$  Å,  $c = 8.1101(4)$  Å,  $\alpha = 92.722(5)^\circ$ ,  $\beta = 108.178(5)^\circ$ , and  $\gamma = 92.269(4)^\circ$  (Figure 2.4*a,b*). The bithiophenes were arranged in parallel-displaced  $\pi$ - $\pi$  stacks along the crystallographic *a*-axis with a tilt angle of the bithiophene long axis relative to the *ac* layer normal of  $58.5^\circ$  and an interlayer distance of  $3.644$  Å, resulting in intermolecular C $\cdots$ C, C $\cdots$ S, and S $\cdots$ S close contacts of  $3.777$ ,  $3.682$ , and  $4.161$  Å, respectively (Figure 2.4*b*). The functional ester groups were tilted away from the plane of the planar bithiophene core at an angle of  $47.6^\circ$  and arranged in opposite directions in neighboring layers, with C-CH<sub>2</sub>-C(=O)-O and CH<sub>2</sub>-C(=O)-O-CH<sub>3</sub> dihedral angles of  $163.7^\circ$  and  $176.7^\circ$ , respectively.

A change in spacer length from  $n = 1$  to 2 or 3 methylene groups resulted in a change in the packing motif of the bithiophene diesters. The bithiophene diesters **1b** and **1c** both crystallized with the space group  $P2_1/c$  and two molecules per unit cell. The respective lattice parameters were  $a = 14.0916(5)$  Å,  $b = 7.5029(2)$  Å,  $c = 8.6268(3)$  Å,  $\alpha = 90^\circ$ ,  $\beta = 104.543(4)^\circ$ , and  $\gamma = 90^\circ$  (Figure 2.4*c,d*) and  $a = 15.4717(4)$  Å,  $b = 6.05317(14)$  Å,  $c = 8.6742(2)$  Å,  $\alpha = 90^\circ$ ,  $\beta = 102.078(3)^\circ$ , and  $\gamma = 90^\circ$  (Figure 2.4*e,f*), respectively, comprising two molecules in the unit cell in both cases. In marked difference to **1a**, the bithiophene cores of **1b** and **1c** were organized into a typical lamellar 2D herringbone arrangement parallel to the crystallographic *ac* and *bc* planes with similar herringbone angles of  $73.0^\circ$  and  $71.6^\circ$  between adjacent edge-to-face bithiophenes but very different respective tilt angles of  $33.1^\circ$  and  $55.3^\circ$  of their bithiophene long axes with respect to the layer normals. This arrangement resulted in intermolecular C $\cdots$ C, C $\cdots$ S, and S $\cdots$ S close contact distances between the edge-to-face and parallel-displaced bithiophene



cores of 3.947, 3.621, and 4.003 Å in **1b**, and 3.985, 3.516, and 3.809 Å in **1c** (Figure 2.4*d,f*). The ester substituents in **1b** were closer to *trans*-conformation with CH<sub>2</sub>–CH<sub>2</sub>–C(=O)–O and CH<sub>2</sub>–C(=O)–O–CH<sub>3</sub> dihedral angles of 170.05 ° and 179.7 °, than in **1c** with dihedral angles of 167.0 ° and 176.4 °. Moreover, the terminal ester segments in **1b** were tilted away from the plane of the planar bithiophene core by an angle of 52.0 °, almost twice as large as observed in **1c** (24.8 °).

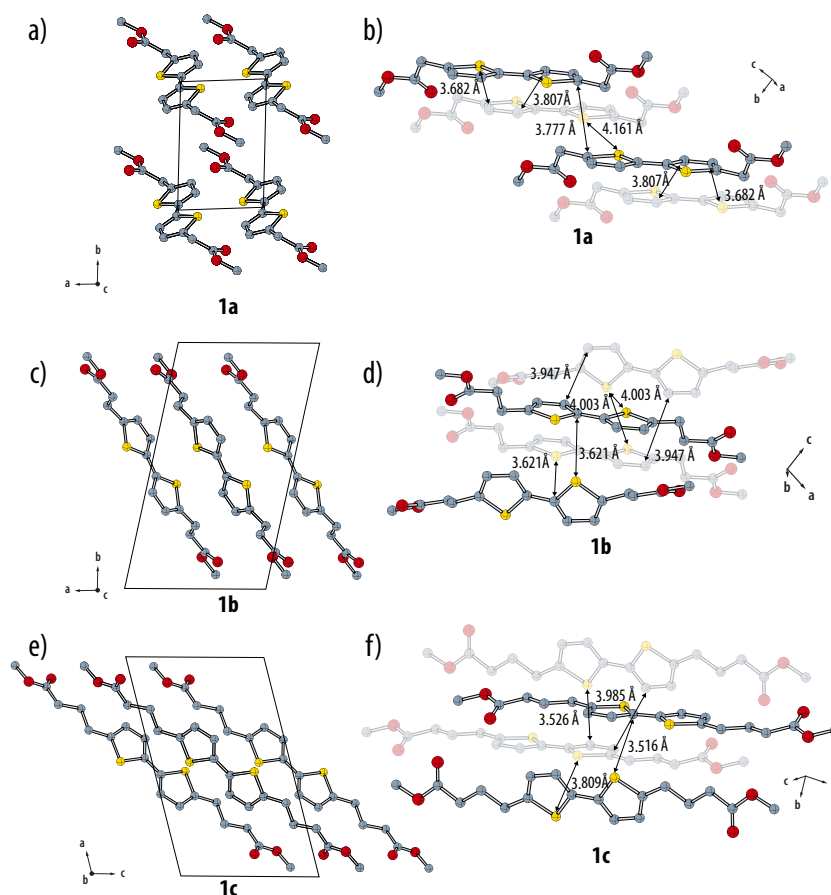


**Figure 2.4.** Ball-and-stick representations of the single-crystal X-ray structures of the bithiophene diesters **1a–c**. Unit cells and short contacts of *a,b*) **1a** (CCDC 1951216), *c,d*) **1b** (CCDC 1951217), and *e,f*) **1c** (CCDC 1951218).

The bithiophene diamides **2a**, with methylene spacers and **2b**, with ethylene spacers, crystallized with the space group  $P2_1/c$  and two molecules per unit cell. The respective lattice parameters were  $a = 17.114(3)$  Å,  $b = 5.7214(7)$  Å,  $c = 9.5335(14)$  Å,  $\alpha = 90^\circ$ ,  $\beta = 101.820(8)^\circ$ , and  $\gamma = 90^\circ$  (Figure 2.5*a,b*), and  $a = 21.8811(10)$  Å,  $b = 4.88737(14)$  Å,  $c = 9.4412(4)$  Å,  $\alpha = 90^\circ$ ,  $\beta = 98.204(4)^\circ$ , and  $\gamma = 90^\circ$  (Figure 2.5*c,d*). In each case, the bithiophene cores were arranged in 2D herringbone structures layered parallel to the  $bc$  plane. However, whereas the herringbone angle of 84.5 ° and the tilt angle of the bithiophene long axis relative to the layer normal of 30.7 ° in **2b** were comparable to values typically observed in 2D herringbone

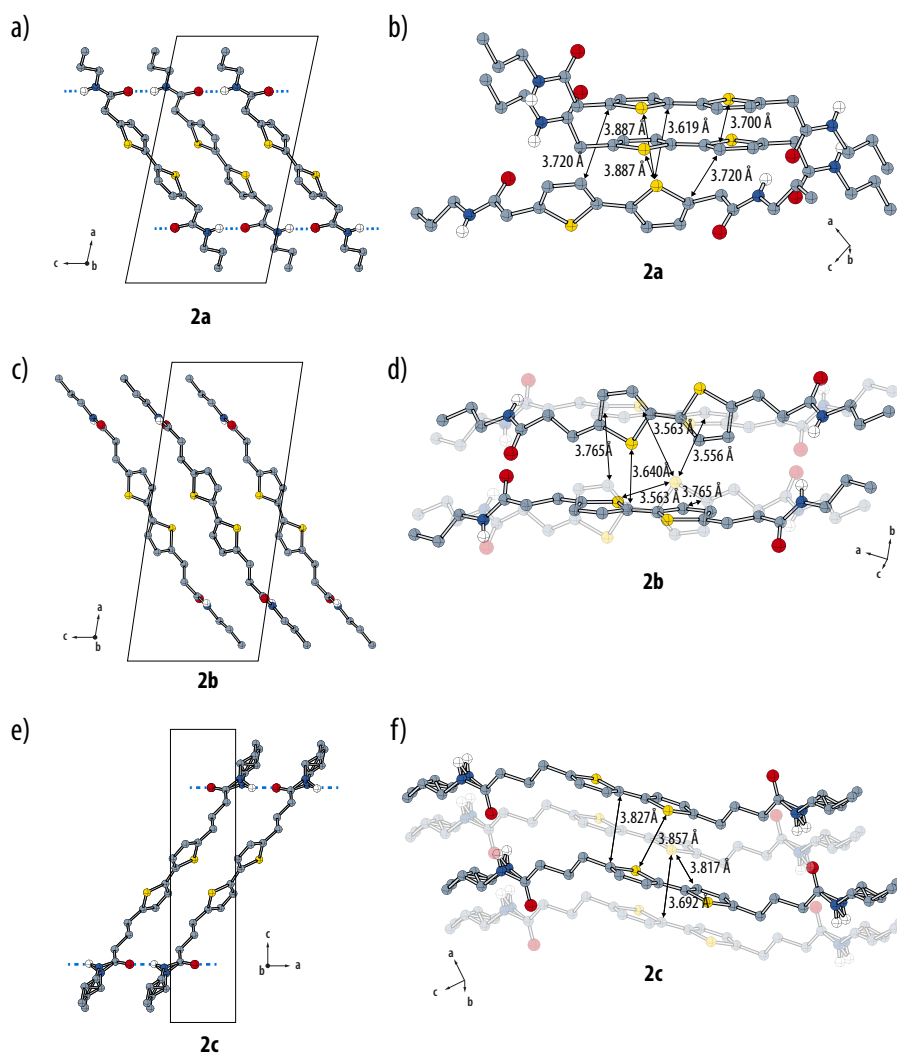


**Figure 2.5.** Ball-and-stick representations of the single-crystal X-ray structures of the bithiophene diamides **2a–c**. Unit cells, and short contacts of *a,b* **2a** (CCDC 1951219), *c,d* **2b** (CCDC 1951220), and *e,f* **2c** (CCDC 1951221). Hydrogen bonds observed in the bithiophene diamides **2a–c** are marked with blue dashed lines.

arrangements of other oligothiophenes,<sup>252,254,255</sup> an unusually small herringbone angle of 52.7 ° and a somewhat larger tilt angle of 41.3 ° were observed in **2a**. The intermolecular C··C, C··S, and S··S close contact distances between the edge-to-face dimers were 3.720, 3.619, and 3.887 Å in **2a**, and 3.765, 3.556, and 3.563 Å in **2b** (Figure 2.5*b,d*). Moreover, both compounds exhibited N–H··O=C hydrogen bonds parallel to the crystallographic *bc* plane between the amide groups of neighboring molecules. The amide units exhibited H<sub>2</sub>C–HN–C(=O)–CH<sub>2</sub> and NH–C(=O)–CH<sub>2</sub>–C dihedral angles of 175.3 ° and 162.0 ° in the case of **2a** as well as 174.6 ° and 132.5 ° in the case of **2b**. It is worth noting that, in the case of **2a**, the plane that contained the amide group was almost orthogonal with the plane of the planar bithiophene core, with an angle of 85.9 °, whereas a much smaller angle of 57.0 ° was observed for **2b**.

Finally, the bithiophene diamide **2c** showed a very large unit cell at 100 K that contained 30 independent molecules, for which refinement was difficult (Figure 2.6). On increasing the temperature to 200 K, the unit cell decreased drastically in size, facilitating refinement, although the propyl chains remained highly disordered. Unlike **2a** and **2b**, **2c** crystallized with a triclinic unit cell  $P\bar{1}$  and one molecule per unit cell. The lattice parameters were  $a = 4.9848(4)$  Å,  $b = 5.6250(5)$  Å,  $c = 21.347(3)$  Å,  $\alpha = 90.584(9)^\circ$ ,  $\beta = 90.140(8)^\circ$ , and  $\gamma = 107.702(8)^\circ$  (Figure 2.5e,f). The bithiophene cores were arranged in parallel-displaced  $\pi$ - $\pi$  stacks along the crystallographic  $a$ -axis, with a tilt angle of  $40.5^\circ$  of the bithiophene long axis with respect to the layer normal, an interlayer distance of 3.641 Å, and intermolecular C $\cdots$ C, C $\cdots$ S, and S $\cdots$ S close contact distances of 3.827, 3.671, and 3.857 Å, respectively (Figure 2.5f). Moreover, the amide functions participated in intermolecular N-H $\cdots$ O=C hydrogen bonds between parallel-displaced bithiophenes along the same direction (Table 2.2). The amide functions exhibited H<sub>2</sub>C-HN-C(=O)-CH<sub>2</sub> and HN-C(=O)-CH<sub>2</sub>-CH<sub>2</sub> dihedral angles of  $178.15^\circ$  and  $143.87^\circ$ , respectively, while the plane of the amide units was tilted by  $71.69^\circ$  with respect to the plane of the planar bithiophene core.

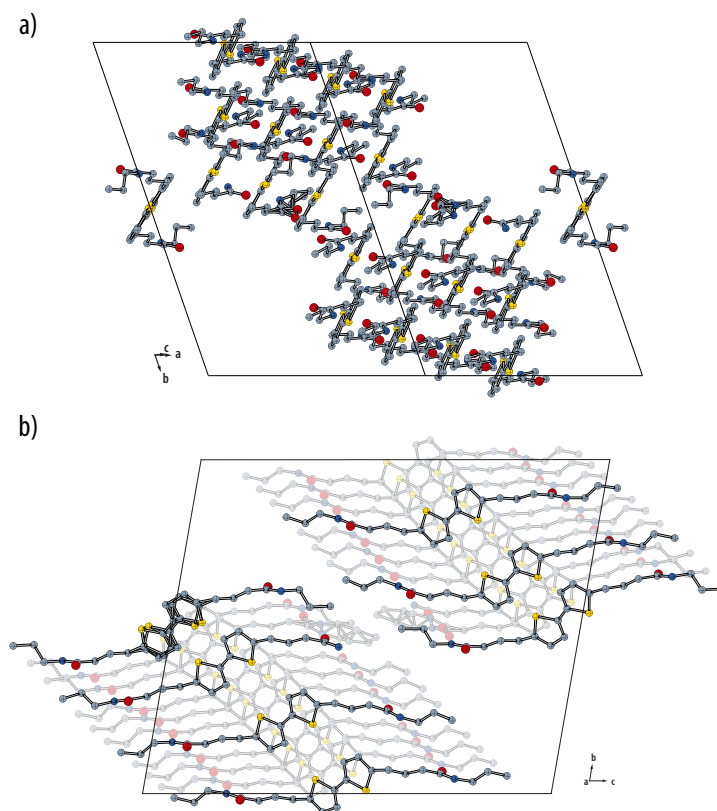


**Figure 2.6.** Ball-and-stick representation of the ill-defined single-crystal X-ray structure of **2c** a) viewed along the crystallographic  $c$ -axis and b) the  $a$ -axis, at 100 K with lattice parameters  $a = 22.3869(15)$  Å,  $b = 25.7597(16)$  Å,  $c = 30.9609(16)$  Å,  $\alpha = 96.751(5)^\circ$ ,  $\beta = 95.932(5)^\circ$ , and  $\gamma = 108.448(6)^\circ$  (all hydrogen atoms have been omitted for clarity).

**Table 2.1:** Comparison of the single-crystal structures of bithiophene diesters **1a–c** and bithiophene diamides **2a–c**.

property	<b>1a</b>	<b>1b</b>	<b>1c</b>	<b>2a</b>	<b>2b</b>	<b>2c</b>
space group	<i>Pa</i>	<i>P2<sub>1</sub>/c</i>	<i>P2<sub>1</sub>/c</i>	<i>P2<sub>1</sub>/c</i>	<i>P2<sub>1</sub>/c</i>	<i>P<math>\bar{1}</math></i>
crystal system	triclinic	monoclinic	monoclinic	monoclinic	monoclinic	triclinic
<i>a</i> [Å]	5.69	15.47	14.09	17.11	21.88	4.98
<i>b</i> [Å]	8.09	6.05	7.50	5.72	4.89	5.63
<i>c</i> [Å]	8.11	8.67	8.63	9.53	9.44	21.35
$\alpha$ [°]	92.7	90.0	90.0	90.0	90.0	90.6
$\beta$ [°]	108.2	102.1	104.5	101.8	98.2	90.1
$\gamma$ [°]	92.3	90.0	90.0	90.0	90.0	107.7
bithiophene packing <sup>a</sup>	p.-d.	2D HB	2D HB	2D HB	2D HB	p.-d.
herringbone angle [°] <sup>b</sup>	(0)	73.0	71.6	52.7	84.5	(0)
tilt angle [°] <sup>c</sup>	58.5 ( <i>b</i> )	33.1	55.3	41.3	30.7	40.5 ( <i>b</i> )
pitch angle [°] <sup>d</sup>	15.1	13.8	65.6	11.6	9.2	41.8
roll angle [°] <sup>e</sup>	61.8	52.9	43.9	63.6	35.3	12.7
volume / T2 [Å <sup>3</sup> ] <sup>f</sup>	297.7	236.2	269.9	226.2	214.3	221.2

<sup>a</sup> p.-d. = parallel displaced packing. 2D HB = two-dimensional herringbone packing.<sup>b</sup> angle between mean planes of two edge-to-face interacting bithiophenes.<sup>c</sup> angle of the mean bithiophene long axis with regard to the layer normal (for a parallel-displaced arrangement, the reference crystallographic axis is given parentheses).<sup>d,e</sup> angle of the slipped  $\pi$ -stack of bithiophenes along the long and short molecular axis, respectively, with respect to the stacking axis (Figure 7.1).<sup>f</sup> volume per bithiophene core (Figure 7.2, Table 7.1).

### 2.2.3 Compatibility of $\pi$ -Interactions and Amide Hydrogen Bonding

In summary, all six crystal structures showed the typical packing motifs of the bithiophene cores, and the three bithiophene amides **2a–c** also showed the expected amide hydrogen bonding. Nevertheless, there were significant differences in the molecular packing, both between the two series and between molecules with different spacer lengths within each series.

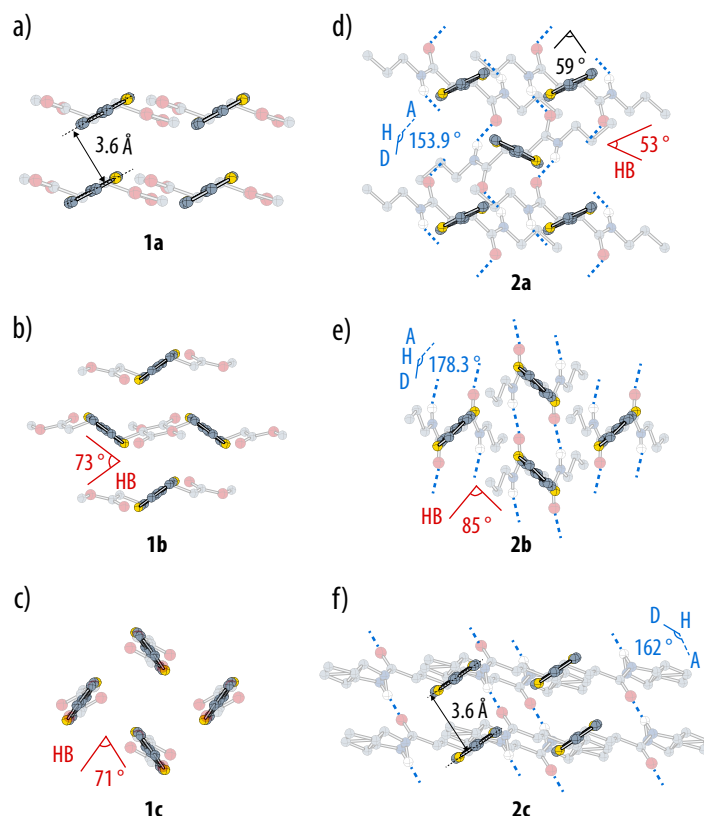


**Figure 2.7.** Bithiophene packing of *a–c*) diesters **1a–c** and *d–f*) diamides **2a–c**. Hydrogen bonding patterns observed in bithiophene diamides **2a–c** are marked with dashed lines. Hydrogen bonding (D–H...A) and herringbone angles are marked in blue and red colors, respectively.

Based on the known crystal structures of bithiophenes and higher oligothiophenes, a layered 2D herringbone packing of calamitic  $\pi$ -conjugated molecules with typical herringbone angles of 65–85 ° and tilt angles (between their long axis and the layer normal) on the order of 30–45 ° may be argued to be optimum in view of their dispersive and quadrupolar interactions..<sup>256,257</sup> The bithiophene diester **1a** may therefore be regarded as an outlier, presumably owing to the insufficient conformational freedom of the methylene spacer between its bithiophene core and the bulky and dipolar ester functions, which renders a parallel-displaced  $\pi$ – $\pi$  stacked arrangement preferable (Figure 2.7*a*). Although this constraint is apparently relaxed for the ethylene and propylene spacers in the bithiophene diesters **1b** and **1c**, which both show layered 2D herringbone packing, the tilt angle of 55.3 ° observed in **1c** is unusually large

(Figure 2.7*b,c*). Hence, it was only in the case of bithiophene diester **1b** with the ethylene spacer that the geometrical parameters of the 2D herringbone packing were consistent with efficient 2D  $\pi$ -overlap between adjacent molecules.

**Table 2.2:** Hydrogen bonds observed in single-crystals of the bithiophene diamides **2a–c**. Symmetry transformations used to generate equivalent atoms: <sup>1</sup>  $+x, 1/2-y, -1/2+z$ ; <sup>2</sup>  $x, -1+y, +z$ ; <sup>3</sup>  $-1+x, -1+y, z$

	D–H...A	$d(\text{D–H})$ [Å]	$d(\text{D–H})$ [Å]	$d(\text{D...A})$ [Å]	$\angle(\text{DHA})$ [°]
<b>2a</b>	N(1)–H(1)...O(1) <sup>1</sup>	0.86	2.03	2.830(10)	153.9
<b>2b</b>	N(1)–H(1)...O(1) <sup>2</sup>	0.86(3)	2.01(3)	2.877(2)	178.3
<b>2c</b>	N(1A)–H(1A)...O(1) <sup>3</sup>	0.88	2.02	2.873(8)	162.0

Because of the partially covalent, short-range, and directional nature of the N–H...O=C amide hydrogen bonds,<sup>84</sup> the constraints imposed by the coupling of the respective supramolecular interactions between the bithiophene cores and the functional groups via the conformational mechanics of the alkyl spacer were found to be even stronger in the case of the bithiophene diamides **2a–c** (Figure 2.7*d–f*). Thus, the bithiophene diamide **2c** exhibited a parallel-displaced  $\pi$ – $\pi$  stacked arrangement, in spite of the supposed conformational flexibility of its propylene spacer (Figure 2.7*f*). Moreover, the diamide **2a** showed a layered 2D herringbone arrangement, but with an untypically small herringbone angle of 52.7°, resulting in pseudo-parallel-displaced columnar  $\pi$ – $\pi$  stacking (Figure 2.7*d*). Only the bithiophene diamide **2b** with an ethylene spacer showed a 2D herringbone packing with typical herringbone and tilt angles (Figure 2.7*e*).

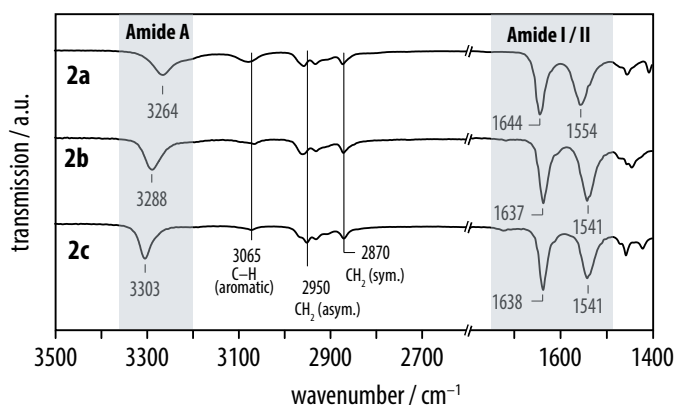


**Figure 2.8.** Solid-state IR spectra of the amide A and the amide I and II regions of bithiophene diamides **2a–c**.

The arrangement of the bithiophene cores also imposed constraints on the hydrogen bonding interactions between the amide functions of **2a–c** (Table 2.2). Thus, the comparatively small N–H...O hydrogen bond angles of 153.9 ° in **2a** and 162.0 ° in **2c** indicated a more electrostatic and less covalent hydrogen bond character than in **2b**, with a hydrogen bond angle of 178.3 °. Moreover, adjacent hydrogen bonds in which a single amide group participated as an N–H donor and a C=O acceptor were not parallel in the bithiophene diamide **2a** but inclined by 59 ° and were therefore not electronically conjugated (Figure 2.7*d*). It was only in the bithiophene diamide **2b**, that we observed both 2D herringbone packing with typical geometric parameters and infinite 1D arrays of parallel and almost linear N–H...O=C hydrogen bonds. The electronically conjugated nature of these hydrogen bonding arrays was also apparent from the solid-state IR spectra where the N–H stretching (amide A) and C=O stretching (amide I) vibrations were both red-shifted compared with the other two bithiophene diamides (Figure 2.8). That the conformational mechanics of the ethylene spacer in **2b** apparently allowed for a synergistic interplay of optimal 2D  $\pi$ -overlap and efficient amide hydrogen bonding, may be regarded as a manifestation of an “odd-even” effect, which has been variously observed in the packing of  $\pi$ -conjugated molecules with strongly interacting side groups,<sup>245,258–261</sup> notably in the topochemical polymerization of diacetylenes.<sup>262–265</sup>

The result is nevertheless significantly denser packing of the bithiophenes. In each series, the volume occupied by one bithiophene core within its sublayer (Table 2.1, Figure 7.2, Table 7.1, Table 2.3) was the smallest for the derivatives **1b** and **2b** with ethylene spacers. More remarkably, all the bithiophene diamides **2a–c** (214–221 Å<sup>3</sup>) showed denser bithiophene packing than the corresponding diesters **1a–c** (236–298 Å<sup>3</sup>), with a reduction of 25% for **2a** versus **1a**, 20% for **2c** versus **1c**, and 10% for **2b** versus **1b**. These are densest bithiophene packings so far reported among disubstituted bithiophenes, including the  $\alpha,\omega$ -dihexylbithiophene **DHT2** (Figure 2.9),  $\alpha,\omega$ -dimethylbithiophene **DMT2**,<sup>266</sup> and even the parent unsubstituted bithiophene<sup>267,268</sup> (Table 7.1, Table 2.3).

This finding is also supported by an analysis of the pitch and roll angles as defined by Curtis and coworkers,<sup>269</sup> which describe the displacement of adjacent calamitic molecules along their long and short axes, respectively (Table 2.1, Table 2.3). Only the bithiophene diamide **2b** showed sufficiently small pitch and roll angles that imply an efficient  $\pi$ -overlap between neighboring molecules (Figure 2.10, Figure 2.11).

**Table 2.3:** Detailed comparison of the crystal structures of  $\alpha$ -T2, measured at 133 K<sup>267</sup> and 173 K,<sup>268</sup> and bithiophenes with terminal alkyl side chains,  $\alpha$ , $\omega$ -dimethylbithiophene (**DMT2**)<sup>266</sup>, and  $\alpha$ , $\omega$ -dihexylbithiophene (**DHT2**).

property	$\alpha$ -T2-133K	$\alpha$ -T2-173K	DMT2	DHT2
space group	$P2_1/c$	$P2_1/c$	$P2_1/n$	$P\bar{1}$
crystal system	monoclinic	monoclinic	monoclinic	triclinic
$a$ [Å]	7.73	7.87	5.24	5.77
$b$ [Å]	5.73	5.77	5.68	7.78
$c$ [Å]	8.93	8.81	15.99	22.36
$\alpha$ [°]	90.0	90.0	90.0	99.1
$\beta$ [°]	106.7	107.1	92.3	91.8
$\gamma$ [°]	90.0	90.0	90.0	105.9
bithiophene packing <sup>a</sup>	2D HB	2D HB	c	p-d
herringbone angle [°] <sup>b</sup>	59.1	58.6	(0)	(0)
tilt angle [°] <sup>c</sup>	33.3	31.5	46.2	66.2 ( $b$ )
pitch angle [°] <sup>d</sup>	7.8	6.9	43.7/36.5	36.8
roll angle [°] <sup>e</sup>	60.2	60.6	13.1/51.9	56.9
volume /T2 [Å <sup>3</sup> ] <sup>f</sup>	222.2	223.4	255.4	262.4

<sup>a</sup> p-d. = parallel displaced packing, 2D HB = two-dimensional herringbone packing, c = columnar packing

<sup>b</sup> angle between mean planes of two edge-to-face interacting bithiophenes.

<sup>c</sup> angle of the mean bithiophene long axis with regard to the layer normal (for a parallel-displaced arrangement, the reference crystallographic axis is given parentheses).

<sup>d,e</sup> angle of the slipped  $\pi$ -stack of bithiophenes along, respectively, the long and short molecular axis with respect to the stacking axis (Figure 7.1).

<sup>f</sup> volume per bithiophene core (Figure 7.2, Table 7.1).



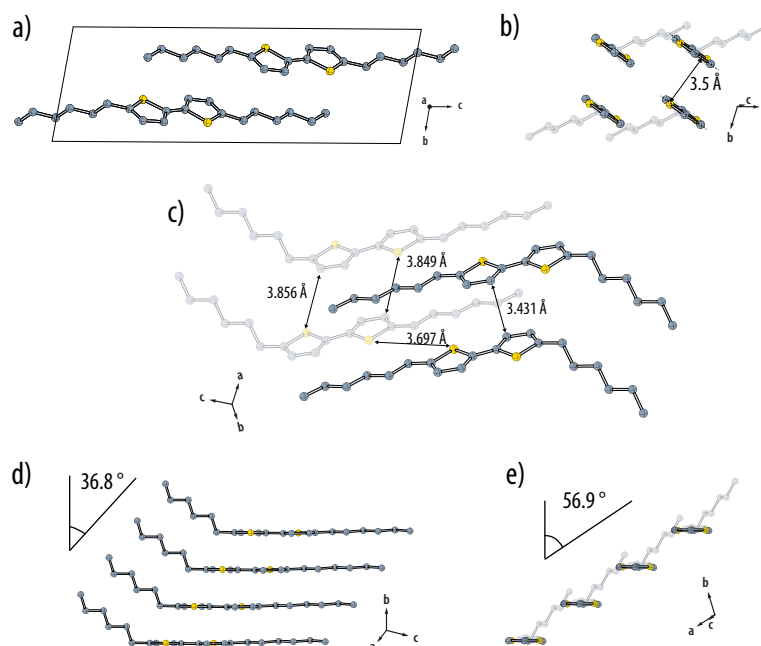


**Figure 2.9.** Ball-and-stick representations of the single-crystal X-ray structure of **DHT2** (CCDC 1951222). Single-crystals of **DHT2** were grown from a solution in ethanol at  $-5\text{ }^{\circ}\text{C}$  by slow evaporation. **DHT2** crystallized in the triclinic space group  $P\bar{1}$ , with the lattice parameters  $a = 5.7717(6)\text{ }\text{\AA}$ ,  $b = 7.7801(9)\text{ }\text{\AA}$ ,  $c = 22.363(2)\text{ }\text{\AA}$ ,  $\alpha = 99.154(9)^{\circ}$ ,  $\beta = 91.780(9)^{\circ}$ , and  $\gamma = 105.885(10)^{\circ}$ . *a*) The unit cell of **DHT2** viewed along the crystallographic *a*-axis, contained two independent molecules of **DHT2**. *b*) The interlayer distance was  $3.547\text{ }\text{\AA}$ , between parallel-displaced neighboring molecules. *c*) Illustration of C...C, C...S, and S...S close contacts of  $3.431$ ,  $3.849$ , and  $3.697\text{ }\text{\AA}$ , respectively, between parallel-displaced neighboring molecules. The molecular axis of the bithiophene was tilted by  $66.17^{\circ}$  with respect to the layer normal. Furthermore, each hexyl substituent was almost in an all-*trans* conformation and tilted differently with respect to the bithiophene core ( $5.23^{\circ}$  or  $67.83^{\circ}$ ). *d*) Illustration of the pitch angle and *e*) the roll angle of **DHT2** (all hydrogen atoms have been omitted for clarity).

**Table 2.4:** Decomposition temperatures  $T_d$ , (from TGA, at 5 wt% mass loss), melting temperatures  $T_m$ , and the absorption and emission maxima,  $\lambda_a^{\text{max}}$  and  $\lambda_e^{\text{max}}$ , respectively, from UV-vis and fluorescence spectroscopy.

	$T_d$ [ $^{\circ}\text{C}$ ]	$T_m$ [ $^{\circ}\text{C}$ ]	$\lambda_a^{\text{max}}$ (solution) [nm]	$\lambda_a^{\text{max}}$ (thin film) [nm]	$\lambda_e^{\text{max}}$ (solution) [nm]
<b>1a</b>	253	76	317	319	380
<b>1b</b>	260	125	320	308	380
<b>1c</b>	271	61	323	326	382
<b>2a</b>	343	237	320	298	384
<b>2b</b>	324	211	320	291	383
<b>2c</b>	333	160	322	321	382
<b>DHT2</b>	257	30	321	326	382

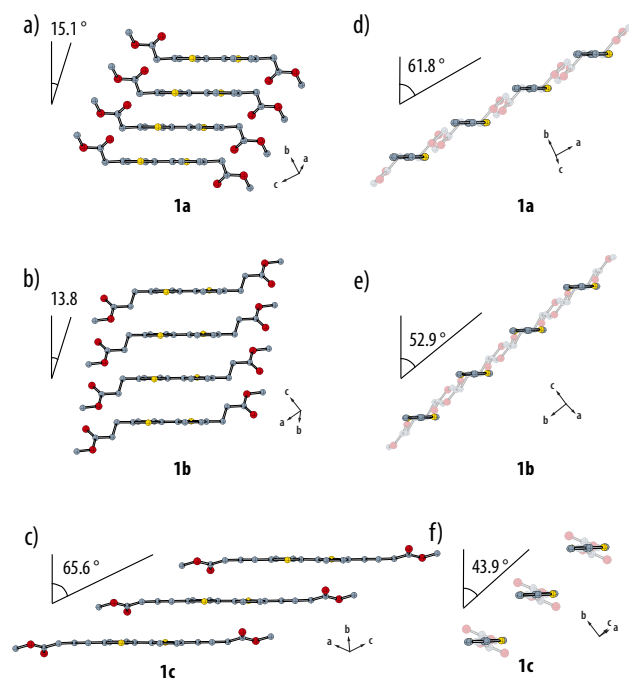


**Figure 2.10.** Illustration of *a-c*) pitch angles, and *d-f*) roll angles of bithiophene diesters **1a-c**.

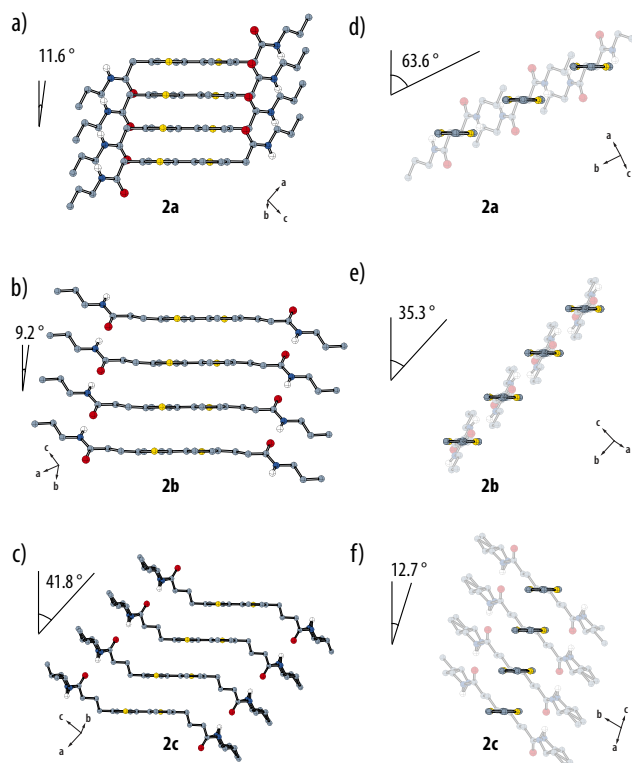


**Figure 2.11.** Illustration of *a-c*) pitch angles, and *d-f*) roll angles of bithiophene diamides **2a-c**.

## 2.2.4 Thermal and Spectroscopic Properties

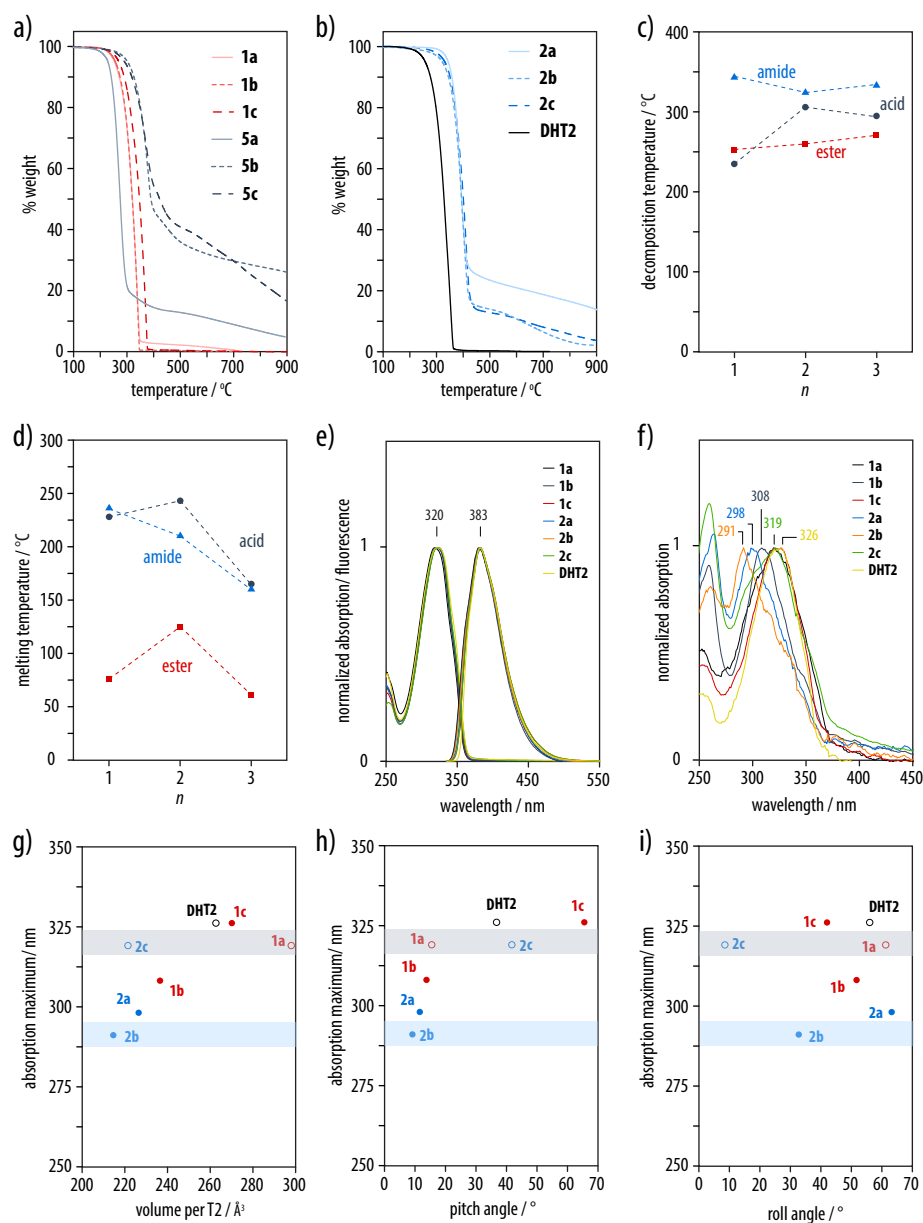


**Figure 2.12.** Thermogravimetric analysis (TGA) scans of bithiophene *a)* diesters **1a–c**, diacids **5a–c**, and *b)* diamides **2a–c**, as well as alkyl substituted DHT2. *c,d)* Decomposition,  $T_d$ , and melting temperatures,  $T_m$ , of the bithiophene diesters **1a–c**, dicarboxylic acids **5a–c**, and diamides **2a–c** as a function of the spacer length. *e)* Normalized solution-phase UV-vis and fluorescence spectra (excitation at 325 nm) of the different bithiophene derivatives in DMSO ( $c = 0.01$  mmol/L). *f)* Normalized UV-vis spectra of solid thin films of the different bithiophene derivatives, prepared by spin-coating onto quartz substrates. *g)* Plot of maximum absorption wavelengths in the solid-state absorption spectra as a function of volume per bithiophene, *h)* pitch, and *i)* roll angles. Full symbols denote a herringbone packing, while empty symbols indicate a parallel-displaced  $\pi$ – $\pi$  stacked arrangement of the bithiophene cores.

According to thermogravimetric analysis (TGA) and differential scanning calorimetry (DSC) measurements, the bithiophene diesters **1a–c** were stable up to at least 253 °C, and the bithiophene diamides **2a–c** were stable up as much as 324–343 °C (Table 2.4, Figure 2.12*a–d*). The melting points of **1a–c** were significantly lower than those of the diamides **2a–c**, decreased with increasing spacer length *n* within both series (Figure 2.12*c*), and showed a weak odd-even effect, similar to that observed in aliphatic and semiaromatic polyamides when the length of the aliphatic repeat units is varied.<sup>206</sup>

As expected, all bithiophene derivatives showed almost identical solution-phase absorption and emission spectra, with a single absorption band at around 320 nm and an emission at 383 nm, that is, a Stokes shift of 63 nm (Table 2.4, Figure 2.12*e*). By contrast, the UV-vis absorption spectra of solid samples, prepared by spin-coating on quartz substrates, became broadened and there were clear differences between the different derivatives (Table 2.4, Figure 2.12*f*). With the exception of **1c** (and the dihexylbithiophene **DHT2**), which showed a small solid-state red shift compared with the solution-phase spectra, the solid-state UV-vis absorption maxima of all the bithiophene derivatives were blue shifted to 291–319 nm. This hypsochromic shift may be attributed to the formation of spectroscopic H-aggregates in the solid-state.

The observed H-type coupling was the strongest for the two bithiophene diamides **2a** (298 nm) and **2b** (291 nm), which showed layered 2D herringbone structures, the densest packing of the bithiophenes and the smallest pitch angles (Figure 2.12*g,h*). This implies the more efficient  $\pi$ -overlap in these two bithiophene diamides, and particularly in **2b** which showed an even smaller roll angle than **2a** (Figure 2.12*i*), to have a significant impact on the electronic interactions of the bithiophene cores.

### 2.3 Conclusions

In summary, we have synthesized two series of  $\alpha,\omega$ -bithiophene diesters **1a–c** and diamides **2a–c**, in which the ester or amide functions are tethered to bithiophene core via short flexible spacers with different lengths. In the crystalline state, the different compounds showed subtle, yet important differences in their supramolecular arrangements. The hydrogen-bonded bithiophene diamides **2a–c** showed 10–25% denser packing of the bithiophene cores than the corresponding diesters **1a–c**. In particular, the bithiophene diamide **2b** showed the densest bithiophene core packing, the smallest pitch angle and a sufficiently small roll angle. It was also the only derivative that featured infinite 1D arrays of electronically conjugated, parallel, and almost linear N–H...O=C hydrogen bonds. This may be attributed to the favorable conformational mechanics of the ethylene spacer, which enabled synergistic hydrogen bonding and  $\pi$ -interactions. The resulting strong H-type coupling between the bithiophene cores in the solid-state has considerable potential for the design of organic and polymer semiconductors and photovoltaic materials with improved (photo)charge generation.<sup>270,271</sup>

**OFET Performance of a  
Hydrogen-Bonded  
Quaterthiophene**



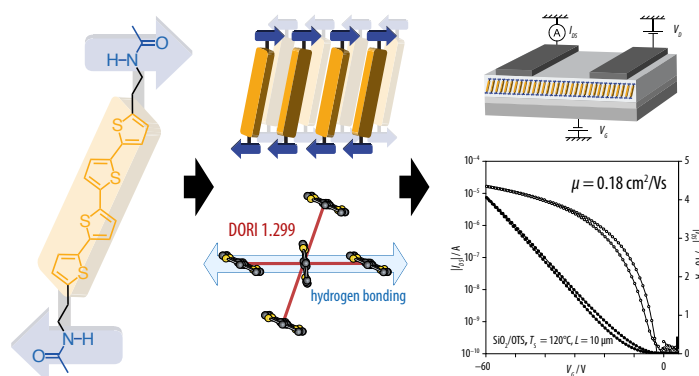
---

The results presented in this chapter are part of the paper, which has been accepted for publication in *Chemistry–A European Journal*. Gebers, J.\*; Özen, B.\*; Hartmann, L.; Schaer, M.; Suárez, S.; Bugnon, P.; Scopelliti, R.; Steinrück, H.-G.; Konovalov, O.; Magerl, A.; Brinkmann, M.; Petraglia, R.; deSilva, P.; Corminbœuf, C.; Frauenrath, H.; "Crystallization and OFET Performance of a Hydrogen-Bonded Quaterthiophene" (\*equally contributed). DOI: 10.1002/chem.201904562.

Single-crystal structure and thin film morphology of **1** have already been disclosed in Gebers, J., Thèse No°6199, EPFL. B.Ö. performed the chemical synthesis (**2**), thin film preparation (**1** and **2**), as well as OFET fabrication and testing (**1** and **2**). R.S. did the X-ray structure analysis. P. S. and C. C. performed DFT computations.

### 3 OFET Performance of a Hydrogen-Bonded Quaterthiophene

The crystalline textures of thin films of  $\pi$ -conjugated molecules play an important role in the active layers of organic electronic devices. Improved control over their supramolecular arrangement, crystallinity, and thin film morphology is therefore desirable. Here, we show that hydrogen-bonded substituents may be highly effective in this respect, with direct benefits for the device performance of p-type organic semiconductors. Thus, a quaterthiophene diacetamide is found to show improved crystal packing efficiency than other quaterthiophenes and hence enhanced intermolecular electronic interactions. These trends are maintained in polycrystalline thin films, which showed a layer-by-layer morphology with large domain sizes and high degrees of internal order. Organic field-effect transistors prepared from these thin films consequently show charge carrier mobilities comparable with the highest mobilities so far reported for single-crystalline quaterthiophenes. The use of amide hydrogen-bonded substituents may therefore provide a general means of optimizing the performance of organic semiconductor thin films and the performance of devices based on such materials.



### 3.1 Introduction

Crystalline thin films of  $\pi$ -conjugated molecules have emerged as efficient semiconductors in electronic devices such as organic field-effect transistors (OFETs),<sup>7,217,272,273</sup> photovoltaics,<sup>274</sup> light-emitting diodes,<sup>213</sup> chemical sensors,<sup>275</sup> and other electronic devices.<sup>276,277</sup> Both a large intermolecular  $\pi$ -overlap and macroscopically continuous charge percolation paths are required for good semiconducting properties. Therefore, materials with enhanced control over the supramolecular arrangement of the  $\pi$ -conjugated segments within the crystal structure, the size of the crystalline domains, and the thin film morphology are desirable. To this end, the modification of the  $\pi$ -conjugated cores themselves, variation of molecular architectures (for instance, linear, cyclic, or branched cores), decoration with non-functional solubilizing groups (mostly linear or branched alkyl substituents), or the application of different processing techniques (such as sublimation, spin- or dip-coating, or guided crystallization) have been explored.<sup>272,273,278,279</sup> Moreover, it has recently been demonstrated that a high degree of short-range intermolecular order is an important performance parameter in the case of polymer semiconductors.<sup>12</sup>

Hydrogen-bonded templates and substituents have proven to be useful structure-directing groups to establish strong and specific intermolecular interactions that guide crystallization or supramolecular self-organization.<sup>73,76,82,280,281</sup> Nevertheless, the effect of hydrogen-bonded functional groups on the structure and properties of organic semiconductors in the solid-state has not been extensively investigated until recently, supposedly because they were suspected to serve as trap states.<sup>282</sup> The effect of hydrogen-bonded end groups on the charge carrier mobility of certain sexithiophenes<sup>283</sup> and naphthalene diimides<sup>130</sup> in OFETs was investigated but no improvement in device performance was observed. An  $\alpha,\omega$ -hydroxypropyl-substituted sexithiophene was found to exhibit enhanced layer-by-layer thin film growth and was successfully used in thin film devices.<sup>132</sup> Hydrogen bonding has been employed in the solution-phase self-assembly of oligothiophene derivatives into one-dimensional nanostructures,<sup>118,241,245,284–287</sup> but while field-effect devices have been used in some cases to determine the properties of the resulting aggregates, the specific role of hydrogen-bonding for macroscopic device performance was not systematically investigated in these studies. Only recently, it was shown that hydrogen bonding positively affected the thin film packing of naphthalene diimide and diketopyrrolopyrrole (DPP) derivatives.<sup>288,289</sup> According to computations on perylene bisimides, hydrogen bonding interactions should have a beneficial effect on device performance.<sup>290</sup> Consistent with these reports, experimental results for n-type semiconductors have indicated no adverse effect of hydrogen bonding on transport properties.<sup>129</sup> Würthner and coworkers even found that the *N*-unsubstituted octachloroperylene bisimide was an efficient n-type organic semiconductor as a consequence of the dense “brickwork” crystal structure induced by the hydrogen-bonded imides.<sup>120</sup> A similar beneficial effect of hydrogen bonding has also been observed for low band gap polymers with hydrogen-bonded side chains.<sup>134</sup> Notably, Glowacki et al. systematically studied hydrogen-bonded  $\pi$ -conjugated compounds as charge-transport materials in organic field-effect transistors.<sup>121,124</sup> For example, that OFETs printed



from intermolecularly N–H...O=C hydrogen-bonded heteroacene pigments showed field-effect mobilities as high as  $1.5 \text{ cm}^2 \text{ V}^{-1} \text{ s}^{-1}$  and good device lifetimes even under ambient conditions.<sup>122</sup> In all of these experimental examples, the hydrogen bonding sites were part of and in plane with the respective  $\pi$ -conjugated systems. Here, we demonstrate that terminal hydrogen-bonded substituents may be used to guide and improve crystallization of calamitic  $\pi$ -conjugated molecules, tailor their thin film morphology and improve the device performance of the resulting p-type organic semiconductors. We observed that the crystalline quaterthiophene diacetamide **1** exhibited significantly denser packing of the molecules in the unit cell and improved  $\pi$ -interactions as compared with other quaterthiophenes,<sup>255,291,292</sup> including the closely related quaterthiophene diacetate **2** (Figure 3.1). We found this trend to be maintained in the structure of crystalline thin films, whose morphology and domain sizes may be tuned depending on the deposition conditions and dielectric surface pre-treatment. As a result, field-effect transistors fabricated from these polycrystalline thin films revealed average mobilities of up to  $0.18 \text{ cm}^2 \text{ V}^{-1} \text{ s}^{-1}$ , which is almost one to two orders of magnitude higher than the reference non-hydrogen-bonded diacetate **2** and in the same range as the best mobilities reported for single-crystalline quaterthiophene specimens to date.<sup>293–295</sup> The use of hydrogen-bonded substituents as an additional structure-directing motif may thus provide a general pathway towards novel organic and polymer semiconducting materials with optimized morphology for better performing device performance.

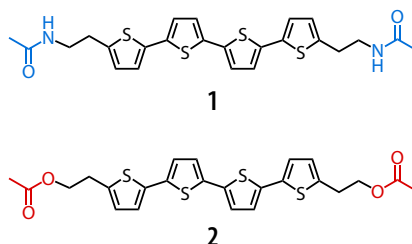


**Figure 3.1.** Molecular structures of the quaterthiophene bisacetamide **1** and the corresponding diacetate **2** investigated in this work.

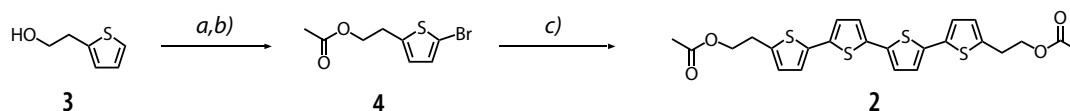
## 3.2 Results and Discussion

### 3.2.1 Synthesis of Non-Hydrogen-Bonded Quaterthiophene

The synthesis of hydrogen-bonded quaterthiophene bisacetamide **1** and all the related intermediates were described in detail elsewhere.<sup>296,297</sup>

The quaterthiophene bisacetate **2** is as close in molecular structure as possible to **1** and hence serves as a non-hydrogen-bonded reference compound for the present study. The compound **2** was prepared in two-steps starting from commercially available 2-(2-thienyl)ethanol **3** (Scheme 3.1). The acetylation of **3** was performed using acetic anhydride and a catalytic amount of 4-(*N,N'*-dimethylamino)pyridine (DMAP) under the basic conditions, followed by regio-selective bromination with *N*-bromosuccinimide (NBS) in acetic acid/DCM (1:1). This

reaction furnished the corresponding 2-(5-bromo-2-thienyl)ethyl acetate **4** as a colorless oil in almost quantitative yield. A subsequent Stille cross-coupling of **4** with 5,5-bis(tributylstannyl)-2,2-bithiophene gave the desired non-hydrogen-bonded quaterthiophene bisacetate **2** as a yellow solid in 55% yield after aqueous work up and column chromatography.



**Scheme 3.1.** Two-step synthesis of quaterthiophene bisacetate **2**. *Reagents and conditions:* a) acetic anhydride, triethylamine, cat. amount of 4-(*N,N'*-dimethylamino)pyridine (DMAP), DCM, room temperature, 30 min, quantitative yield; b) *N*-bromosuccinimide, acetic acid, DCM, room temperature, 3 h, 97% yield; c) 5,5-Bis(tributylstannyl)-2,2-bithiophene, Pd(PPh<sub>3</sub>)<sub>4</sub>, dry DMF, 80 °C, 12 h, 55% yield.

To better understand the influence of the lateral amide hydrogen bonding substituents on solid-state organization, single-crystals of hydrogen-bonded **1** and its structural non-hydrogen-bonded analogue **2** suitable for X-ray crystal structure analysis were obtained from sublimation<sup>296</sup> at 240–265 °C under high vacuum (10<sup>−6</sup> mbar) and grown from a toluene solution by slow evaporation at room temperature over 3–4 weeks, respectively.

### 3.2.2 Single-Crystal X-Ray Structure

In the quaterthiophene diacetamide **1**,<sup>296</sup> the terminal acetamide functions offer the possibility of intermolecular N–H...O=C hydrogen bonding. Solid-state infrared (IR) spectroscopy of **1** revealed strongly, resonance-enhanced amide hydrogen bonding at room temperature with characteristic amide A, amide I and II absorption bands at around 3280, 1636, and 1550 cm<sup>−1</sup>, respectively, similar to the those observed in crystalline domains of polyamides (Figure 3.2).<sup>100</sup> The amide groups are linked to the  $\pi$ -conjugated core via a short flexible spacer to decouple the respective packing requirements.

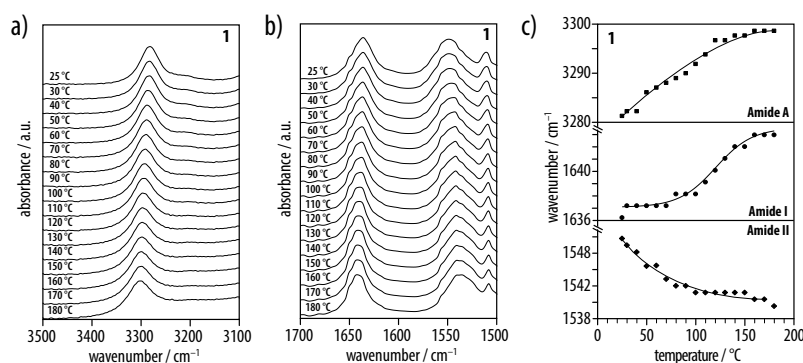


**Figure 3.2.** a) The amide A, and b) amide I and II regions of the solid-state infrared (IR) spectra of **1** revealed strongly, resonance-enhanced amide hydrogen bonding at room temperature with absorption bands at around 3280, 1636, and 1550 cm<sup>−1</sup>, respectively. c) By increasing the temperature, these bands were shifted to higher (for amide A and I) and lower (for amide II) wavenumbers.

Hydrogen bonding is indeed observed in the single-crystal structure of **1** and appears to induce overall tighter packing of the quaterthiophene cores. This results in a noticeably smaller unit cell and increased  $\pi$ -interactions of neighboring molecules compared with the non-hydrogen-bonded quaterthiophene diacetate **2** and other quaterthiophene derivatives without hydrogen-bonded lateral substituents. **1** crystallized as flat needles or elongated platelets<sup>296</sup> in the triclinic  $P\bar{1}$  space group ( $a = 5.89 \text{ \AA}$ ,  $b = 7.65 \text{ \AA}$ ,  $c = 25.78 \text{ \AA}$ ,  $\alpha = 97.4^\circ$ ,  $\beta = 93.8^\circ$ , and  $\gamma = 91.1^\circ$ ), while monoclinic or orthorhombic unit cells were typically observed for other representative examples of quaterthiophenes such as the quaterthiophene diacetate **2**, the low-temperature polymorph of  $\alpha$ -quaterthiophene ( $\alpha$ -4T),<sup>255</sup>  $\alpha,\omega$ -dimethylquaterthiophene (DM4T),<sup>291</sup> or  $\alpha,\omega$ -dihexylquaterthiophene (DH4T).<sup>292</sup>

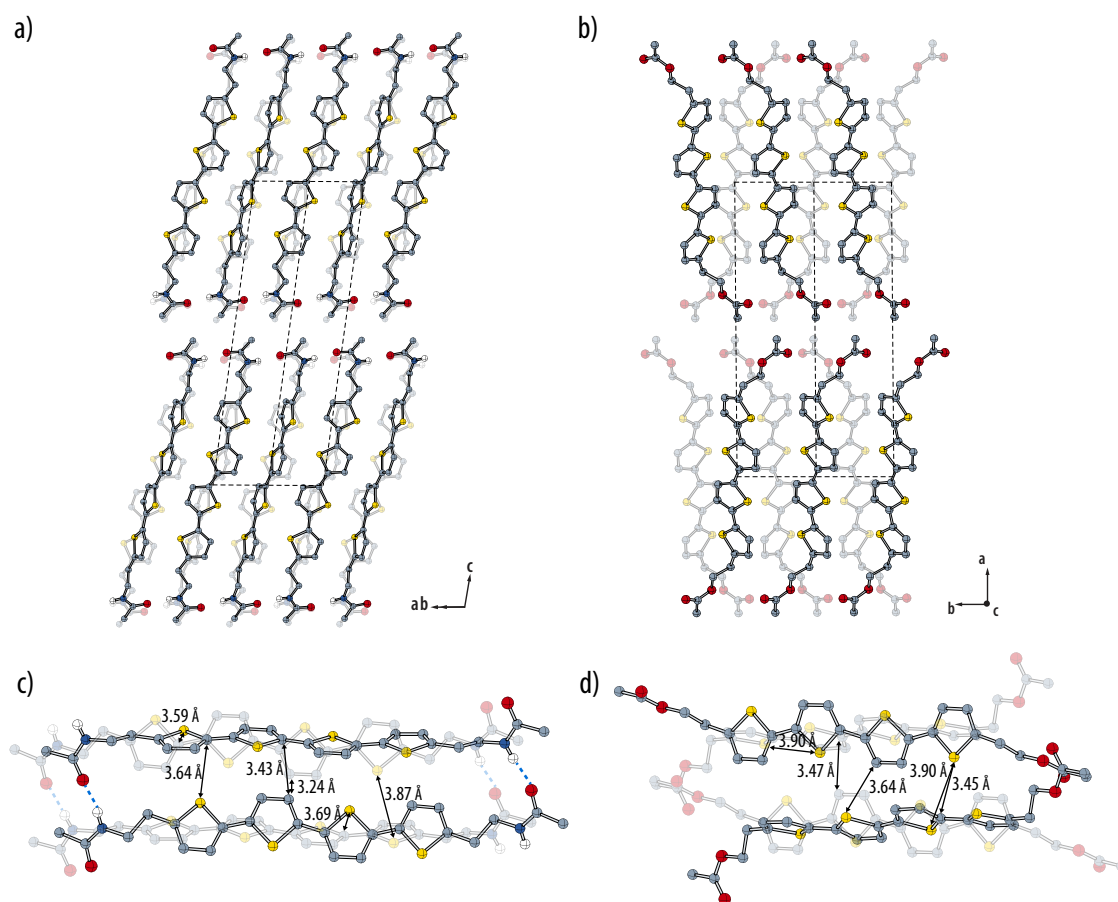


**Figure 3.3.** Ball-and-stick representations of the single-crystal X-ray structure of *a*) quaterthiophene diacetamide **1** (CCDC 976399) viewed along the crystallographic [110] axis, and *b*) quaterthiophene diacetate **2** (CCDC 1043812) viewed along the *c*-axis, with *c*, *d*) an illustration of the C...C, C...S, and S...S short contacts between edge-to-face and parallel-displaced neighboring pairs of **1** and **2** (all hydrogen atoms except the amide hydrogens omitted for clarity).

**Table 3.1:** Comparison of the crystal structure of **1** (CCDC 976399) with the structures of the quaterthiophene diacetate **2** (CCDC 1043812), the low temperature polymorph of  $\alpha$ -4T,<sup>255</sup>  $\alpha,\omega$ -dimethylquaterthiophene (DM4T),<sup>291</sup> and  $\alpha,\omega$ -dihexylquaterthiophene (DH4T).<sup>292</sup>

property	<b>1</b>	<b>2</b>	$\alpha$ -4T	DM4T	DH4T
space group	$P\bar{1}$	$P2_1/c$	$P2_1/c$	Pbca	$P2_1/a$
crystal system	triclinic	monoclinic	monoclinic	orthorhombic	monoclinic
$a$ [Å]	5.89	5.88	6.09	7.71	6.05
$b$ [Å]	7.65	9.01	7.86	5.94	7.81
$c$ [Å]	25.8	22.09	30.5	36.0	28.53
$\alpha$ [°]	97.4	90	90	90	90
$\beta$ [°]	93.8	91.8	91.8	90	92.4
$\gamma$ [°]	91.1	90	90	90	90
herringbone angle [°] <sup>a</sup>	60.0	60.8	63.1	62.1	62.8
tilt angle [°] <sup>b</sup>	23.9 / 24.2	35.0	24.8	23.3	23.9
ab area / 4T [Å <sup>2</sup> ] <sup>c</sup>	22.5	26.5	23.9	22.9	23.6
volume / 4T [Å <sup>3</sup> ] <sup>d</sup>	291	308	307	297	306

<sup>a</sup> angle between the mean planes of two edge-to-face interacting quaterthiophene cores.

<sup>b</sup> angle of the quaterthiophene long axis with respect to the layer normal.

<sup>c</sup> area span between the a and b vectors of the unit cell divided by the number of quaterthiophenes in this plane.

<sup>d</sup> volume per quaterthiophene core calculated using the ab-area, tilt angle and distance between the  $\alpha$ -, and  $\omega$ -carbons of the quaterthiophene.

The packing of **1** (Figure 3.3*a*), **2** (Figure 3.3*b*), and the other quaterthiophenes shared several common features (Table 3.1). In all cases, the quaterthiophene cores were arranged in layers along the *ab* plane with their long axes oriented along the *c*-axis, and they exhibited a herringbone arrangement with very similar herringbone and tilt angles. In the case of **1**, however, the packing symmetry in the *ab* plane was broken because the molecules formed N–H...O=C hydrogen-bonded chains along the crystallographic [110] direction. Each amide function was thus involved in two slightly different hydrogen bonds (Table 3.2). Most importantly, however, the volume per quaterthiophene unit in the quaterthiophene diacetamide **1** was calculated to be 291 Å<sup>3</sup> and was hence significantly smaller than for **2** (308 Å<sup>3</sup>), as well as  $\alpha$ -4T (307 Å<sup>3</sup>) or DH4T (306 Å<sup>3</sup>), that is, derivatives typically used in organic electronic devices (only DM4T with its entirely different intermolecular arrangement exhibited a comparable, albeit still somewhat larger volume of 297 Å<sup>3</sup> per quaterthiophene).

**Table 3.2:** Hydrogen bonds observed in single crystals of **1**. Symmetry transformations used to generate equivalent atoms: <sup>1</sup>  $-x+1, -y, -z$ ; <sup>2</sup>  $-x+2, -y+1, -z$ ; <sup>3</sup>  $x-1, y-1, z$

D–H...A	<i>d</i> (D–H) [Å]	<i>d</i> (D–H) [Å]	<i>d</i> (D...A) [Å]	$\angle$ (DHA) [°]
N(1A)–H(1A)...O(2A) <sup>1</sup>	0.88	1.94	2.820(11)	178.5
N(1B)–H(1B)...O(2B) <sup>1</sup>	0.88	2.03	2.90(3)	172.8
N(2A)–H(2A)...O(1A) <sup>2</sup>	0.88	1.93	2.808(11)	172.1
N(2B)–H(2B)...O(1B) <sup>3</sup>	0.88	1.94	2.81(3)	168.9

Considering how remarkably similar the volume per quaterthiophene is for **2**,  $\alpha$ -4T, and DH4T, despite the very different steric demand of their respective terminal substituents, it is tempting to assume that its value represents the “inherent” spatial requirements for a  $\pi$ – $\pi$  stacked quaterthiophene as a result of van der Waals and quadrupolar interactions. From direct comparison with the diacetate **2**, the higher packing density in the case of **1** would hence appear to result from the additional hydrogen bonding interactions between the terminal acetamide substituents of **1**. Consistent with this noticeably denser packing in the unit cell, the distances between both the parallel-displaced  $\pi$ – $\pi$  stacked neighbors and edge-to-face pairs were significantly reduced, as reflected by the C...C short contacts of 3.208 Å and 3.415 Å, respectively (versus 4.081 and 3.469 Å for **2**, versus 3.442 and 3.540 Å for  $\alpha$ -4T, versus 3.450 and 3.558 Å for DH4T, and 3.287 and 3.502 Å for DM4T) (Figure 3.3*c,d*). Likewise, the intermolecular C...S and S...S short contacts of 3.597 Å and 3.871 Å, respectively, were smaller than most of the corresponding distances observed in the reference materials (versus 3.450 and 3.904 for **2**, versus 3.712 and 4.111 Å for  $\alpha$ -4T, versus 3.787 and 4.075 Å for DH4T, and 3.659 and 3.899 Å for DM4T), with the exception of the C...S short contacts (3.450 Å for **2**) (Figure 3.3*c,d*).

### 3.2.3 DFT Computations of Electron Overlap Effects

We regard the higher packing density of the  $\pi$ -conjugated cores and the smaller short contacts in **1** to result from the hydrogen-bonded substituents, which could potentially result in an improved  $\pi$ -overlap and, consequently, better transport properties. In order to quantify the effect of packing density on the electronic structure of the investigated crystals, we developed an electronic compactness index based on the density overlap regions indicator (DORI).<sup>298</sup> As DORI is a density-based scalar field revealing regions of high-density overlap between atoms and molecules, the number of electrons encapsulated within an intermolecular DORI domain may be used to compare electronic overlap effects between corresponding sites in crystal lattices (Figure 3.4).

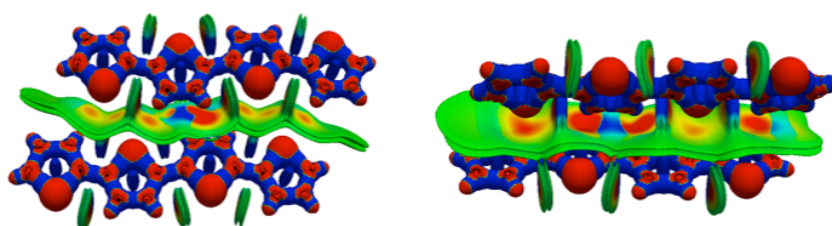


**Figure 3.4.** Representative examples for DORI = 0.5 isovalues for two pairs of molecules in the crystal structure of **1**. The surfaces are color-coded according to the values of the function  $\text{sgn}(\lambda_2)\rho$  in the  $-0.01$  to  $0.01$  a.u. range, where  $\lambda_2$  is the second isovalue of the electron density Hessian and  $\rho$  is the electron density. The compactness index was computed as integral of the electron density over the intermolecular regions.

This new method has recently shown good correlation with experimental results and has the advantage of being less sensitive to small changes in the molecular geometry (e.g. DFT optimization level vs. experimental X-Ray structures) than the computation of charge transfer integrals. The compactness index was computed for different pairs of neighboring quaterthiophene cores within the ab plane, using the atom positions as determined for the crystal structures of **1**, **2**,  $\alpha$ -4T, DM4T and DH4T (Figure 3.5). The DORI values for **1** were the highest of all the quaterthiophenes for all pairs of nearest neighbors, with maximum values between edge-to-face pairs being more than 18% higher than for any of the reference compounds. In marked contrast, the values for the non-hydrogen-bonded quaterthiophene diacetate **2** were comparatively low, which confirms that the formation of hydrogen bonds and the resulting denser packing of the quaterthiophene cores plays a decisive role in electronic overlap.

Interestingly, the symmetry breaking of the two-dimensional herringbone packing within a quaterthiophene layer in **1**, caused by the intermolecular  $\text{N-H}\cdots\text{O}=\text{C}$  hydrogen bonding, does not seem to be reflected in the compactness index, because the DORI values were identical for all edge-to-face dimers. Closer inspection revealed that this was in fact a coincidence, because the integration domains differed in volume for hydrogen-bonded ( $52.8 \text{ \AA}^3$ ) and non-bonded ( $54.5 \text{ \AA}^3$ ) dimers, resulting in the expected higher average electron density for the former. Overall, the DORI results confirmed that hydrogen bonding in **1** induced a denser packing with improved  $\pi$ -interactions, as required for improved charge transport.

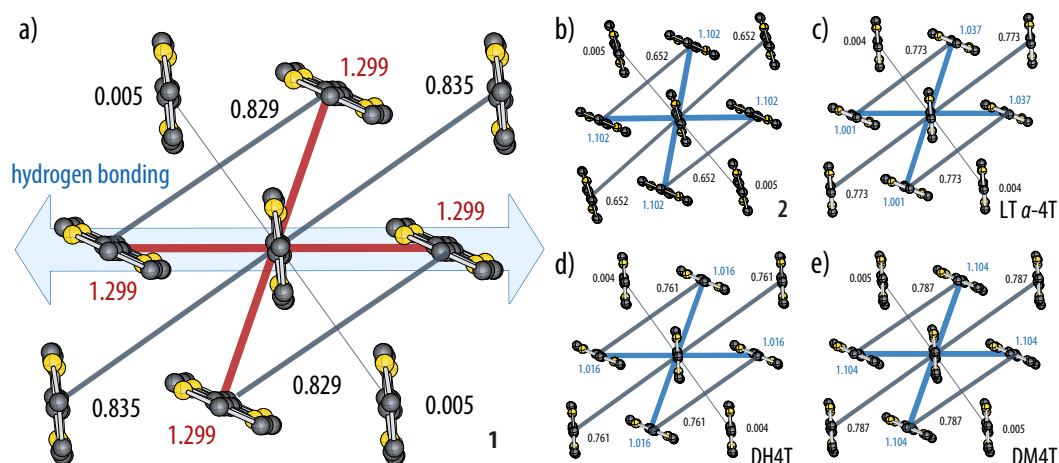


**Figure 3.5.** Top views onto the herringbone packing of the quaterthiophene cores in *a*) **1**, in comparison to *b*) **2**, *c*) LT,<sup>255</sup>  $\alpha$ -4T, *d*) DM4T,<sup>291</sup> and *e*) DH4T<sup>292</sup> (all hydrogen atoms and side chains omitted for clarity). The numbers and line widths represent the computed density overlap regions indicator (DORI) values of quaterthiophene pairs.

### 3.2.4 Thin Film Morphology

Crystalline thin films of **1** suitable for the fabrication of organic field-effect transistors (OFETs) were prepared by physical vapor deposition at  $T_S = 120^\circ\text{C}$  onto two different types of substrates, that is, (*i*) bare p-doped silicon with a 200 nm thermal oxide layer ( $\text{SiO}_2$ ), and (*ii*) the same substrate covered with a self-assembled monolayer of octadecyltrichlorosilane (OTS). The influence of the substrate temperature on the thin film morphology and growth as well as resulting device performance of **1** is reported elsewhere.<sup>296</sup>

Atomic force microscopy (AFM) imaging on thin films deposited on  $\text{SiO}_2$  showed several micrometer-sized grains, following Stranski–Krastanov growth mechanism (Figure 3.6*a–c*).<sup>299</sup> The first layers showed two-dimensional growth of continuous layers up to a certain threshold thickness, followed by three-dimensional growth of needle-like features with an average height of 20 nm protruding from the  $\text{SiO}_2$  surface. The crystalline islands and terraces in thin films of **1** exhibited a uniform height of 2.7 nm, matching the interplanar distance between the *ab* layers observed in the single-crystal structure of **1**. Accordingly, these flat-on crystals were inferred to comprise monolayers of **1** with the molecular long axis “standing up” on the substrate. Moreover, the second and subsequent layers appeared only to form once the surface coverage by the previous layer was almost complete, suggesting that the layer edges may be preferential sites for the adsorption of new molecules. Furthermore, layer-by-layer two-dimensional (Frank-van der Merwe type) versus needle-like growth was strongly favored on OTS-treated  $\text{SiO}_2$ , as demonstrated by AFM (Figure 3.6*d–f*). In this way, micrometer-sized crystalline two-dimensional layers of **1** with a limited number of grain boundaries were obtained, originating either from a low nucleation density or coalescence of adjacent domains with the same orientation on the substrate.



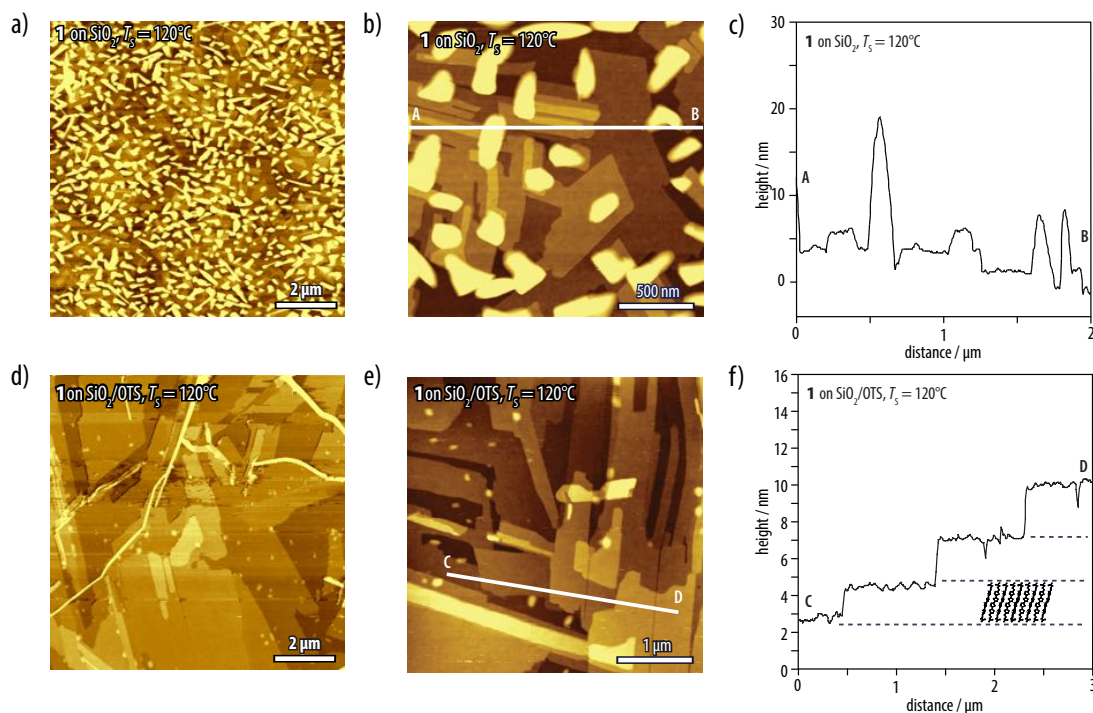


**Figure 3.6.** Atomic force microscopy (AFM) height images of thin films of **1** vapor-deposited onto *a,b*)  $\text{Si}^+/\text{SiO}_2$  or *d,e*) OTS-treated  $\text{Si}^+/\text{SiO}_2$  substrates, as well as *c,f*) height profiles obtained from *b,e*). Figure adapted from ref. [296].

In marked contrast to **1**, AFM imaging of vapor-deposited thin films of **2**, prepared at  $T_S \approx 120^\circ\text{C}$  on OTS-treated substrates, revealed separated islands, leading to a discontinuous thin film morphology (Figure 3.7*a*). This may however be explained by the choice of the substrate temperature ( $T_S \approx 120^\circ\text{C}$ ), which may be unsuitable for obtaining continuous thin films of **2** owing to its markedly different thermal properties to **1**, as evidenced by thermogravimetric analysis (TGA) and differential scanning calorimetry (DSC) (Figure 3.7*b,c*). By reducing the substrate temperature to  $T_S \approx 40^\circ\text{C}$ , however, almost complete coverage of the substrate was observed by AFM imaging (Figure 3.7*d-f*). The resulting thin film texture, prepared at  $T_S \approx 40^\circ\text{C}$  was more promising than that obtained at the higher substrate temperature, and was therefore used later for the fabrication of bottom-gate top-contact organic field-effect transistors.

### 3.2.5 Organic Field-Effect Transistors

Thin films of **1** vapor-deposited at  $T_S \approx 120^\circ\text{C}$  on OTS-treated substrates exhibited a particularly promising morphology and internal crystal structure for two-dimensional charge transport. Therefore, we fabricated bottom-gate top-contact organic field-effect transistors (OFETs) with channel lengths  $L = 5\text{--}20\ \mu\text{m}$  from thin films of **1** by thermal deposition of Au source and drain electrodes. The output curves as well as the transfer curves in the saturation



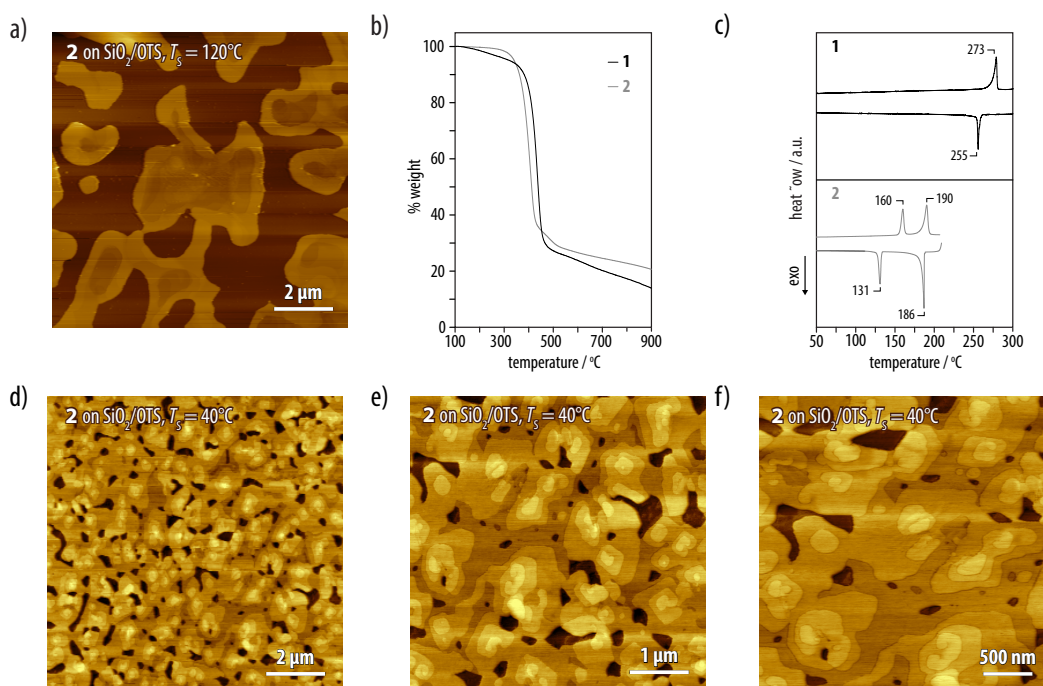


**Figure 3.7.** *a)* Atomic force microscopy (AFM) height images of films of **2** vapor-deposited onto OTS-treated substrates at  $T_S \approx 120$  °C. Thermal properties of **1** and **2** were characterized by *b)* thermogravimetric analysis (TGA) and *c)* differential scanning calorimetry (DSC). TGA scans indicated the main decomposition temperatures of both compounds to be above 300 °C. DSC heating and cooling scans of **2** showed multiple thermal transitions, suggesting the presence of different phases on heating, while **1** showed only single melting and cooling transitions. *d–f)* Atomic force microscopy (AFM) height images of films of **2** vapor-deposited onto OTS-treated substrates at temperatures of 40 °C.

regime ( $V_D = -60$  V or  $V_D = -40$  V) were measured independently in an inert atmosphere, in order to obtain the field-effect mobilities  $\mu$ , current on/off ratios  $I_{\text{on}}/I_{\text{off}}$ , and threshold voltages  $V_T$  (Table 3.3). All devices showed typical OFET characteristics for organic p-type semiconducting materials (Figure 3.8).

Devices prepared on OTS-treated substrates showed significantly better performance according to all the measures than those on bare SiO<sub>2</sub> substrates. Thin films deposited at 120 °C on OTS-treated substrates showed average mobilities of up to  $0.18 \text{ cm}^2 \text{ V}^{-1} \text{ s}^{-1}$ , which is almost one to two orders of magnitude higher than for the reference non-hydrogen-bonded diacetate **2** (Table 3.3 and Figure 3.8) and in the same range as the highest mobilities previously reported for single-crystalline specimens.<sup>293–295,300</sup> Moreover, the devices exhibited good on-off ratios of  $I_{\text{on}}/I_{\text{off}} = 10^5$  as well as improved threshold voltages compared with the device on bare SiO<sub>2</sub> substrates. The threshold voltages nevertheless remained large, so that there is room for device optimization, even in the case of the OTS-treated substrates. However, only limited hysteresis was observed when measuring the transfer characteristics in the forward and reverse directions (Figure 3.8*d,e,g,h,j,k*). This implies that the hydrogen-bonded substituents in quaterthiophene **1** are not a major source of trap states.

**Table 3.3:** Average and maximum mobilities  $\mu$ ,  $I_{\text{on}}/I_{\text{off}}$ , and threshold voltages  $V_T$  of bottom-gate ( $\text{Si}^+$ ) top-contact (Au) OFETs with  $W/L = 10$ ; entries **1–3**: variation of channel length for devices of **1** on bare and; entries **4–6**: OTS-treated  $\text{SiO}_2$  substrates at  $T_S = 120^\circ\text{C}$ ; entries **7–9**: variation of channel length for devices of **2** on OTS-treated  $\text{SiO}_2$  substrates at  $T_S = 40^\circ\text{C}$ . All devices were measured in inert atmosphere. The reported device characteristics were averaged out over three to five devices from two different batches.

Entry	$L$ [ $\mu\text{m}$ ]	$\mu_{\text{average}} (\mu_{\text{max}})$ [ $\text{cm}^2 \text{V}^{-1} \text{s}^{-1}$ ]	$I_{\text{on}}/I_{\text{off}}$	$V_T$ [V]
<b>1</b>	20	$7.4 \pm 0.62 (8.5) \cdot 10^{-3}$	$10^3$ – $10^4$	$-(36 \pm 2)$
<b>2</b>	10	$4.7 \pm 1.04 (6.1) \cdot 10^{-3}$	$10^3$ – $10^4$	$-(37 \pm 8)$
<b>3</b>	5	$8.9 \pm 1.59 (11.4) \cdot 10^{-3}$	$10^3$ – $10^4$	$-(30 \pm 6)$
<b>4</b>	20	$1.4 \pm 0.14 (1.5) \cdot 10^{-1}$	$10^5$	$-(24 \pm 6)$
<b>5</b>	10	$1.8 \pm 0.23 (2.1) \cdot 10^{-1}$	$10^5$	$-(21 \pm 3)$
<b>6</b>	5	$0.6 \pm 0.06 (0.8) \cdot 10^{-1}$	$>10^5$	$-(18 \pm 12)$
<b>7</b>	20	$1.7 \pm 0.24 (1.9) \cdot 10^{-3}$	$10^3$ – $10^4$	$-(26 \pm 11)$
<b>8</b>	10	$6.6 \pm 2.89 (8.7) \cdot 10^{-3}$	$10^4$	$-(21 \pm 4)$
<b>9</b>	5	$2.4 \pm 1.46 (2.1) \cdot 10^{-3}$	$10^4$	$-(28 \pm 7)$

### 3.3 Conclusions

In conclusion, we found that the performance of OFET devices fabricated from polycrystalline thin films of the quaterthiophene acetamide **1** was comparable with devices from quaterthiophene single crystals. We infer from this that the hydrogen-bonded terminal substituents act as an additional structure-directing element. In order for hydrogen bonding to benefit OFET performance, it should not disrupt but rather promote the formation of extended layered structures parallel to the plane of the substrate with the preferred herringbone arrangement of the calamitic  $\pi$ -conjugated cores, which is favorable for two-dimensional charge transport. A simple but crucial factor in this regard is the short flexible spacer between the hydrogen-bonded substituents and the core, which decouples the conflicting geometric requirements of the herringbone arrangement and hydrogen bonding. In this way, the dispersive and quadrupolar contributions to the  $\pi$ -interactions may be optimized, while hydrogen bonding of the amide groups in the lattice direction parallel to the substrate promotes rapid in-plane crystal growth. This is reminiscent of the role of synergistic lateral hydrogen bonding in the formation of well-defined nanowires comprising tightly  $\pi$ – $\pi$  stacked chromophores.<sup>238</sup> It is possible because the *ab* lattice parameters in a typical herringbone arrangement (about 10 Å) are similar to the intermolecular distance required by N–H...O=C hydrogen bonding (typically 9.2–9.8 Å over two molecules). Moreover, because this latter is somewhat smaller, the hydrogen-bonded side groups induce tighter packing of the molecules in the crystal structure. On an appropriate substrate surface, the overall result is the formation of two-dimensional layers with large domain sizes, high internal crystalline order, and tighter packing of the calamitic  $\pi$ -conjugated pores in both dimensions, which results in a larger  $\pi$ -overlap. Consistent with these structural

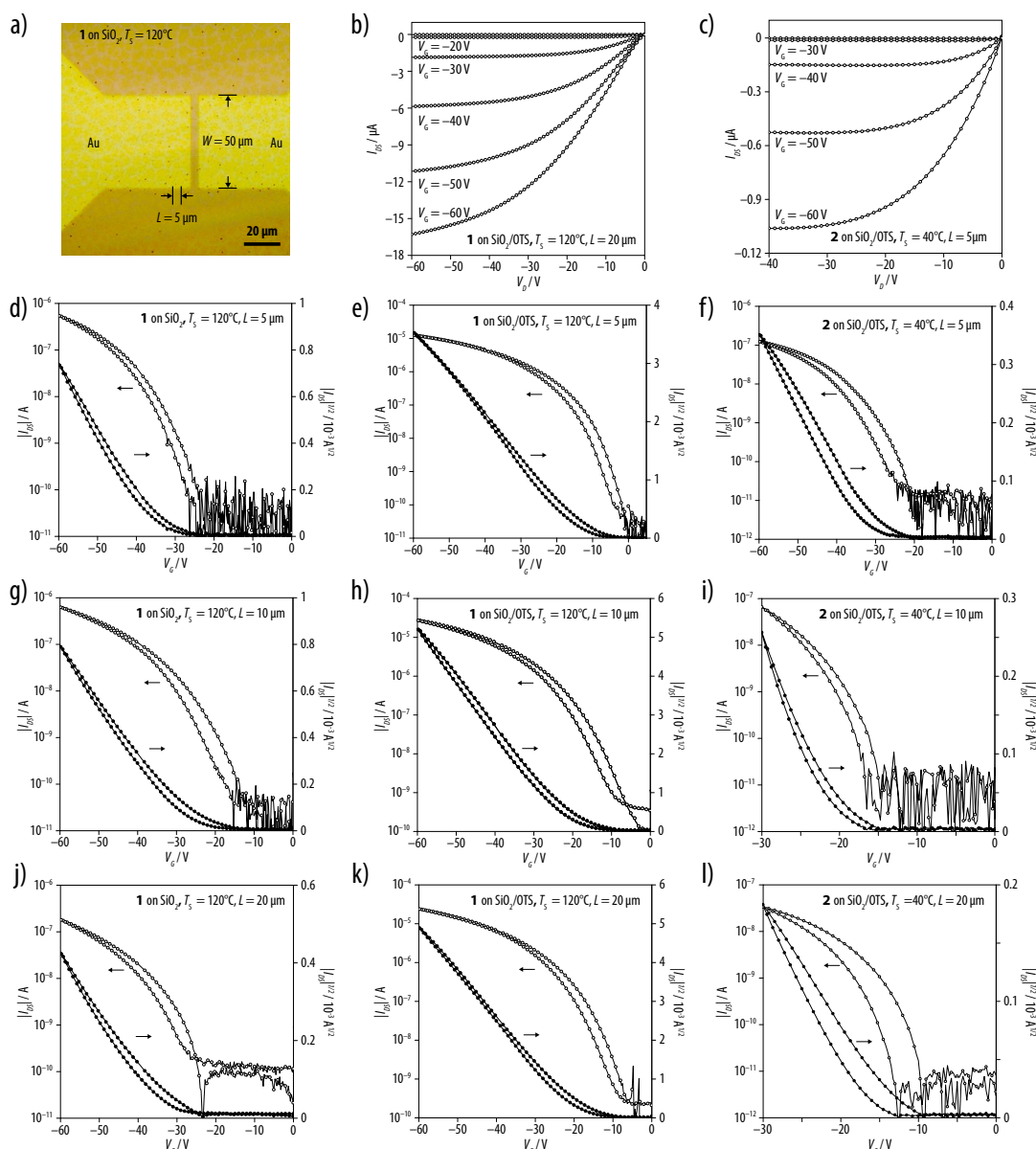


**Figure 3.8.** a) Optical micrograph of a bottom-gate top-contact OFET device with a channel length  $L = 5 \mu\text{m}$  and width  $W = 50 \mu\text{m}$  fabricated from a thin film of **1** on  $\text{SiO}_2$  at  $T_S \approx 120^\circ\text{C}$ . The bright yellow areas are the Au source and drain electrodes. Representative examples of b,c) a directly measured output and transfer curves (measured in the forward and reverse directions) for the bottom-gate top-contact transistors fabricated from films of **1** and **2** on a bare or an OTS-treated  $\text{SiO}_2$  substrate; devices with a channel length d-f)  $L = 5 \mu\text{m}$ , g-i)  $10 \mu\text{m}$ , and j-l)  $20 \mu\text{m}$ .

changes, we observed average field-effect mobilities that are almost one to two orders of magnitude higher than the reference non-hydrogen-bonded diacetate **2** and in the range of the best values previously reported for single-crystalline quaterthiophene specimens.<sup>293–295</sup> The moderate absolute mobility values reflect the fact that quaterthiophenes are comparably

poor organic semiconductors, and other factors such as surface treatment and processing are also very important for device performance.<sup>301</sup> Nevertheless, our results demonstrate that hydrogen bonding is not only compatible with charge transport in p-type organic semiconductors but reinforces the structural elements required for good  $\pi$ -overlap. Hence, the use of amide hydrogen-bonded substituents may therefore provide a general means of optimizing the performance of organic semiconductor thin films and the performance of devices based on such materials.

# **Engineering Polymers from Bithiophene-Containing Polyamides**



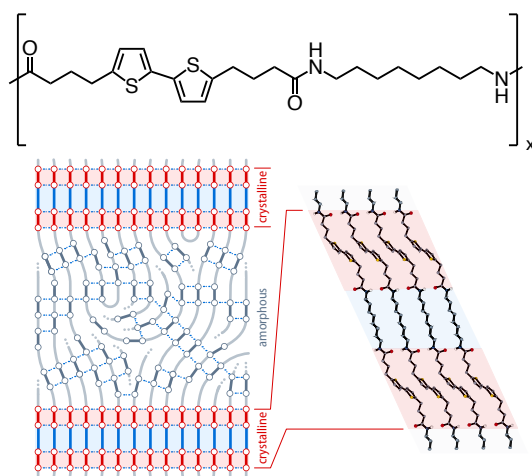
---

The results presented in this chapter have been published in *Journal of Materials Chemistry C*. Özen, B.; Candau, N.; Temiz, C.; Grozema, F. C.; Tirani, F. F.; Scopelliti, R.; Chenal, J.-M.; Plummer, C. J. G.; Frauenrath, H. "Engineering Polymers with Improved Charge Transport Properties from Bithiophene-Containing Polyamides". DOI: 10.1039/C9TC06544J.

B.Ö. performed the chemical synthesis, optical and thermomechanical characterization, as well as OFET fabrication and characterization. WAXD and SAXS measurements were carried out by N.C., with the assistance of J.M.C. Microwave conductivity measurements were conducted by C.T. and supervised by F.C.G. F.F.T. and R.S. did the X-ray structure analysis. C.J.G.P. contributed WAXD simulation, AFM imaging (together with B.Ö), as well as electron diffraction.

## 4 Engineering Polymers from Bithiophene-Containing Polyamides

Polymer semiconductors show unique combinations of mechanical and optoelectronic properties that strongly depend on their microstructure and morphology. Here, we have used a model  $\pi$ -conjugated bithiophene repeat unit to incorporate optoelectronic functionality into an aliphatic polyamide backbone by solution-phase polycondensation. Intermolecular hydrogen bonding between the amide groups ensured stable short-range order in the form of lamellar crystalline domains in the resulting semiaromatic polyamides, which could be processed from the melt and exhibited structural and thermomechanical characteristics comparable with those of existing engineering polyamides. At the same time, however, pulse-radiolysis time-resolved microwave conductivity (PR-TRMC) measurements indicated charge carrier mobilities that were an order of magnitude greater than previously observed in bithiophene based materials. Our results hence provide a convincing demonstration of the potential of amide hydrogen bonding interactions for obtaining unique combinations of mechanical and optoelectronic properties in thermoplastic polymers.



## 4.1 Introduction

Polymer semiconductors are an important class of materials with charge transport behavior similar to conventional semiconductors, but which are inherently viscoelastic owing to their ability to form continuous elastic networks with a locally dissipative response, depending on the time scale of the measurement.<sup>8</sup> They may therefore show greatly enhanced strength and toughness compared with low molecular weight organic semiconductors.<sup>302</sup> However, they also show varying degrees of structural order, with important consequences for their macroscopic behavior. It is hence possible to tune the mechanical and optoelectronic properties of polymer semiconductors by controlling their structural order at different length scales.<sup>12,25,303</sup> This has led to a considerable effort over the last two decades to better understand the corresponding structure-property relationships, with the aim of designing and developing materials with increased charge carrier mobilities.<sup>6,304</sup> However, systematic investigations of the mechanical properties of polymer semiconductors are scarce and have largely focused on stretchable materials for wearable electronic devices, with little emphasis to date on high performance engineering materials with useful electronic properties.<sup>305</sup>

Polymer semiconductors are typically semicrystalline, comprising amorphous regions and well-ordered crystalline domains characterized by two-dimensional lamellar stacks with a  $\pi$ -conjugated backbone, separated by layers of aliphatic side chains, as in the case of the prototypical regioregular poly(3-hexylthiophene-2,5-diyl) (P3HT).<sup>64,306</sup> The resulting morphology is complex, and understanding charge transport in such systems has consequently remained a challenge. However, recent studies have shown that efficient intermolecular charge transport may be achieved in polymers with high degrees of short-range order but no significant long range order, provided that aligned conjugated chain backbones form continuous paths between the locally ordered domains.<sup>12,14</sup>

Well-defined short-range order but limited long-range order are also characteristic features of many polyamides, which may exhibit lamellar crystalline domains with thicknesses of as little as 2 nm in the chain direction, corresponding to fewer than two repeat units, depending on their chemical structure.<sup>199,204</sup> These materials are highly sought after for engineering applications owing to their excellent specific mechanical strength, stiffness, and heat resistance, particularly when hydrogen bonding between the amide groups is combined with a partly or fully aromatic chain backbone.<sup>206,307</sup> We have recently used transamidation during high-temperature melt compounding to introduce aliphatic substitutional defects into a high-performance semiaromatic copolyamide, with the aim of generating disorder in the crystalline lamellae while maintaining the degree of crystallinity and promoting strain-induced ordering in the amorphous regions, providing materials with improved toughness without compromising strength and stiffness.<sup>168,199</sup> By contrast, the use of amide chemistry to control order and disorder at the nanoscale has seldom been investigated from the standpoint of organic electronics. Muguruma and coworkers prepared thin films from polyamides and polyurethanes containing quaterthiophene segments by co-deposition of appropriate difunctional monomers, but they did not provide details of the resulting structures nor the



mechanical or electronic properties.<sup>308,309</sup> To the best of our knowledge, no other studies of the properties of polyamides containing organic semiconducting segments have so far been published. The effects of hydrogen bonding on the electronic properties of small molecules and polymers have nevertheless been extensively investigated both experimentally and through numerical modeling. It was originally supposed that hydrogen bonding might be detrimental to charge transport in organic semiconductors.<sup>282</sup> However, the subsequent emergence of small molecule and polymer semiconductors containing hydrogen bonds has shown this not to be the case. For instance, Głowacki et al. reported field-effect mobilities of up to  $1.5 \text{ cm}^2 \text{ V}^{-1} \text{ s}^{-1}$  in certain hydrogen-bonded heteroanalogues of pentacene and tetracene, and enhanced device lifetimes compared with those of their non-hydrogen bonded acene analogues.<sup>122</sup> Similarly, Würthner et al. found hydrogen-bonded octachloroperylene bisimide to be an efficient n-type semiconductor with field-effect mobilities of up to  $0.9 \text{ cm}^2 \text{ V}^{-1} \text{ s}^{-1}$ , and to show useful device lifetimes even under ambient conditions.<sup>120</sup> Moreover, recent computational studies of hydrogen-bonded n-type or p-type organic semiconductors have provided corroborating evidence of a beneficial effect of hydrogen bonding for electronic properties.<sup>290,310</sup> It follows that polyamide-based semiconductors may provide a means of combining outstanding mechanical performance with improved charge transport in a compositionally heterogeneous material, particularly if their local order can be tailored through a suitable choice of the molecular architecture and disposition of the functional groups.

Here, we demonstrate that hydrogen bonding associated with amide groups is indeed effective as a means of stabilizing the local packing of  $\pi$ -conjugated segments in a polymer. To this end, we have focused on the use of a bithiophene core as a model repeat unit to provide optoelectronic functionality. Different polyamides were obtained by solution-phase polycondensation of a bithiophene dicarboxylic acid monomer with a range of aliphatic diamine monomers under Yamazaki-Higashi conditions. These materials were shown from extensive structural and thermomechanical analyses to reproduce many of the characteristics of typical engineering materials obtained from semiaromatic polyamides. At the same time, certain formulations showed significant charge carrier mobility, suggesting this to be a promising first step towards a functioning semiconducting engineering thermoplastic.

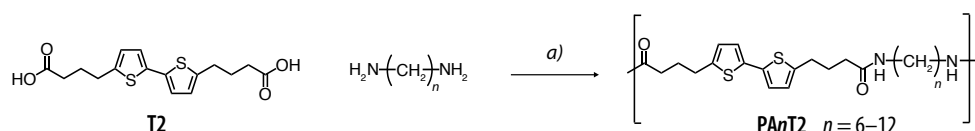
## 4.2 Results and Discussion

### 4.2.1 Synthesis of Bithiophene-Containing Semiaromatic Polyamides

We prepared a series of polyamides **PA $n$ T2** by solution-phase polycondensation of bithiophene dibutyric acid **T2** with different aliphatic diamines (with  $n$  carbon atoms) under standard Yamazaki-Higashi conditions,<sup>150–152</sup> that is, using triphenylphosphite (TPP) and LiCl in a mixture of anhydrous NMP and pyridine (Scheme 4.1, Table 4.1). Successful conversion was proven by 1D and 2D NMR as well as solid-state infrared (IR) spectroscopy (Figure 4.1, Figure 4.3*a,b*). Gel permeation chromatography (GPC) in 1,1,1,3,3,3-hexafluoro-2-propanol (HFIP) indicated number average molar masses ( $M_n$ ) on the order of 8'600–13'000 g/mol and

## Chapter 4. Engineering Polymers from Bithiophene-Containing Polyamides

dispersities ( $\bar{D}$ ) of 1.5–2.0 (Table 4.1). The polymers were soluble in HFIP at room temperature and in polar solvents such as hexamethylphosphoramide (HMPA), *m*-cresol, dimethylacetamide upon heating, but insoluble in dimethyl sulfoxide (DMSO), dimethylformamide (DMF), *N*-methyl-2-pyrrolidone (NMP), 1,2-dichlorobenzene, glacial acetic acid, xylenes, cyclohexanone, or chlorobenzene even at elevated temperatures.



**Scheme 4.1.** Synthesis of semiaromatic polyamides **PAnT2** by solution-phase polycondensation using Yamazaki-Higashi conditions. *Reagents and conditions:* a) triphenylphosphite (TPP), LiCl, NMP/pyridine (4:1), 120 °C, 4 h, 86–91%.

**Table 4.1:** Yields, molecular weights ( $M_n$ ,  $M_w$ ), and dispersities of ( $\bar{D}$ ) obtained from gel permeation chromatography of the bithiophene-containing polyamides **PAnT2**.

<b>PAnT2</b>	Amount [g]	Yield [%]	$M_n$ [g/mol]	$M_w$ [g/mol]	$\bar{D}$
<b>PA6T2</b>	1.04	90	13'500	20'100	1.5
<b>PA7T2</b>	0.27	88	12'500	20'100	1.6
<b>PA8T2</b>	0.81	90	12'700	19'400	1.5
<b>PA9T2</b>	0.39	88	10'600	20'800	2.0
<b>PA10T2</b>	0.38	91	10'300	20'300	2.0
<b>PA11T2</b>	0.30	86	8'600	16'100	1.9
<b>PA12T2</b>	0.33	89	10'700	20'600	1.9

Thermogravimetric analysis (TGA) measurements on **PAnT2** indicated a mass loss of 1–2% at about 250 °C, marking the onset of decomposition, and more substantial mass loss above 300 °C (Figure 4.2a). Differential scanning calorimetry (DSC) scans were hence performed in the temperature range below 250 °C to minimize thermal degradation effects. All polymers **PAnT2** were semicrystalline according to DSC heating scans at 10 °C/min but showed distinct melting and crystallization behavior depending on  $n$  (Figure 4.2b,c). The highest melting ( $T_m$ ) and crystallization temperatures ( $T_c$ ) of 210 and 171 °C, respectively, were observed for **PA6T2**. However, although the main  $T_m$  and  $T_c$  showed a global decrease with increasing  $n$ , there was also a clear odd-even effect, with odd  $n$  resulting in significantly lower transition temperatures than adjacent even  $n$  (Figure 4.2c), as reported previously for other polyamides, such as the series **PA $n$ 10** ( $n = 6–12$ ).<sup>311</sup> By contrast, the **PAnT2** glass transition temperature ( $T_g$ ) measured from the heating scans showed only a weak global decrease with increasing  $n$  with a correspondingly slight odd-even effect (Figure 4.2c).

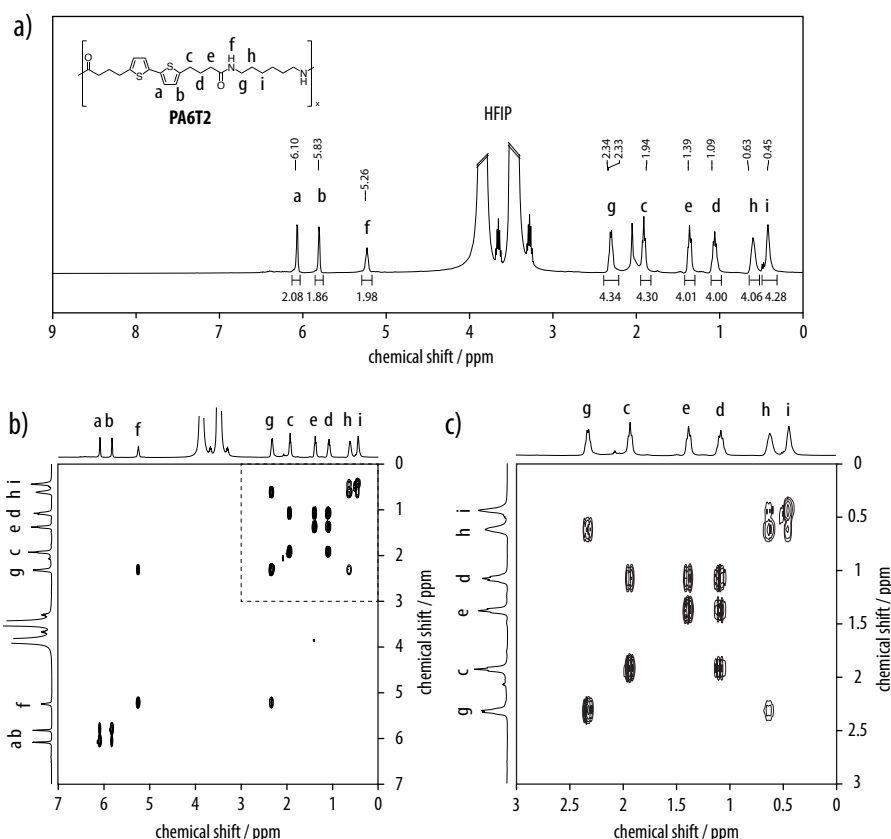


**Figure 4.1.** a) Representative  $^1\text{H}$  NMR spectra for **PA6T2** in non-deuterated HFIP with acetone- $d_6$  as the internal standard showed the expected proton signals, including those of the amide protons. The  $^1\text{H}$  NMR chemical shifts in the range of 5.8–6.1 ppm originated from the two chemically different thiophene protons, whereas the aliphatic protons of the diamine and the spacer gave rise to six distinct peaks below 2.5 ppm. b) From the cross-peaks observed in  $^1\text{H}$ - $^1\text{H}$  COSY experiments, the peaks at 2.33, 0.65, 0.45 ppm were attributed to the aliphatic protons of the diamine, while the peaks at 1.94, 1.39, 1.09 ppm corresponded to the protons of the propylene spacer. Distinct amide protons were also observed at around 5.2 ppm. c) Expanded view of the dashed area of the full spectrum in b).

The crystalline structures of polyamides **PA $n$ T2** are expected to follow the trends typical of other dyadic aliphatic polyamides. Optimum hydrogen bonding between parallel chains in the all-*trans* conformation is only possible in even-even polyamides that are therefore able to adopt the triclinic  $\alpha$ -type crystalline form, consisting of stacks of planar hydrogen-bonded sheets of fully extended chains.<sup>206,311,312</sup> By contrast, even-odd, odd-even and odd-odd polyamides typically form pseudo-hexagonal pleated sheet structures, collectively referred to as the  $\gamma$  phase, in which the plane of the amide groups tilts away from that of the methylene groups to allow formation of intersheet hydrogen bonds.<sup>161</sup> Because the **T2** repeat units are effectively “even” repeat units, the stability of crystalline **PA $n$ T2** as reflected by the melting point should be significantly higher for even  $n$  than for odd  $n$ , as observed here. **PA $n$ T2** with odd  $n$  also showed a single melting endotherm in DSC heating scans at 10  $^\circ\text{C}/\text{min}$ , whereas at least two endotherms were observed for **PA $n$ T2** with even  $n$  (Figure 4.2b). The separation of

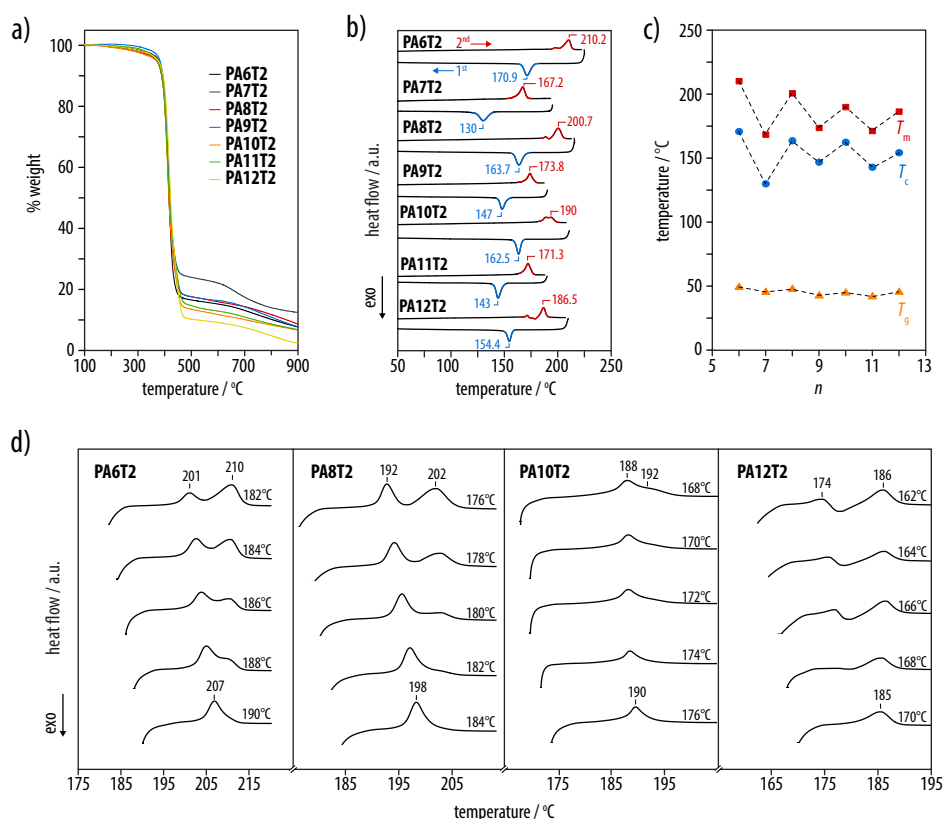


**Figure 4.2.** a) Results from thermogravimetric analysis (TGA) scans of PA<sub>n</sub>T<sub>2</sub> indicated a main decomposition temperature above 300 °C. b) Successive dynamic scanning calorimetry (DSC) cooling and heating scans from PA<sub>n</sub>T<sub>2</sub> (*n* = 6–12) at 10 °C/min. Melting of PA<sub>n</sub>T<sub>2</sub> with even *n* was characterized by multiple melting endotherms, whereas only a single endotherm was observed for odd *n*. c) The corresponding melting (*T<sub>m</sub>*) and crystallization temperatures (*T<sub>c</sub>*) showed a global decrease with increasing *n* but were reduced for odd *n* with respect to the values obtained for adjacent even *n*. d) DSC heating scans at 10 °C/min from PA<sub>n</sub>T<sub>2</sub> with even *n* after isothermal crystallization from the melt at the specified temperatures.

these endotherms was most marked after isothermal crystallization at comparatively low temperatures, suggesting the odd-even effect to influence the recrystallization or reorganization behavior of the crystalline phase (Figure 4.2d).<sup>313</sup>

**Table 4.2:** The exact positions and full-width at half maximums (FWHMs) of the characteristic IR vibrations, including the amide A, I, and II, and asymmetric / symmetric CH<sub>2</sub> peaks, for all the bithiophene-containing polyamides **PA $n$ T2** and the model compound **T2a**.

	PA6T2	PA7T2	PA8T2	PA9T2	PA10T2	PA11T2	PA12T2	T2a
<b>Amide A</b>	3301	3304	3300	3306	3305	3292	3292	3303
<b>FWHM Amide A</b>	71	83	78	81	71	86	81	30
<b>Amide I</b>	1634	1633	1634	1635	1635	1634	1634	1638
<b>FWHM Amide I</b>	28	31	31	26	27	27	29	19
<b>Amide II</b>	1533	1532	1532	1533	1534	1534	1535	1540
<b>FWHM Amide II</b>	39	41	40	38	37	45	46	30
<b>Arom. CH<sub>2</sub></b>	3065	3066	3065	3069	3068	3072	3067	3072
<b>Asym. CH<sub>2</sub></b>	2930	2928	2925	2922	2922	2920	2920	2950
<b>FWHM Asym. CH<sub>2</sub></b>	39	41	38	36	33	32	32	–
<b>Sym. CH<sub>2</sub></b>	2856	2854	2852	2852	2850	2850	2850	2870
<b>FWHM Sym. CH<sub>2</sub></b>	25	23	21	19	17	18	17	–

## 4.2.2 Structural Characterization

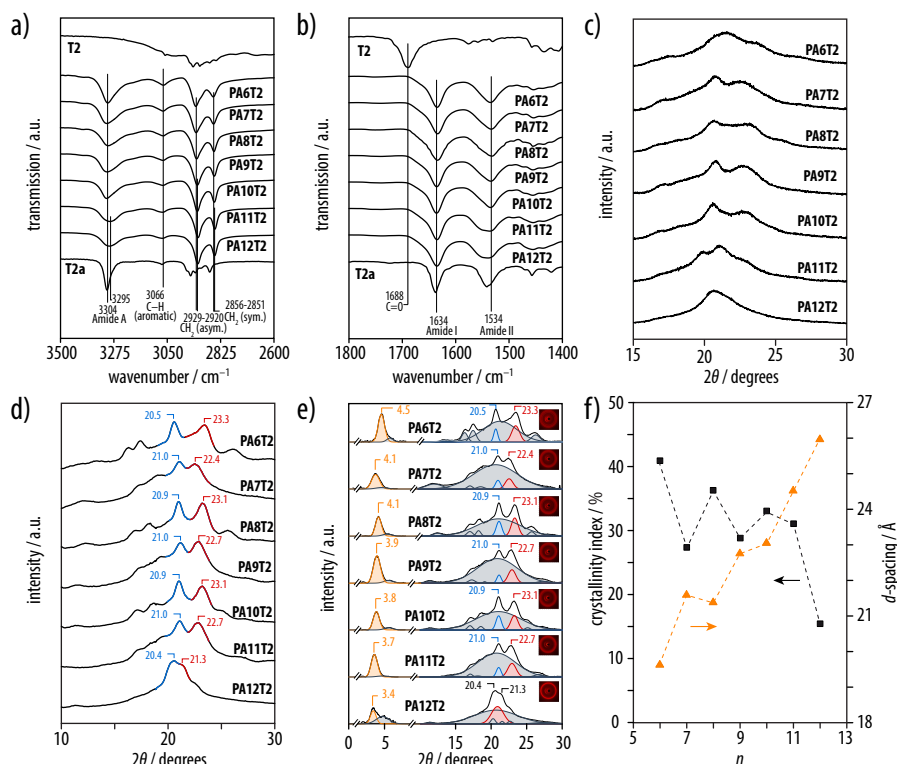


**Figure 4.3.** *a, b*) Solid-state IR spectra of the bithiophene dibutyric acid **T2**, model compound **T2a** and the resulting polyamides **PAnT2**. After polycondensation, the C=O stretching vibration of the free carboxylic acid was replaced by the amide A, I, and II bands of the amide functions. *c*) Wide-angle X-Ray diffraction (WAXD) patterns from the as-synthesized (powder) and *d*) isothermally crystallized (bulk) specimens recorded at room temperature in reflection and transmission, respectively. *e*) Deconvoluted WAXD pattern of **PAnT2** allowed roughly to estimate degree of crystallinity by distinguishing the Bragg peaks from the amorphous halo. The inset showed the 2D WAXD pattern of the polyamides, suggesting absence of the preferential orientation of the crystallites. *f*) Degree of crystallinity for **PAnT2** estimated from deconvolution of the WAXD profiles. Spacings corresponding to the lowest angle Bragg reflections from the WAXD patterns of the melt-crystallized polyamides shown as a function of *n*.

Solid-state IR spectra of the polyamides **PAnT2** (Figure 4.3*a, b*) with *n* = 6–10 showed that the broad absorption at 2700–3300 cm<sup>−1</sup> and the band at 1688 cm<sup>−1</sup> associated with the O–H and C=O stretching vibrations of the free carboxylic acid group of the **T2** monomer to be replaced by the characteristic amide A (3304 cm<sup>−1</sup>, FWHM 82 cm<sup>−1</sup>, N–H stretching), amide I (1634 cm<sup>−1</sup>, FWHM 32 cm<sup>−1</sup>, C=O stretching), and amide II (1534 cm<sup>−1</sup>, C=O bending), consistent with typical IR spectral features in semicrystalline polyamides (Table 4.2).<sup>100</sup> Because the same N–H and C=O stretching vibrations were observed in specimens of the bithiophene dipropylamide model compound **T2a**, whose of which the crystal structure was known (Figure 4.4), one may infer from the IR spectra that the polymers **PAnT2** comprised polymer chains organized into hydrogen-bonded sheets. The same principal absorptions were also observed for the polyamides **PAnT2** (Figure 4.3*a, b*) with *n* = 11–12, but their amide A and amide II absorptions were significantly broadened, indicating a lower degree of order.

WAXD patterns confirmed the presence of an ordered phase in the as-synthesized **PA $n$ T2** (Figure 4.3c), and sharp well-defined Bragg peaks were visible after isothermal crystallization at a temperature 10 °C higher than the temperature of the crystallization peak in the cooling scans (Figure 4.3d). Consistent with the DSC results and IR spectra, the degree of crystallinity estimated from the WAXD patterns (Figure 4.3e,f) showed a global decrease with  $n$ , and again some suggestion of an odd-even effect at low  $n$ , although it fell off sharply for  $n = 12$ .

For  $n < 12$ , strong, well-separated reflections were observed at  $2\theta = 22.4\text{--}23.3^\circ$  and  $2\theta = 20.4\text{--}21^\circ$ , corresponding to  $d$ -spacings in the range 3.80–3.97 and 4.23–4.35 Å, respectively, while for  $n = 12$ , the main peaks overlapped. Prominent low-angle peaks corresponding to  $d$ -spacings in the range of 19–26 Å were also present (Figure 4.3e,f). The  $d$ -spacings corresponding to the low angle WAXD peaks for **PA $n$ T2** with odd  $n$  were greater than expected from interpolation of the data for even  $n$  (Figure 4.3f), suggesting the  $c$ -axis of the unit cell to lie closer to the basal plane normal for odd  $n$ . As discussed above, if  $n$  is odd, optimum hydrogen bonding is no longer possible with the aliphatic sub-chains in the all-*trans* conformation. Hence, by analogy with aliphatic polyamides with odd  $n$ , such as PA56, consecutive amide groups along the chain may tilt in opposite directions away from the plane of the methyl groups to form hydrogen bonds, leading to more compact conformations and a reduction in the  $c$ -repeat distance. The required tilt of the amide groups is nevertheless small, resulting in monoclinic packing and a centered unit cell in which the overall chain conformations remain close to the all-*trans* conformations characteristic of the  $\alpha$  phase.<sup>164</sup>

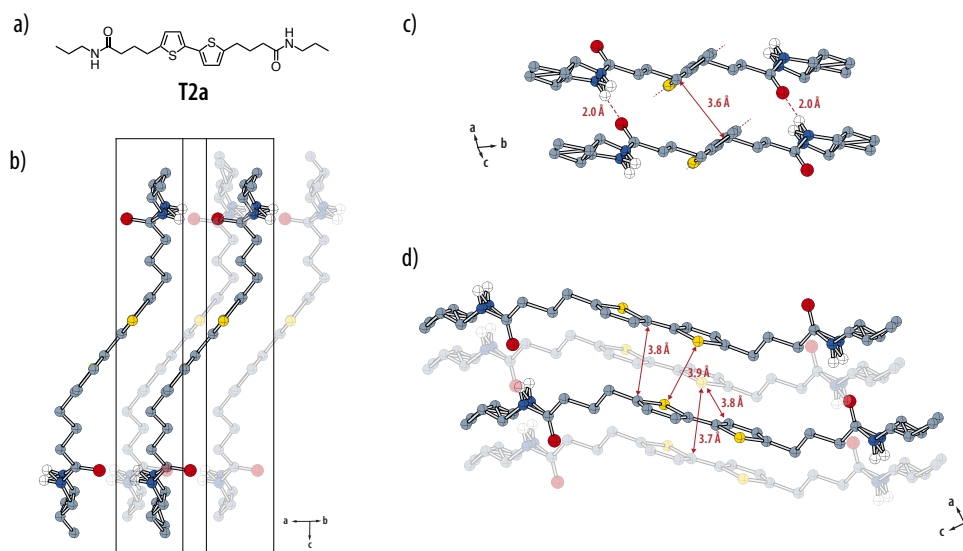


**Figure 4.4.** a) Molecular structure of the bithiophene diamide model compound **T2a**. b) Ball-and-stick representations of the single-crystal X-ray structure of **T2a** viewed along the  $ab$ -plane, showing the presence of both N–H $\cdots$ O=C hydrogen bonds and the parallel-displaced  $\pi$ -stacked arrangement of the bithiophene units with c) a hydrogen bonding distance (H $\cdots$ O) of 2.0 Å and a bithiophene interlayer distance of 3.6 Å. d) C $\cdots$ S and C $\cdots$ C and S $\cdots$ S close contacts between parallel-displaced pairs of bithiophenes (all hydrogen atoms except those that participate in hydrogen bonding have been omitted for clarity).

To model the molecular arrangement of the polyamides **PA $n$ T2**, and specifically the packing behavior of the bithiophene unit, we used the single-crystal X-ray structure of model compound **T2a** as a starting point (Chapter 2), because its solid-state IR spectra showed very similar features (Figure 4.3*a,b*). **T2a** crystallized in the triclinic space group  $P\bar{1}$  with the lattice parameters  $a = 4.9848(4)$  Å,  $b = 5.6250(5)$  Å,  $c = 21.347(3)$  Å,  $\alpha = 90.584(9)^\circ$ ,  $\beta = 90.140(8)^\circ$ , and  $\gamma = 107.702(8)^\circ$  and a single molecule in the unit cell (Figure 4.4). The amide functions formed two infinite arrays of almost linear intermolecular N–H...O=C hydrogen bonds (N–H...O  $\angle$  162°, H...O  $d$  = 2.02 Å) with opposite orientation along the crystallographic  $a$ -axis. Simultaneously, the bithiophenes adopted a parallel-displaced  $\pi$ -stacked arrangement with an interlayer spacing of 3.6 Å, a tilt angle of 40.5° relative to the crystallographic  $c$ -direction, and various intermolecular C...C, C...S, and S...S close contacts (Figure 4.4*c,d*).

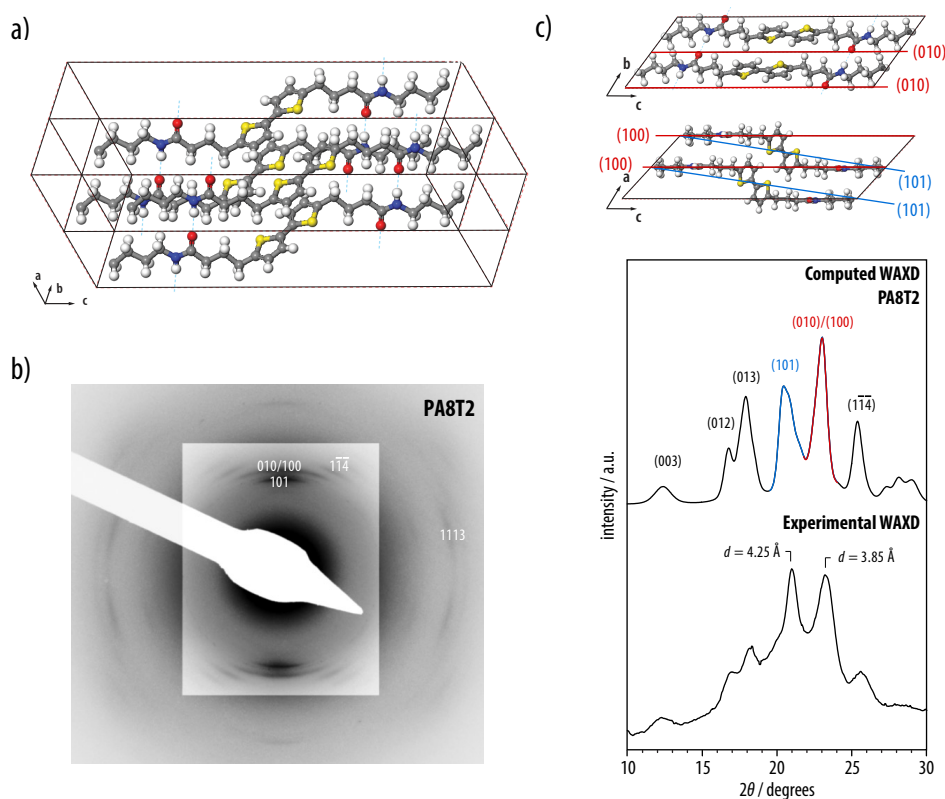


**Figure 4.5.** *a*) Model structure for **PA $n$ T2** with even  $n$ , shown here for  $n = 8$ , assuming a triclinic  $P\bar{1}$  space group with the  $c$ -axis parallel to the axes of the main methyl sub-chain. *b*) Selected area electron diffraction (SAED) pattern from an oriented film of **PA8T2**. *c*) Comparison of the experimental WAXD data for a melt crystallized film of **PA8T2** with a simulated WAXD powder pattern from the structure in *a*) with lattice parameters  $a = 5.10$  Å,  $b = 5.68$  Å,  $c = 30.61$  Å,  $\alpha = 60.40^\circ$ ,  $\beta = 71.24^\circ$ ,  $\gamma = 109.68^\circ$  derived from the SAED pattern.

Trial crystal structures for **PA $n$ T2** with even  $n$  (Figure 4.5*a*) were hence generated assuming a triclinic unit cell, packing and conformations analogous to those observed for **T2a**, and an all-*trans* conformation for the aliphatic segments, consistent with the solid-state IR spectra. For convenience, the  $c$ -axis of the unit cell was chosen to be parallel to the axis of the aliphatic



sub-chains, so that changes in  $n$  could be accommodated by adjusting  $c$ . In the case of  $n = 8$ , the unit cell parameters were adjusted to fit the peak positions from selected-area electron diffraction (SAED) patterns from oriented friction deposited films (Figure 4.5b), in which the higher order peaks were well resolved and the layer line spacing provided an estimate of the  $c$ -repeat distance along the orientation axis. The energy was then minimized, resulting in a hydrogen bond distance (H...O) of 2.0 Å, as observed for the model compound **T2a**. Simulated WAXD powder patterns based on this structure, with crystal dimensions of 150 Å in the  $a$ - and  $b$ -directions and 50 Å in the  $c$ -direction, were in satisfactory agreement with the experimental WAXD data from **PA8T2** isothermally crystallized from the melt at 175 °C (Figure 4.5c). The peak at  $2\theta$  of around 23 ° in **PA6T2**, **PA8T2**, and **PA10T2** was hence identified with scattering from the (100) and (010) planes, whereas the peak at  $2\theta$  of 20.5 to 20.9 ° was dominated by contributions from the (101) planes. Hence, in contrast to the  $\alpha$  phase of PA66<sup>162</sup> and its homologues, there was little scattering from the planes perpendicular to the hydrogen bond direction, because the alignment of the sheets formed locally by the hydrogen-bonded aliphatic chains was interrupted by the bithiophene units.

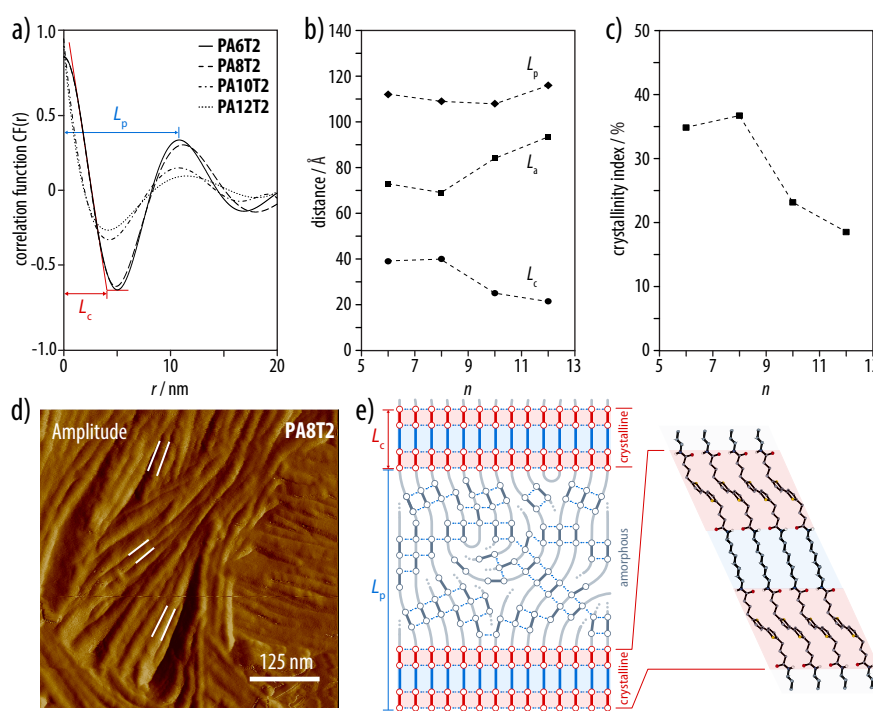


**Figure 4.6.** *a)* Estimation of the lamellar thickness ( $L_c$ ) and lamellar long period ( $L_p$ ) from the small-angle X-Ray scattering (SAXS) correlation function for even  $n$ , assuming a two-phase model. *b)* Estimated  $L_c$  and  $L_p$  for the even polyamides along with  $L_a$ , the thickness of the corresponding amorphous layer, taken to be equal to  $L_p - L_c$ . *c)* Degree of crystallinity for **PA $n$ T2** estimated from the SAXS measurements (even  $n$  only). *d)* Atomic force microscopy (AFM) intermittent contact mode height image the local lamellar structure in a film of **PA8T2** isothermally crystallized from the melt at 176 °C. The white markers are separated by 10 nm. *e)* Schematic representation of the lamellar morphology of **PA8T2**.

SAXS data for **PA $n$ T2** with even  $n$  crystallized under the same conditions as for the WAXD measurements suggested lamellar thicknesses,  $L_c$ , that decreased from about 40 Å in **PA6T2** and **PA8T2** to 22 Å in **PA10T2** and **PA12T2**, assuming a two-phase lamellar structure (Figure 4.6*a, b*). Hence, the  $L_c$  for **PA6T2** and **PA8T2** were about  $2.0 d_{001}$  and  $1.9 d_{001}$ , respectively, while for **PA10T2** and **PA12T2**,  $L_c$  and  $d_{001}$  were roughly equal. For comparison, lamellar thicknesses of as little as 20 Å have been reported for rapidly cooled aliphatic and semiaromatic polyamides.<sup>204</sup> The lamellar spacing,  $L_p$ , determined by SAXS remained close to 110 Å for all polyamides **PA $n$ T2**. The corresponding SAXS degree of crystallinity was therefore about 35 vol% for  $n = 6$  and 8 but decreased to about 20 vol% at higher  $n$  (Figure 4.6*c*), consistent with the values obtained from WAXD (Figure 4.3*f*). This compares with typical values of 30 vol% for semiaromatic polyamides<sup>314,315</sup> with comparable aliphatic sequence lengths.

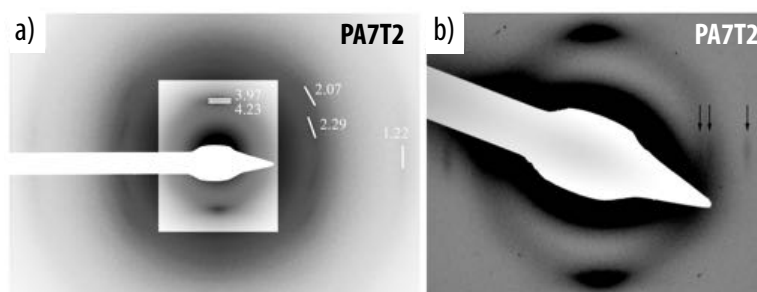


**Figure 4.7.** Selected area electron diffraction (SAED) from an oriented film of **PA7T2** prepared at about 140 °C. Approximate  $d$ -spacings corresponding to the visible reflections are also indicated. The layer lines corresponded to the axial spacing of the methyl groups, and hence did not provide a direct indication of the unit cell dimensions. However, *b*) oriented films of **PA7T2** prepared at about 130 °C and in which the equatorial reflections were less well-resolved, showed additional meridional reflections. The spacings of these reflections suggested a repeat distance in the orientation direction of approximately 55 Å, implying the spacing given in Figure 4.3*f* for  $n = 7$  to correspond to the (002) planes in the oriented films, and a putative (100) spacing of about 43 Å, which was significantly greater than the lamellar thicknesses observed for even  $n$ . It was hence tentatively concluded based on these results that specimens of **PA $n$ T2** melt-crystallized under quiescent conditions showed more limited three-dimensional order when  $n$  was odd.

Images obtained by AFM of films of **PA8T2** on glass substrates melt-crystallized at 176 °C in air indicated a two-dimensional banded spherulitic texture and a minimum lamellar spacing, corresponding to edge-on lamellae, of 100–140 Å in thickness (Figure 4.6*d*), in good agreement with the SAXS data for  $L_p$ . As the rigid bithiophene unit cannot easily accommodate chain folding, we conclude that the crystalline lamellar structure in melt-crystallized **PA $n$ T2** (with even  $n$  from 6 to 10) consisted of two layers of parallel-displaced,  $\pi$ -stacked bithiophenes separated by a layer of inclined hydrogen-bonded aliphatic chains in the all-*trans* conformation (Figure 4.6*e*). In the case of **PA $n$ T2** with odd  $n$ , when melt-crystallized under quiescent conditions, the corresponding SAED results indicated more limited three-dimensional order (Figure 4.7), in agreement with the observations from DSC and WAXD.

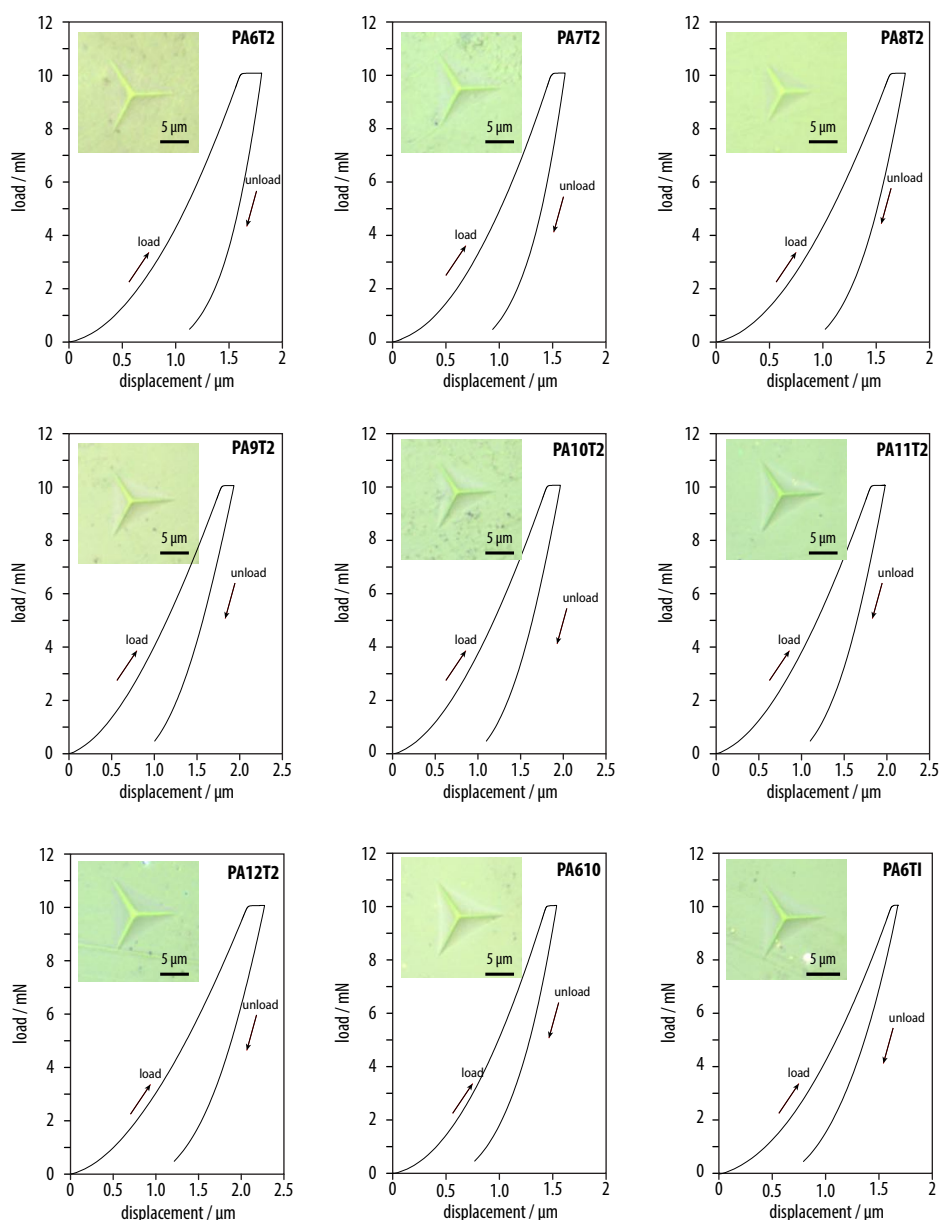


**Figure 4.8.** Typical load-displacement curves with the residual imprint (inset) from nanoindentation measurements on the **PA $n$ T2**, industrial-grade PA6I0, and PA6TI specimens.

### 4.2.3 Mechanical Characterization

Nanoindentation and dynamic mechanical analysis (DMA) measurements were used to evaluate the mechanical properties of polyamide **PA $n$ T2** films compression molded at their nominal melting temperature and subsequently cooled at 10 °C/min (Figure 4.8). A peak at about 210 MPa was observed in the mean instrumented hardness from the nanoindentation measurements,  $H_{IT}$ , for  $n = 7$ , and then a gradual decrease with increasing  $n$  (Figure 4.9a), consistent with the evolution of the melting enthalpy of the films measured by DSC (Figure 4.9b).

The absolute values of  $H_{IT}$  were hence similar to the value of 176 MPa obtained from the aliphatic polyamide PA610 ( $H_{IT} = 176$  MPa), but lower than the value of 404 MPa obtained from the industrial-grade semiaromatic polyamide poly(hexamethylene terephthalamide-co-isophthalamide) (PA6TI). Elastic moduli,  $E_{IT}$ , close to 2.9 GPa were obtained for  $n = 6$  and 7 from the unloading curves (Figure 4.8) according to the method of Oliver and Pharr, as compared to 3.8 MPa for PA6TI.  $E_{IT}$  then decreased gradually from 2.5 to 1.5 GPa for  $n$  between 8 and 9, that is, to below the value of around 1.8 GPa observed for PA610 (Figure 4.9c).

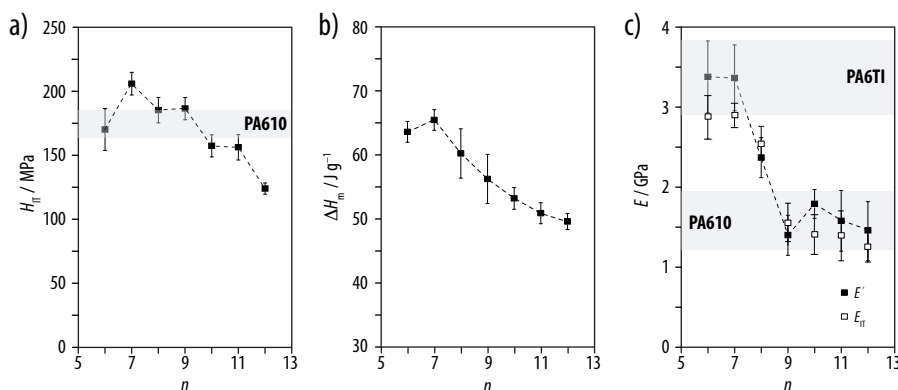


**Figure 4.9.** a) Instrumented hardness ( $H_{IT}$ ) and b) Melting enthalpy of the specimens hot-pressed at their melting maxima. c) elastic modulus from the indentation measurements,  $E_{IT}$ , and from dynamic mechanical analysis,  $E'$ , of **PA6T2** as a function of  $n$ . For comparison, the moduli of industrial-grade PA610 and PA6TI were shown as a broad range, representing the results obtained from nanoindentation and DMA.

The average tensile storage moduli,  $E'$ , determined for comparison by DMA measurements on the same **PA6T2** films showed a similar trend, decreasing gradually from 3.4 to 1.5 GPa for  $n$  between 6 and 12 (Figure 4.9c), consistent with a reported decrease in the tensile modulus from 2.1 GPa to 1.7 GPa as  $n$  is increased from 6 to 10 in PA $n$ 10.<sup>316</sup> The bithiophene-containing polyamides were hence confirmed to show similar effective strengths and stiffnesses to representative industrial-grade engineering polymers such as PA610 and PA6TI.<sup>137</sup>

### 4.2.4 Optoelectronic Properties

UV-vis absorption spectroscopy of **PA6T2** and the model compound **T2a** in HFIP showed an absorption band with a maximum at 317 nm and a shoulder at around 340 nm (Figure 4.10a, solid lines). Thin films of **PA6T2** and the model compound **T2a** spin-coated onto quartz substrates exhibited similar absorptions with slightly red-shifted absorption maxima at 323 and 321 nm, respectively, and shoulders at around 360 nm (Figure 4.10a, dashed lines). **PA6T2** also underwent photo-bleaching in HFIP when irradiated at 317 nm (Figure 4.10b), indicating that the photo-excited state is prone irreversible electron transfer and oxidation reactions.

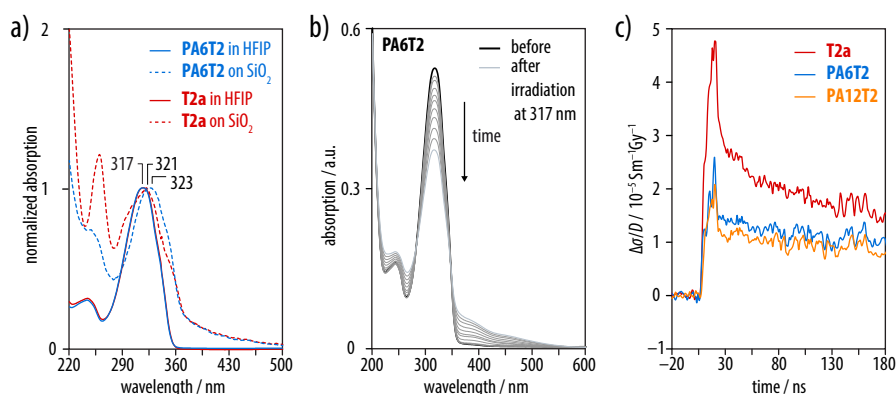


**Figure 4.10.** *a*) Normalized UV-vis absorption spectra of **PA6T2** compared with those of the model compound **T2a** from solutions (solid lines) and spin-coated thin films on a quartz substrate (dashed lines). *b*) Absorption spectra of the **PA6T2** before and after irradiation for several minutes at 317 nm, showing the photo-bleaching effect. *c*) Transient change in conductivity of **T2a**, **PA6T2** and **PA12T2** on irradiation with a 10 ns electron pulse normalized by the irradiation dose,  $D$ .

Pulse-radiolysis time-resolved microwave conductivity (PR-TRMC) was used as an initial probe of the charge transport properties. PR-TRMC measurements on specimens of the polyamides **PA $n$ T2** for  $n = 6$  and 12, as well as the model compound **T2a** at room temperature in the range of 28 to 38 GHz with pulse widths of 2–20 ns (Figure 4.10c) resulted in mobilities,  $\mu$ , of  $0.044 \text{ cm}^2 \text{ V}^{-1} \text{ s}^{-1}$  (**T2a**),  $0.017 \text{ cm}^2 \text{ V}^{-1} \text{ s}^{-1}$  (**PA6T2**) and  $0.018 \text{ cm}^2 \text{ V}^{-1} \text{ s}^{-1}$  (**PA12T2**). These mobilities are around one order of magnitude higher than the highest values of  $0.005 \text{ cm}^2 \text{ V}^{-1} \text{ s}^{-1}$  reported for other bithiophene-based systems,<sup>287</sup> and close to those in crystalline quaterthiophene and sexithiophene-based systems.<sup>244,317–319</sup> This is considered to reflect the beneficial effect of hydrogen bonded substituents on the packing of  $\pi$ -conjugated systems and hence the charge transport properties of the materials (Chapter 3).

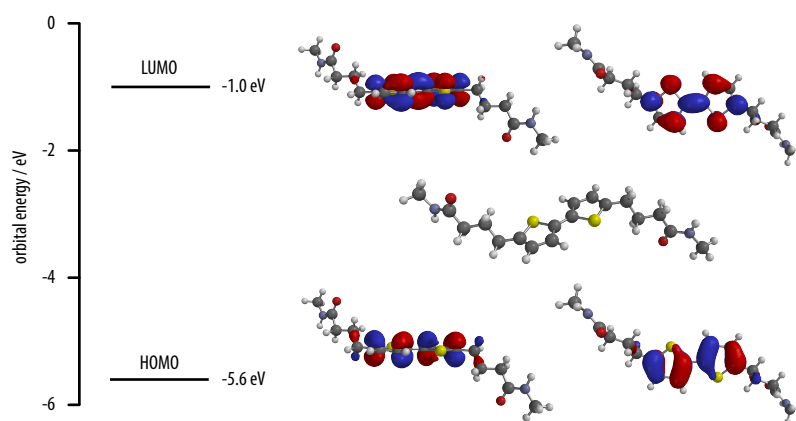


**Figure 4.11.** Orbital energy levels of 4,4'-(2,2'-bithiophene-5,5'-diyl)bis(*N*-methylbutanamide) were obtained by density functional theory (DFT) (B97-3/def2-SV(P)) calculations. The methyl diamide bithiophene was used as proxy for **PA $n$ T2** instead of model compound **T2a** to reduce the calculation time.

Despite the promising charge carrier mobilities, field-effect transistors in either top-contact or bottom-contact configuration showed no detectable currents. We attribute this observation to the large HOMO–LUMO gap (4.6 eV) and the irreversible electron transfer reactions of bithiophene systems owing to the high-lying LUMO level (–1 eV) (Figure 4.11). The energetic mismatch of the HOMO and LUMO levels with the gold source/drain electrodes may also render the charge carrier injection energetically unfavorable.

### 4.3 Conclusions

We prepared a series of melt-processable semicrystalline bithiophene-containing polyamides by solution-phase polycondensation under Yamazaki-Higashi conditions. The crystal structure of these polyamides was characterized by a close, parallel-displaced  $\pi$ -arrangement unlike many existing oligothiophenes but similar to that observed in the model compound bithiophene butanamide **T2a**. As a result, PR-TRMC measurements demonstrated charge carrier mobilities that were an order of magnitude greater than in their low molar mass analogues. The morphologies obtained on solidification from melt were similar to those of typical engineering semicrystalline polyamides, consisting of spherulitic agglomerates of interconnected stacked crystalline lamellae. It follows that the resulting hardnesses and elastic moduli were also similar to those of engineering semicrystalline polyamides. Bithiophene-containing polyamides may therefore represent an important step towards polyamide-based semiconductors suitable for application in which mechanical properties play an important role.

**Semiaromatic  
Polyamides Containing  
Perylene Bisimide  
Repeat Units**



---

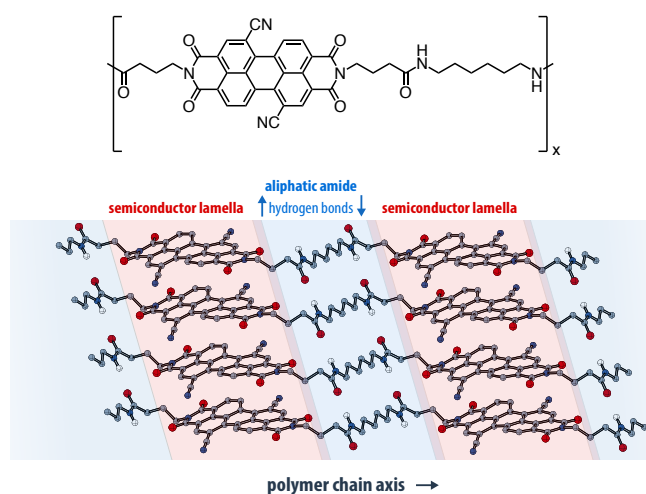
The results presented in this chapter are part of a manuscript in preparation. Özen, B.; Candau, N.; Temiz, C.; Grozema, F. C.; Stoclet, G. ; Plummer, C. J. G.; Frauenrath, H. "Semiaromatic Polyamides Containing Perylene Bisimide Repeat Units".

B.Ö. performed the chemical synthesis, optical and thermomechanical characterization, as well as OFET fabrication and characterization. WAXD (together with B.Ö) and SAXS measurements were carried out by N.C., with the assistance of G.S. Microwave conductivity measurements were conducted by C.T. and supervised by F.C.G. C.J.G.P. contributed WAXD simulation.



## 5 Semiaromatic Polyamides Containing Perylene Bisimide Repeat Units

The control of local order in polymer semiconductors using non-covalent interactions may be used to engineer materials with interesting combinations of mechanical and optoelectronic properties. To investigate the possibility of preparing n-type polymer semiconductors in which hydrogen bonding plays an important role in structural order and stability, we have used solution-phase polycondensation to incorporate dicyanoperylene bisimide repeat units into an aliphatic polyamide chain backbone. The morphology and thermomechanical characteristics of the resulting polyamides, in which the aliphatic spacer length was varied systematically, were comparable with those of existing semiaromatic engineering polyamides. At the same time, the charge carrier mobility as determined by pulse-radiolysis time-resolved microwave conductivity (PR-TRMC) measurements was found to be about  $0.01 \text{ cm}^2 \text{ V}^{-1} \text{ s}^{-1}$ , which is similar to that reported for low molecular weight perylene bisimides. Our results hence demonstrate that it is possible to use hydrogen bonding interactions as a means to introduce promising optoelectronic properties into high-performance engineering polymers.



## 5.1 Introduction

Semiaromatic polyamides, particularly the polyphthalamides, are high-performance engineering thermoplastics because they exhibit outstanding thermomechanical property profiles,<sup>206,320,321</sup> but remain compatible with conventional industrial melt processing routes such as extrusion and injection moulding, in contrast to fully aromatic polyamides (polyaramids).<sup>178,322,323</sup> Although the development of semiaromatic polyamides and copolyamides has strongly focused on structural applications,<sup>320,322,324</sup> they also often show similar morphological features to recent high-performance polymer semiconductors, namely thin lamellar crystals and significant residual local order in the amorphous regions.<sup>12,14,199,204</sup> Semiaromatic polyamides whose repeat units contain  $\pi$ -conjugated segments may hence provide a promising route to engineering materials with novel combinations of optoelectronic and thermomechanical properties.

The widespread recognition of the importance of the morphology of semiconducting polymers at different length scales for their optoelectronic and thermomechanical properties<sup>8,302</sup> has led to a concerted effort to better understand their structure and property relationships, with emphasis on controlling the balance between short-range order and overall disorder.<sup>325–327</sup> Modification of the chain backbone with non- $\pi$ -conjugated segments and side chain engineering, in particular, have played a significant role in improving both the mechanical properties of  $\pi$ -conjugated polymers and device performance, through their influence on local order and hence the electronic coupling between neighboring chains.<sup>28,328</sup> A promising approach in this respect is the use of hydrogen bonding motifs that promote specific non-covalent intermolecular interactions.<sup>51</sup> Hydrogen bonding has been widely used to promote self-assembly of  $\pi$ -conjugated compounds into one-dimensional nanostructures in solution,<sup>110,113,118,119,238–250</sup> and to tailor the packing of  $\pi$ -conjugated compounds in the solid-state.<sup>252</sup> At the same time, it is well known to be key to the unique thermomechanical properties of engineering polyamides.<sup>161</sup> The introduction of hydrogen-bonded side chains into semiconducting polymers has consequently gained considerable recent attention. For instance, the presence of amide groups in the side chains of  $\pi$ -conjugated polymers based on diketopyrrolopyrrole<sup>134,135</sup> or isoindigo<sup>329,330</sup> repeat units has been found both to increase the strength of aggregation and crystallinity, resulting in enhanced charge carrier mobility and photovoltaic performance compared with the corresponding polymers with non-hydrogen-bonded side chains, and to enhance energy dissipation during mechanical deformation.<sup>330,331</sup>

By contrast, incorporation of hydrogen-bonded segments as non-conjugated spacers into semiconducting polymers has so far received limited attention. Bao et al. introduced a non-conjugated unit containing an amide group into the backbone of a  $\pi$ -conjugated polymer.<sup>332</sup> They found that 10 mol% of this comonomer sufficed to alter the thin film morphology of the polymer network, leading to a reduction in elastic modulus and a moderate increase in the crack onset strain, but no significant changes in charge carrier properties. In another approach, the possibility of incorporating  $\pi$ -conjugated segments into a polyamide repeat

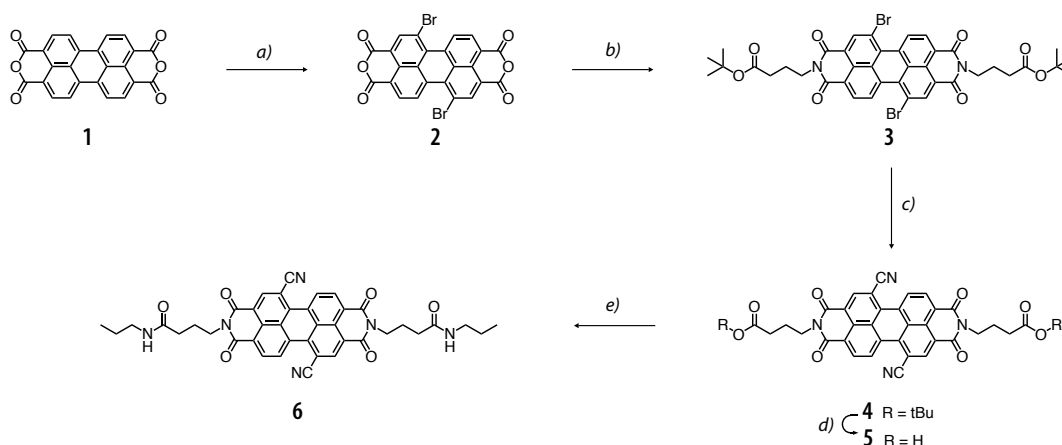
unit was investigated by Mugurama et al., who prepared semiaromatic polyamides with oligothiophene units but provided no details of either their morphology, or their mechanical and optoelectronic properties.<sup>308,309</sup> We recently reported semicrystalline semiaromatic polyamides with bithiophene units and demonstrated that such materials indeed combined the thermomechanical characteristics of typical semiaromatic engineering polyamides with significant charge carrier mobility.<sup>251</sup>

Here, we report the first example of polyamides containing electron deficient, n-type semiconducting dicyanoperylene bisimide repeat units. Four such polyamides with different aliphatic spacer lengths were found to show not only good thermal stability and shear moduli in the range 0.75–0.93 GPa, but also H-type coupling of the dicyanoperylene bisimide chromophores in the solid-state, and charge carrier mobilities of about  $0.01 \text{ cm}^2 \text{ V}^{-1} \text{ s}^{-1}$ . The dicyanoperylene bisimide-containing polyamides thus combined the thermomechanical properties of typical engineering polyamides with optoelectronic properties typical of organic and polymer semiconductors.

## 5.2 Results and Discussion

### 5.2.1 Synthesis of Perylene Bisimide-Containing Semiaromatic Polyamides

The synthesis of dicyanoperylene bisimide dibutyric acid **5** was performed in four steps starting from commercially available perylene bisanhydride (Scheme 5.1). Following a published procedure,<sup>333</sup> the bromination of perylene bisanhydride was carried out by electrophilic substitution with bromine, using iodine as a Lewis catalyst.



**Scheme 5.1.** Synthesis of the dicyanoperylene bisimide *N,N'*-dibutanoic acid **5** and the corresponding diamide model compound **6**. *Reagents and conditions:* a)  $\text{Br}_2$ , cat. amount of  $\text{I}_2$ , conc.  $\text{H}_2\text{SO}_4$  (96%), 85 °C, 3 d, 97% yield; b) 4-aminobutyric acid *tert*-butyl ester hydrochloride,  $\text{Zn}(\text{OAc})_2$ , quinoline, 100 °C, 16 h, 79% yield; c)  $\text{Zn}(\text{CN})_2$ ,  $\text{Pd}_2(\text{dba})_3$ , dppf, dioxane, 95 °C, 48 h, 40% yield; d)  $\text{CHCl}_3$ , TFA, reflux, 15 h, 96% yield; e) chlorendic hydroxylimide, DIC, propylamine, DMF/THF, 50 °C, 28 h, 84% yield.

The insolubility of the crude product prohibited further purification, resulting in a mixture of non-separable 1,7-dibromo, 1,6-dibromo, and 1,7,6-tribromoperylene bisimides **2** in a ratio of 75:17:8 in a yield of 97% (26 g) (Figure 5.1). The butyl spacer between the chromophore and ester functionality was introduced by subsequent imidization of the regioisomeric mixture with 4-aminobutyric acid *tert*-butyl ester hydrochloride to give di(*tert*-butyl ester) **3** after purification with column chromatography in a yield of 79% (15.5 g), as a mixture of the desired 1,7-dibromo and the 1,6-dibromo regioisomers in a ratio of 75:25, which also remained inseparable in the subsequent synthetic steps. The corresponding dicyanoperylene bisimide dibutanoate **4** was prepared by a Pd-catalyzed cyanation of compound **3** with  $\text{Zn}(\text{OAc})_2$ , 1,1'-bis(diphenylphosphino)-ferrocene (dppf) and tris(dibenzylideneacetone)-dipalladium(0) ( $\text{Pd}_2(\text{dba})_3$ ) in dry dioxane at 95 °C for 2 d. After suspension in EtOAc and filtration, purification by column chromatography gave compound **4** as a red solid powder in a yield of 40% (4.6 g). Subsequent deprotection of the *tert*-butyl esters with TFA gave dicyanoperylene bisimide dibutanoic acid **5** in almost quantitative yield (1.3 g).

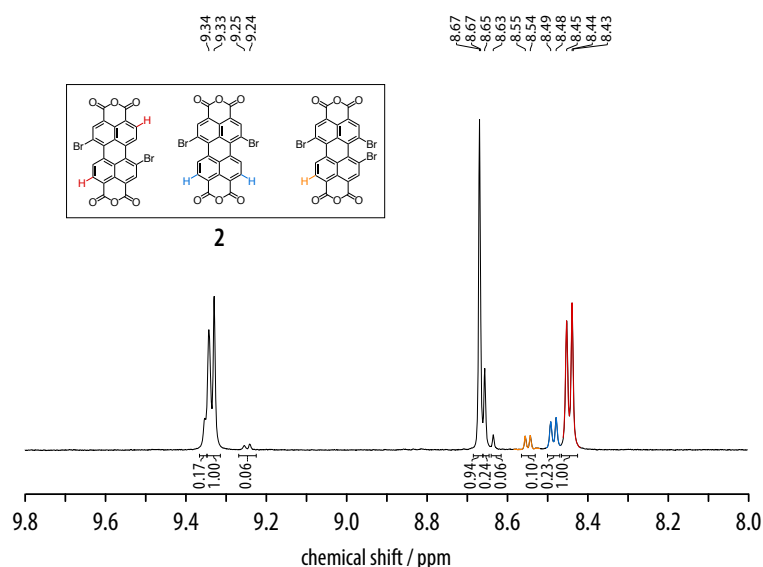
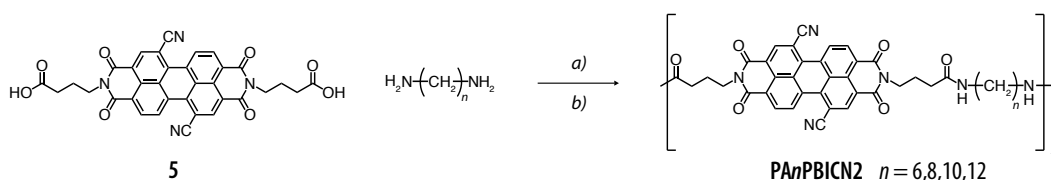


**Figure 5.1.**  $^1\text{H}$  NMR spectrum (600 MHz, calibrated with 4,4-dimethyl-4-silapentane-1-sulfonic acid) of **2** in conc.  $\text{D}_2\text{SO}_4$  indicating the presence of the 1,7-dibromo, 1,6-dibromo, and 1,7,6-tribromoperylene bisimide regioisomers.

Because of solubility issues encountered with **5**, the Yamazaki-Higashi solution-phase polycondensation route<sup>150</sup> was not an option and an alternative procedure was therefore used. The carbodiimide-promoted reaction of compound **5** with chlorendic hydroxyimide resulted in the corresponding active ester monomer, which was used *in situ* for the synthesis of the dicyanoperylene bisimide-containing polyamides **PanPBICN2** ( $n = 6, 8, 10, 12$ ) by solution-phase polycondensation with 1,6-hexanediamine, 1,8-octanediamine, 1,10-decanediamine, and 1,12-dodecanediamine, respectively, in yields of 85–92% (240–280 mg) after precipitation (Scheme 5.2, Table 5.1). Likewise, the *in situ* activation of dibutanoic acid **5** with chlorendic hydroxyimide followed by coupling to propylamine gave the diamide model compound **6** in a yield of 84% (95 mg). The continued presence of the 1,6-dicyano regioisomer was shown by

2D NMR spectroscopy (Appendix 9.2.4). All polyamides were soluble in trifluoroacetic acid (TFA) and *m*-cresol at room temperature, but remained insoluble in most common polar aprotic solvents, including dimethyl sulfoxide (DMSO), dimethylformamide (DMF), *N*-methyl-2-pyrrolidone (NMP), hexamethylphosphoramide (HMPA), *o*-dichlorobenzene, cyclohexanone, or dimethylacetamide, as well as quinoline, glacial acetic acid, 1,1,1,3,3,3-hexafluoro-2-propanol (HFIP), *o*-/*m*-xylene or chlorobenzene, even at elevated temperatures.



**Scheme 5.2.** Synthesis of dicyanoperylene bisimide-containing polyamides **PA<sub>n</sub>PBICN2**. *Reagents and conditions:* a) Chlorendic hydroxylimide, DIC, DMF, 50 °C, 14 h, b) DMSO, 120 °C, 2 d, 85–92%.

A combination of <sup>1</sup>H NMR spectroscopy, solid-state IR spectroscopy, and gel permeation chromatography (GPC), confirmed the chemical structures of the resulting polyamides (Figure 5.2, Table 5.1). However, their insolubility in common organic solvents required derivatization with trifluoroacetic anhydride (TFAA) to give the corresponding poly(trifluoroacetylimide)s. GPC could then be performed with HFIP as the eluent. The number average molecular weights (*M<sub>n</sub>*) of 9'400 to 15'500 g/mol and the dispersities (*D*) of around 2.0 implied a degree of polymerization of between 13 and 20, indicative of a robust polycondensation procedure (Table 5.1).

**Table 5.1:** Yields, number and molecular weights (*M<sub>n</sub>*, *M<sub>w</sub>*, and dispersities (*D*) obtained from gel permeation chromatography of the dicyanoperylene bisimide-containing polyamides **PA<sub>n</sub>PBICN2**.

<b>PA<sub>n</sub>PBICN2</b>	Amount [mg]	Yield [%]	<i>M<sub>n</sub></i> [g/mol]	<i>M<sub>w</sub></i> [g/mol]	<i>D</i>
<b>PA6PBICN2</b>	240	85	9'700	19'700	2.0
<b>PA8PBICN2</b>	272	92	11'100	22'500	1.9
<b>PA10PBICN2</b>	280	92	9'400	19'000	2.0
<b>PA12PBICN2</b>	270	85	15'500	32'000	2.0

The broad absorption at 2800–3300 cm<sup>-1</sup> in the solid-state infrared (IR) spectra of compound **5** can be assigned to the O–H stretching vibration, while the band at 1712 cm<sup>-1</sup> corresponds to the C=O stretching vibration of a free carboxylic acid group (Figure 5.2a). After polycondensation, these bands were replaced by a characteristic amide A (N–H stretching) absorption at 3302–3307 cm<sup>-1</sup> with a shoulder at around 3390 cm<sup>-1</sup> (Figure 5.2b), the amide I (C=O stretching) peak at 1631–1642 cm<sup>-1</sup>, and the amide II band at 1537–1545 cm<sup>-1</sup>, along with with C=O stretching bands and benzene C=C vibrations from the perylene bisimide core at 1703–1706, 1657–1664, and 1597–1600 cm<sup>-1</sup> (Figure 5.2c).<sup>334</sup> In each case, the maximum

and the shoulder of the amide A peak were associated with hydrogen-bonded and free (non-hydrogen-bonded) amide groups, respectively. The peak position and its full width at half maximum (FWHM < 100  $\text{cm}^{-1}$ ) were similar to those observed in typical semicrystalline polyamides.<sup>100</sup>

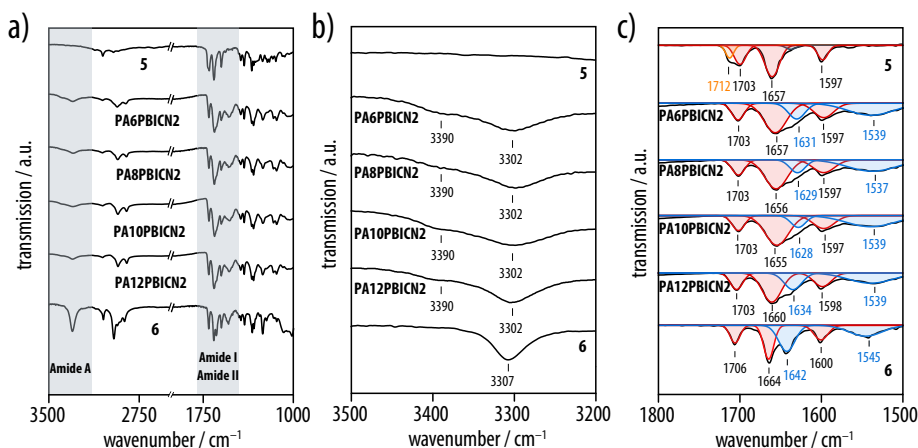


**Figure 5.2.** Solid-state IR spectra of the dicyanoperylene bisimide-containing polyamides **PA $n$ PBICN2**. *a*) The formation of amide bonds was confirmed from comparison of the solid-state IR spectra of the polyamides **PA $n$ PBICN2** with that of compounds **5** and **6**. *b*) The characteristic amide A and amide I and II bands (blue) appeared after polycondensation, along with the C=O stretching vibrations of the perylene bisimide core (red).

### 5.2.2 Crystalline Morphology of the Polyamides

Wide-angle X-ray diffraction (WAXD) patterns of the as-synthesized polyamides **PA $n$ PBICN2** ( $n = 6, 8, 10, 12$ ) powders showed clear Bragg peaks superimposed on an amorphous background, indicating the presence of an ordered phase in the solid-state, consistent with the IR spectroscopic data. Peaks were observed for all the materials at  $2\theta$  ranging from  $42.0\text{--}43.1^\circ$  (broad),  $23.8\text{--}29.5^\circ$  (strong),  $18.2\text{--}19.9^\circ$  (strong),  $12.1\text{--}12.9^\circ$ ,  $10.3\text{--}10.5^\circ$ , and  $3.7\text{--}4.5^\circ$  (strong), corresponding to spacings of 2.1–2.2 Å, 3.0–3.7 Å, 4.5–4.9 Å, 6.9–7.3 Å, 8.4–8.6 Å and 19.5–23.5 Å (Figure 5.3*a*). This suggested the increase in the length of the aliphatic segment ( $n$ ) not to have a major qualitative influence on the crystalline morphology of the polyamides. However, the spacings associated with the lowest angle peak visible in the WAXD patterns increased from 19.5 to 23.5 Å with increasing  $n$  (Figure 5.3*b*), suggesting a systematic increase in the long period of the unit-cell. Peak deconvolution followed by subtraction of the amorphous background suggested a crystallinity index,  $\chi$ , of 43–53%, which is similar to the degrees of crystallinity observed in other semiaromatic polyamides obtained with the same method (Figure 5.3*c*).<sup>335,336</sup>

The lamellar long period ( $L_p$ ) arising from the periodic stacking of alternating crystalline and amorphous lamellae was estimated from small-angle X-ray scattering (SAXS) measurements to be in the range of 19–22.5 nm (Figure 5.3*c*). Combining WAXD crystallinity indexes and

SAXS long period, it therefore implied lamellar thicknesses of roughly 9.1 nm for  $n = 6$ , 8.5 nm for  $n = 8$ , 10.2 nm for  $n = 10$  and 11.9 nm for  $n = 12$ , assuming a simple two phase model, which was between 4 and 5 times the spacings corresponding to the lowest angle WAXD peaks in each case.

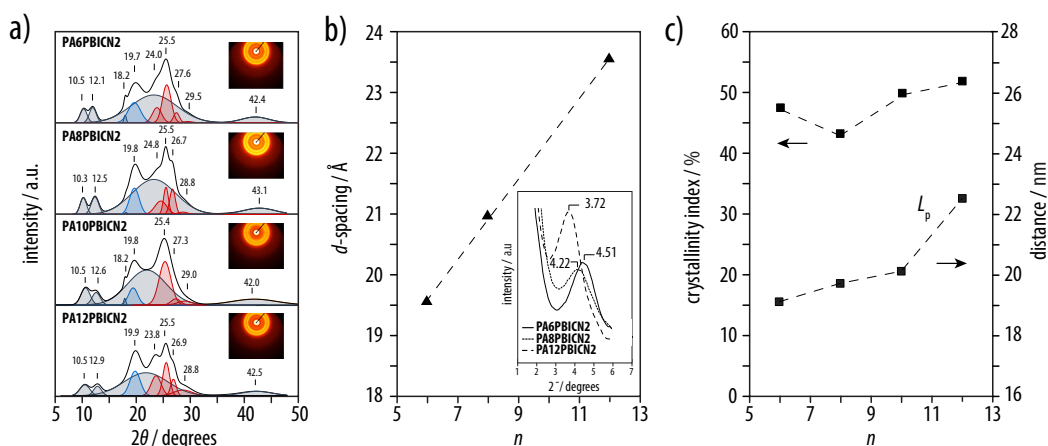


**Figure 5.3.** *a*) Wide angle X-Ray diffraction (WAXD) patterns of the as-synthesized  $\text{PANPBICN2}$  ( $n = 6, 8, 10, 12$ ) powders were recorded at room temperature in transmission mode, along with the corresponding 2D patterns (insets). Deconvolution of these patterns was used to separate the amorphous background from the Bragg peaks. *b*) Systematic increase in the  $d$ -spacings corresponding to the lowest angle peaks in the WAXD patterns with increasing  $n$  from 19.5 to 23.5 Å (inset: corresponding Bragg peaks). *c*) Estimated crystallinity index as a function of  $n$  based on the deconvolution of the WAXD patterns, together with the corresponding long period ( $L_p$ ) estimated from small-angle X-ray scattering (SAXS) measurements.

Attempts to obtain a suitable single-crystal for WAXD analysis from model compound **6** from solution or by vacuum sublimation were unsuccessful. However, crystalline structures obtained for similar centrosymmetric **PBICN2** derivatives without amide groups, as well as our own UV-vis spectroscopic investigations (see below) suggest that the roughly planar perylene bisimide moieties should show parallel-displaced  $\pi$ - $\pi$  stacking with an interplanar distance of approximately 3.4 Å, consistent with the strong Bragg reflection at  $2\theta = 25.4$ – $25.5^\circ$  observed in the present case, and the aliphatic groups in an extended conformation.<sup>337–339</sup> Moreover, in common with other polyamides derived from centrosymmetric aromatic diacids and linear aliphatic diamines with even  $n$ ,  $\text{PANPBICN2}$  ( $n = 6, 8, 10, 12$ ) is expected to show a stable  $\alpha$ -type crystalline phase in which fully extended aliphatic linkages form stacked planar hydrogen-bonded sheets.<sup>199,251</sup> At the same time, in order to maintain a reasonable packing density, the chain direction of the aliphatic linkages must be strongly tilted away from the planes of the more bulky perylene moieties.

A model triclinic unit cell for  $\text{PA6PBICN2}$  containing a single repeat unit was constructed on this basis and energy-minimized using the Dreiding II force-field and charge equilibration, resulting in unit cell parameters,  $a = 8.37$  Å,  $b = 5.24$  Å,  $c = 23.08$  Å,  $\alpha = 102.55^\circ$ ,  $\beta = 96.4^\circ$ , and  $\gamma = 112.65^\circ$ , and a relative density of 1.295 (Figure 5.4*a*). The planes of the perylene

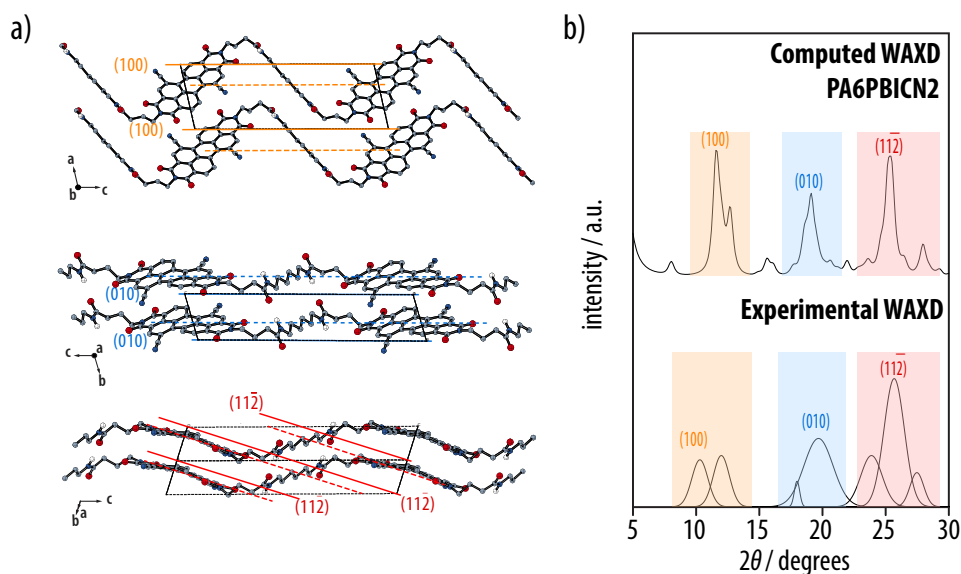


**Figure 5.4.** *a)* Model structure for **PA6PBICN2** assuming a triclinic unit cell with the *c*-axis parallel to the polymer backbone. *b)* Simulated WAXD powder pattern from the structure in *a)* in comparison with a fitting of the experimental WAXD peaks in Figure 5.3*a*.

bisimide cores were twisted by about 15.6° in the relaxed structure, consistent with previously reported values for similar model compounds,<sup>340</sup> and their interplanar spacing was 3.4 Å. The intermolecular hydrogen bond angles and distances associated with the amide groups were N–H...O  $\angle$  169° and H...O  $d$  = 2.2 Å, respectively. Simulated WAXD powder patterns from this structure confirmed strong scattering at  $2\theta$  of around 25° from the perylene stacks, whose planes were approximately parallel to (11 $\bar{2}$ ) in this representation, a strong (010) peak at  $2\theta \approx 19.2^\circ$  and significant additional scattering at lower angles from the (10 $l$ ) planes, in reasonable qualitative agreement with the corresponding experimental WAXD patterns (Figure 5.4*b*), bearing in mind the significant 1,6-regioisomer content of the specimens. Indeed, while the experimental WAXD patterns did not permit unambiguous independent determination of the unit cell parameters, the diffraction peaks for **PA6PBICN2** could be indexed by analogy with the model structure, implying  $a$  = 9.22 Å,  $b$  = 5.00 Å,  $c$  = 20.45 Å,  $\alpha$  = 100.50°,  $\beta$  = 93.50°, and  $\gamma$  = 112.85°, and a relative density of 1.37, suggesting stronger tilting of the chain direction of the aliphatic linkages away from the planes of the perylene moieties than in the model structure, and hence a reduced long period.

### 5.2.3 Thermomechanical Properties of the Polyamides

The thermal stability of the polyamides was investigated by thermogravimetric analysis (TGA) at a heating rate of 10 °C/min under a nitrogen atmosphere. All the polyamides **PA $n$ PBICN2** ( $n$  = 6, 8, 10, 12) as well as the monomer **5** and the model compound **6** exhibited a mass loss of 1–2 wt% at about 300 °C, defined as the onset of decomposition, followed by a strong increase in the rate of mass loss above 350 °C (Figure 5.5*a*).



Differential scanning calorimetry (DSC) indicated there to be no significant melting transition prior to the onset of degradation (Figure 5.5*b*). Dynamic mechanical analysis (DMA) performed on powder specimens of **PA $n$ PBICN2** ( $n = 6, 8, 10, 12$ ) at room temperature revealed a shear modulus in the range 0.75–0.93 GPa in each case, which is significantly higher than that of the fully aliphatic PA610 but lower than that of the commercially available engineering semiaromatic polyamide PA6TI (Figure 5.5*c*). Increasing the length of the aliphatic segment,  $n$ , is not expected to have a major effect on the resulting modulus, as the apparent crystallinities of the different polyamides **PA $n$ PBICN2** ( $n = 6, 8, 10, 12$ ) as obtained by WAXD were similar (Figure 5.3*c*).

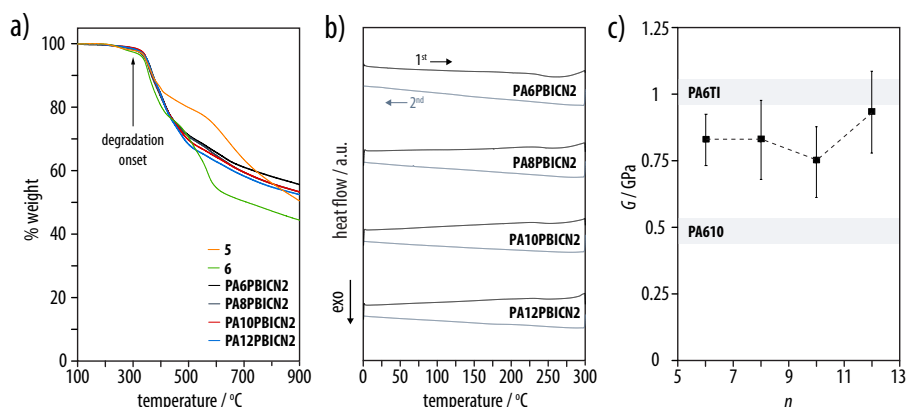


**Figure 5.5.** *a*) Thermogravimetric analysis (TGA) scans of **PA $n$ PBICN2** ( $n = 6, 8, 10, 12$ ) as well as **5** and **6** performed at heating rate of 10 °C/min under nitrogen atmosphere. *b*) Differential scanning calorimetry (DSC) heating and cooling runs of **PA $n$ PBICN2** ( $n = 6, 8, 10, 12$ ) confirmed the absence of any significant thermal transitions before the degradation onset temperature of 300 °C. *c*) The shear modulus,  $G$ , of **PA $n$ PBICN2** as a function of  $n$  calculated from dynamic mechanical analysis measurements (shear mode, 1 Hz at room temperature). Representative values from the commercially available polyamides PA610 and PA6TI are shown for comparison.

#### 5.2.4 Optoelectronic Properties of the Polyamides

UV-vis absorption and fluorescence spectroscopy used to investigate the packing and the photophysical properties of the polyamide **PA6PBICN2** as a representative example and model compound **6** in solution and in the solid-state. Both **PA6PBICN2** and **6** showed a strong  $S_0$ – $S_1$  absorption in TFA ( $c = 10^{-4}$  mol/L) at 527 nm (0–0) with higher energy vibronic bands at 492 (0–1) and 462 nm (0–2) (Figure 5.6*a,b*, solid black lines).<sup>341</sup> The ratio of the 0–0 and the 0–1 ( $A_{0-0}/A_{0-1}$ ) absorption intensities was around 1.48, which is similar to typical values for perylene bisimide derivatives in solution and indicated spectroscopic aggregates to be absent in TFA at this concentration.<sup>342–344</sup> The weak absorption band at 391 nm was attributed to the  $S_0$ – $S_2$  transition of the perylene bisimide.<sup>341</sup> Emission spectra from dilute solutions of both **PA6PBICN2** and **6** in TFA ( $c = 10^{-6}$  mol/L) revealed a Stokes shift of 15 nm and well-resolved vibronic fine structure patterns with fluorescence maxima at 542 nm and shoulders at 574 nm (Figure 5.6*a,b*, solid red lines) mirroring the corresponding absorption spectra.

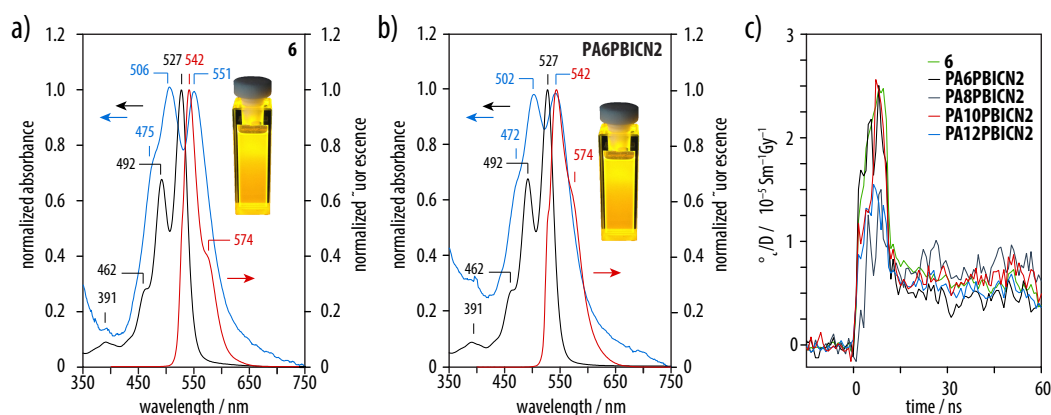


**Figure 5.6.** Normalized UV-vis (solution-phase and thin film) absorption and solution-phase fluorescence spectra of *a*) model compound **6** and *b*) **PA6PBICN2**. The solution-phase spectra were obtained from TFA solutions (black: absorption spectra,  $c = 10^{-4}$  mol/L; red: fluorescence spectra ( $c = 10^{-6}$  mol/L), while thin film spectra were obtained from spin-coated thin films on quartz substrates (blue). The inset shows the corresponding specimens under UV light (254 nm). *c*) The change in conductivity on irradiation with a 10 ns electron pulse for **PA $n$ PBICN2** ( $n = 6, 8, 10, 12$ ) and model compound **6**, measured by time-resolved microwave conductivity.

Thin films prepared by spin coating of **PA6PBICN2** and **6** from TFA ( $c = 10^{-3}$  mol/L) onto quartz substrates exhibited spectral signatures that were markedly different from the solution-phase spectra. The two main absorptions at 551 and 506 nm for **6**, and 542 and 522 nm for **PA6PBICN2**, as well as the shoulders at 472–475 nm could be assigned to the 0–0, 0–1, and 0–2 bands of the  $S_0$ – $S_1$  transitions, and a weak  $S_0$ – $S_2$  absorption was observed at 391 nm in both cases (Figure 5.6*a,b*, blue lines). The weak red-shift (15–20 nm) of the highest wavelength absorptions, the strong decrease in the respective  $A_{0-0}/A_{0-1}$  ratios to 0.98 for **6** and 1.0 for **PA6PBICN2**, and the almost complete quenching of fluorescence suggested pronounced H-type coupling of the dicyanoperylene bisimide chromophores, typical of an almost cofacial, parallel-displaced arrangement of these chromophores in the solid-state.<sup>345–348</sup>

Finally, in order to gain insight in the conductive properties of these materials, we performed pulse-radiolysis time-resolved microwave conductivity (PR-TRMC) experiments on bulk specimens of **PA $n$ PBICN2** ( $n = 6, 8, 10, 12$ ) and the model compound **6** at 31 GHz with pulse widths of 10 ns at room temperature. The PR-TRMC measurements resulted in clear conductivity transients, yielding one-dimensional charge carrier mobilities,  $\mu_{1D} = 1.4 \times 10^{-2} \text{ cm}^2 \text{ V}^{-1} \text{ s}^{-1}$  (**6**),  $1.1 \times 10^{-2} \text{ cm}^2 \text{ V}^{-1} \text{ s}^{-1}$  (**PA6PBICN2**),  $1.2 \times 10^{-2} \text{ cm}^2 \text{ V}^{-1} \text{ s}^{-1}$  (**PA8PBICN2**),  $1.0 \times 10^{-2} \text{ cm}^2 \text{ V}^{-1} \text{ s}^{-1}$  (**PA10PBICN2**), and  $1.0 \times 10^{-2} \text{ cm}^2 \text{ V}^{-1} \text{ s}^{-1}$  (**PA12PBICN2**) (Figure 5.6*c*). These values were comparable with those reported for other bisubstituted perylene bisimides, including liquid-crystalline materials<sup>349,350</sup> and hydrogen-bonded perylene bisimide organogelators,<sup>351</sup> and about one order of magnitude higher than those of hole-conducting, hydrogen-bonded oligothiophene derivatives.<sup>244,287</sup>

## 5.3 Conclusions

We used solution-phase polycondensation to prepare a series of novel polyamides containing dicyanoperylene bisimide repeat units, which showed morphologies and thermomechanical characteristics similar to existing semiaromatic polyamides. Based on IR and optical spectroscopy as well as molecular modelling and WAXD, we suggest the perylene bisimide units in the polyamides to form stacks with a parallel-displaced  $\pi$ - $\pi$  arrangement. This arrangement gives rise to strong H-type coupling in the solid-state UV-vis spectra and is expected to provide percolation pathways for charge transport, as reflected by charge carrier mobilities of about  $0.01 \text{ cm}^2 \text{ V}^{-1} \text{ s}^{-1}$ , which is in the same range as for crystalline materials based on perylene bisimide derivatives. Our results hence demonstrate that the incorporation of cyanoperylene bisimide repeat units into a polyamide backbone may be used to prepare polymers that combine the charge transport properties of typical electron-deficient  $\pi$ -conjugated segments with thermomechanical properties characteristic of high-performance engineering polyamides.



# **Conclusions and Outlook**





## 6 Conclusions and Outlook

The present thesis aimed at exploring the use of hydrogen bonding sites incorporated in the substituents attached to  $\pi$ -conjugated chromophores as a means to guide the supramolecular arrangement of the chromophores in the solid-state across different length scales. This was achieved by following two complementary approaches in two different classes of materials. In the first part, we successfully prepared hydrogen-bonded bithiophenes and quaterthiophenes together with their non-hydrogen-bonded analogues, in which amide and ester groups, respectively, were connected to the  $\pi$ -conjugated core via flexible spacers of different lengths.

- We derived a comprehensive structure-property relationship in bithiophenes with hydrogen-bonded substituents and found that the packing of the bithiophene cores within its sublayer was about 10–25% denser for bithiophene diamides than the respective diesters. Notably, the bithiophene diamide with an ethylene spacer showed the smallest pitch angle combined with a sufficiently small roll angle, resulting in strong H-type coupling in optical spectroscopy the solid-state. The coexistence of the  $\pi$ -interactions with N–H...O=C hydrogen bonding was observed in all cases, but only synergistic in the case of the ethylene spacer, leading to optimized hydrogen bonding and  $\pi$ -interactions.
- Consistent with the previous observations in bithiophene diamides, a quaterthiophene bisacetamide also revealed the smallest volume occupied by its quaterthiophene core, resulting in a more efficient  $\pi$ -overlap and a stronger preference for layer-by-layer thin film growth, resulting in micrometer-sized crystalline domains, as compared with other quaterthiophenes including a structurally related quaterthiophene diacetate. These factors resulted in average field-effect mobilities of up to  $0.18 \text{ cm}^2 \text{ V}^{-1} \text{ s}^{-1}$ , which is almost two orders of magnitude higher than the reference non-hydrogen-bonded diacetate and in the same range as the best mobilities reported for single-crystalline quaterthiophenes to date.

From the investigations above, it follows that the use of terminal amide hydrogen bonding sites is not detrimental for macroscopic charge transport. We thus extended our investigations to polymer semiconductors in the second part. To this end, we designed and synthesized novel semiaromatic polyamides containing either bithiophene (p-type) or dicyanoperylene bisimide (n-type) repeat units to add optoelectronic function to these materials. In both cases, we used solution phase polycondensation and obtained a series of semiaromatic polyamides with different aliphatic spacer lengths.

- We demonstrated that the polyamides containing bithiophene or dicyanoperylene bisimide repeat units were semicrystalline and exhibited a microscopic structure similar to other semicrystalline, semiaromatic polyamides, featuring nanometer thick, interconnected lamellar crystalline domains, providing thermoplastic properties with an elastic modulus and a shear modulus comparable to those of industrial-grade semiaromatic polyamides.
- Moreover, these polyamides containing bithiophene or dicyanoperylene bisimide repeat units exhibited charge carrier mobilities on the order of  $10^{-2} \text{ cm}^2 \text{ V}^{-1} \text{ s}^{-1}$  that are either in the same range as their low molecular weight counterparts, or even one order of magnitude higher, as demonstrated by pulse-radiolysis time-resolved microwave conductivity measurements.

Our study may, therefore, pave the step towards polyamide-based semiconductors, in which the synergistic interplay of interchain hydrogen bonding and  $\pi$ - $\pi$  stacking renders them suitable for applications in which both mechanical and optoelectronic properties are important. However, several interesting aspects still need to be addressed in future work:

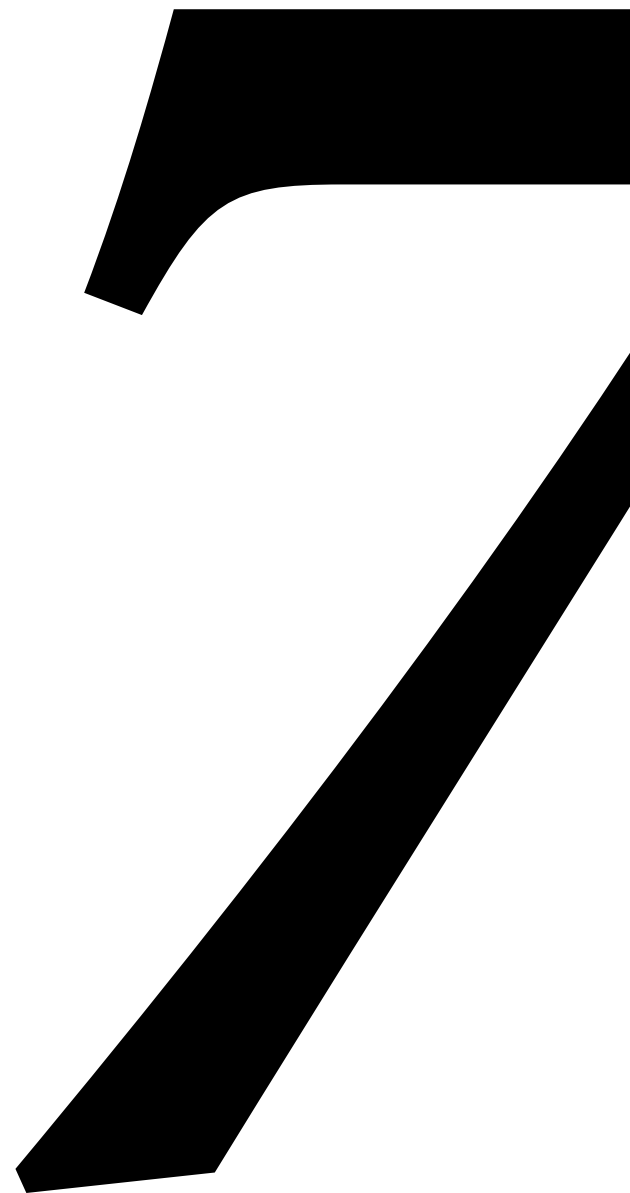
- It would be important to complement the microwave conductivity experiments with macroscopic charge transport measurements using, for instance, a field-effect transistor set-up.
- In this context, the preparation of polymers with significantly improved processability from solution or from the melt will be relevant. We envisage this to be possible by copolymerization, so that the disorder introduced in the molecular structure of the resulting polyamides will decrease the crystallinity, lower the melting points, and/or increase solubility in organic solvents.
- The resulting materials can then be processed into oriented thin films via friction transfer or fibers via electrospinning directly onto a substrate of choice. In both cases, the structure formation of the materials is expected to remain dominated by the segregation of the chromophores, as demonstrated in this thesis. The potential of this approach has already been confirmed by preliminary investigations on the electrospinning of bithiophene-containing polyamides from solution, resulting in continuous, long microfibrils.



- After addressing the macroscopic device performance, this concept may subsequently be applied to the inherently better  $\pi$ -conjugated cores, such as benzo[thienobenzothio]phene (BTBT) or diketopyrrolopyrrole (DPP).



**Experimental Part**





## 7 Experimental Part

### 7.1 Instrumentation and Methods

**1D Wide-Angle X-ray Diffraction (WAXD).** 1D powder WAXD patterns for the as-synthesized polyamides were obtained in reflection mode using a PANalytical X'Pert Pro MPD diffractometer (CuK $\alpha$  radiation,  $\lambda = 1.54 \text{ \AA}$ ) in the Bragg-Brentano geometry. The X-ray tube was operated at 45 kV and 40 mA and scanning was carried out from  $2\theta = 15\text{--}30^\circ$  angles using a fixed divergence slit of  $0.25^\circ$ , a step size of  $0.0167^\circ$  and a time per step of 120.015 s.

**2D Small-Angle X-Ray Scattering & Wide-Angle X-ray Diffraction (SAXS & WAXD).** 2D SAXS and WAXD patterns for the polyamides **PA $n$ T2** were obtained using a rotating anode X-Ray tube (CuK $\alpha$  radiation,  $\lambda = 1.54 \text{ \AA}$ ) at the MATEIS laboratory of the Institut National des Sciences Appliquées de Lyon, France. The data were recorded in transmission with a beam size of  $500 \mu\text{m} \times 500 \mu\text{m}$  and a 2D CCD detector (Princeton Instruments) with specimen-detector distances of 343 mm and 42.1 mm and exposure times of 180 and 1200 s for SAXS and WAXD respectively, corrected for the thickness and the absorption of the specimens, and integrated azimuthally. A broad low-angle peak observed in the SAXS patterns was assumed to arise from approximately periodic stacking of high aspect ratio crystalline lamellae, giving direct access to the lamellar long period,  $L_p$ . The lamellar thickness,  $L_c$ , was estimated from the corresponding correlation function following Strobl and Schneider.<sup>352</sup> The volume fraction of the crystalline phase was then estimated from the ratio  $L_c / L_p$ .

2D SAXS and WAXD measurements on polyamides **PA $n$ PBICN2** were performed at the Unité Matériaux et Transformations (UMET) laboratory in University of Lille, France using a Xeuss 2.0 apparatus (Xenocs) equipped with a micro source (CuK $\alpha$  radiation,  $\lambda = 1.54 \text{ \AA}$ ) and point collimation. The sample-to-detector distance, which was around 18 cm for WAXD and 150 cm for SAXS, was calibrated using silver behenate as a standard. The data were recorded in transmission mode with a beam size of  $500 \times 500 \mu\text{m}^2$  and a 2D Pilatus 200K detector. Standard corrections were applied to the WAXD and SAXS patterns before their analysis. The intensity profiles were obtained by azimuthal integration of the 2D patterns using the fit2D software.

**Atomic Force Microscopy (AFM).** Pressed films of **PA8T2** with thicknesses of the order of 100  $\mu\text{m}$  were deposited on a flat glass substrate, heated to a temperature about 30  $^{\circ}\text{C}$  above their melting point as determined by DSC, and crystallized isothermally in air at the required temperature. The resulting surface textures were observed by intermittent-contact-mode AFM (Bruker Nanoscope IIIa) with a MikroMasch NSC14 silicon probe (root-mean-square free amplitude = 2 V, set-point amplitude = 0.6–1.2 V).

AFM images of Chapter 3 were obtained in tapping mode using a Nanoscope IIIa (Veeco Instruments Inc., Santa Barbara, USA) instrument or a NT-MDT Solver Pro with a SMENA scanner at room temperature in air. Cantilevers with an average resonance frequency of  $f_0 = 75$  or 150 kHz and  $k = 3.5$  or 5 N/m were used, respectively. Scan rates of 0.1–2.0 Hz were applied, and the image resolution was  $512 \times 512$  pixels. The images were processed using the Gwyddion software package.

**Computational Details.** Pairs of molecules were extracted from the five crystal structures of **1**, **2**,  $\alpha$ -4T, DM4T, and DH4T. The lateral chains were removed, and hydrogen atoms positions were optimized at the B3LYP/6-31G(d) level in Gaussian 09.<sup>353</sup> The electron density was calculated at B3LYP/TZP level in ADF2013.<sup>354–356</sup> The DORI-based electronic compactness index was computed in locally modified version of DGrid.<sup>357</sup> The compactness index was computed as integral of the electron density over the intermolecular regions as reported previously.<sup>298</sup>

**Differential scanning calorimetry (DSC).** DSC was carried out with either a TA Instruments Q100 calorimeter or a Mettler Toledo, DSC 3+ STAR<sup>e</sup> System calorimeter at a scanning rate of 10 $^{\circ}\text{C}/\text{min}$  under nitrogen flow (50 mL/min). Specimens of about 3–5 mg were first heated to a temperature 30  $^{\circ}\text{C}$  above their melting point and then cooled to 0  $^{\circ}\text{C}$  at a cooling rate of  $-10$   $^{\circ}\text{C}/\text{min}$  in order to erase the effects of their thermal history. The data given for the thermal transitions were obtained from the second heating and first cooling scans. Melting ( $T_m$ ) and crystallization ( $T_c$ ) temperatures were defined as the temperatures corresponding to the maxima of the respective enthalpy peaks, while  $T_g$  was defined as the half-height of the heat capacity step associated with the glass transition. The melting enthalpies  $\Delta H_m$  were estimated by integrating the area under the melting peaks. The corresponding experimental errors are essentially due to the sensitivity of these measurements to the choice of baseline.

**Dynamic Mechanical Analysis (DMA).** Dynamic mechanical testing (861<sup>e</sup>, Mettler Toledo) was performed in shear mode at room temperature with a strain amplitude of 0.1%. Each specimen was tested at successive frequencies of 10, 1 and 0.1 Hz). The test specimens were either hot-pressed or compressed into a cylindrical pellet with dimension ranging between 0.30–0.60 mm in thickness and 5 mm in diameter, with a geometric factor between 20–50  $\text{m}^{-1}$ .

**Electron Microscopy.** Thin films of the polyamides **PA<sub>n</sub>T2** for selected area electron diffraction (SAED) were obtained by friction deposition from a small block of the solid polyamide onto a freshly cleaved crystal of KBr held at 20–30 °C below the melting point of the polyamide, followed by dissolution of the KBr and deposition of the remaining oriented film onto a carbon covered 400 mesh grid. Electron fiber diffraction patterns were recorded using a Thermo Scientific Talos transmission electron microscope (TEM) operated at 200 kV.

**Fluorescence Spectroscopy.** Solution-phase fluorescence spectra were obtained with a Jasco FP-6500 spectrofluorometer from TFA solutions (0.1 mg/mL) using Hellma quartz cuvettes (1 × 1 cm<sup>2</sup>) with an excitation wavelength of 527 nm. Solid-state fluorescence spectroscopy made use of films prepared from disperions of 5 mg of the compounds in 5.2 g of a 17% w/v solution of PMMA in toluene under strong magnetic stirring. These disperions were spin-coated (4000 rpm, 1 min) onto transparent polyester substrates (Byko-Charts, BYK Gardner, USA) and the resulting films were first dried in air for 2 h and then under high vacuum for a week after removal of the substrate. The fluorescence spectra of these films were recorded with a Horiba Jobin FluoroMax-3.

**Gel Permeation Chromatography (GPC).** The number and weight average molecular weights,  $M_n$  and  $M_w$ , and the dispersity,  $\bar{D}$ , of the polyamides were determined using an Agilent 1260 Infinity GPC/SEC system with a refractive index detector and a total column length of 650 mm (PSS PFG, 100 Å). 1,1,1,3,3,3-Hexafluoro-2-propanol (HFIP) was used as the eluent at a flow rate of 1 mL/min and temperature of 25 °C. Six poly(methyl methacrylate) (PMMA) standards with molar masses of between 2'000 and 44'000 g/mol and  $\bar{D}$  1.1 were used for calibration. The polyamides and the PMMA standards were all dissolved in neat HFIP ( $c$  = 2–3 mg/mL).

**Infrared (IR) Spectroscopy.** IR spectra were measured on a JASCO FT/IR 6300 spectrometer using the Miracle attenuated total reflection (ATR) accessory from PIKE.

**Mass Spectrometry.** High-resolution mass spectrometry was carried out with either a Waters Q-ToF Ultima for ESI, or on a Bruker AutoFlex Speed for MALDI-ToF, or on a Waters QTOF Xevo G2-S for APPI/APCI.

**Nanoindentation Measurements.** Nanoindentation experiments were performed on 300 µm thick pressed films of the polyamides **PA<sub>n</sub>T2**, cooled at 10 °C/min from the melt, using an NHT<sup>2</sup> Nanoindentation Tester from Anton Paar equipped with a Berkovich diamond indenter ( $\alpha$  = 65.3 ± 0.3). Loading and unloading rates were set to 100 mN/min with a pause of 30 s, and the maximum load was 10 mN. Two to three films were made from each material and a minimum of 25 indents were performed on two different areas of each. Hardness ( $H_{IT}$ ) and

elastic modulus ( $E_{IT}$ ) were determined from the unloading part of the measurement using the method of Oliver and Pharr<sup>358</sup> and assuming a Poisson's ratio of 0.4 throughout.

**Nuclear Magnetic Resonance (NMR) Spectroscopy.** 1D and 2D NMR spectra were recorded at 298 K on Bruker Avance III 400, 600 or 800 spectrometers at frequencies of 400 MHz, 600 MHz, 800 MHz for  $^1\text{H}$  nuclei, and 101 MHz, 150 MHz, 200 MHz for  $^{13}\text{C}$  nuclei at 298 K, respectively. Deuterated solvents were purchased from Cambridge Isotope Laboratories, Inc. The spectra were calibrated to the respective residual solvent peaks of DMSO- $d_6$  (2.50 ppm  $^1\text{H}$  NMR; 39.52 ppm  $^{13}\text{C}$  NMR),  $\text{CDCl}_3$  (7.26 ppm  $^1\text{H}$  NMR; 77.16 ppm  $^{13}\text{C}$  NMR) or  $\text{CD}_2\text{Cl}_2$  (5.32 ppm  $^1\text{H}$  NMR; 53.84 ppm  $^{13}\text{C}$  NMR). The  $^1\text{H}$  NMR spectra of the **PA $n$ T2** and **PA $n$ PBICN2** polyamides were recorded in non-deuterated HFIP with acetone- $d_6$  as the internal standard (2.05 ppm in  $^1\text{H}$  NMR) and in TFA- $d$  and  $\text{CDCl}_3$  mixtures in 1:3 ratio, respectively. The  $^1\text{H}$  NMR of 1,7-dibromoperylene-3,4:9,10-tetracarboxylic dianhydride was recorded in conc.  $\text{D}_2\text{SO}_4$  (96–98% in  $\text{D}_2\text{O}$ ) with 4,4-dimethyl-4-silapentane-1-sulfonic acid (DSS) as an internal reference material. Chemical shifts are expressed in parts per million (ppm) and coupling constants are given in Hz) (s = singlet, d = doublet, t = triplet, q = quadruplet, p = quintet, m = multiplet, br = broad signal).

**Numerical Simulations.** Trial crystal structures for the polyamides were generated using the BIOVIA Materials Studio graphics user interface. Their geometry was then optimized with respect to all structural degrees of freedom subject to periodic boundary conditions, using classical force field-based energy minimization with the generic Dreiding force field<sup>359</sup> and the method of steepest descents with charge equilibration. WAXD patterns were simulated using the BIOVIA Reflex software package.

**OFET Device Fabrication.** Bottom-gate top-contact transistors were fabricated from thin films of **1** and **2** via thermal deposition of Au source and drain electrodes (80 nm) in high vacuum ( $10^{-6}$  mbar) and at a substrate temperature of  $-185^\circ\text{C}$  through different shadow masks. Transistors with channel lengths  $L = 5, 10, \text{ or } 20 \mu\text{m}$  and an aspect ratio  $W/L = 10$  were patterned by stencil masks made of low-stress  $\text{Si}_3\text{N}_4$  membranes supported by bulk Si. These stencils were fabricated in the Microsystems Laboratory 1 of Prof. J. Brugger at EPFL.<sup>360,361</sup>

**OFET Characterization.** The transfer characteristics of all transistor devices were recorded directly by measuring the channel current  $I_{DS}$  in dependence of the gate voltage  $V_G$  in the saturation regime of the transistor ( $V_D = -60 \text{ V}$  or  $V_D = -40 \text{ V}$ ) in an inert atmosphere and at ambient temperature using a Keithley 4200 semiconductor characterization system. All measurements were performed at scan rates of  $0.25\text{--}0.5 \text{ V s}^{-1}$ .



The field effect mobility,  $\mu$ , in the saturation regime was extracted from the slope and the threshold voltage  $V_T$  from the  $V_G$ -axis interception of a linear fit of the square root of the absolute saturation drain current  $I_{DS}$  as a function of the gate voltage  $V_G$ , according to

$$I_{DS} = \frac{W}{2L} \cdot C_i \cdot \mu \cdot (V_G - V_T)^2 \quad (7.1)$$

**Pulse-Radiolysis Time-Resolved Microwave Conductivity.** Charges were generated in powder samples (20–50 mg) by irradiation with short pulses (2–20 ns) of high-energy electrons (3 MeV) from a Van de Graaff accelerator. The penetration depth of these high-energy electrons in the materials is several millimeters, resulting in close to homogenous ionization and hence a uniform concentration of charges. The change in conductivity of the material due to charges generated by the irradiation was probed using high frequency microwaves (28 to 38 GHz). The fractional change in the microwave power ( $\Delta P/P$ ) absorbed on irradiation is directly proportional to the change in the conductivity ( $\Delta\sigma$ ) according to

$$\frac{\Delta P}{P} = -A \cdot \Delta\sigma \quad (7.2)$$

where the sensitivity factor,  $A$ , is a sensitivity factor that depends on the geometric and dielectric properties of the material.<sup>362</sup> The conductivity ( $\Delta\sigma$ ) is related to the mobility of all charged species, and their concentration,  $N_p$ , through

$$\Delta\sigma = e \cdot N_p \sum \mu \quad (7.3)$$

where  $e$  is the elementary charge ( $1.6 \cdot 10^{-19}$  C). This equation allows the mobility of the charge carriers to be calculated given a reasonable estimate of their concentration. Such an estimate may be obtained from dosimetry measurements, which provides the amount of energy deposited by the electron pulse, as described in detail previously.<sup>363</sup>

**Polarized Optical Microscopy.** Polarized optical microscopy was carried out either on an Olympus BH2 microscope or Olympus BX-60 equipped with Colorview I and Olympus XC50 digital cameras, respectively.

**Thermogravimetric analysis.** Thermogravimetric analysis (TGA) scans were recorded using a Perkin Elmer TGA 4000. The specimens (5–10 mg) were dried in high vacuum at 80 °C for 24 h and then heated from 30 °C to 950 °C at a scanning rate of 10 °C/min in a flow of nitrogen (20 mL/min).

**Thin Film Deposition.** The SiO<sub>2</sub> and SiO<sub>2</sub>/OTS substrates were heated to the desired substrate temperatures  $T_s = 24\text{--}140$  °C in high vacuum ( $10^{-7}$  mbar) overnight prior to quaterthiophene deposition. Deposition of compounds **1** and **2** was monitored using a quartz crystal microbalance, and the deposition rate was maintained constant at around 3 Å/min. The distance between the alumina crucible and the sample holder was around 40 cm.

**UV-vis Spectroscopy.** UV-vis spectra were measured on a Jasco V-670 spectrometer, solution phase spectra (5 mg/mL in HFIP, TFA or DMSO) were obtained using Hellma quartz cuvettes (1 mm path length), and spectra of thin films were measured on samples prepared onto a quartz substrate by spin-coating (4000 rpm, 1 min) using 100 µL of a stock solution (2 mg/mL).

**X-ray Crystallography.** Bragg-intensities of **1a–c**, **2a–c**, **DHT2** and **6a** were collected at low temperature using CuK $\alpha$  radiation ( $\lambda = 1.54184$  Å). A Rigaku SuperNova dual-system diffractometer with an Atlas CCD detector was used for compounds **1a–c**, **2b** and **DHT2**, while an Atlas S2 CCD detector was used for compounds **2a**, **2c** and **6a**. The datasets were reduced and corrected for absorption, with the help of a set of faces enclosing the crystals as tightly as possible, with CrysAlisPro.<sup>364</sup>

The solutions and refinements of the structures were performed by the latest available version of *ShelXT*<sup>365</sup> and *ShelXL*.<sup>366</sup> All non-hydrogen atoms were refined anisotropically using full-matrix least-squares based on  $|F|^2$ . The hydrogen atoms were placed at calculated positions by means of the “riding” model where each H-atom was assigned a fixed isotropic displacement parameter with a value equal to 1.2  $U_{eq}$  of its parent C-atom (1.5  $U_{eq}$  for the methyl groups). However, in structures **1a** and **1b**, hydrogen atom positions were found in a difference map and refined freely. Crystallographic and refinement data are summarized in Section 9.1. The crystal structures of the compounds **1a–c**, **2a–c**, **DHT2** and **6a** have been assigned the CCDC numbers 1951216–1951223.

Structure **2a**, was refined as a two-component twin, yielding a batch scale factor (BASF) parameter of 0.40(7). In the structure **2b**, the 2-methylthiophene moiety was disordered over two positions found in a difference map, and which were refined anisotropically imposing distance and ADP restraints (SADI and SIMU) for the least-squares refinement, yielding site occupancies of 0.58(2)/0.42(2). In the structure **2c**, the propyl substituents were found to be disordered over two orientations found in a difference map and which were refined anisotropically using SADI and SIMU cards for the least-squares refinement, yielding site occupancies of 0.544(8)/0.456(8). The asymmetric unit of **6a** contained two crystallographically independent

molecules in which one of the thiophene rings was disordered over two positions. Atoms of both orientations were located in a difference Fourier map. The major and minor parts were refined anisotropically, but SADI restraints were used to optimize the bond lengths and SIMU restraints were applied to refine the displacement-ellipsoids of the atoms. The site occupancy factors were refined to 0.856(6) and 0.144(6).

The data collection of compound **2** (CCDC 1043812) was performed at low temperatures [100(2) K] using Mo  $K\alpha$  radiation on an Agilent Technologies SuperNova dual system in combination with an Atlas CCD detector (Section 9.1).

**Calculation of Pitch and Roll Angles.** The distances between successive planes within a  $\pi$ -stack is denoted by  $d$ , while the distances between equivalent atoms of the molecules in the stack is marked by  $z$  (Figure 7.1). According to the definition by Curtis et al.,<sup>269</sup> the pitch and roll-angles were computed with the help of the CrystalMaker and IgorPro programs. First, the stack was identified, the molecular plane and original values of  $d$  and  $z$ ,  $d_o$  and  $z_o$ , computed. Then, the origin of the crystallographic unit cell was moved to one of the sulfur atoms of the bithiophene moiety. A local, orthogonal base was defined as follows:

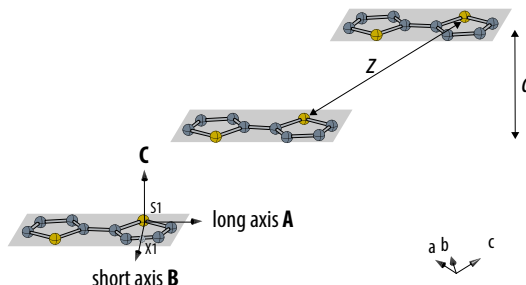


**Figure 7.1.** Representative illustration for determination of pitch and roll angles showing the definition of the bithiophene short and long axis.

- base vector **C**: the normal of the molecular plane as contravariant coordinates;
- base vector **B**: the short axis is the vector from the sulfur atom **S1** through the dummy atom **X1**, which is lying in the molecular plane and is necessarily perpendicular to the vector **C**;
- base vector **A**: the “long axis” is the orthogonal complement to the base vectors **B** and **C** according to  $\mathbf{A} = \mathbf{B} \times \mathbf{C}$ .

A transformation matrix, **M**, was defined such that  $\mathbf{A} = \mathbf{a} \cdot \mathbf{M}$ , where **a** is a  $1 \times 3$  row-matrix containing the crystallographic base vectors, **A** is a  $1 \times 3$  row-matrix containing the orthogonal local base vectors, and **M** is the  $3 \times 3$  transformation matrix. Then, the atomic coordinates were transformed according to  $\mathbf{R} = \mathbf{M}^{-1} \cdot \mathbf{r}$ , where **r** is a  $3 \times 1$  column-matrix containing the

coordinates of an atom  $j$  with respect to the crystallographic basis and  $\mathbf{R}$  is a  $3 \times 1$  column-matrix containing the coordinates of the same atom  $j$  in the local coordinate system. The determinant of  $\mathbf{M}$  was confirmed to be positive and the  $d$  and  $z$  values of the transformed atoms were compared with  $d_o$  and  $z_o$  and judged to be close enough. Finally, the resulting atoms were written into a CIF file which was finally examined in CrystalMaker to compute pitch and roll angles.

**Calculation of Volume per Bithiophenes.** The volume per bithiophene core calculated using the crystallographic plane in which the bithiophenes were organized, and the distance,  $d$ , between the planes touching the Van der Waals surface of the bithiophene's outermost carbons within a layer (Figure 7.2, Table 7.1).

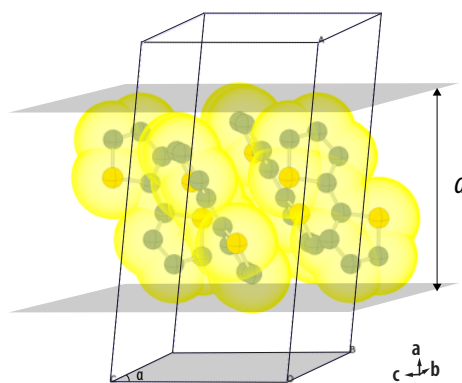


**Figure 7.2.** Illustration of packing arrangement of bithiophenes within a layer. The yellow cloud illustrates the van der Waals surface of the corresponding bithiophenes.

**Table 7.1:** Values that were used for calculation of volume per bithiophenes, where  $a, b$  represented the both crystallographic planes in which the bithiophenes were arranged in a layer;  $\alpha$  is the angle between those crystallographic axes,  $d$  is the distance between planes of the bithiophene's outermost carbons within a layer.

	$a$ [Å]	$b$ [Å]	$\alpha$ [°]	$d$ [Å]	#T2	$V$ [Å <sup>3</sup> ]
<b>1a</b>	5.70	8.11	108.2	6.78	1	297.7
<b>1b</b>	6.05	8.67	90.0	9.00	2	236.2
<b>1c</b>	7.50	8.63	90.0	8.34	2	269.9
<b>2a</b>	5.72	9.53	90.0	8.29	2	226.2
<b>2b</b>	4.89	9.44	90.0	9.29	2	214.3
<b>2c</b>	4.98	5.62	107.7	8.30	1	221.2
<b>T2-133K</b>	5.73	8.93	90.0	8.68	2	222.2
<b>T2-173K</b>	5.77	8.81	90.0	8.78	2	223.4
<b>DMT2</b>	5.24	5.68	90.0	8.59	1	255.4
<b>DHT2</b>	5.91	4.99	105.9	9.26	1	262.4

## 7.2 Synthesis Procedures and Analytical Data for Compounds

**Materials.** Unless otherwise stated, all materials and solvents were purchased from commercial suppliers and used without further purification. Chromatography solvents were purchased as reagent grades and distilled once prior to use. The progress of the reactions was monitored by thin-layer chromatography (TLC) on Merck TLC plates (Silica gel 60 F254). UV light (254 or 366 nm) was used for detection of compounds on the TLC plates. Purification by column chromatography was performed with Geduran<sup>®</sup> silica gel (Si 60, 40–60) from Merck. Spectroscopy grade solvents were used for all spectroscopic investigations.

Heavily boron-doped silicon wafers ( $\text{Si}^+$ ) with a thermal oxide layer of 200 nm, 525  $\mu\text{m}$  thick and with a capacitance  $C_i$  of 19.5 nF/cm<sup>2</sup> were purchased from the Center of Micronanotechnology at EPFL. These wafers were used without further treatment as substrates for the fabrication of thin films of **1** and **2**. Treatment of the  $\text{SiO}_2$  substrates with octadecyltrichlorosilane (OTS) was performed in a glovebox by immersing the silicon wafers into a solution of 15 mg OTS in 5 mL of toluene at 65–70 °C for 10 min followed by rinsing with isopropanol. Contact angles of approximately 110° were obtained after the treatment.

### 7.2.1 Bithiophenes with Hydrogen-Bonded Substituents

Methyl 2-(thiophen-2-yl)acetate (**2a**), dimethyl 2,2'-(2,2'-bithiophene-5,5'-diyl)diacetate (**1a**), dimethyl 3,3'-(2,2'-bithiophene-5,5'-diyl)dipropionate (**1b**), and methyl 4-(thiophen-2-yl)butanoate (**2c**) were prepared following literature procedures.<sup>253,297,367</sup>  $\alpha,\omega$ -Dihexylbithiophene (**DHT2**) was purchased from Sigma-Aldrich.

**Dimethyl 2,2'-(2,2'-bithiophene-5,5'-diyl)diacetate (1a).**  $\text{Pd}(\text{OAc})_2$  (10 mol %) was dissolved in DMSO (350 mL) in an oxygen atmosphere. Trifluoroacetic acid (TFA, 13.3 mL, 173.5 mmol, 1 equiv.) was added dropwise, and compound **4a** (27.1 g, 173.5 mmol, 1 equiv.) was added. The reaction mixture was heated to 60 °C for 48 h. After completion of the reaction, all volatiles were removed in vacuo. The resulting residue was diluted with DCM and washed three times with water and once with a saturated aqueous NaCl solution. The organic phase was dried over  $\text{MgSO}_4$  and concentrated in vacuo. Purification by column chromatography (silica gel, DCM) yielded the pure diester **1a** as a yellow crystalline powder (7.1 g, 26% yield).

<sup>1</sup>H NMR (400 MHz,  $\text{CDCl}_3$ ):  $\delta$  = 6.97 (d,  $J$  = 3.6 Hz, 2H), 6.82 (d,  $J$  = 3.6 Hz, 2H), 3.81 (s, 4H), 3.74 (s, 4H) ppm. <sup>13</sup>C NMR (101 MHz,  $\text{CDCl}_3$ ):  $\delta$  = 170.69, 137.07, 134.02, 127.57, 127.56, 123.23, 52.37, 35.45 ppm. HRMS (ESI): calcd for  $\text{C}_{14}\text{H}_{14}\text{O}_4\text{S}_2$ : 311.0411 ( $[M+H]^+$ ); found: 311.0412.  $R_f$ : 0.62 (DCM). M.p. (DSC in  $\text{N}_2$ ): 76 °C.

**Dimethyl 3,3'-(2,2'-bithiophene-5,5'-diyl)dipropionate (1b).** Compound **4b** (27.33 g, 160.55 mmol) and AgF (40.7 g, 321.1 mmol) were dissolved in dry DMSO (400 mL) in a flow of

argon. Bis(benzonitrile)palladium(II) dichloride (2.45 g, 6.8 mmol) was added, and the flask was shielded from light with aluminum foil. The reaction mixture was heated to 85 °C for 14 h. The same amounts of AgF and bis(benzonitrile)palladium(II) dichloride were added once more, and the reaction was continued under stirring at 85 °C for 5 h. The reaction mixture was cooled to room temperature and the solvent was removed in vacuo. The resulting residue was loaded onto celite (500 mL) from a DCM suspension (2 L), and the filtrate was concentrated in vacuo. Purification by column chromatography (silica gel, DCM) yield compound **1b** as a yellow crystalline powder (16 g, 59% yield). Crystals suitable for single crystal X-ray analysis were obtained by recrystallization from a hot ethyl acetate solution.

$^1\text{H}$  NMR (400 MHz,  $\text{CDCl}_3$ ):  $\delta$  = 6.89 (d,  $J$  = 3.6 Hz), 2H), 6.70 (dd,  $J$  = 2.9, 1.8 Hz), 2H), 3.70 (s, 6H), 3.12 (t,  $J$  = 7.4 Hz), 4H), 2.69 (t,  $J$  = 7.5 Hz), 4H) ppm.  $^{13}\text{C}$  NMR (101 MHz,  $\text{CDCl}_3$ ):  $\delta$  = 172.73, 142.00, 135.78, 125.38, 123.02, 51.78, 35.73, 25.36 ppm. HRMS (ESI): calcd for  $\text{C}_{16}\text{H}_{18}\text{O}_4\text{S}_2$ : 339.0725 ( $[\text{M}+\text{H}]^+$ ); found: 339.0717.  $R_f$ : 0.53 (DCM). M.p. (DSC in  $\text{N}_2$ ): 125 °C.

**Dimethyl 4,4'-(2,2'-bithiophene-5,5'-diyl)dibutanoate (1c).** Compound **4c** (21 g, 114 mmol) and AgF (29 g, 228.5 mmol) were dissolved in dry DMSO (400 mL) in a flow of argon. Bis(benzonitrile)palladium(II) dichloride (2.17 g, 5.17 mmol) was added, and the reaction mixture was shielded from light by wrapping the flask with aluminum foil. The reaction mixture was heated to 85 °C for 14 h. The same amounts of AgF and bis(benzonitrile)palladium(II) dichloride were added once more, and the reaction was continued under stirring at 85 °C for 5 h. The reaction mixture was cooled to room temperature, and the solvent was removed in vacuo. The resulting residue was loaded onto celite (500 mL) from a DCM suspension (2 L), and the filtrate was concentrated in vacuo. Purification by column chromatography (silica gel, DCM) yielded compound **1c** as a yellow crystalline powder (12.5 g, 60% yield). Crystals suitable for single-crystal X-ray analysis were obtained by recrystallization from a hot ethyl acetate solution.

$^1\text{H}$  NMR (400 MHz,  $\text{CDCl}_3$ ):  $\delta$  = 6.89 (s, 2H), 6.67 (s, 2H), 3.68 (s, 6H), 2.84 (t,  $J$  = 7.4 Hz), 4H), 2.39 (t,  $J$  = 7.4 Hz), 4H), 2.00 (p,  $J$  = 7.4 Hz), 4H) ppm.  $^{13}\text{C}$  NMR (101 MHz,  $\text{CDCl}_3$ ):  $\delta$  = 173.65, 142.97, 135.63, 125.27, 122.86, 51.59, 33.07, 29.33, 26.61 ppm. HRMS (ESI): calcd for  $\text{C}_{18}\text{H}_{22}\text{O}_4\text{S}_2$ : 367.1035 ( $[\text{M}+\text{H}]^+$ ); found: 367.1038.  $R_f$ : 0.36 (DCM). M.p. (DSC in  $\text{N}_2$ ): 61 °C.

**2,2'-(2,2'-Bithiophene-5,5'-diyl)bis (N-propylacetamide) (2a).**  $\text{Pd}(\text{OAc})_2$  (10 mol %) was dissolved in DMSO (125 mL) in an oxygen atmosphere. Then, TFA (5.6 mL, 73.6 mmol, 1 equiv.) and compound **6a** (13.5 g, 73.6 mmol, 1 equiv.) were added to the reaction mixture. The reaction mixture was heated to 60 °C for 48 h. After completion of the reaction, all volatiles were removed in vacuo. The crude product was then suspended in EtOH (300 mL) and filtered off. Subsequent extraction of the solid residue with dioxane using a Soxhlet apparatus for 24 h furnished the desired compound **2a** as a white powder (4.6 g, 34% yield).

## 7.2. Synthesis Procedures and Analytical Data for Compounds

$^1\text{H}$ NMR (400 MHz,  $\text{CD}_2\text{Cl}_2$ ):  $\delta$  = 7.02 (d,  $J$  = 3.7 Hz), 2H), 6.83 (dd,  $J$  = 3.6, 0.9 Hz), 2H), 5.66 (s, 2H), 3.68 (s, 4H), 3.22–3.07 (m, 4H), 1.47 (h,  $J$  = 14.6, 7.3 Hz), 4H), 0.88 (t,  $J$  = 7.4 Hz), 6H) ppm.  $^{13}\text{C}$  NMR (101 MHz,  $\text{CD}_2\text{Cl}_2$ ):  $\delta$  = 169.49, 137.64, 136.55, 128.38, 124.02, 41.94, 38.34, 23.32, 11.62 ppm. HRMS (ESI): calcd for  $\text{C}_{18}\text{H}_{24}\text{N}_2\text{NaO}_2\text{S}_2$ : 387.1171 ( $[\text{M}+\text{Na}]^+$ ); found: 387.1161. M.p. (DSC in  $\text{N}_2$ ): 237 °C.

**3,3'-(2,2'-Bithiophene-5,5'-diyl)bis(*N*-propylpropanamide) (2b).** The dipropionic acid **5b** (0.5 g, 1.6 mmol) was suspended in DMF (10 mL). 1-Ethyl-3-(3-dimethylaminopropyl)carbodiimide (EDCI) (0.68 g, 3.54 mmol, 2.2 equiv.) and 1-hydroxybenzotriazole monohydrate (HOBt) (0.54 g, 3.54 mmol, 2.2 equiv.) were then added. The mixture was stirred at room temperature for 30 min, propylamine (0.29 mL, 3.54 mmol, 2.2 equiv.) and *N,N*-diisopropylethylamine (DIPEA) (1.2 mL, 6.7 mmol, 4.2 equiv.) were added, and the resulting solution was stirred at room temperature for 12 h. The solvent was removed in vacuo, 150 mL of water was added, and the precipitate was filtered off, washed with water, and dried in vacuo. Yellow, needle-like single crystals of **2b** (0.5 g, 79% yield) suitable for X-ray analysis were obtained by vapor diffusion recrystallization from dioxane and *n*-heptane.

$^1\text{H}$  NMR (400 MHz,  $\text{DMSO}-d_6$ ):  $\delta$  = 7.85 (t,  $J$  = 5.7 Hz), 2H), 6.97 (d,  $J$  = 3.6 Hz), 2H), 6.76 (d,  $J$  = 3.6 Hz), 2H), 3.16–2.80 (m, 8H), 2.41 (t,  $J$  = 7.4 Hz), 4H), 1.38 (h,  $J$  = 7.3 Hz), 4H), 0.81 (t,  $J$  = 7.2 Hz), 6H) ppm.  $^{13}\text{C}$  NMR (101 MHz,  $\text{DMSO}-d_6$ ):  $\delta$  = 170.46, 142.95, 134.59, 125.53, 122.82, 40.30, 36.79, 25.43, 22.35, 11.38 ppm. HRMS (ESI): calcd for  $\text{C}_{20}\text{H}_{28}\text{N}_2\text{NaO}_2\text{S}_2$  ( $[\text{M}+\text{Na}]^+$ ): 415.1484; found: 415.1490. M.p. (DSC in  $\text{N}_2$ ): 211 °C.

**4,4'-(2,2'-Bithiophene-5,5'-diyl)bis (*N*-propylbutanamide) (2c).** The dibutyric acid **5c** (0.51 g, 1.51 mmol) was suspended in DMF (10 mL). 1-Ethyl-3-(3-dimethylaminopropyl)carbodiimide (EDCI) (0.63 g, 3.32 mmol, 2.2 equiv.) and 1-hydroxybenzotriazole monohydrate (HOBt) (0.51 g, 3.32 mmol, 2.2 equiv.) were then added. The mixture was stirred at room temperature for 30 min, propylamine (0.27 mL, 3.32 mmol, 2.2 equiv.) and *N,N*-diisopropylethylamine (DIPEA) (1.1 mL, 6.34 mmol, 4.2 equiv.) were added, and the resulting solution was stirred at room temperature for 12 h. The solvent was removed in vacuo, and the crude product was suspended in water (150 mL). The resulting precipitate was filtered off, washed with water, and dried in vacuo. Yellow, needle-like single-crystals of **2c** (0.55 g, 87% yield) suitable for X-ray analysis were obtained by vapor diffusion recrystallization from dioxane and *n*-heptane.

$^1\text{H}$  NMR (400 MHz,  $\text{DMSO}-d_6$ ):  $\delta$  = 7.78 (s, 2H), 7.00 (s, 2H), 6.76 (s, 2H), 2.99 (q,  $J$  = 6.3 Hz), 4H), 2.74 (t,  $J$  = 7.3 Hz), 4H), 2.12 (t,  $J$  = 7.2 Hz), 4H), 1.82 (p,  $J$  = 7.1 Hz), 4H), 1.39 (h,  $J$  = 6.9 Hz), 4H), 0.83 (t,  $J$  = 7.3 Hz), 6H) ppm.  $^{13}\text{C}$  NMR (101 MHz,  $\text{DMSO}-d_6$ ):  $\delta$  = 171.79, 143.96, 134.94, 126.02, 123.47, 40.70, 34.94, 29.33, 27.67, 22.89, 11.90 ppm. HRMS (ESI): calcd for  $\text{C}_{22}\text{H}_{32}\text{N}_2\text{O}_2\text{S}_2$  ( $[\text{M}+\text{H}]^+$ ): 421.1979; found: 421.1983.  $R_f$ : 0.63 (DCM/MeOH 39:1); M.p. (DSC in  $\text{N}_2$ ): 160°C.

**Methyl 2-(thiophen-2-yl)acetate (4a).** A solution of 2-thiopheneacetic acid **3a** (26 g, 189 mmol) in methanol (500 mL) and concentrated H<sub>2</sub>SO<sub>4</sub> (0.25 mL) were refluxed for 8 h. The mixture was cooled to room temperature, diluted with diisopropylether, washed three times with 10% NaHCO<sub>3</sub> and dried over MgSO<sub>4</sub>. Evaporation of the solvent yielded methyl 2-(thiophen-2-yl)acetate **4a** as a clear brown liquid, which was used without further purification (27.1 g, 95% yield).

<sup>1</sup>H NMR (400 MHz, CDCl<sub>3</sub>): δ = 7.22 (dd, *J* = 4.9, 1.5 Hz), 1H), 7.00–6.90 (m, 1H), 3.85 (s, 2H), 3.73 (s, 3H) ppm. <sup>13</sup>C NMR (101 MHz, CDCl<sub>3</sub>): δ = 171.05, 135.12, 126.98, 126.96, 125.18, 52.39, 35.34 ppm. HRMS (APCI): calcd for C<sub>7</sub>H<sub>8</sub>O<sub>2</sub>S: 156.0240 [*M*]<sup>+</sup>; found: 156.0240. *R*<sub>f</sub>: 0.72 (DCM).

**Methyl 3-(thiophen-2-yl)propanoate (4b).** A solution of 2-thiophenepropionic acid **3b** (26 g, 166.45 mmol) in methanol (500 mL) and concentrated H<sub>2</sub>SO<sub>4</sub> were refluxed for 8 h. The mixture was cooled to room temperature, diluted with diisopropylether, washed three times with 10% NaHCO<sub>3</sub> and dried over MgSO<sub>4</sub>. Evaporation of the solvent yielded methyl 3-(thiophen-2-yl)propanoate **4b** as a clear brown liquid, which was used without further purification (27.33 g, 96% yield).

<sup>1</sup>H NMR (400 MHz, CDCl<sub>3</sub>): δ = 7.13 (dd, *J* = 5.2, 1.2 Hz), 1H), 6.92 (dd, *J* = 5.2, 3.5 Hz), 1H), 6.84–6.78 (m, 1H), 3.69 (s, 3H), 3.17 (t, *J* = 7.6 Hz), 2H), 2.69 (t, *J* = 7.6 Hz), 2H) ppm. <sup>13</sup>C NMR (101 MHz, CDCl<sub>3</sub>): δ = 172.82, 143.05, 126.85, 124.66, 123.54, 51.73, 35.98, 25.16 ppm. HRMS (APPI): calcd for C<sub>8</sub>H<sub>10</sub>O<sub>2</sub>S: 170.0396 [*M*]<sup>+</sup>; found: 170.0396. *R*<sub>f</sub>: 0.73 (DCM).

**Methyl 4-(thiophen-2-yl)butanoate (4c).** A solution of 4-(thiophen-2-yl)butyric acid **3c** (24 g, 141 mmol) in methanol (500 mL) and concentrated H<sub>2</sub>SO<sub>4</sub> (0.25 mL) were refluxed for 8 h. The mixture was cooled to room temperature, diluted with diisopropylether, washed three times with 10% NaHCO<sub>3</sub>, and dried over MgSO<sub>4</sub>. Evaporation of the solvent yielded methyl 4-(thiophen-2-yl)butanoate **4c** as a clear brown liquid, which was used without further purification (25.1 g, 97% yield).

<sup>1</sup>H NMR (400 MHz, CDCl<sub>3</sub>): δ = 7.12 (d, *J* = 5.0 Hz), 1H), 6.92 (dd, *J* = 5.1, 3.6 Hz), 1H), 6.80 (d, *J* = 2.9 Hz), 1H), 3.67 (s, 3H), 2.88 (t, *J* = 7.4 Hz), 2H), 2.38 (t, *J* = 7.4 Hz), 2H), 2.01 (p, *J* = 7.5 Hz), 2H) ppm. <sup>13</sup>C NMR (101 MHz, CDCl<sub>3</sub>): δ = 173.82, 144.18, 126.90, 124.66, 123.36, 51.69, 33.27, 29.25, 26.93 ppm. HRMS (APCI): calcd for C<sub>9</sub>H<sub>12</sub>O<sub>2</sub>S: 184.0553 [*M*]<sup>+</sup>; found: 184.0551. *R*<sub>f</sub>: 0.7 (DCM).

**2,2'-(2,2'-Bithiophene-5,5'-diyl)diacetic acid (5a).** The bithiophene diester **1a** (2 g, 6.4 mmol) and LiOH (0.96 g, 40 mmol) were dissolved in a mixture of THF/H<sub>2</sub>O (50 mL, 1:1). The mixture was refluxed for 8 h. The THF was removed in vacuo, after cooling the solution to room temperature. The aqueous residue was diluted with more water (50 mL) and acidified to pH 1



## 7.2. Synthesis Procedures and Analytical Data for Compounds

with HCl (6 M). The resulting precipitate was filtered off and washed several times with water. After drying in vacuo, compound **5a** was obtained as a yellow powder and used without further purification (1.75 g, 96% yield).

$^1\text{H}$  NMR (400 MHz, DMSO- $d_6$ ):  $\delta$  = 12.61 (s, 2H), 7.06 (d,  $J$  = 3.6 Hz), 2H), 6.88 (d,  $J$  = 3.6 Hz), 2H), 3.81 (s, 4H) ppm.  $^{13}\text{C}$  NMR (101 MHz, DMSO- $d_6$ ):  $\delta$  = 172.00, 136.32, 135.89, 128.23, 123.37, 35.49 ppm. HRMS (APPI): calcd for  $\text{C}_{12}\text{H}_{10}\text{O}_4\text{S}_2$  [ $M$ ] $^+$ : 282.0015; found: 282.0008. M.p. (DSC in  $\text{N}_2$ ): 229 °C.

**3,3'-(2,2'-Bithiophene-5,5'-diyl)dipropionic acid (5b).** The bithiophene diester **1b** (14.6 g, 43.1 mmol) and LiOH (6.2 g, 258.8 mmol) were dissolved in a mixture of THF/ $\text{H}_2\text{O}$  (400 mL, 1:1). The mixture was then refluxed for 8 h. The THF was removed in vacuo, after cooling the solution to room temperature. The aqueous residue was diluted with more water (150 mL) and acidified to pH 1 with an aqueous HCl solution (6 M). The resulting precipitate was filtered off and washed several times with water. After drying in vacuo, compound **5b** was obtained as a yellow powder and used without further purification (12.2 g, 91% yield).

$^1\text{H}$  NMR (400 MHz, DMSO- $d_6$ ):  $\delta$  = 12.27 (s, 2H), 7.00 (d,  $J$  = 3.6 Hz), 2H), 6.80 (d,  $J$  = 3.6 Hz), 2H), 2.99 (t,  $J$  = 7.3 Hz), 4H), 2.58 (t,  $J$  = 7.3 Hz), 4H) ppm.  $^{13}\text{C}$  NMR (101 MHz, DMSO- $d_6$ ):  $\delta$  = 173.77, 142.97, 135.09, 126.23, 123.50, 35.71, 25.28 ppm. HRMS (ESI): calcd for  $\text{C}_{14}\text{H}_{14}\text{O}_4\text{S}_2$  ([ $M$ -H] $^-$ ): 309.0251; found: 309.0255. M.p. (DSC in  $\text{N}_2$ ): 243 °C.

**4,4'-(2,2'-Bithiophene-5,5'-diyl)dibutyric acid (5c).** The diester **1c** (10 g, 27.29 mmol) and LiOH (3.92 g, 163.2 mmol) were dissolved in a mixture of THF/ $\text{H}_2\text{O}$  (400 mL, 1:1). The reaction mixture was then refluxed for 8 h. The THF was removed in vacuo, after cooling the solution to room temperature. The aqueous residue was diluted with more water (200 mL) and acidified to pH 1 with an aqueous HCl solution (6 M). The resulting precipitate was filtered off and washed several times with water. After drying in vacuo, compound **5c** was obtained as a white powder and used without further purification (8.8 g, 95% yield).

$^1\text{H}$  NMR (400 MHz, DMSO- $d_6$ ):  $\delta$  = 12.09 (s, 2H), 7.01 (s, 2H), 6.78 (s, 2H), 2.78 (t,  $J$  = 7.5 Hz), 4H), 2.28 (t,  $J$  = 7.3 Hz), 4H), 1.83 (p,  $J$  = 7.4 Hz), 4H) ppm.  $^{13}\text{C}$  NMR (101 MHz, DMSO- $d_6$ ):  $\delta$  = 174.52, 143.72, 134.98, 126.12, 123.54, 33.23, 29.08, 26.88 ppm. HRMS (ESI): calcd for  $\text{C}_{16}\text{H}_{18}\text{O}_4\text{S}_2$  ([ $M$ -H] $^-$ ): 337.0569; found: 337.0568. ; M.p. (DSC in  $\text{N}_2$ ): 165 °C.

**N-propyl-2-(thiophen-2-yl)acetamide (6a).** 2-Thiopheneacetyl chloride (10 mL, 80.9 mmol, 1 equiv.) was added slowly to propylamine (35.2 mL, 428.9 mmol, 5.3 equiv.) at 0 °C over 30 min. During this addition, HCl gas was formed, which was scavenged by a gentle stream of argon that was bubbled through a 2 M NaOH solution. After completion of the addition, the reaction mixture was allowed to warm up to room temperature and stirred for another 30 min. All volatiles were removed in vacuo. The resulting crude product was dissolved in DCM. The

organic phase was washed three times with 1 M HCl and once with a saturated aqueous NaCl solution, and finally dried over  $\text{MgSO}_4$ . Evaporation of solvent furnished compound **6a** as light-brown crystalline powder, which was used without further purification in the next step (13.5 g, 91% yield).

$^1\text{H}$  NMR (400 MHz,  $\text{CDCl}_3$ ):  $\delta$  = 7.24 (dd,  $J$  = 5.2, 1.2 Hz), 1H), 6.99 (dd,  $J$  = 5.2, 3.4 Hz), 1H), 6.95–6.89 (m, 1H), 5.69 (s, 1H), 3.76 (s, 2H), 3.23–3.12 (m, 2H), 1.46 (h,  $J$  = 7.3 Hz), 2H), 0.85 (t,  $J$  = 7.4 Hz), 3H) ppm.  $^{13}\text{C}$  NMR (101 MHz,  $\text{CDCl}_3$ ):  $\delta$  = 169.96, 136.46, 127.51, 127.49, 125.70, 41.50, 37.69, 22.77, 11.33 ppm. HRMS (ESI): calcd for  $\text{C}_9\text{H}_{14}\text{NOS}$ : 184.0791 ( $[\text{M}+\text{H}]^+$ ); found: 184.0794.

## 7.2.2 OFET Performance of a Hydrogen-Bonded Quaterthiophene

The synthetic precursors 2-(5-bromo-2-thienyl)ethyl acetate and 5,5'-bis(tributylstannyl)-2,2'-bithiophene were prepared as reported in the literature.<sup>297,368</sup>

**(5,5-Bis(2-acetyloxyethyl)-2,2:5,2:5,2-quaterthiophene).** 2-(5-bromo-2-thienyl)ethyl acetate (3.43 g, 13.77 mmol) and 5,5'-bis(tributylstannyl)-2,2'-bithiophene (5.00 g, 6.72 mmol) were dissolved in 50 mL DMF in an inert atmosphere in a well-dried 100 mL Schlenk flask. Tetrakis(triphenylphosphine)palladium ( $\text{Pd}(\text{PPh}_3)_4$ ) (35 mg, 0.03 mmol) was added, and the reaction mixture was stirred overnight at 80 °C. After allowing the mixture to cool to room temperature, an orange precipitate formed that was filtered off and washed with diisopropylether (150 mL) as well as diethylether (50 mL). The residue was dried in vacuum and purified by column chromatography (silica gel, DCM/*n*-heptane 4:1). The product was isolated as a yellow powder in 55% yield (1.87 g). Single crystals of **2** suitable for X-ray crystal structure analysis were grown from a toluene solution by slow evaporation at room temperature over 3–4 weeks.

$^1\text{H}$  NMR (400 MHz,  $\text{CD}_2\text{Cl}_2$ ):  $\delta$  = 7.08 (d,  $J$  = 3.8 Hz), 2H, Ar-H), 7.02–7.06 (m, 4H, Ar-H), 6.80 (d,  $J$  = 3.8 Hz), 2H, Ar-H), 4.28 (t,  $J$  = 6.6 Hz), 4H,  $\text{CH}_2$ ), 3.13 (t,  $J$  = 6.6 Hz), 4H,  $\text{CH}_2$ ), 2.06 (s, 6H,  $\text{CH}_3$ ) ppm.  $^{13}\text{C}$  NMR (101 MHz,  $\text{CD}_2\text{Cl}_2$ ):  $\delta$  = 20.63, 29.43, 64.16, 123.47, 123.88, 124.14, 126.40, 135.39, 135.41, 136.31, 139.99, 170.55, 139.99, 136.31, 135.41, 135.39, 126.40, 124.14, 123.88, 123.47, 64.16, 29.43, 20.63 ppm. HRMS (APCI): calcd  $\text{C}_{24}\text{H}_{22}\text{O}_4\text{S}_4$  ( $[\text{M}]^+$ ) 503.0479; found: 503.0477.  $R_f$  (DCM/*n*-heptane 4:1): 0.25.

## 7.2.3 Engineering Polymers from Bithiophene-Containing Polyamides

**General Procedure for the Synthesis of Semiaromatic Polyamides (PA/*n*T2).** A flame-dried 50 mL Schlenk tube equipped with a stirring bar was charged with the aliphatic diamine (0.50–3.00 mmol), bithiophene dibutyric acid **T2** (1.00 eq.), a mixture of anhydrous *N*-Methyl-2-pyrrolidone (NMP) and anhydrous pyridine (4:1, 3–11 mL), triphenylphosphite (TPP) (2.01 equiv.), as well as anhydrous LiCl (4 wt%) in a flow of argon. The suspension was heated to 120 °C

## 7.2. Synthesis Procedures and Analytical Data for Compounds

under vigorous stirring. After 4 h, the solution was poured into MeOH (250 mL). The resulting precipitate was filtered off, washed several times with hot MeOH, and dried in vacuum to yield the desired polyamide **PA<sub>n</sub>T2** as a yellow powder.

**Poly(hexamethylene bithiophenedibutanamide) (PA6T2).** The general procedure for the synthesis of semiaromatic polyamides was followed, starting from 1,6-hexanediamine (316 mg, 2.72 mmol) and bithiophene dibutyric acid **T2** (2.72 mmol), to give the desired polyamide **PA6T2** in a yield of 1.04 g (90%) after precipitation.

<sup>1</sup>H NMR (400 MHz, acetone-*d*<sub>6</sub>):  $\delta$  = 6.10 (s, 2H), 5.83 (s, 2H), 5.26 (br, 2H), 2.33 (q,  $J$  = 6.1, 5.6 Hz), 4H), 1.93 (t,  $J$  = 6.0 Hz), 4H), 1.43–1.33 (m, 4H), 1.16–0.98 (m, 4H), 0.63 (br, 4H), 0.45 (br, 4H) ppm. GPC (HFIP):  $M_n$  = 13'500 ( $D$  = 1.5).

**Poly(heptamethylene bithiophenedibutanamide) (PA7T2).** The general procedure for the synthesis of semiaromatic polyamides was followed, starting from 1,7-heptanediamine (100 mg, 0.77 mmol) and bithiophene dibutyric acid **T2** (0.77 mmol), to give the desired polyamide **PA7T2** in a yield of 270 mg (88%) after precipitation.

<sup>1</sup>H NMR (400 MHz, acetone-*d*<sub>6</sub>):  $\delta$  = 6.10 (s, 2H), 5.84 (s, 2H), 5.22 (br, 2H), 2.34 (dd,  $J$  = 12.1, 6.2 Hz), 3H), 1.94 (t,  $J$  = 7.3 Hz), 3H), 1.39 (t,  $J$  = 7.3 Hz), 2H), 1.14–1.03 (m, 2H), 0.63 (br, 2H), 0.45 (br, 4H) ppm. GPC (HFIP):  $M_n$  = 12'500 ( $D$  = 1.6).

**Poly(octamethylene bithiophenedibutanamide) (PA8T2).** The general procedure was followed for the synthesis of semiaromatic polyamides, starting from 1,8-octanediamine (282 mg, 1.96 mmol) and bithiophene dibutyric acid **T2** (1.96 mmol), to give the desired polyamide **PA8T2** in a yield of 810 mg (90%) after precipitation.

<sup>1</sup>H NMR (400 MHz, acetone-*d*<sub>6</sub>):  $\delta$  = 6.10 (d,  $J$  = 1.9 Hz), 2H), 5.84 (s, 2H), 2.33 (dd,  $J$  = 12.7, 7.3 Hz), 4H), 1.94 (t,  $J$  = 7.0 Hz), 4H), 1.39 (t,  $J$  = 7.5 Hz), 4H), 1.14–1.03 (m, 4H), 0.63 (br, 2H), 0.44 (br, 8H) ppm. GPC (HFIP):  $M_n$  = 12'700 ( $D$  = 1.5).

**Poly(nonamethylene bithiophenedibutanamide) (PA9T2).** The general procedure for the synthesis of semiaromatic polyamides was followed, starting from 1,9-nonanediamine (146 mg, 0.92 mmol) and bithiophene dibutyric acid **T2** (0.92 mmol), to give the desired polyamide **PA9T2** in a yield of 390 mg (88%) after precipitation.

<sup>1</sup>H NMR (400 MHz, acetone-*d*<sub>6</sub>):  $\delta$  = 6.10 (d,  $J$  = 2.7 Hz), 2H), 5.84 (s, 2H), 5.20 (br, 2H), 2.33 (dd,  $J$  = 11.5, 5.4 Hz), 4H), 1.95 (t,  $J$  = 5.4 Hz), 4H), 1.39 (t,  $J$  = 7.7 Hz), 4H), 1.14–1.03 (m, 4H), 0.62 (br, 4H), 0.43 (br, 10H) ppm. GPC (HFIP):  $M_n$  = 10'600 ( $D$  = 2).

**Poly(decamethylene bithiophenedibutanamide) (PA10T2).** The general procedure for the synthesis of semiaromatic polyamides was followed, starting from 1,10-decanediamine (146 mg, 0.85 mmol) and bithiophene dibutyric acid **T2** (0.85 mmol), to give the desired polyamide **PA10T2** in a yield of 380 mg (91%) after precipitation.

$^1\text{H}$  NMR (400 MHz, acetone- $d_6$ ):  $\delta$  = 6.08 (d,  $J$  = 2.3 Hz), 2H), 5.81 (d,  $J$  = 2.1 Hz), 2H), 5.17 (br, 2H), 2.30 (d,  $J$  = 6.0 Hz), 4H), 1.92 (t,  $J$  = 6.6 Hz), 4H), 1.36 (t,  $J$  = 7.2 Hz), 4H), 1.15–0.97 (m, 4H), 0.59 (br, 4H), 0.40 (br, 12H) ppm. GPC (HFIP):  $M_n$  = 10'300 ( $\bar{D}$  = 2).

**Poly(undecamethylene bithiophenedibutanamide) (PA11T2).** The general procedure was followed for the synthesis of semiaromatic polyamides, starting from 1,11-undecanediamine (120 mg, 0.64 mmol) and bithiophene dibutyric acid **T2** (0.64 mmol), to give the desired polyamide **PA11T2** in a yield of 300 mg (86%) after precipitation.

$^1\text{H}$  NMR (400 MHz, acetone- $d_6$ ):  $\delta$  = 6.14–6.06 (m, 2H), 5.84 (s, 2H), 5.20 (br, 2H), 2.32 (dd,  $J$  = 11.4, 5.2 Hz), 4H), 2.02–1.88 (m, 4H), 1.48–1.30 (m, 4H), 1.15–1.02 (m, 4H), 0.61 (br, 4H), 0.42 (br, 14H) ppm. GPC (HFIP):  $M_n$  = 8'600 ( $\bar{D}$  = 1.9).

**Poly(dodecamethylene bithiophenedibutanamide) (PA12T2).** The general procedure for the synthesis of semiaromatic polyamides was followed, starting from 1,12-dodecanediamine (142 mg, 0.71 mmol) and bithiophene dibutyric acid **T2** (0.71 mmol), to give the desired polyamide **PA12T2** in a yield of 330 mg (89%) after precipitation.

$^1\text{H}$  NMR (400 MHz, acetone- $d_6$ ):  $\delta$  = 6.07 (d,  $J$  = 2.2 Hz), 2H), 5.81 (s, 2H), 5.16 (s, 2H), 2.30 (d,  $J$  = 5.9 Hz), 4H), 1.92 (s, 4H), 1.36 (t,  $J$  = 7.0 Hz), 4H), 1.14–0.95 (m, 4H), 0.59 (br, 4H), 0.39 (br, 16H) ppm. GPC (HFIP):  $M_n$  = 10'700 ( $\bar{D}$  = 1.9).

### 7.2.4 Semiaromatic Polyamides Containing Perylene Bisimide Repeat Units

Chlorendic hydroxyimide<sup>297</sup> and 1,7-dibromoperylene-3,4:9,10-tetracarboxylic dianhydride **2** were prepared as published previously.<sup>333</sup>

**1,7-Dibromoperylene-3,4:9,10-tetracarboxylic dianhydride (2).** Perylene-3,4:9,10-tetracarboxylic acid bisanhydride (20 g, 51 mmol) was suspended in concentrated  $\text{H}_2\text{SO}_4$  (300 mL). This mixture was stirred for 16 h at room temperature before powdered iodine (0.52 g, 2.05 mmol) was added. It was then heated to 85 °C, and bromine (5.8 mL, 112 mmol, 2.2 equiv.) added dropwise over 6 h. On completion of the addition, the reaction mixture was heated for a further 48 h and then allowed to cool to room temperature. The excess bromine was removed with a gentle stream of argon and reduced by bubbling the stream through a saturated  $\text{Na}_2\text{S}_2\text{O}_3$  solution. After cooling to 0 °C, 100 mL of deionized water was carefully added. Filtration of the resulting precipitate and washing with concentrated  $\text{H}_2\text{SO}_4$  (50 mL) and deionized

## 7.2. Synthesis Procedures and Analytical Data for Compounds

water (2 L) yielded a red solid powder, comprising a mixture of 1,7-dibromo, 1,6-dibromo and 1,7,6-tribromoperylene bisimide in a ratio of 75:17:8, as revealed by  $^1\text{H}$  NMR in conc.  $\text{D}_2\text{SO}_4$  (96–98% in  $\text{D}_2\text{O}$ ). This mixture was used without further purification in the next step (26.4 g, 97%). HRMS (APPI): calcd for  $\text{C}_{24}\text{H}_6\text{Br}_2\text{O}_6$ : 547.8537  $[M]^-$ ; found: 547.8519.

### **1,7-Dibromoperylene-3,4:9,10-tetracarboximide-*N,N'*-di(butanoic acid) di(*tert*-butyl ester)**

**(3).** Compound **2** (13 g, 23.6 mmol), 4-aminobutyric acid *tert*-butyl ester hydrochloride (19 g, 97.1 mmol) and  $\text{Zn}(\text{OAc})_2$  (4.3 g, 23.6 mmol) were suspended in freshly distilled quinoline (350 mL) in an argon flow. The reaction mixture was heated to 100 °C for 16 h and then cooled to room temperature prior to solvent removal in vacuum. The resulting residue was redissolved in DCM (2 L), washed twice with 1 M HCl twice and once with brine, and finally dried over  $\text{MgSO}_4$ . After solvent removal, the crude product was purified by column chromatography (silica gel, 5% EtOAc in DCM) to give **3** as a mixture of the 1,7-dibromo and the 1,6-dibromo regioisomers (75:25) as a dark red powder (15.5 g, 79% yield).

$^1\text{H}$  NMR (400 MHz,  $\text{CDCl}_3$ ):  $\delta$  = 9.50 (d,  $J$  = 8.2 Hz), 2H), 8.94 (s, 2H), 8.72 (d,  $J$  = 8.1 Hz), 2H), 4.28 (t,  $J$  = 7.2 Hz), 4H), 2.39 (t,  $J$  = 7.4 Hz), 4H), 2.19–1.90 (m, 4H), 1.44 (s, 18H) ppm.  $^{13}\text{C}$  NMR (101 MHz,  $\text{CDCl}_3$ , [m,n] stands for the corresponding isomer):  $\delta$  = 172.19, 163.21 [1,6], 162.83 [1,7], 162.33 [1,7], 161.97 [1,6], 138.13 [1,6], 138.04 [1,7], 133.09 [1,6], 132.84 [1,7], 132.71 [1,7], 132.29 [1,6], 130.02 [1,7], 129.90 [1,6], 129.10 [1,7], 128.46 [1,7], 128.10 [1,6], 127.87 [1,6], 127.70 [1,6], 126.89 [1,7], 126.06 [1,6], 123.28 [1,6], 123.09 [1,7], 122.65 [1,7], 122.35 [1,6], 121.70 [1,6], 120.90 [1,7], 80.53, 40.13, 33.27, 28.21, 23.59 ppm. HRMS (APPI): calcd for  $\text{C}_{40}\text{H}_{36}\text{Br}_2\text{N}_2\text{O}_8$ : 830.0833  $[M]^+$ ; found: 830.0819.  $R_f$ : 0.34 (5% EtOAc in DCM).

### **1,7-Dicyanoperylene-3,4:9,10-tetracarboximide-*N,N'*-di(butanoic acid) di(*tert*-butyl ester)**

**(4).** Compound **3** (13.5 g, 15.95 mmol),  $\text{Zn}(\text{OAc})_2$  (15.9 g, 135.55 mmol), tris(dibenzylideneacetone)-dipalladium(0) ( $\text{Pd}_2(\text{dba})_3$ ) (3.65 g, 4 mmol) and 1,1'-bis(diphenylphosphino)-ferrocene (dppf) (2.21 g, 4 mmol), were suspended in dry dioxane (1 L) in an argon atmosphere. The dark-orange suspension was heated to 95 °C for 48 h and then cooled to room temperature. The amount of solvent was reduced to about one third in vacuum, before diluting the solution with DCM (600 mL) and filtering over celite. After solvent removal, the crude product was suspended in EtOAc, filtered, and purified by column chromatography (silica gel, 7% EtOAc in DCM) to give **4** as a mixture of the 1,7-dibromo and the 1,6-dibromo regioisomers (75:25) as a red solid powder (4.6 g, 40%).

$^1\text{H}$  NMR (400 MHz, TFA-*d*: $\text{CD}_2\text{Cl}_2$  = 1:3, [m,n] stands for the corresponding isomer):  $\delta$  = 9.79–9.68 (m, [1,6] and [1,7], 2H), 9.18 (s, [1,6], 2H), 9.13 (s, [1,7], 2H), 9.04 (d, [1,7],  $J$  = 8.2 Hz), 2H), 8.98 (d, [1,6],  $J$  = 8.2 Hz), 2H), 4.41 (t,  $J$  = 7.1 Hz), 4H), 2.69 (t,  $J$  = 7.3 Hz), 4H), 2.22 (m, 4H), 1.59 (s, 18H) ppm.  $^{13}\text{C}$  NMR (101 MHz, TFA-*d*: $\text{CD}_2\text{Cl}_2$  = 1:3):  $\delta$  = 181.30, 165.13 [1,6], 164.60 [1,7], 163.92 [1,7], 163.40 [1,6], 140.07 [1,6], 139.75 [1,6], 138.17 [1,7], 137.84, [1,7], 135.45 [1,7], 133.66 [1,7], 133.26 [1,6], 132.00 [1,6], 130.54 [1,7], 130.34 [1,7], 129.06 [1,6], 128.29

[**1,6**], 127.71 [**1,7**], 127.09 [**1,6**], 125.87 [**1,6**], 124.96 [**1,7**], 123.99 [**1,7**], 123.19 [**1,6**], 118.99 [**1,7**], 109.46 [**1,6**], 109.10 [**1,7**], 89.72, 41.32, 31.94, 27.84, 23.33 ppm. HRMS (APPI): calcd for  $C_{42}H_{36}N_4O_8$ : 724.2528  $[M]^+$ ; found: 724.2528.  $R_f$ : 0.38 (7% EtOAc in DCM).

**1,7-Dicyanoperylene-3,4:9,10-tetracarboximide-*N,N'*-di(butanoic acid) (5).** Compound **4** (1.6 g, 2.2 mmol) was suspended in 180 mL  $CHCl_3$  before addition of TFA (96 mL, 1.2 mol). The mixture was heated to reflux and stirred for 15 h. It was then cooled to room temperature, and the volatiles removed under vacuum. The crude product was suspended in 1 M HCl (300 mL) and ultrasonicated for 20 min. Filtration and subsequent drying of the resulting precipitate yielded **5** as a mixture of the 1,7-dibromo and the 1,6-dibromo regioisomers (75:25) as a red solid powder (1.3 g, 96%), which was used without further purification in the next step.

$^1H$  NMR (400 MHz, TFA- $d$ : $CD_2Cl_2$  = 1:3, [**m,n**] stands for the corresponding isomer):  $\delta$  = 9.78–9.74 (m, [**1,6**] and [**1,7**], 2H), 9.22 (s, [**1,6**], 2H), 9.17 (s, [**1,7**], 2H), 9.08 (d, [**1,7**],  $J$  = 8.2 Hz), 2H), 9.01 (d, [**1,6**],  $J$  = 8.2 Hz), 2H), 4.44 (t,  $J$  = 7.0 Hz), 4H), 2.71 (t,  $J$  = 7.1 Hz), 4H), 2.30–2.20 (m, 4H) ppm.  $^{13}C$  NMR (101 MHz, TFA- $d$ : $CD_2Cl_2$  = 1:3):  $\delta$  = 180.54, 165.54 [**1,6**], 165.00 [**1,7**], 164.32 [**1,7**], 163.79 [**1,6**], 140.48 [**1,6**], 140.08 [**1,6**], 138.54 [**1,7**], 138.14, [**1,7**], 135.81 [**1,7**], 133.92 [**1,7**], 133.58 [**1,6**], 132.24 [**1,6**], 130.80 [**1,7**], 130.62 [**1,7**], 129.28 [**1,6**], 128.51 [**1,6**], 127.92 [**1,7**], 127.28 [**1,6**], 126.07 [**1,6**], 125.15 [**1,7**], 124.17 [**1,7**], 123.37 [**1,6**], 118.98 [**1,7**], 109.57 [**1,6**], 109.20 [**1,7**], 40.53, 31.02, 22.42 ppm. HRMS (APPI): calcd for  $C_{34}H_{20}N_4O_8$ : 612.1287 ( $[M]^-$ ); found: 612.1271.

**1,7-Dicyanoperylene-3,4:9,10-tetracarboximide-*N,N'*-bis(*N*-propylbutanamide) (6).** Compound **5** (100 mg, 0.16 mmol) was suspended in dry DMF (10 mL) in a flame-dried 50 mL Schlenk tube prior to the addition of chlorendic hydroxyimide (132 mg, 0.34 mmol) and *N,N'*-diisopropylcarbodiimide (DIC) (0.17 mL, 1.1 mmol, 6.5 equiv.) in an argon atmosphere. The reaction mixture was heated to 50 °C for 14 h. The volatiles were then removed in vacuum, and the residue was dissolved in dry THF (20 mL). Propylamine (0.27 mL, 3.3 mmol, 20 equiv.) was then added, and the reaction mixture was heated to 50 °C for 14 h. After removal of the volatiles, the crude product was suspended in MeOH. Filtration and subsequent washing with MeOH yielded **6** as a mixture of the 1,7-dibromo and the 1,6-dibromo regioisomers (75:25) as a dark red solid powder (95 mg, 84%).

$^1H$  NMR (800 MHz, TFA- $d$ , [**m,n**] stands for corresponding isomer):  $\delta$  = 9.94 (d, [**1,6**],  $J$  = 8.6 Hz), 2H), 9.93 (d, [**1,7**],  $J$  = 8.2 Hz), 2H), 9.37 (s, [**1,6**], 2H), 9.32 (s, [**1,7**], 2H), 9.24 (d, [**1,7**],  $J$  = 8.1 Hz), 2H), 9.17 (d, [**1,6**],  $J$  = 8.1 Hz), 2H), 4.60 (h,  $J$  = 7.6, 7.1 Hz), 4H), 3.74 (q,  $J$  = 8.0, 7.5 Hz), 4H), 3.06 (t,  $J$  = 7.3 Hz), 4H), 2.52 (p,  $J$  = 6.6 Hz), 4H), 1.93 (h,  $J$  = 7.2 Hz), 4H), 1.19 (t,  $J$  = 7.5 Hz), 6H) ppm.  $^{13}C$  NMR (201 MHz, TFA- $d$ ):  $\delta$  = 178.55, 165.73 [**1,6**], 165.18 [**1,7**], 164.47 [**1,7**], 163.94 [**1,6**], 140.35 [**1,6**], 139.61 [**1,6**], 138.44 [**1,7**], 137.65 [**1,7**], 135.47 [**1,7**], 133.62 [**1,7**], 133.19 [**1,6**], 132.00 [**1,6**], 131.92 [**1,6**], 130.35 [**1,7**], 130.13 [**1,7**], 128.75 [**1,6**], 127.95 [**1,6**], 127.33 [**1,7**], 126.66 [**1,6**], 125.12 [**1,6**], 124.30 [**1,7**], 123.32 [**1,7**], 122.63 [**1,6**], 117.68 [**1,6**], 117.12 [**1,7**], 108.86 [**1,6**],

## 7.2. Synthesis Procedures and Analytical Data for Compounds

108.45 [1,7], 45.13, 40.17, 30.96, 24.29, 21.18, 9.68 ppm. HRMS (APPI): calcd for  $C_{40}H_{35}N_6O_6$ : 695.2613 ( $[M+H]^+$ ); found: 695.2603.

**General Procedure for the Synthesis of Dicyanoperylene Bisimide-Containing Polyamides (PA $n$ PBICN2).** Compound **5** (250 mg, 0.41 mmol) was suspended in dry DMF (25 mL) in a flame-dried 50 mL Schlenk tube before the addition of chlorendic hydroxyimide (331 mg, 0.86 mmol) and *N,N'*-diisopropylcarbodiimide (DIC) (0.38 mL, 2.5 mmol, 6 equiv.) in an argon atmosphere. The reaction mixture was heated to 50 °C for 14 h. The volatiles were removed in vacuum, and the residue was dissolved in dry DMSO (10 mL). The aliphatic diamine (1 equiv.) was then added, and the reaction mixture was heated to 120 °C under vigorous stirring. After 48 h, the solution was poured into MeOH (250 mL), and the resulting slurry was stirred for 15 min. The precipitate was filtered off, washed several times with hot MeOH and dried in vacuum to yield the desired polyamide as dark red powder.

**General Procedure for the Derivatization of Dicyanoperylene Bisimide-Containing Polyamides (PA $n$ PBICN2).** For molecular weight determination by GPC, the polyamides were derivatized as follows. The polyamide **PA $n$ PBICN2** (20 mg) was suspended in dry DCM (3 mL) in a flame-dried 10 mL Schlenk tube before the addition of trifluoroacetic anhydride (TFAA) (0.8 mL, 5.75 mmol) in an argon atmosphere. The reaction mixture was stirred at room temperature for 48 h and the derivatized polyamides, i.e., the corresponding poly(trifluoroacetyl imide)s, were obtained by gently evaporating the volatiles at 40 °C. The polymers were soluble in HFIP ( $c = 3$  mg/mL).

**Poly(hexamethylene dicyanoperylene bisimide *N,N'*-dibutanamide) (PA6PBICN2).** The general procedure for the synthesis of dicyanoperylene bisimide-containing polyamides was followed, starting from **5** (250 mg, 0.41 mmol), chlorendic hydroxyimide (331 mg, 0.86 mmol), *N,N'*-diisopropylcarbodiimide (DIC) (0.38 mL, 2.5 mmol, 6 equiv.), and 1,6-hexanediamine (47 mg, 0.41 mmol), to give the desired polyamide **PA6PBICN2** in a yield of 240 mg (85%) after precipitation.

$^1H$  NMR (400 MHz, TFA-*d*:CDCl<sub>3</sub> = 1:3):  $\delta$  = 9.88–9.77 (m, 2H), 9.30–9.20 (m, 2H), 9.20–9.01 (m, 2H), 4.51 (br, 4H), 3.70 (br, 4H), 2.96 (br, 4H), 2.43 (br, 4H), 1.87 (br, 4H), 1.59 (br, 4H) ppm. GPC (HFIP):  $M_n = 9'700$  ( $D = 2.0$ ).

**Poly(octamethylene dicyanoperylene bisimide *N,N'*-dibutanamide) (PA8PBICN2).** The general procedure for the synthesis of dicyanoperylene bisimide-containing polyamides was followed, starting from **5** (250 mg, 0.41 mmol), chlorendic hydroxyimide (331 mg, 0.86 mmol), *N,N'*-diisopropylcarbodiimide (DIC) (0.38 mL, 2.5 mmol, 6 equiv.), and 1,8-octanediamine (58.85 mg, 0.41 mmol), to give the desired polyamide **PA8PBICN2** in a yield of 272 mg (92%) after precipitation.

$^1\text{H}$  NMR (400 MHz, TFA-*d*: $\text{CDCl}_3$  = 1:3):  $\delta$  = 9.92–9.72 (m, 2H), 9.30–9.20 (m, 2H), 9.20–9.05 (m, 2H), 4.51 (br, 4H), 3.69 (br, 4H), 2.96 (br, 4H), 2.43 (br, 4H), 1.85 (br, 2H), 1.51 (br, 8H) ppm. GPC (HFIP):  $M_n$  = 11'100 ( $D$  = 1.9).

**Poly(decamethylene dicyanoperylene bisimide *N,N'*-dibutanamide) (PA10PBICN2).** The general procedure for the synthesis of dicyanoperylene bisimide-containing polyamides was followed, starting from **5** (250 mg, 0.41 mmol), chlorendic hydroxyimide (331 mg, 0.86 mmol), *N,N'*-diisopropylcarbodiimide (DIC) (0.38 mL, 2.5 mmol, 6 equiv.), and 1,10-decanediamine (70.3 mg, 0.41 mmol), to give the desired polyamide **PA10PBICN2** in a yield of 280 mg (92%) after precipitation.

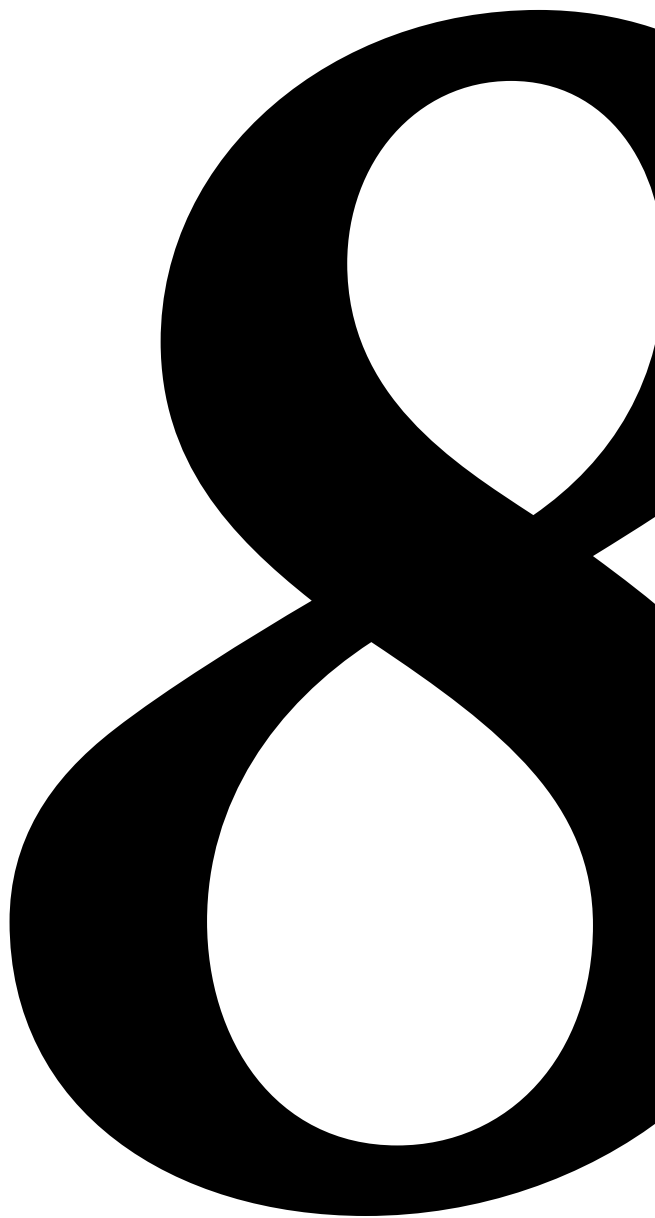
$^1\text{H}$  NMR (400 MHz, TFA-*d*: $\text{CDCl}_3$  = 1:3):  $\delta$  = 9.88–9.82 (m, 2H), 9.30–9.20 (m, 2H), 9.20–9.06 (m, 2H), 4.52 (br, 4H), 3.70 (br, 4H), 2.98 (br, 4H), 2.44 (br, 4H), 1.94–1.78 (m, 4H), 1.47 (m, 12H) ppm. GPC (HFIP):  $M_n$  = 9'400 ( $D$  = 2).

**Poly(dodecamethylene dicyanoperylene bisimide *N,N'*-dibutanamide) (PA12PBICN2).** The general procedure for the synthesis of dicyanoperylene bisimide-containing polyamides, was followed starting from **5** (250 mg, 0.41 mmol), chlorendic hydroxyimide (331 mg, 0.86 mmol), *N,N'*-diisopropylcarbodiimide (DIC) (0.38 mL, 2.5 mmol, 6 equiv.), and 1,12-dodecanediamine (81.7 mg, 0.41 mmol), to give the desired polyamide **PA12PBICN2** in a yield of 270 mg (85%) after precipitation.

$^1\text{H}$  NMR (400 MHz, TFA-*d*: $\text{CDCl}_3$  = 1:3):  $\delta$  = 9.92–9.82 (m, 2H), 9.30–9.20 (m, 2H), 9.20–9.05 (m, 2H), 4.51 (br, 4H), 3.69 (t,  $J$  = 7.2 Hz), 4H), 2.97 (br, 4H), 2.43 (m, 4H), 1.83 (br, 4H), 1.44 (m, 4H) ppm. GPC (HFIP):  $M_n$  = 15'500 ( $D$  = 2.0).



## **Bibliography**





## 8 Bibliography

- [1] G. Moore, *Electronics* **1965**, 114–117.
- [2] G. Moore, *IEEE, IEDM Tech Digest* **1975**, 11–13.
- [3] W. F.-W., B.-P. J., *International Journal of Earth Sciences* **2002**, 91, 723–745.
- [4] K. Binnemans, P. T. Jones, T. Müller, L. Yurramendi, *Journal of Sustainable Metallurgy* **2018**, 4, 126–146.
- [5] M. M. Waldrop, *Nature* **2016**, 530, 144–147.
- [6] H. Sirringhaus, *Advanced Materials* **2014**, 26, 1319–1335.
- [7] A. F. Paterson, S. Singh, K. J. Fallon, T. Hodsden, Y. Han, B. C. Schroeder, H. Bronstein, M. Heeney, I. McCulloch, T. D. Anthopoulos, *Advanced Materials* **2018**, 30, 1801079.
- [8] S. E. Root, S. Savagatrup, A. D. Printz, D. Rodriguez, D. J. Lipomi, *Chemical Reviews* **2017**, 117, 6467–6499.
- [9] H. Tran, V. R. Feig, K. Liu, Y. Zheng, Z. Bao, *Macromolecules* **2019**, 52, 3965–3974.
- [10] B. O'Connor, E. P. Chan, C. Chan, B. R. Conrad, L. J. Richter, R. J. Kline, M. Heeney, I. McCulloch, C. L. Soles, D. M. DeLongchamp, *ACS Nano* **2010**, 4, 7538–7544.
- [11] J. C. Sumrak, A. N. Sokolov, L. R. Macgillivray, “Crystal Engineering Organic Semiconductors”, in *Self-Organized Organic Semiconductors*, Q. Li (Ed.), John Wiley & Sons, Inc., Hoboken, NJ, USA, **2011**.
- [12] R. Noriega, J. Rivnay, K. Vandewal, F. P. V. Koch, N. Stingelin, P. Smith, M. F. Toney, A. Salleo, *Nature Materials* **2013**, 12, 1038–1044.
- [13] S. Himmelberger, A. Salleo, *MRS Communications* **2015**, 5, 383–395.
- [14] S. Wang, S. Fabiano, S. Himmelberger, S. Puzinas, X. Crispin, A. Salleo, M. Berggren, *Proceedings of the National Academy of Sciences* **2015**, 112, 10599–10604.
- [15] J. E. Northrup, *Applied Physics Letters* **2015**, 106, 023303.
- [16] H. E. A. Huitema, G. H. Gelinck, J. B. P. H. van der Putten, K. E. Kuijk, C. M. Hart, E. Cantatore, D. M. de Leeuw, *Advanced Materials* **2002**, 14, 1201–1204.
- [17] A. C. Arias, S. E. Ready, R. Lujan, W. S. Wong, K. E. Paul, A. Salleo, M. L. Chabinyc, R. Apte, R. A. Street, Y. Wu, P. Liu, B. Ong, *Applied Physics Letters* **2004**, 85, 3304.
- [18] S. Steudel, K. Myny, V. Arkhipov, C. Deibel, S. De Vusser, J. Genoe, P. Heremans, *Nature Materials* **2005**, 4, 597–600.
- [19] E. J. Meijer, D. M. de Leeuw, S. Setayesh, E. van Veenendaal, B. H. Huisman, P. W. M. Blom, J. C. Hummelen, U. Scherf, T. M. Klapwijk, *Nature Materials* **2003**, 2, 678–682.

- [20] H. Yan, Z. Chen, Y. Zheng, C. Newman, J. R. Quinn, F. Dötz, M. Kastler, A. Facchetti, *Nature* **2009**, 457, 679–686.
- [21] H. Lars, M. Cölle, S. Tierney, X. Crispin, M. Berggren, *Advanced Materials* **2009**, 22, 72–76.
- [22] J. Mei, D. H. Kim, A. L. Ayzner, M. F. Toney, Z. Bao, *Journal of the American Chemical Society* **2011**, 133, 20130–20133.
- [23] T. Lei, J.-H. Dou, J. Pei, *Advanced Materials* **2012**, 24, 6457–6461.
- [24] J. Li, Y. Zhao, H. S. Tan, Y. Guo, C.-A. Di, G. Yu, Y. Liu, M. Lin, S. H. Lim, Y. Zhou, H. Su, B. S. Ong, *Scientific Reports* **2012**, 2, 754.
- [25] F. P. V. Koch, J. Rivnay, S. Foster, C. Müller, J. M. Downing, E. Buchaca-Domingo, P. Westacott, L. Yu, M. Yuan, M. Baklar, Z. Fei, C. Luscombe, M. A. McLachlan, M. Heeney, G. Rumbles, C. Silva, A. Salleo, J. Nelson, P. Smith, N. Stingelin, *Progress in Polymer Science* **2013**, 38, 1978–1989.
- [26] K. Gu, Y. Loo, *Journal of Polymer Science Part B: Polymer Physics* **2019**, polb.24873.
- [27] A. Salleo, *Materials Today* **2007**, 10, 38–45.
- [28] A. Rahmanudin, L. Yao, K. Sivula, *Polymer Journal* **2018**, 50, 725–736.
- [29] J.-L. Brédas, *Materials Horizons* **2014**, 1, 17–19.
- [30] H. Sirringhaus, T. Sakanoue, J. Chang, *Physica Status Solidi (B)* **2012**, 249, 1655–1676.
- [31] J.-L. Brédas, J. P. Calbert, D. A. d. S. Filho, J. Cornil, *Proceedings of the National Academy of Sciences* **2002**, 99, 5804–5809.
- [32] H. Bässler, A. Köhler, “Charge Transport in Organic Semiconductors”, in *Unimolecular and Supramolecular Electronics IVol. 312*, R. M. Metzger (Ed.), Springer Berlin Heidelberg, Berlin, Heidelberg, **2011**.
- [33] A. Köhler, H. Bässler, *Electronic Processes in Organic Semiconductors*, Wiley-VCH Verlag GmbH & Co. KGaA, Weinheim, Germany, **2015**.
- [34] J.-L. Brédas, G. B. Street, *Accounts of Chemical Research* **1985**, 18, 309–315.
- [35] S. Himmelberger, J. Dacuña, J. Rivnay, L. H. Jimison, McCarthy, M. Heeney, I. McCulloch, M. F. Toney, A. Salleo, *Advanced Functional Materials* **2013**, 23, 2091–2098.
- [36] J. Xu, H.-C. Wu, C. Zhu, A. Ehrlich, L. Shaw, M. Nikolka, S. Wang, F. Molina-Lopez, X. Gu, S. Luo, D. Zhou, Y.-H. Kim, G.-J. N. Wang, K. Gu, V. R. Feig, S. Chen, Y. Kim, T. Katsumata, Y.-Q. Zheng, H. Yan, J. W. Chung, J. Lopez, B. Murmann, Z. Bao, *Nature Materials* **2019**, 18, 594–601.
- [37] R. Noriega, A. Salleo, A. J. Spakowitz, *Proceedings of the National Academy of Sciences of the United States of America* **2013**, 110, 16315–16320.
- [38] S. A. Mollinger, B. A. Krajina, R. Noriega, A. Salleo, A. J. Spakowitz, *ACS Macro Letters* **2015**, 4, 708–712.
- [39] H. Tanaka, A. Wakamatsu, M. Kondo, S. Kawamura, S.-i. Kuroda, Y. Shimoj, W.-T. Park, Y.-Y. Noh, T. Takenobu, *Communications Physics* **2019**, 2, 96.
- [40] D. Venkateshvaran, M. Nikolka, A. Sadhanala, V. Lemaur, M. Zelazny, M. Kepa, M. Hurhangee, A. J. Kronemeijer, V. Pecunia, I. Nasrallah, I. Romanov, K. Broch, I. McCulloch, D. Emin, Y. Olivier, J. Cornil, D. Beljonne, H. Sirringhaus, *Nature* **2014**, 515, 384–388.

- [41] W. Zhang, J. Smith, S. E. Watkins, R. Gysel, M. McGehee, A. Salleo, J. Kirkpatrick, S. Ashraf, T. Anthopoulos, M. Heeney, I. McCulloch, *Journal of the American Chemical Society* **2010**, *132*, 11437–11439.
- [42] X. Zhang, H. Bronstein, A. J. Kronemeijer, J. Smith, Y. Kim, R. J. Kline, L. J. Richter, T. D. Anthopoulos, H. Sirringhaus, K. Song, M. Heeney, W. Zhang, I. McCulloch, D. M. DeLongchamp, *Nature Communications* **2013**, *4*, 2238.
- [43] H. Sirringhaus, *Advanced Materials* **2005**, *17*, 2411–2425.
- [44] M. Brinkmann, L. Hartmann, L. Biniek, K. Tremel, N. Kayunkid, *Macromolecular Rapid Communications* **2014**, *35*, 9–26.
- [45] H. Tseng, H. Phan, C. Luo, M. Wang, L. A. Perez, S. N. Patel, L. Ying, E. J. Kramer, T. Nguyen, G. C. Bazan, A. J. Heeger, *Advanced Materials* **2014**, *26*, 2993–2998.
- [46] H.-R. Tseng, L. Ying, B. B. Y. Hsu, L. A. Perez, C. J. Takacs, G. C. Bazan, A. J. Heeger, *Nano Letters* **2012**, *12*, 6353–6357.
- [47] V. Lemaire, D. A. da Silva Filho, V. Coropceanu, M. Lehmann, Y. Geerts, J. Piris, M. G. Debije, A. M. van de Craats, K. Senthilkumar, L. D. A. Siebbeles, J. M. Warman, J.-L. Brédas, J. Cornil, *Journal of the American Chemical Society* **2004**, *126*, 3271–3279.
- [48] O. Kwon, V. Coropceanu, N. E. Gruhn, J. C. Durivage, J. G. Laquindanum, H. E. Katz, J. Cornil, J.-L. Brédas, *The Journal of Chemical Physics* **2004**, *120*, 8186–8194.
- [49] J.-L. Brédas, D. Beljonne, V. Coropceanu, J. Cornil, *Chemical Reviews* **2004**, *104*, 4971–5004.
- [50] V. Coropceanu, J. Cornil, D. A. da Silva Filho, Y. Olivier, R. Silbey, J.-L. Brédas, *Chemical Reviews* **2007**, *107*, 926–952.
- [51] J. Mei, Z. Bao, *Chemistry of Materials* **2014**, *26*, 604–615.
- [52] I. Kang, H.-J. Yun, D. S. Chung, S.-K. Kwon, Y.-H. Kim, *Journal of the American Chemical Society* **2013**, *135*, 14896–14899.
- [53] J. Y. Back, H. Yu, I. Song, I. Kang, H. Ahn, T. J. Shin, S.-K. Kwon, J. H. Oh, Y.-H. Kim, *Chemistry of Materials* **2015**, *27*, 1732–1739.
- [54] C. R. Bridges, M. J. Ford, E. M. Thomas, C. Gomez, G. C. Bazan, R. A. Segalman, *Macromolecules* **2018**, *51*, 8597–8604.
- [55] P. Pingel, A. Zen, R. D. Abellón, F. C. Grozema, L. D. A. Siebbeles, D. Neher, *Advanced Functional Materials* **2010**, *20*, 2286–2295.
- [56] J.-C. Bolsée, W. D. Oosterbaan, L. Lutsen, D. Vanderzande, J. Manca, *Advanced Functional Materials* **2013**, *23*, 862–869.
- [57] N. E. Jackson, K. L. Kohlstedt, B. M. Savoie, M. Olvera de la Cruz, G. C. Schatz, L. X. Chen, M. A. Ratner, *Journal of the American Chemical Society* **2015**, *137*, 6254–6262.
- [58] R. J. Kline, M. D. McGehee, E. N. Kadnikova, J. Liu, J. M. J. Fréchet, M. F. Toney, *Macromolecules* **2005**, *38*, 3312–3319.
- [59] M. Brinkmann, P. Rannou, *Advanced Functional Materials* **2006**, *17*, 101–108.
- [60] H. Yang, T. J. Shin, L. Yang, K. Cho, C. Y. Ryu, Z. Bao, *Advanced Functional Materials* **2005**, *15*, 671–676.
- [61] M. Zhang, H. N. Tsao, W. Pisula, C. Yang, A. K. Mishra, K. Müllen, *Journal of the American Chemical Society* **2007**, *129*, 3472–3473.

- [62] H. N. Tsao, D. Cho, J. W. Andreasen, A. Rouhanipour, D. W. Breiby, W. Pisula, K. Müllen, *Advanced Materials* **2009**, *21*, 209–212.
- [63] H. N. Tsao, D. M. Cho, I. Park, M. R. Hansen, A. Mavrinskiy, D. Y. Yoon, R. Graf, W. Pisula, H. W. Spiess, K. Müllen, *Journal of the American Chemical Society* **2011**, *133*, 2605–2612.
- [64] H. Sirringhaus, P. J. Brown, R. H. Friend, M. M. Nielsen, K. Bechgaard, B. Langeveld-Voss, A. Spiering, R. A. Janssen, E. W. Meijer, P. Herwig, *Nature* **1999**, *401*, 685–688.
- [65] B. S. Ong, Y. Wu, P. Liu, S. Gardner, *Journal of the American Chemical Society* **2004**, *126*, 3378–3379.
- [66] I. McCulloch, M. Heeney, C. Bailey, K. Genevicius, I. MacDonald, M. Shkunov, D. Sparrowe, S. Tierney, R. Wagner, W. Zhang, M. L. Chabinyc, R. J. Kline, M. D. McGehee, M. F. Toney, *Nature Materials* **2006**, *5*, 328–333.
- [67] J. Rivnay, M. F. Toney, Y. Zheng, I. V. Kauvar, Z. Chen, V. Wagner, A. Facchetti, A. Salleo, *Advanced Materials* **2010**, *22*, 4359–4363.
- [68] F. S. Kim, X. Guo, M. D. Watson, S. A. Jenekhe, *Advanced Materials* **2010**, *22*, 478–482.
- [69] H. Bronstein, Z. Chen, R. S. Ashraf, W. Zhang, J. Du, J. R. Durrant, P. Shakya Tuladhar, K. Song, S. E. Watkins, Y. Geerts, M. M. Wienk, R. A. J. Janssen, T. Anthopoulos, H. Sirringhaus, M. Heeney, I. McCulloch, *Journal of the American Chemical Society* **2011**, *133*, 3272–3275.
- [70] S. Park, B. T. Lim, B. Kim, H. J. Son, D. S. Chung, *Scientific Reports* **2014**, *4*, 5482.
- [71] H.-J. Yun, J. Cho, D. S. Chung, Y.-H. Kim, S.-K. Kwon, *Macromolecules* **2014**, *47*, 7030–7035.
- [72] G. R. Desiraju, *Crystal Growth & Design* **2011**, *11*, 896–898.
- [73] G. R. Desiraju, *Accounts of Chemical Research* **2002**, *35*, 565–573.
- [74] G. R. Desiraju, *Current Opinion in Solid State and Materials Science* **1997**, *2*, 451–454.
- [75] P. Gómez, M. Más-Montoya, I. da Silva, J. P. Cerón-Carrasco, A. Tárraga, D. Curiel, *Crystal Growth & Design* **2017**, *17*, 3371–3378.
- [76] T. L. Nguyen, F. W. Fowler, J. W. Lauher, *Journal of the American Chemical Society* **2001**, *123*, 11057–11064.
- [77] Desiraju Gautam R., *Angewandte Chemie International Edition* **2010**, *50*, 52–59.
- [78] E. Arunan, G. R. Desiraju, R. A. Klein, J. Sadlej, S. Scheiner, I. Alkorta, D. C. Clary, R. H. Crabtree, J. J. Dannenberg, P. Hobza, H. G. Kjaergaard, A. C. Legon, B. Mennucci, D. J. Nesbitt, *Pure and Applied Chemistry* **2011**, *83*, 1637–1641.
- [79] P. Gilli, G. Gilli, *Journal of Molecular Structure* **2010**, *972*, 2–10.
- [80] M. Meot-Ner (Mautner), *Chemical Reviews* **2005**, *105*, 213–284.
- [81] C. B. Aakeroy, K. R. Seddon, *Chemical Society Reviews* **1993**, *11*.
- [82] T. Steiner, *Angewandte Chemie International Edition* **2002**, *41*, 48–76.
- [83] H. Umeyama, K. Morokuma, *Journal of the American Chemical Society* **1977**, *99*, 1316–1332.
- [84] S. J. Grabowski, *Chemical Reviews* **2011**, *111*, 2597–2625.
- [85] A. D. Buckingham, P. W. Fowler, J. M. Hutson, *Chemical Reviews* **1988**, *88*, 963–988.
- [86] A. D. Buckingham, P. W. Fowler, *Canadian Journal of Chemistry* **1985**, *63*(7), 2018–2025.
- [87] A. D. Buckingham, P. W. Fowler, *The Journal of Chemical Physics* **1983**, *79*, 6426–6428.

- [88] G. Gilli, P. Gilli, *Journal of Molecular Structure* **2000**, 552, 1–15.
- [89] P. Gilli, V. Bertolasi, V. Ferretti, G. Gilli, *Journal of the American Chemical Society* **1994**, 116, 909–915.
- [90] P. Gilli, L. Pretto, V. Bertolasi, G. Gilli, *Accounts of Chemical Research* **2009**, 42, 33–44.
- [91] G. R. Desiraju, T. Steiner, *The Weak Hydrogen Bond in Structural Chemistry and Biology*, Oxford University Press Inc.: New York, **1999**.
- [92] A. S. Mahadevi, G. N. Sastry, *Chemical Reviews* **2016**, 116, 2775–2825.
- [93] G. Jeffrey, W. Saenger, *Hydrogen Bonding in Biological Structures*, Springer Verlag, Berlin, **1991**.
- [94] V. Bertolasi, L. Pretto, G. Gilli, P. Gilli, *Acta Crystallographica Section B Structural Science* **2006**, 62, 850–863.
- [95] N. Kobko, L. Paraskevas, E. del Rio, J. J. Dannenberg, *Journal of the American Chemical Society* **2001**, 123, 4348–4349.
- [96] N. Kobko, J. J. Dannenberg, *The Journal of Physical Chemistry A* **2003**, 107, 6688–6697.
- [97] G. Vladilo, A. Hassanali, *Life* **2018**, 8, 1–22.
- [98] G. Jeffrey, *Introduction to Hydrogen Bonding*, Oxford University Press, Oxford, **1997**.
- [99] S. E. Howe, P. C. Painter, M. M. Coleman, *Macromolecules* **1985**, 18, 1676–1683.
- [100] D. J. Skrovanek, P. C. Painter, M. M. Coleman, *Macromolecules* **1986**, 19, 699–705.
- [101] M. M. Coleman, K. H. Lee, D. J. Skrovanek, P. C. Painter, *Macromolecules* **1986**, 19, 2149–2157.
- [102] D. Herschlag, M. M. Pinney, *Biochemistry* **2018**, 57, 3338–3352.
- [103] V. Bertolasi, P. Gilli, V. Ferretti, G. Gilli, *Journal of the Chemical Society, Perkin Transactions 2* **1997**, 945–952.
- [104] A. J. Dingley, F. Cordier, S. Grzesiek, *Concepts in Magnetic Resonance* **2001**, 13(2), 103–127.
- [105] F. Cordier, L. Nisius, A. J. Dingley, S. Grzesiek, *Nature Protocols* **2008**, 3, 235–241.
- [106] A. J. Dingley, L. Nisius, F. Cordier, S. Grzesiek, *Nature Protocols* **2008**, 3, 242–248.
- [107] G. Cornilescu, J.-S. Hu, A. Bax, *Journal of the American Chemical Society* **1999**, 121, 2949–2950.
- [108] A. J. Dingley, S. Grzesiek, *Journal of the American Chemical Society* **1998**, 120, 8293–8297.
- [109] M. R. Chierotti, R. Gobetto, *Chemical Communications* **2008**, 1621.
- [110] K. Besar, H. A. M. Ardoña, J. D. Tovar, H. E. Katz, *ACS Nano* **2015**, 9, 12401–12409.
- [111] T. S. Kale, H. A. M. Ardoña, A. Ertel, J. D. Tovar, *Langmuir* **2019**, 35, 2270–2282.
- [112] S. R. Diegelmann, J. M. Gorham, J. D. Tovar, *Journal of the American Chemical Society* **2008**, 130, 13840–13841.
- [113] H. A. M. Ardoña, J. D. Tovar, *Bioconjugate Chemistry* **2015**, 26, 2290–2302.
- [114] A. M. Sanders, T. J. Dawidczyk, H. E. Katz, J. D. Tovar, *ACS Macro Letters* **2012**, 1, 1326–1329.
- [115] A. M. Sanders, J. D. Tovar, *Supramolecular Chemistry* **2014**, 26, 259–266.
- [116] W.-W. Tsai, I. D. Tevis, A. S. Tayi, H. Cui, S. I. Stupp, *The Journal of Physical Chemistry B* **2010**, 114, 14778–14786.

- [117] R. J. Kumar, J. M. MacDonald, T. B. Singh, L. J. Waddington, A. B. Holmes, *Journal of the American Chemical Society* **2011**, 133, 8564–8573.
- [118] B. D. Wall, S. R. Diegelmann, S. Zhang, T. J. Dawidczyk, W. L. Wilson, H. E. Katz, H.-Q. Mao, J. D. Tovar, *Advanced Materials* **2011**, 23, 5009–5014.
- [119] I. D. Tevis, W.-W. Tsai, L. C. Palmer, T. Aytun, S. I. Stupp, *ACS Nano* **2012**, 6, 2032–2040.
- [120] M. Gsänger, J. Oh, M. Könemann, H. Höffken, A.-M. Krause, Z. Bao, F. Würthner, *Angewandte Chemie International Edition* **2010**, 49, 740–743.
- [121] E. D. Głowacki, L. Leonat, M. Irimia-Vladu, R. Schwödiauer, M. Ullah, H. Sitter, S. Bauer, N. Serdar Sariciftci, *Applied Physics Letters* **2012**, 101, 023305.
- [122] E. D. Głowacki, M. Irimia-Vladu, M. Kaltenbrunner, J. Gsiorowski, M. S. White, U. Monkowius, G. Romanazzi, G. P. Suranna, P. Mastorilli, T. Sekitani, S. Bauer, T. Someya, L. Torsi, N. S. Sariciftci, *Advanced Materials* **2013**, 25, 1563–1569.
- [123] C. Enengl, S. Enengl, M. Havlicek, P. Stadler, E. D. Głowacki, M. C. Scharber, M. White, K. Hingerl, E. Ehrenfreund, H. Neugebauer, N. S. Sariciftci, *Advanced Functional Materials* **2015**, 25, 6679–6688.
- [124] Y. Kanbur, H. Coskun, E. D. Głowacki, M. Irimia-Vladu, N. S. Sariciftci, C. Yumusak, *Organic Electronics* **2019**, 66, 53–57.
- [125] E. Miglbauer, N. Demitri, M. Himmelsbach, U. Monkowius, N. S. Sariciftci, E. D. Głowacki, K. T. Oppelt, *ChemistrySelect* **2016**, 1, 6349–6355.
- [126] M. Sytnyk, E. D. Głowacki, S. Yakunin, G. Voss, W. Schöffberger, D. Kriegner, J. Stangl, R. Trotta, C. Gollner, S. Tollabimazraehno, G. Romanazzi, Z. Bozkurt, M. Havlicek, N. S. Sariciftci, W. Heiss, *Journal of the American Chemical Society* **2014**, 136, 16522–16532.
- [127] E. D. Głowacki, H. Coskun, M. A. Blood-Forsythe, U. Monkowius, L. Leonat, M. Grzybowski, D. Gryko, M. S. White, A. Aspuru-Guzik, N. S. Sariciftci, *Organic Electronics* **2014**, 15, 3521–3528.
- [128] E. D. Głowacki, G. Romanazzi, C. Yumusak, Coskun, U. Monkowius, G. Voss, M. Burian, R. T. Lechner, N. Demitri, G. J. Redhammer, N. Sünger, G. P. Suranna, N. S. Sariciftci, *Advanced Functional Materials* **2015**, 25, 776–787.
- [129] H. T. Black, D. F. Perepichka, *Angewandte Chemie International Edition* **2014**, 53, 2138–2142.
- [130] N. B. Kolhe, R. N. Devi, S. P. Senanayak, B. Jancy, K. S. Narayan, S. K. Asha, *Journal of Materials Chemistry* **2012**, 22, 15235.
- [131] G. H. Roche, Y.-T. Tsai, S. Clevers, D. Thuau, F. Castet, Y. H. Geerts, J. J. E. Moreau, G. Wantz, O. J. Dautel, *Journal of Materials Chemistry C* **2016**, 4, 6742–6749.
- [132] S.-M. Jeong, T.-G. Kim, E. Jung, J.-W. Park, *ACS Applied Materials & Interfaces* **2013**, 5, 6837–6842.
- [133] M. Halik, H. Klauk, U. Zschieschang, G. Schmid, S. Ponomarenko, S. Kirchmeyer, W. Weber, *Advanced Materials* **2003**, 15, 917–922.
- [134] J. Yao, C. Yu, Z. Liu, H. Luo, Y. Yang, G. Zhang, D. Zhang, *Journal of the American Chemical Society* **2016**, 138, 173–185.
- [135] M. U. Ocheje, B. P. Charron, Y.-H. Cheng, C.-H. Chuang, A. Soldera, Y.-C. Chiu, S. Rondeau-Gagné, *Macromolecules* **2018**, 51, 1336–1344.



- [136] W. H. Carothers, "Linear polyamides and their production", , 1938.
- [137] M. I. Kohan, S. A. Mestemacher, R. U. Pagilagan, K. Redmond, "Polyamides", in *Ullmann's Encyclopedia of Industrial Chemistry*, Wiley-VCH Verlag GmbH & Co. KGaA (Ed.), Wiley-VCH Verlag GmbH & Co. KGaA, Weinheim, Germany, **2003**.
- [138] R. J. Gaymans, "Polyamides", in *Synthetic Methods in Step-Growth Polymers*, John Wiley & Sons, Ltd, **2003**.
- [139] W. H. Carothers, *Journal of the American Chemical Society* **1929**, 51, 2548–2559.
- [140] A. Ravve, "Step-Growth Polymerization and Step-Growth Polymers", in *Principles of Polymer Chemistry*, A. Ravve (Ed.), Springer US, Boston, MA, **2000**.
- [141] M. Chanda, S. Roy, *Plastics Technology Handbook*, CRC Press, Boca Raton, FL, USA, 4th edition Edition, **2007**.
- [142] J. Lin, D. C. Sherrington, "Recent developments in the synthesis, thermostability and liquid crystal properties of aromatic polyamides", in *Polymer Synthesis* Vol. 111, Springer-Verlag, Berlin/Heidelberg, **1994**.
- [143] P. W. Morgan, S. L. Kwolek, *Journal of Polymer Science* **1962**, 62, 33–58.
- [144] M. Takayanagi, T. Ogata, M. Morikawa, T. Kai, *Journal of Macromolecular Science, Part B* **1980**, 17, 591–615.
- [145] W. Hatke, H.-W. Schmidt, W. Heitz, *Journal of Polymer Science Part A: Polymer Chemistry* **1991**, 29, 1387–1398.
- [146] H.-J. Jeong, M.-A. Kakimoto, Y. Imai, *Journal of Polymer Science Part A: Polymer Chemistry* **1991**, 29, 767–772.
- [147] H. Mera, T. Takata, "High-Performance Fibers", in *Ullmann's Encyclopedia of Industrial Chemistry*, American Cancer Society, **2000**.
- [148] J. Zuo, S. Li, L. Bouzidi, S. S. Narine, *Polymer* **2011**, 52, 4503 – 4516.
- [149] H. Kricheldorf, *Polycondensation: History and New Results*, SpringerLink : Bücher, Springer Berlin Heidelberg, **2013**.
- [150] N. Yamazaki, F. Higashi, J. Kawabata, *Journal of Polymer Science: Polymer Chemistry Edition* **1974**, 12, 2149–2154.
- [151] N. Yamazaki, F. Higashi, *Journal of Polymer Science: Polymer Letters Edition* **1974**, 12, 185–191.
- [152] N. Yamazaki, M. Matsumoto, F. Higashi, *Journal of Polymer Science: Polymer Chemistry Edition* **1975**, 13, 1373–1380.
- [153] F. Higashi, Y. Taguchi, N. Kokubo, H. Ohta, *Journal of Polymer Science: Polymer Chemistry Edition* **1981**, 19, 2745–2750.
- [154] F. Higashi, A. Mochizuki, *Journal of Polymer Science: Polymer Chemistry Edition* **1983**, 21, 3337–3340.
- [155] N. Ogata, K. Sanui, S. Tan, *Polymer Journal* **1984**, 16, 569.
- [156] R. Katsarava, D. Kharadze, L. Avalishvili, M. Zaalishvili, *Polymer Science U.S.S.R.* **1984**, 26, 1668–1678.
- [157] R. Katsarava, D. Kunchuliya, L. Avalishvili, G. Andronikashvili, M. Zaalishvili, *Polymer Science U.S.S.R.* **1979**, 21, 2978–2984.

- [158] C. G. Overberger, J. Sebenda, *Journal of Polymer Science Part A-1: Polymer Chemistry* **1969**, 7, 2875–2887.
- [159] N. Ogata, K. Sanui, K. Kanasugi, N. Ohira, *Polymer Journal* **1975**, 7, 544.
- [160] H. R. Kricheldorf, K. Bornhorst, J. Schellenberg, G. Schwarz, *Journal of Macromolecular Science, Part A* **2007**, 44, 119–124.
- [161] Murthy N. Sanjeeva, *Journal of Polymer Science Part B: Polymer Physics* **2006**, 44, 1763–1782.
- [162] C. W. Bunn, E. V. Garner, *Proceedings of the Royal Society A: Mathematical, Physical and Engineering Sciences* **1947**, 189, 39–68.
- [163] C. Silva, A. Cavaco-Paulo, J. Fu, “Enzymatic Biofinishes for Synthetic Textiles”, in *Functional Finishes for Textiles*, Elsevier, **2015**.
- [164] L. Morales-Gámez, D. Soto, L. Franco, J. Puiggali, *Polymer* **2010**, 51, 5788–5798.
- [165] N. A. Jones, E. D. T. Atkins, M. J. Hill, S. J. Cooper, L. Franco, *Macromolecules* **1996**, 29, 6011–6018.
- [166] S. Dasgupta, W. B. Hammond, W. A. Goddard, *Journal of the American Chemical Society* **1996**, 118, 12291–12301.
- [167] C. Ramesh, A. Keller, S. Eltink, *Polymer* **1994**, 35, 5300–5308.
- [168] J. Cretenoud, S. Galland, C. J. G. Plummer, V. Michaud, A. Bayer, N. Lamberts, B. Hoffmann, H. Frauenrath, *Journal of Applied Polymer Science* **2017**, 134, 44349.
- [169] P. Dreyfus, A. Keller, *Journal of Polymer Science Part B: Polymer Letters* **1970**, 8, 253–258.
- [170] R. Brill, *Journal für Praktische Chemie* **1942**, 161, 49–64.
- [171] A. Y. Feldman, E. Wachtel, G. B. M. Vaughan, A. Weinberg, G. Marom, *Macromolecules* **2006**, 39, 4455–4459.
- [172] C. Ramesh, *Macromolecules* **1999**, 32, 3721–3726.
- [173] N. Vasanthan, N. S. Murthy, R. G. Bray, *Macromolecules* **1998**, 31, 8433–8435.
- [174] M. J. Hill, E. D. T. Atkins, *Macromolecules* **1995**, 28, 604–609.
- [175] E. Navarro, L. Franco, J. A. Subirana, J. Puiggali, *Macromolecules* **1995**, 28, 8742–8750.
- [176] P. Dreyfuss, A. Keller, *Journal of Macromolecular Science, Part B* **1970**, 4, 811–835.
- [177] Y. Li, W. A. Goddard, *Macromolecules* **2002**, 35, 8440–8455.
- [178] D. Ahmed, Z. Hongpeng, K. Haijuan, L. Jing, M. Yu, Y. Muhuo, *Materials Research* **2014**, 17, 1180–1200.
- [179] M. Northolt, *European Polymer Journal* **1974**, 10, 799–804.
- [180] M. G. Northolt, J. J. v. Aartsen, *Journal of Polymer Science: Polymer Letters Edition* **1973**, 11, 333–337.
- [181] R. Hasegawa, Y. Chatani, H. Tadokoro, **1973**, 21.
- [182] K. Haraguchi, T. Kajiyama, M. Takayanagi, *Journal of Applied Polymer Science* **1979**, 23, 915–926.
- [183] K. Haraguchi, T. Kajiyama, M. Takayanagi, *Journal of Applied Polymer Science* **1979**, 23, 903–914.
- [184] M. Panar, P. Avakian, R. C. Blume, K. H. Gardner, T. D. Gierke, H. H. Yang, *Journal of Polymer Science: Polymer Physics Edition* **1983**, 21, 1955–1969.

- [185] M. G. Dobb, D. J. Johnson, B. P. Saville, *Journal of Polymer Science: Polymer Physics Edition* **1977**, 15, 2201–2211.
- [186] A. Donald, C. Viney, A. Windle, *Polymer* **1983**, 24, 155–159.
- [187] Y. S. Deshmukh, C. H. R. M. Wilsens, R. Verhoef, M. R. Hansen, D. Dudenko, R. Graf, E. A. Klop, S. Rastogi, *Macromolecules* **2016**, 49, 950–962.
- [188] A. J. Uddin, Y. Gotoh, Y. Ohkoshi, M. Nagura, R. Endo, T. Hara, *Journal of Polymer Science Part B: Polymer Physics* **2005**, 43, 1640–1648.
- [189] K. Zhang, J. Zhao, S. Liu, M. Zhang, *Petrochemical Technology* **2015**, 44, 536–542.
- [190] H. Yamamoto, K. Tashiro, K. Ishino, M. Takahashi, R. Endo, M. Asada, Y. Li, K. Katsube, T. Ishii, *Polymer* **2017**, 116, 378–394.
- [191] P. Nimmanpipug, K. Tashiro, O. Rangsiman, *The Journal of Physical Chemistry B* **2003**, 107, 8343–8350.
- [192] P. Nimmanpipug, K. Tashiro, O. Rangsiman, *The Journal of Physical Chemistry B* **2006**, 110, 20858–20864.
- [193] P. Nimmanpipug, K. Tashiro, Y. Maeda, O. Rangsiman, *The Journal of Physical Chemistry B* **2002**, 106, 6842–6848.
- [194] K. Tashiro, P. Nimmanpipug, O. Rangsiman, *The Journal of Physical Chemistry B* **2002**, 106, 12884–12895.
- [195] K. Tashiro, M. Kobayashi, H. Tadokoro, *Macromolecules* **1977**, 10, 413–420.
- [196] R. Chapman, D. Holmer, O. Pickett, K. Lea, J. Saunders, *Textile Research Journal* **1981**, 51, 564–573.
- [197] D. J. Kemmish, *Practical Guide to High Performance Engineering Plastics*, iSmithers, A Smithers Group Company, Shawbury, **2011**.
- [198] J. Cretenoud, *Semiaromatic Polyamides and Copolyamides Comprising Kinked Repeating Units*, Ph. D. Thesis, École Polytechnique Fédérale Lausanne, Lausanne, **2018**.
- [199] N. Candau, S. Galland, J. Cretenoud, S. Balog, V. Michaud, J.-M. Chenal, O. Lame, C. J. G. Plummer, H. Frauenrath, *submitted*.
- [200] F. Khoury, *Journal of Polymer Science* **1958**, 33, 389–403.
- [201] C. Berti, A. Celli, P. Marchese, S. Sullalti, M. Vannini, C. Lorenzetti, *European Polymer Journal* **2012**, 48, 1923–1931.
- [202] K. Eersels, G. Groeninckx, M. Koch, H. Reynaers, *Polymer* **1998**, 39, 3893–3900.
- [203] K. L. L. Eersels, G. Groeninckx, *Polymer* **1996**, 37, 983–989.
- [204] S. S. Lee, P. J. Phillips, *European Polymer Journal* **2007**, 43, 1933–1951.
- [205] B. Goderis, P. G. Klein, S. P. Hill, C. E. Koning, “A comparative DSC, X-Ray and NMR study on the crystallinity of isomeric aliphatic polyamides”, in *Scattering Methods and the Properties of Polymer Materials*, Springer Berlin Heidelberg, Berlin, Heidelberg, **2005**.
- [206] K. Marchildon, *Macromolecular Reaction Engineering* **2011**, 5, 22–54.
- [207] J. G. Hardy, L. M. Römer, T. R. Scheibel, *Polymer* **2008**, 49, 4309–4327.
- [208] C. Bennett, L. J. Mathias, *Journal of Polymer Science Part A: Polymer Chemistry* **2005**, 43, 936–945.
- [209] M. Chemical, “MX-Nylon, Nylon-MXD6”, , 2020.

- [210] V. Gabara, J. Hartzler, K. Lee, H. Yang, "In Handbook of Fiber Chemistry", , CRC Press, Boca Raton, FL, USA, **2010**.
- [211] H. Elias, F. Vohwinkel, "New Commercial Polymers 2", , Gordon and Breach Science Publishers, Inc, New York, NY, **1986**.
- [212] A. Facchetti, *Chemistry of Materials* **2011**, 23, 733–758.
- [213] M. C. Gather, A. Köhnen, K. Meerholz, *Advanced Materials* **2011**, 23, 233–248.
- [214] L. Torsi, M. Magliulo, K. Manoli, G. Palazzo, *Chemical Society Reviews* **2013**, 42, 8612.
- [215] Z.-F. Yao, J.-Y. Wang, J. Pei, *Crystal Growth & Design* **2018**, 18, 7–15.
- [216] G. Gryn'ova, K.-H. Lin, C. Corminboeuf, *Journal of the American Chemical Society* **2018**, 140, 16370–16386.
- [217] D. Braga, G. Horowitz, *Advanced Materials* **2009**, 21, 1473–1486.
- [218] X. Yao, W. Shao, X. Xiang, W.-J. Xiao, L. Liang, F.-G. Zhao, J. Ling, Z. Lu, J. Li, W.-S. Li, *Organic Electronics* **2018**, 61, 56–64.
- [219] A. Facchetti, M. Mushrush, M.-H. Yoon, G. R. Hutchison, M. A. Ratner, T. J. Marks, *Journal of the American Chemical Society* **2004**, 126, 13859–13874.
- [220] S. Inoue, H. Minemawari, J. Tsutsumi, M. Chikamatsu, T. Yamada, S. Horiuchi, M. Tanaka, R. Kumai, M. Yoneya, T. Hasegawa, *Chemistry of Materials* **2015**, 27, 3809–3812.
- [221] M. J. Kang, I. Doi, H. Mori, E. Miyazaki, K. Takimiya, M. Ikeda, H. Kuwabara, *Advanced Materials* **2011**, 23, 1222–1225.
- [222] T. Kashiki, E. Miyazaki, K. Takimiya, *Chemistry Letters* **2008**, 37, 284–285.
- [223] T. Marszalek, I. Krygier, A. Pron, Z. Wrobel, P. M. Blom, I. Kulszewicz-Bajer, W. Pisula, *Organic Electronics* **2019**, 65, 127–134.
- [224] H. Minemawari, M. Tanaka, S. Tsuzuki, S. Inoue, T. Yamada, R. Kumai, Y. Shimoi, T. Hasegawa, *Chemistry of Materials* **2017**, 29, 1245–1254.
- [225] W. Zajackowski, S. K. Nanajunda, Y. Eichen, W. Pisula, *RSC Advances* **2017**, 7, 1664–1670.
- [226] R. B. Campbell, J. M. Robertson, J. Trotter, *Acta Crystallographica* **1961**, 14, 705–711.
- [227] H. Ebata, T. Izawa, E. Miyazaki, K. Takimiya, M. Ikeda, H. Kuwabara, T. Yui, *Journal of the American Chemical Society* **2007**, 129, 15732–15733.
- [228] T. Yamamoto, K. Takimiya, *Journal of the American Chemical Society* **2007**, 129, 2224–2225.
- [229] H. E. Katz, A. J. Lovinger, J. Johnson, C. Kloc, T. Siegrist, W. Li, Y.-Y. Lin, A. Dodabalapur, *Nature* **2000**, 404, 478–481.
- [230] G. Horowitz, B. Bachet, A. Yassar, P. Lang, F. Demanze, J.-L. Fave, F. Garnier, *Chem. Mater.* **2007**, 7, 1337–1341.
- [231] D. González-Rodríguez, A. P. H. J. Schenning, *Chemistry of Materials* **2011**, 23, 310–325.
- [232] L. C. Gilday, S. W. Robinson, T. A. Barendt, M. J. Langton, B. R. Mullaney, P. D. Beer, *Chemical Reviews* **2015**, 115, 7118–7195.
- [233] H. Huang, L. Yang, A. Facchetti, T. J. Marks, *Chemical Reviews* **2017**, 117, 10291–10318.
- [234] P. Gómez, S. Georgakopoulos, J. P. Cerón, I. da Silva, M. Más-Montoya, J. Pérez, A. Tárraga, D. Curiel, *Journal of Materials Chemistry C* **2018**, 6, 3968–3975.

- [235] F. Zhang, V. Lemaire, W. Choi, P. Kafle, S. Seki, J. Cornil, D. Beljonne, Y. Diao, *Nature Communications* **2019**, *10*, 4217.
- [236] M. Gsänger, D. Bialas, L. Huang, M. Stolte, F. Würthner, *Advanced Materials* **2016**, *28*, 3615–3645.
- [237] K. H. Lam, T. R. B. Foong, Z. E. Ooi, J. Zhang, A. C. Grimsdale, Y. M. Lam, *ACS Applied Materials & Interfaces* **2013**, *5*, 13265–13274.
- [238] R. Marty, R. Szilluweit, A. Sánchez-Ferrer, S. Bolisetty, J. Adamcik, R. Mezzenga, E.-C. Spitzner, M. Feifer, S. N. Steinmann, C. Corminboeuf, H. Frauenrath, *ACS Nano* **2013**, *7*, 8498–8508.
- [239] E.-C. Spitzner, C. Riesch, R. Szilluweit, L. Tian, H. Frauenrath, R. Magerle, *ACS Macro Letters* **2012**, *1*, 380–383.
- [240] R. J. Hafner, D. Görl, A. Sienkiewicz, S. Balog, H. Frauenrath, *Chemistry – A European Journal* **2020**, DOI: 10.1002/chem.201904561.
- [241] D. A. Stone, L. Hsu, S. I. Stupp, *Soft Matter* **2009**, *5*, 1990–1993.
- [242] D. A. Stone, A. S. Tayi, J. E. Goldberger, L. C. Palmer, S. I. Stupp, *Chemical Communications* **2011**, *47*, 5702.
- [243] J. D. Tovar, *Accounts of Chemical Research* **2013**, *46*, 1527–1537.
- [244] P. Pratihar, S. Ghosh, V. Stepanenko, S. Patwardhan, F. C. Grozema, L. D. A. Siebbeles, F. Würthner, *Beilstein Journal of Organic Chemistry* **2010**, *6*, 1070–1078.
- [245] R. Marty, R. Nigon, D. Leite, H. Frauenrath, *Journal of the American Chemical Society* **2014**, *136*, 3919–3927.
- [246] R. Marty, H. Frauenrath, J. Helbing, *The Journal of Physical Chemistry B* **2014**, *118*, 11152–11160.
- [247] F. Würthner, C. Bauer, V. Stepanenko, S. Yagai, *Advanced Materials* **2008**, *20*, 1695–1698.
- [248] F. Würthner, C. Thalacker, A. Sautter, W. Schärftl, W. Ibach, O. Hollricher, *Chemistry – A European Journal* **2000**, *6*, 3871–3886.
- [249] E. R. Draper, J. J. Walsh, T. O. McDonald, M. A. Zwijnenburg, P. J. Cameron, A. J. Cowan, D. J. Adams, *J. Mater. Chem. C* **2014**, *2*, 5570–5575.
- [250] L. Tian, R. Szilluweit, R. Marty, L. Bertschi, M. Zerson, E.-C. Spitzner, R. Magerle, H. Frauenrath, *Chemical Science* **2012**, *3*, 1512–1521.
- [251] B. Özen, N. Candau, C. Temiz, F. C. Grozema, F. Fadaei Tirani, R. Scopelliti, J.-M. Chenal, C. J. G. Plummer, H. Frauenrath, *Journal of Materials Chemistry C* **2020**, *8*, 6281–6292.
- [252] J. Gebers, B. Özen, L. Hartmann, M. Schaer, S. Suárez, P. Bugnon, R. Scopelliti, H.-G. Steinrück, O. Konovalov, A. Magerl, M. Brinkmann, R. Petraglia, P. de Silva, C. Corminboeuf, H. Frauenrath, *Chemistry – A European Journal* **2020**, DOI: 10.1002/chem.201904562.
- [253] N.-N. Li, Y.-L. Zhang, S. Mao, Y.-R. Gao, D.-D. Guo, Y.-Q. Wang, *Organic Letters* **2014**, *16*, 2732–2735.
- [254] D. Fichou, B. Bachet, F. Demanze, I. Billy, G. Horowitz, F. Garnier, *Advanced Materials* **1996**, *8*, 500–504.
- [255] T. Siegrist, C. Kloc, R. A. Laudise, H. E. Katz, R. C. Haddon, *Advanced Materials* **1998**, *10*, 379–382.

- [256] G. R. Desiraju, A. Gavezzotti, *Acta Crystallographica Section B Structural Science* **1989**, 45, 473–482.
- [257] C. A. Hunter, J. Sanders, *Journal of the American Chemical Society* **1990**, 112,.
- [258] S. S. Panda, K. Shmilovich, A. L. Ferguson, J. D. Tovar, *Langmuir* **2019**, 35, 14060–14073.
- [259] H. B. Akkerman, S. C. B. Mannsfeld, A. P. Kaushik, E. Verploegen, L. Burnier, A. P. Zoombelt, J. D. Saathoff, S. Hong, S. Atahan-Evrenk, X. Liu, A. Aspuru-Guzik, M. F. Toney, P. Clancy, Z. Bao, *Journal of the American Chemical Society* **2013**, 135, 11006–11014.
- [260] E. K. Burnett, Q. Ai, B. P. Cherniawski, S. R. Parkin, C. Risko, A. L. Briseno, *Chemistry of Materials* **2019**, 31, 6900–6907.
- [261] F. Tao, S. L. Bernasek, *Chemical Reviews* **2007**, 107, 1408–1453.
- [262] K. Aoki, M. Kudo, N. Tamaoki, *Org. Lett.* **2004**, 6, 4.
- [263] H. Menzel, S. Horstmann, M. D. Mowery, M. Cai, C. E. Evans, *Polymer* **2000**, 41, 8113–8119.
- [264] N. Fujita, Y. Sakamoto, M. Shirakawa, M. Ojima, A. Fujii, M. Ozaki, S. Shinkai, *Journal of the American Chemical Society* **2007**, 129, 4134–4135.
- [265] M. J. Kim, S. Angupillai, K. Min, M. Ramalingam, Y.-A. Son, *ACS Applied Materials & Interfaces* **2018**, 10, 24767–24775.
- [266] C. Aleman, E. Brillas, A. G. Davies, L. Fajari, D. Giro, L. Julia, J. J. Perez, J. Rius, *The Journal of Organic Chemistry* **1993**, 58, 3091–3099.
- [267] M. Pelletier, F. Brisse, *Acta Crystallographica Section C Crystal Structure Communications* **1994**, 50, 1942–1945.
- [268] P. A. Chaloner, S. R. Gunatunga, P. B. Hitchcock, *Acta Crystallographica Section C Crystal Structure Communications* **1994**, 50, 1941–1942.
- [269] M. D. Curtis, J. Cao, J. W. Kampf, *Journal of the American Chemical Society* **2004**, 126, 4318–4328.
- [270] R. J. Hafner, L. Tian, J. C. Brauer, T. Schmaltz, A. Sienkiewicz, S. Balog, V. Flauraud, J. Brugger, H. Frauenrath, *ACS Nano* **2018**, 12, 9116–9125.
- [271] A. K. Thomas, J. A. Garcia, J. Ulibarri-Sanchez, J. Gao, J. K. Grey, *ACS Nano* **2014**, 8, 10559–10568.
- [272] A. R. Murphy, J. M. J. Fréchet, *Chemical Reviews* **2007**, 107, 1066–1096.
- [273] C. Wang, H. Dong, W. Hu, Y. Liu, D. Zhu, *Chemical Reviews* **2012**, 112, 2208–2267.
- [274] X. Zhan, A. Facchetti, S. Barlow, T. J. Marks, M. A. Ratner, M. R. Wasielewski, S. R. Marder, *Advanced Materials* **2011**, 23, 268–284.
- [275] P. Lin, F. Yan, *Advanced Materials* **2012**, 24, 34–51.
- [276] Y. Guo, G. Yu, Y. Liu, *Advanced Materials* **2010**, 22, 4427–4447.
- [277] G. Zhao, H. Dong, Q. Liao, J. Jiang, Y. Luo, H. Fu, W. Hu, *Nature Communications* **2018**, 9, 4790.
- [278] A. Mishra, C.-Q. Ma, P. Bäuerle, *Chemical Reviews* **2009**, 109, 1141–1276.
- [279] I. Vladimirov, M. Kellermeier, T. Geßner, Z. Molla, S. Grigorian, U. Pietsch, L. S. Schaffroth, M. Kühn, F. May, R. T. Weitz, *Nano Letters* **2018**, 18, 9–14.
- [280] R. Custelcean, *Chemical Society Reviews* **2010**, 39, 3675–3685.

- [281] E. Jahnke, I. Lieberwirth, N. Severin, J. P. Rabe, H. Frauenrath, *Angewandte Chemie International Edition* **2006**, 45, 5383–5386.
- [282] S. Bauer, M. Kaltenbrunner, *Nature* **2016**, 539, 365–367.
- [283] A. Dell’Aquila, P. Mastrorilli, C. F. Nobile, G. Romanazzi, G. P. Suranna, L. Torsi, M. C. Tanese, D. Acierno, E. Amendola, P. Morales, *Journal of Materials Chemistry* **2006**, 16, 1183.
- [284] S.-I. Kawano, N. Fujita, S. Shinkai, *Chemistry – A European Journal* **2005**, 11, 4735–4742.
- [285] S. Yagai, T. Seki, H. Murayama, Y. Wakikawa, T. Ikoma, Y. Kikkawa, T. Karatsu, A. Kitamura, Y. Honsho, S. Seki, *Small* **2010**, 6, 2731–2740.
- [286] E.-K. Schillinger, E. Mena-Osteritz, J. Hentschel, H. G. Börner, P. Bäuerle, *Advanced Materials* **2009**, 21, 1562–1567.
- [287] F. S. Schoonbeek, J. H. van Esch, B. Wegewijs, D. B. A. Rep, M. P. de Haas, T. M. Klapwijk, R. M. Kellogg, B. L. Feringa, *Angewandte Chemie International Edition* **1999**, 38, 1393–1397.
- [288] H. T. Black, N. Yee, Y. Zems, D. F. Perepichka, *Chemistry – A European Journal* **2016**, 22, 17251–17261.
- [289] C. Fu, P. J. Beldon, D. F. Perepichka, *Chemistry of Materials* **2017**, 29, 2979–2987.
- [290] M.-X. Zhang, G.-J. Zhao, *ChemSusChem* **2012**, 5, 879–887.
- [291] S. Hotta, K. Waragai, *Journal of Materials Chemistry* **1991**, 1, 835–842.
- [292] M. Moret, M. Campione, A. Borghesi, L. Miozzo, A. Sassella, S. Trabattoni, B. Lotz, A. Thierry, *Journal of Materials Chemistry* **2005**, 15, 2444–2449.
- [293] H. E. Katz, A. J. Lovinger, J. G. Laquindanum, *Chemistry of Materials* **1998**, 10, 457–459.
- [294] S. Mannsfeld, J. Locklin, C. Reese, M. Roberts, A. Lovinger, Z. Bao, *Advanced Functional Materials* **2007**, 17, 1617–1622.
- [295] C. Reese, M. E. Roberts, S. R. Parkin, Z. Bao, *Advanced Materials* **2009**, 21, 3678–3681.
- [296] J. Gebers, *Hydrogen-Bonded Oligothiophenes for Organic Electronics*, Ph. D. Thesis, École Polytechnique Fédérale Lausanne, Lausanne, **2014**.
- [297] J. Gebers, D. Rolland, Marty, S. Suárez, L. Cervini, R. Scopelliti, J. C. Brauer, H. Frauenrath, *Chemistry – A European Journal* **2014**, 21, 1542–1553.
- [298] P. de Silva, C. Corminboeuf, *Journal of Chemical Theory and Computation* **2014**, 10, 3745–3756.
- [299] A. Pimpinelli, J. Villain, *Physics of Crystal Growth*, Collection Alea-Saclay: Monographs and Texts in Statistical Physics, Cambridge University Press, **1998**.
- [300] L. Zhang, N. S. Colella, B. P. Cherniawski, S. C. B. Mannsfeld, A. L. Briseno, *ACS Applied Materials & Interfaces* **2014**, 6, 5327–5343.
- [301] Y. Yuan, G. Giri, A. L. Ayzner, A. P. Zoombelt, S. C. B. Mannsfeld, J. Chen, D. Nordlund, M. F. Toney, J. Huang, Z. Bao, *Nature Communications* **2014**, 5, 3005.
- [302] A. J. Heeger, *Reviews of Modern Physics* **2001**, 73, 681–700.
- [303] J. Rivnay, S. C. B. Mannsfeld, C. E. Miller, A. Salleo, M. F. Toney, *Chemical Reviews* **2012**, 112, 5488–5519.
- [304] F. C. Grozema, L. D. A. Siebbeles, *International Reviews in Physical Chemistry* **2008**, 27, 87–138.

- [305] M. Ashizawa, Y. Zheng, H. Tran, Z. Bao, *Progress in Polymer Science* **2020**, *100*, 101181.
- [306] R. D. McCullough, S. Tristram-Nagle, S. P. Williams, R. D. Lowe, M. Jayaraman, *Journal of the American Chemical Society* **1993**, *115*, 4910–4911.
- [307] A. Jalal Uddin, Y. Ohkoshi, Y. Gotoh, M. Nagura, R. Endo, T. Hara, *Journal of Polymer Science Part B: Polymer Physics* **2004**, *42*, 433–444.
- [308] H. Muguruma, M. Yudasaka, S. Hotta, *Thin Solid Films* **1999**, *339*, 120–122.
- [309] H. Muguruma, K. Matsumura, S. Hotta, *Thin Solid Films* **2002**, *405*, 77–80.
- [310] H. Liu, Brémond, A. Prlj, J. F. Gonthier, C. Corminboeuf, *The Journal of Physical Chemistry Letters* **2014**, *5*, 2320–2324.
- [311] D. D. Coffman, G. J. Berchet, W. R. Peterson, E. W. Spanagel, *Journal of Polymer Science* **1947**, *2*, 306–313.
- [312] Y. Kinoshita, *Die Makromolekulare Chemie* **1959**, 1–20.
- [313] Y. Li, X. Zhu, G. Tian, D. Yan, E. Zhou, *Polymer International* **2001**, *50*, 677–682.
- [314] M. Fereydoon, S. H. Tabatabaei, A. Ajji, *Polymer Engineering & Science* **2014**, *54*, 2617–2631.
- [315] B. B. Doudou, E. Dargent, J. Grenet, *Journal of Plastic Film & Sheeting* **2005**, *21*, 233–251.
- [316] M. Biron, *Industrial Applications of Renewable Plastics: Environmental, Technological, and Economic Advances*, Elsevier Science, **2017**.
- [317] M. de Haas, G. van der Laan, B. Wegewijs, D. de Leeuw, P. Bäuerle, D. B. A. Rep, D. Fichou, *Synthetic Metals* **1999**, *101*, 524–525.
- [318] F. C. Grozema, B. R. Wegewijs, M. de Haas, L. D. A. Siebbeles, D. de Leeuw, R. Wilson, H. Sirringhaus, *Synthetic Metals* **2001**, *119*, 463–464.
- [319] B. Wegewijs, M. de Haas, D. de Leeuw, R. Wilson, H. Sirringhaus, *Synthetic Metals* **1999**, *101*, 534–535.
- [320] C. Zhang, *e-Polymers* **2018**, *18*, 373–408.
- [321] M. Brady, P. Brady, *Reinforced Plastics* **2010**, *54*, 25–29.
- [322] J. M. García, F. C. García, F. Serna, J. L. de la Peña, *Progress in Polymer Science* **2010**, *35*, 623–686.
- [323] J. M. García, F. C. García, F. Serna, J. L. de la Peña, “Aromatic Polyamides (Aramids)”, in *Handbook of Engineering and Specialty Thermoplastics*, S. Thomas, P. M. Visakh (Eds.), John Wiley & Sons, Inc., Hoboken, NJ, USA, **2011**.
- [324] K. Luo, Y. Wang, J. Yu, J. Zhu, Z. Hu, *RSC Advances* **2016**, *6*, 87013–87020.
- [325] P. M. Beaujuge, J. M. J. Fréchet, *Journal of the American Chemical Society* **2011**, *133*, 20009–20029.
- [326] A. Rahmanudin, K. Sivula, *CHIMIA International Journal for Chemistry* **2017**, *71*, 369–375.
- [327] Y. Yang, Z. Liu, G. Zhang, X. Zhang, D. Zhang, *Advanced Materials* **2019**, *31*, 1903104.
- [328] M. U. Ocheje, B. P. Charron, A. Nyayachavadi, S. Rondeau-Gagné, *Flexible and Printed Electronics* **2017**, *2*, 043002.
- [329] B. P. Charron, M. U. Ocheje, M. Selivanova, A. D. Hendsbee, Y. Li, S. Rondeau-Gagné, *Journal of Materials Chemistry C* **2018**, *6*, 12070–12078.



- [330] Y.-C. Lin, C.-C. Shih, Y.-C. Chiang, C.-K. Chen, W.-C. Chen, *Polymer Chemistry* **2019**, *10*, 5172–5183.
- [331] M. U. Ocheje, M. Selivanova, S. Zhang, T. H. Van Nguyen, B. P. Charron, C.-H. Chuang, Y.-H. Cheng, B. Billet, S. Noori, Y.-C. Chiu, X. Gu, S. Rondeau-Gagné, *Polymer Chemistry* **2018**, *9*, 5531–5542.
- [332] J. Y. Oh, S. Rondeau-Gagné, Y.-C. Chiu, A. Chortos, F. Lissel, G.-J. N. Wang, B. C. Schroeder, T. Kurosawa, J. Lopez, T. Katsumata, J. Xu, C. Zhu, X. Gu, W.-G. Bae, Y. Kim, L. Jin, J. W. Chung, J. B.-H. Tok, Z. Bao, *Nature* **2016**, *539*, 411–415.
- [333] F. Würthner, V. Stepanenko, Z. Chen, C. R. Saha-Möller, N. Kocher, D. Stalke, *The Journal of Organic Chemistry* **2004**, *69*, 7933–7939.
- [334] K. Akers, R. Aroca, A. M. Hort, R. O. Loutfy, *Spectrochimica Acta* **1988**, *44A*, 1129–1135.
- [335] M. Li, T. J. Dingemans, *Polymer* **2017**, *108*, 372–382.
- [336] X. Guan, *Crystallization of Polyamide 66 Copolymers at High Supercoolings*, Ph. D. Thesis, University of Tennessee, Knoxville, **2004**.
- [337] F. Liscio, S. Milita, C. Albonetti, P. D'Angelo, A. Guagliardi, N. Masciocchi, R. G. Della Valle, E. Venuti, A. Brillante, F. Biscarini, *Advanced Functional Materials* **2012**, *22*, 943–953.
- [338] J. Rivnay, L. H. Jimison, J. E. Northrup, M. F. Toney, R. Noriega, S. Lu, T. J. Marks, A. Facchetti, A. Salleo, *Nature Materials* **2009**, *8*, 952–958.
- [339] E. Hädicke, F. Graser, *Acta Crystallographica Section C* **1986**, *42*, 195–198.
- [340] M. C. R. Delgado, E.-G. Kim, D. A. d. S. Filho, J.-L. Brédas, *Journal of the American Chemical Society* **2010**, *132*, 3375–3387.
- [341] J. Jiménez, M.-J. Lin, C. Burschka, J. Becker, V. Settels, B. Engels, F. Würthner, *Chem. Sci.* **2014**, *5*, 608–619.
- [342] C. Kaufmann, D. Bialas, M. Stolte, F. Würthner, *Journal of the American Chemical Society* **2018**, *140*, 9986–9995.
- [343] S. Yagai, M. Usui, T. Seki, H. Murayama, Y. Kikkawa, S. Uemura, T. Karatsu, A. Kitamura, A. Asano, S. Seki, *Journal of the American Chemical Society* **2012**, *134*, 7983–7994.
- [344] J. M. Giaimo, J. V. Lockard, L. E. Sinks, A. M. Scott, T. M. Wilson, M. R. Wasielewski, *The Journal of Physical Chemistry A* **2008**, *112*, 2322–2330.
- [345] F. C. Spano, *Accounts of Chemical Research* **2010**, *43*, 429–439.
- [346] F. Würthner, Z. Chen, V. Dehm, V. Stepanenko, *Chemical Communications* **2006**, 1188.
- [347] J. Seibt, P. Marquetand, V. Engel, Z. Chen, V. Dehm, F. Würthner, *Chemical Physics* **2006**, *328*, 354–362.
- [348] V. Dehm, Z. Chen, U. Baumeister, P. Prins, L. D. A. Siebbeles, F. Würthner, *Organic Letters* **2007**, *9*, 1085–1088.
- [349] Z. Chen, M. G. Debije, T. Debaerdemaeker, P. Osswald, F. Würthner, *ChemPhysChem* **2004**, *5*, 137–140.
- [350] M. G. Debije, Z. Chen, J. Piris, R. B. Neder, M. M. Watson, K. Müllen, F. Würthner, *J. Mater. Chem.* **2005**, *15*, 1270–1276.
- [351] X.-Q. Li, V. Stepanenko, Z. Chen, P. Prins, L. D. A. Siebbeles, F. Würthner, *Chem. Commun.* **2006**, 3871–3873.

- [352] G. R. Strobl, M. Schneider, *Journal of Polymer Science: Polymer Physics Edition* **1980**, *18*, 1343–1359.
- [353] M. J. Frisch, G. W. Trucks, H. B. Schlegel, G. E. Scuseria, M. A. Robb, J. R. Cheeseman, G. Scalmani, V. Barone, B. Mennucci, G. A. Petersson, H. Nakatsuji, M. Caricato, X. Li, H. P. Hratchian, A. F. Izmaylov, J. Bloino, G. Zheng, J. L. Sonnenberg, M. Hada, M. Ehara, K. Toyota, R. Fukuda, J. Hasegawa, M. Ishida, T. Nakajima, Y. Honda, O. Kitao, H. Nakai, T. Vreven, J. A. Montgomery, Jr., J. E. Peralta, F. Ogliaro, M. Bearpark, J. J. Heyd, E. Brothers, K. N. Kudin, V. N. Staroverov, R. Kobayashi, J. Normand, K. Raghavachari, A. Rendell, J. C. Burant, S. S. Iyengar, J. Tomasi, M. Cossi, N. Rega, J. M. Millam, M. Klene, J. E. Knox, J. B. Cross, V. Bakken, C. Adamo, J. Jaramillo, R. Gomperts, R. E. Stratmann, O. Yazyev, A. J. Austin, R. Cammi, C. Pomelli, J. W. Ochterski, R. L. Martin, K. Morokuma, V. G. Zakrzewski, G. A. Voth, P. Salvador, J. J. Dannenberg, S. Dapprich, A. D. Daniels, Farkas, J. B. Foresman, J. V. Ortiz, J. Cioslowski, D. J. Fox, *Gaussian09 Revision E.01*, **2009**.
- [354] G. t. Velde, F. M. Bickelhaupt, E. J. Baerends, C. F. Guerra, S. J. A. v. Gisbergen, J. G. Snijders, T. Ziegler, *Journal of Computational Chemistry* **2001**, *22*, 931–967.
- [355] C. Fonseca Guerra, J. G. Snijders, G. te Velde, E. J. Baerends, *Theoretical Chemistry Accounts: Theory, Computation, and Modeling (Theoretica Chimica Acta)* **1998**, *99*, 391–403.
- [356] *Recent Developments in the Synthesis, Thermostability and Liquid Crystal Properties of Aromatic Polyamides*, **2013**.
- [357] M. Kohout, “DGrid 4.6”, , 2011.
- [358] W. Oliver, G. Pharr, *Journal of Materials Research* **1992**, *7*, 1564–1583.
- [359] S. L. Mayo, B. D. Olafson, W. A. Goddard, *The Journal of Physical Chemistry* **1990**, *94*, 8897–8909.
- [360] K. Sidler, N. V. Cvetkovic, V. Savu, D. Tsamados, A. M. Ionescu, J. Brugger, *Sensors and Actuators A: Physical* **2010**, *162*, 155–159.
- [361] F. D. Fleischli, K. Sidler, M. Schaer, V. Savu, J. Brugger, L. Zuppiroli, *Organic Electronics* **2011**, *12*, 336–340.
- [362] P. P. Infelta, M. P. de Haas, J. M. Warman, *Radiation Physics and Chemistry* **1977**, *10*, 353–365.
- [363] J. M. Warman, M. P. de Haas, G. Dicker, F. C. Grozema, J. Piris, M. G. Debije, *Chemistry of Materials* **2004**, *16*, 4600–4609.
- [364] “CrysAlisPro Software System”, , 2015.
- [365] G. M. Sheldrick, *Acta Crystallographica Section A Foundations and Advances* **2015**, *71*, 3–8.
- [366] G. M. Sheldrick, *Acta Crystallographica Section C Structural Chemistry* **2015**, *71*, 3–8.
- [367] K. Masui, H. Ikegami, A. Mori, *Journal of the American Chemical Society* **2004**, *126*, 5074–5075.
- [368] L. Jiang, R. C. Hughes, D. Y. Sasaki, *Chem. Commun.* **2004**, *35*,.

# Appendix





## 9 Appendix

### 9.1 Crystallographic and Refinement Data

The supplementary crystallographic data can be obtained free of charge from the Cambridge Crystallographic Data Center (CCDC) via [www.ccdc.cam.ac.uk/datarequest/cif](http://www.ccdc.cam.ac.uk/datarequest/cif) using the corresponding CCDC deposition numbers:

Chapter	single-crystal	CCDC Deposition Number
2	<b>1a</b>	CCDC 1951216
2	<b>1b</b>	CCDC 1951217
2	<b>1c</b>	CCDC 1951218
2	<b>2a</b>	CCDC 1951219
2	<b>2b</b>	CCDC 1951220
2 and 4	<b>2c<sup>a</sup></b>	CCDC 1951221
2	<b>DHT2</b>	CCDC 1951222
2	<b>6a</b>	CCDC 1951223
3	<b>2</b>	CCDC 1043812

<sup>a</sup> denoted as **T2a** in Chapter 4.

**Table 9.1:** Crystallographic and refinement data of compound **1a**.

Identification code	CCDC 1951216
Empirical formula	C <sub>14</sub> H <sub>14</sub> O <sub>4</sub> S <sub>2</sub>
Formula weight [g/mol]	310.37
Temperature [K]	100.01(10)
Wavelength [Å]	1.54184
Crystal system	Triclinic
Space group	$P\bar{1}$
Unit cell dimensions	$a = 5.6993(3)\text{Å}; \quad \alpha = 92.722(5)^\circ$ $b = 8.0985(4); \quad \beta = 108.178(5)^\circ$ $c = 8.1101(4); \quad \gamma = 92.269(4)^\circ$
Volume [Å <sup>3</sup> ]	354.66(3)
<i>Z</i>	1
Density (calculated) [Mg/m <sup>3</sup> ]	1.453
Absorption coefficient [mm <sup>-1</sup> ]	3.503
<i>F</i> (000)	162
Crystal size [mm <sup>3</sup> ]	0.467 × 0.308 × 0.248
Theta range for data collection [°]	5.478 to 75.008
Index ranges	$-4 \leq h \leq 4, -10 \leq k \leq 10, -10 \leq l \leq 10$
Reflections collected	2164
Independent reflections	1396 [ <i>R</i> (int) = 0.0133]
Completeness to theta = 67.684°	99.1%
Absorption correction	Gaussian
Max. and min. transmission	0.586 and 0.359
Refinement method	Full-matrix least-squares on <i>F</i> <sup>2</sup>
Data / restraints / parameters	1396 / 0 / 119
Goodness-of-fit on <i>F</i> <sup>2</sup>	1.087
Final <i>R</i> indices [ <i>I</i> > 2σ( <i>I</i> )]	<i>R</i> <sub>1</sub> = 0.0307, <i>wR</i> <sub>2</sub> = 0.0829
<i>R</i> indices (all data)	<i>R</i> <sub>1</sub> = 0.0312, <i>wR</i> <sub>2</sub> = 0.0833
Largest diff. peak and hole [e·Å <sup>-3</sup> ]	0.311 and -0.265

## 9.1. Crystallographic and Refinement Data

**Table 9.2:** Atomic coordinates ( $\times 10^4$ ) and equivalent isotropic displacement parameters ( $\text{\AA}^2 \times 10^3$ ) for **1a**.  $U_{\text{eq}}$  is defined as one third of the trace of the orthogonalized  $U^{\text{ij}}$  tensor.

	$x$	$y$	$z$	$U_{\text{eq}}$
S(1)	2335(1)	540(1)	2705(1)	18(1)
O(1)	5724(2)	3248(1)	5431(1)	23(1)
O(2)	4683(2)	3980(1)	7802(1)	22(1)
C(1)	−96(3)	450(2)	773(2)	17(1)
C(2)	−2007(3)	1329(2)	971(2)	20(1)
C(3)	−1511(3)	2073(2)	2673(2)	20(1)
C(4)	757(3)	1757(2)	3767(2)	18(1)
C(5)	1779(3)	2274(2)	5668(2)	21(1)
C(6)	4264(3)	3215(2)	6224(2)	17(1)
C(7)	7077(3)	4855(2)	8526(2)	26(1)

**Table 9.3:** Crystallographic and refinement data of compound **1b**.

Identification code	CCDC 1951217
Empirical formula	C <sub>16</sub> H <sub>18</sub> O <sub>4</sub> S <sub>2</sub>
Formula weight [g/mol]	338.42
Temperature [K]	140.00(10)
Wavelength [Å]	1.54184
Crystal system	Monoclinic
Space group	<i>P</i> 2 <sub>1</sub> / <i>c</i>
Unit cell dimensions	<i>a</i> = 15.4717(4)Å; <i>α</i> = 90° <i>b</i> = 6.05317(14); <i>β</i> = 102.078(3)° <i>c</i> = 8.6742(2); <i>γ</i> = 90°
Volume [Å <sup>3</sup> ]	794.39(4)
<i>Z</i>	2
Density (calculated) [Mg/m <sup>3</sup> ]	1.415
Absorption coefficient [mm <sup>-1</sup> ]	3.174
<i>F</i> (100)	356
Crystal size [mm <sup>3</sup> ]	0.893 × 0.168 × 0.096
Theta range for data collection [°]	5.849 to 75.599
Index ranges	−19 ≤ <i>h</i> ≤ 18, −4 ≤ <i>k</i> ≤ 7, −10 ≤ <i>l</i> ≤ 10
Reflections collected	4995
Independent reflections	1599 [ <i>R</i> (int) = 0.0196]
Completeness to theta = 67.679°	99.6%
Absorption correction	Gaussian
Max. and min. transmission	0.795 and 0.322
Refinement method	Full-matrix least-squares on <i>F</i> <sup>2</sup>
Data / restraints / parameters	1599 / 0 / 136
Goodness-of-fit on <i>F</i> <sup>2</sup>	1.051
Final <i>R</i> indices [ <i>I</i> > 2σ( <i>I</i> )]	<i>R</i> <sub>1</sub> = 0.0273, <i>wR</i> <sub>2</sub> = 0.0755
<i>R</i> indices (all data)	<i>R</i> <sub>1</sub> = 0.0282, <i>wR</i> <sub>2</sub> = 0.0762
Largest diff. peak and hole [e·Å <sup>-3</sup> ]	0.319 and −0.238



## 9.1. Crystallographic and Refinement Data

**Table 9.4:** Atomic coordinates ( $\times 10^4$ ) and equivalent isotropic displacement parameters ( $\text{\AA}^2 \times 10^3$ ) for **1b**.  $U_{\text{eq}}$  is defined as one third of the trace of the orthogonalized  $U^{\text{ij}}$  tensor.

	$x$	$y$	$z$	$U_{\text{eq}}$
S(1)	4246(1)	8206(1)	2960(1)	25(1)
O(1)	1107(1)	6782(2)	−1181(1)	30(1)
O(2)	1296(1)	3481(1)	1(1)	26(1)
C(1)	4567(1)	10075(2)	4488(1)	19(1)
C(2)	3912(1)	11583(2)	4502(2)	24(1)
C(3)	3151(1)	11222(2)	3291(1)	24(1)
C(4)	3227(1)	9465(2)	2356(1)	23(1)
C(5)	2567(1)	8629(2)	957(2)	28(1)
C(6)	2218(1)	6346(2)	1204(1)	21(1)
C(7)	1489(1)	5619(2)	−133(1)	20(1)
C(8)	595(1)	2616(2)	−1231(2)	31(1)

**Table 9.5:** Crystallographic and refinement data of compound **1c**.

Identification code	CCDC 1951218
Empirical formula	C <sub>18</sub> H <sub>22</sub> O <sub>4</sub> S <sub>2</sub>
Formula weight [g/mol]	366.47
Temperature [K]	100.00(10)
Wavelength [Å]	1.54184
Crystal system	Monoclinic
Space group	<i>P</i> 2 <sub>1</sub> /c
Unit cell dimensions	<i>a</i> = 14.0916(5)Å; <i>α</i> = 90° <i>b</i> = 7.5029(2); <i>β</i> = 104.543(4)° <i>c</i> = 8.6268(3); <i>γ</i> = 90°
Volume [Å <sup>3</sup> ]	882.87(5)
<i>Z</i>	2
Density (calculated) [Mg/m <sup>3</sup> ]	1.379
Absorption coefficient [mm <sup>-1</sup> ]	2.897
<i>F</i> (000)	388
Crystal size [mm <sup>3</sup> ]	0.741 × 0.565 × 0.279
Theta range for data collection [°]	6.490 to 75.268
Index ranges	−17 ≤ <i>h</i> ≤ 17, −9 ≤ <i>k</i> ≤ 9, −5 ≤ <i>l</i> ≤ 10
Reflections collected	5561
Independent reflections	1798 [ <i>R</i> (int) = 0.0274]
Completeness to theta = 67.684°	99.4%
Absorption correction	Gaussian
Max. and min. transmission	0.572 and 0.304
Refinement method	Full-matrix least-squares on <i>F</i> <sup>2</sup>
Data / restraints / parameters	1798 / 0 / 110
Goodness-of-fit on <i>F</i> <sup>2</sup>	1.069
Final <i>R</i> indices [ <i>I</i> > 2σ( <i>I</i> )]	<i>R</i> <sub>1</sub> = 0.0345, <i>wR</i> <sub>2</sub> = 0.0957
<i>R</i> indices (all data)	<i>R</i> <sub>1</sub> = 0.0356, <i>wR</i> <sub>2</sub> = 0.0967
Largest diff. peak and hole [e·Å <sup>-3</sup> ]	0.325 and −0.430

## 9.1. Crystallographic and Refinement Data

**Table 9.6:** Atomic coordinates ( $\times 10^4$ ) and equivalent isotropic displacement parameters ( $\text{\AA}^2 \times 10^3$ ) for **1c**.  $U_{\text{eq}}$  is defined as one third of the trace of the orthogonalized  $U^{\text{ij}}$  tensor.

	$x$	$y$	$z$	$U_{\text{eq}}$
S(1)	5217(1)	6074(1)	7760(1)	18(1)
O(1)	8969(1)	3562(2)	4244(1)	32(1)
O(2)	8837(1)	5895(1)	2580(1)	26(1)
C(1)	5377(1)	4959(2)	9561(2)	18(1)
C(2)	6259(1)	4090(2)	9939(2)	20(1)
C(3)	6806(1)	4308(2)	8766(2)	19(1)
C(4)	6336(1)	5345(2)	7509(2)	18(1)
C(5)	6633(1)	5920(2)	6032(2)	21(1)
C(6)	7610(1)	5196(2)	5860(2)	20(1)
C(7)	7794(1)	5883(2)	4299(2)	25(1)
C(8)	8600(1)	4960(2)	3754(2)	21(1)
C(9)	9566(1)	5096(2)	1875(2)	30(1)

**Table 9.7:** Crystallographic and refinement data of compound **2a**.

Identification code	CCDC 1951219
Empirical formula	C <sub>18</sub> H <sub>24</sub> N <sub>2</sub> O <sub>2</sub> S <sub>2</sub>
Formula weight [g/mol]	364.51
Temperature [K]	100.01(10)
Wavelength [Å]	1.54184
Crystal system	Monoclinic
Space group	<i>P</i> 2 <sub>1</sub> /c
Unit cell dimensions	<i>a</i> = 17.114(3)Å; <i>α</i> = 90° <i>b</i> = 5.7214(7); <i>β</i> = 101.820(18)° <i>c</i> = 9.5335(14); <i>γ</i> = 90°
Volume [Å <sup>3</sup> ]	913.7(3)
<i>Z</i>	2
Density (calculated) [Mg/m <sup>3</sup> ]	1.325
Absorption coefficient [mm <sup>-1</sup> ]	2.742
<i>F</i> (000)	388
Crystal size [mm <sup>3</sup> ]	0.59 × 0.1 × 0.06
Theta range for data collection [°]	5.281 to 66.595
Reflections collected	1842
Independent reflections	1842 [ <i>R</i> (int) = <i>n</i> / <i>a</i> ]
Completeness to theta = 66.595°	97.8%
Absorption correction	Analytical
Max. and min. transmission	0.925 and 0.392
Refinement method	Full-matrix least-squares on <i>F</i> <sup>2</sup>
Data / restraints / parameters	1842 / 0 / 111
Goodness-of-fit on <i>F</i> <sup>2</sup>	1.394
Final <i>R</i> indices [ <i>I</i> > 2σ( <i>I</i> )]	<i>R</i> <sub>1</sub> = 0.1178, <i>wR</i> <sub>2</sub> = 0.3277
<i>R</i> indices (all data)	<i>R</i> <sub>1</sub> = 0.1382, <i>wR</i> <sub>2</sub> = 0.3448
Largest diff. peak and hole [e·Å <sup>-3</sup> ]	0.964 and -0.624

## 9.1. Crystallographic and Refinement Data

**Table 9.8:** Atomic coordinates ( $\times 10^4$ ) and equivalent isotropic displacement parameters ( $\text{\AA}^2 \times 10^3$ ) for **2a**.  $U_{\text{eq}}$  is defined as one third of the trace of the orthogonalized  $U^{\text{ij}}$  tensor.

	$x$	$y$	$z$	$U_{\text{eq}}$
S(1)	4368.3(14)	1843(3)	8088(3)	36.3(7)
O(1)	2239(4)	3136(10)	7317(7)	37.0(14)
N(1)	2055(5)	3865(13)	4946(9)	38.5(18)
C(1)	4647(5)	−166(14)	9413(9)	29.7(17)
C(2)	4142(6)	−2050(15)	9218(12)	43(2)
C(3)	3534(6)	−1880(15)	7963(12)	43(2)
C(4)	3569(6)	195(15)	7271(10)	38(2)
C(5)	3015(6)	937(17)	5944(10)	40(2)
C(6)	2393(5)	2744(15)	6135(11)	38(2)
C(7)	1400(6)	5531(16)	4948(10)	42(2)
C(8)	1255(6)	6985(16)	3587(11)	42(2)
C(9)	619(6)	8846(18)	3646(14)	52(3)

**Table 9.9:** Crystallographic and refinement data of compound **2b**.

Identification code	CCDC 1951220
Empirical formula	C <sub>20</sub> H <sub>28</sub> N <sub>2</sub> O <sub>2</sub> S <sub>2</sub>
Formula weight [g/mol]	392.56
Temperature [K]	140.01(10)
Wavelength [Å]	1.54184
Crystal system	Monoclinic
Space group	<i>P</i> 2 <sub>1</sub> /c
Unit cell dimensions	<i>a</i> = 21.8811(10)Å; $\alpha = 90^\circ$ <i>b</i> = 4.88737(14); $\beta = 98.204(4)^\circ$ <i>c</i> = 9.4412(4); $\gamma = 90^\circ$
Volume [Å <sup>3</sup> ]	999.32(7)
<i>Z</i>	2
Density (calculated) [Mg/m <sup>3</sup> ]	1.305
Absorption coefficient [mm <sup>-1</sup> ]	2.544
Crystal size [mm <sup>3</sup> ]	0.62 × 0.08 × 0.05
Theta range for data collection [°]	4.083 to 76.530
Reflections collected	6986
Independent reflections	2023 [ <i>R</i> (int) = 0.0650]
Completeness to theta = 76.530°	97.6%
Absorption correction	Gaussian
Max. and min. transmission	1.0 and 0.321
Refinement method	Full-matrix least-squares on <i>F</i> <sup>2</sup>
Data / restraints / parameters	2023 / 195 / 178
Goodness-of-fit on <i>F</i> <sup>2</sup>	1.030
Final <i>R</i> indices [ <i>I</i> > 2σ( <i>I</i> )]	<i>R</i> <sub>1</sub> = 0.0527, <i>wR</i> <sub>2</sub> = 0.1419
<i>R</i> indices (all data)	<i>R</i> <sub>1</sub> = 0.0642, <i>wR</i> <sub>2</sub> = 0.1499
Largest diff. peak and hole [e·Å <sup>-3</sup> ]	0.385 and -0.226

## 9.1. Crystallographic and Refinement Data

**Table 9.10:** Atomic coordinates ( $\times 10^4$ ) and equivalent isotropic displacement parameters ( $\text{\AA}^2 \times 10^3$ ) for **2b**.  $U_{\text{eq}}$  is defined as one third of the trace of the orthogonalized  $U^{\text{ij}}$  tensor.

	$x$	$y$	$z$	$U_{\text{eq}}$
S(1A)	4482.3(15)	6860(10)	8018(6)	43.7(6)
S(1B)	4399(3)	7157(8)	8422(12)	48.1(12)
O(1)	2089.6(7)	8842(3)	5241.7(18)	47.3(4)
N(1)	1849.5(8)	4521(3)	4578.4(18)	38.0(4)
C(1A)	4683(6)	5100(40)	9595(18)	40(2)
C(1B)	4681(9)	4760(50)	9700(30)	39(3)
C(2A)	4190(4)	3760(20)	9990(9)	44.2(16)
C(2B)	4229(5)	2890(30)	9848(13)	43(2)
C(3A)	3646(5)	4180(20)	8987(11)	42.6(18)
C(3B)	3655(6)	3380(30)	8950(16)	39(2)
C(4A)	3727(4)	5810(30)	7867(13)	38.0(18)
C(4B)	3684(5)	5600(40)	8094(19)	36(3)
C(5A)	3259(4)	6690(20)	6631(11)	37.4(16)
C(5B)	3219(6)	6890(30)	6970(20)	50(3)
C(6)	2640.1(9)	5231(4)	6611(2)	39.3(4)
C(7)	2174.4(9)	6367(4)	5413(2)	35.5(4)
C(8)	1347.8(10)	5347(4)	3463(2)	43.8(5)
C(9)	1065.8(10)	2945(4)	2630(2)	44.8(5)
C(10)	546.1(11)	3819(6)	1468(3)	52.4(5)

**Table 9.11:** Crystallographic and refinement data of compound **2c**.

Identification code	CCDC 1951221
Empirical formula	C <sub>22</sub> H <sub>32</sub> N <sub>2</sub> O <sub>2</sub> S <sub>2</sub>
Formula weight [g/mol]	420.61
Temperature [K]	199.99(10)
Wavelength [Å]	1.54184
Crystal system	Triclinic
Space group	$P\bar{1}$
Unit cell dimensions	$a = 4.9848(4)\text{Å}; \quad \alpha = 90.584(9)^\circ$ $b = 5.6250(5); \quad \beta = 90.140(8)^\circ$ $c = 21.347(3); \quad \gamma = 107.702(8)^\circ$
Volume [Å <sup>3</sup> ]	570.18(10)
<i>Z</i>	1
Density (calculated) [Mg/m <sup>3</sup> ]	1.225
Absorption coefficient [mm <sup>-1</sup> ]	2.261
<i>F</i> (000)	226
Crystal size [mm <sup>3</sup> ]	0.742 × 0.271 × 0.034
Theta range for data collection [°]	4.142 to 75.947
Index ranges	$-6 \leq h \leq 3, -6 \leq k \leq 7, -26 \leq l \leq 26$
Reflections collected	3263
Independent reflections	2231 [ <i>R</i> (int) = 0.0356]
Completeness to theta = 67.684°	99.1%
Absorption correction	Analytical
Max. and min. transmission	0.925 and 0.392
Refinement method	Full-matrix least-squares on <i>F</i> <sup>2</sup>
Data / restraints / parameters	2231 / 100 / 166
Goodness-of-fit on <i>F</i> <sup>2</sup>	1.063
Final <i>R</i> indices [ <i>I</i> > 2σ( <i>I</i> )]	<i>R</i> <sub>1</sub> = 0.0585, <i>wR</i> <sub>2</sub> = 0.1532
<i>R</i> indices (all data)	<i>R</i> <sub>1</sub> = 0.0675, <i>wR</i> <sub>2</sub> = 0.1617
Largest diff. peak and hole [e·Å <sup>-3</sup> ]	0.519 and -0.418



## 9.1. Crystallographic and Refinement Data

**Table 9.12:** Atomic coordinates ( $\times 10^4$ ) and equivalent isotropic displacement parameters ( $\text{\AA}^2 \times 10^3$ ) for **2c**.  $U_{\text{eq}}$  is defined as one third of the trace of the orthogonalized  $U^{\text{ij}}$  tensor.

	$x$	$y$	$z$	$U_{\text{eq}}$
S(1)	6366(1)	7959(1)	4429(1)	43(1)
O(1)	3725(5)	3493(7)	1975(2)	83(1)
N(1A)	−981(14)	2484(14)	1862(4)	57(2)
N(1B)	−720(18)	3180(20)	1672(4)	59(2)
C(1)	9224(5)	10259(5)	4736(1)	38(1)
C(2)	9661(6)	12408(5)	4406(2)	46(1)
C(3)	7709(6)	12183(5)	3911(2)	48(1)
C(4)	5775(6)	9898(5)	3858(2)	42(1)
C(5)	3426(6)	9000(6)	3387(2)	47(1)
C(6)	3652(6)	6828(6)	2985(2)	46(1)
C(7)	1408(6)	6156(7)	2476(2)	51(1)
C(8)	1536(7)	4034(8)	2057(2)	58(1)
C(9A)	−1414(16)	247(15)	1467(3)	63(2)
C(9B)	−728(18)	1452(18)	1152(5)	68(2)
C(10A)	−2920(20)	301(19)	872(4)	81(2)
C(10B)	−3180(20)	−811(18)	1200(5)	80(2)
C(11A)	−3100(50)	−2020(30)	473(7)	105(4)
C(11B)	−3630(60)	−2650(30)	650(8)	96(5)

**Table 9.13:** Crystallographic and refinement data of compound **DHT2**.

Identification code	CCDC 1951222
Empirical formula	C <sub>20</sub> H <sub>30</sub> S <sub>2</sub>
Formula weight [g/mol]	334.56
Temperature [K]	140.01(10)
Wavelength [Å]	1.54184
Crystal system	Triclinic
Space group	$P\bar{1}$
Unit cell dimensions	$a = 5.7717(6)\text{Å}; \quad \alpha = 99.154(9)^\circ$ $b = 7.7801(9); \quad \beta = 91.780(9)^\circ$ $c = 22.363(2); \quad \gamma = 105.885(10)^\circ$
Volume [Å <sup>3</sup> ]	950.60(18)
<i>Z</i>	2
Density (calculated) [Mg/m <sup>3</sup> ]	1.169
Absorption coefficient [mm <sup>-1</sup> ]	2.474
<i>F</i> (000)	364
Crystal size [mm <sup>3</sup> ]	0.841 × 0.687 × 0.114
Theta range for data collection [°]	4.017 to 73.184
Index ranges	$-4 \leq h \leq 6, -9 \leq k \leq 9, -27 \leq l \leq 27$
Reflections collected	5840
Independent reflections	3641 [ <i>R</i> (int) = 0.0718]
Completeness to theta = 67.684°	99.5%
Absorption correction	Gaussian
Max. and min. transmission	1.000 and 0.152
Refinement method	Full-matrix least-squares on <i>F</i> <sup>2</sup>
Data / restraints / parameters	3641 / 0 / 201
Goodness-of-fit on <i>F</i> <sup>2</sup>	1.094
Final <i>R</i> indices [ <i>I</i> > 2σ( <i>I</i> )]	<i>R</i> <sub>1</sub> = 0.1137, <i>wR</i> <sub>2</sub> = 0.3190
<i>R</i> indices (all data)	<i>R</i> <sub>1</sub> = 0.1212, <i>wR</i> <sub>2</sub> = 0.3237
Largest diff. peak and hole [e·Å <sup>-3</sup> ]	1.099 and -0.945

## 9.1. Crystallographic and Refinement Data

**Table 9.14:** Atomic coordinates ( $\times 10^4$ ) and equivalent isotropic displacement parameters ( $\text{\AA}^2 \times 10^3$ ) for **DHT2**.  $U_{\text{eq}}$  is defined as one third of the trace of the orthogonalized  $U^{\text{ij}}$  tensor.

	$x$	$y$	$z$	$U_{\text{eq}}$
S(1)	7014(3)	6300(2)	2393(1)	41(1)
S(2)	8301(2)	8243(2)	4364(1)	36(1)
C(1)	5327(16)	8308(13)	−1057(3)	70(2)
C(2)	6872(13)	7445(11)	−706(3)	56(2)
C(3)	6836(12)	7934(9)	−24(3)	50(2)
C(4)	8372(12)	7097(9)	339(3)	50(2)
C(5)	8280(11)	7567(8)	1025(3)	45(1)
C(6)	9772(13)	6697(10)	1384(3)	52(2)
C(7)	9678(11)	7123(8)	2062(3)	43(1)
C(8)	11442(11)	8129(8)	2498(3)	44(1)
C(9)	10690(10)	8237(8)	3097(3)	40(1)
C(10)	8323(10)	7314(7)	3117(3)	36(1)
C(11)	6950(9)	7136(7)	3648(3)	34(1)
C(12)	4608(10)	6229(7)	3698(3)	37(1)
C(13)	3872(9)	6424(7)	4300(3)	34(1)
C(14)	5676(10)	7487(7)	4718(3)	34(1)
C(15)	5673(10)	8068(7)	5386(3)	36(1)
C(16)	3328(9)	7315(7)	5663(3)	35(1)
C(17)	3546(10)	8062(7)	6344(3)	36(1)
C(18)	1306(9)	7360(7)	6671(3)	35(1)
C(19)	1628(10)	8120(8)	7346(3)	39(1)
C(20)	−570(12)	7387(9)	7690(3)	49(2)

**Table 9.15:** Crystallographic and refinement data of compound **6a**.

Identification code	CCDC 1951223
Empirical formula	C <sub>9</sub> H <sub>13</sub> NOS
Formula weight [g/mol]	183.26
Temperature [K]	140.00(10)
Wavelength [Å]	1.54184
Crystal system	Orthorhombic
Space group	<i>Pca</i> 2 <sub>1</sub>
Unit cell dimensions	$a = 9.48958(16)\text{Å}; \alpha = 90^\circ$ $b = 5.37710(10); \beta = 90^\circ$ $c = 38.1047(6); \gamma = 90^\circ$
Volume [Å <sup>3</sup> ]	1944.34(6)
<i>Z</i>	8
Density (calculated) [Mg/m <sup>3</sup> ]	1.252
Absorption coefficient [mm <sup>-1</sup> ]	2.578
Crystal size [mm <sup>3</sup> ]	0.51 × 0.12 × 0.05
Theta range for data collection [°]	4.642 to 76.071
Reflections collected	16567
Independent reflections	3641 [ <i>R</i> (int) = 0.0405]
Completeness to theta = 76.071°	99.90%
Absorption correction	Analytical
Max. and min. transmission	0.886 and 0.506
Refinement method	Full-matrix least-squares on <i>F</i> <sup>2</sup>
Data / restraints / parameters	3980 / 159 / 265
Goodness-of-fit on <i>F</i> <sup>2</sup>	1.071
Final <i>R</i> indices [ <i>I</i> > 2σ( <i>I</i> )]	<i>R</i> <sub>1</sub> = 0.0487, <i>wR</i> <sub>2</sub> = 0.1308
<i>R</i> indices (all data)	<i>R</i> <sub>1</sub> = 0.0492, <i>wR</i> <sub>2</sub> = 0.1314
Largest diff. peak and hole [e·Å <sup>-3</sup> ]	0.369 and -0.252

## 9.1. Crystallographic and Refinement Data

**Table 9.16:** Atomic coordinates ( $\times 10^4$ ) and equivalent isotropic displacement parameters ( $\text{\AA}^2 \times 10^3$ ) for **6a**.  $U_{\text{eq}}$  is defined as one third of the trace of the orthogonalized  $U^{\text{ij}}$  tensor.

	$x$	$y$	$z$	$U_{\text{eq}}$
S(1)	1222.8(10)	4707.7(16)	4552.6(3)	26.8(2)
O(1)	1438(3)	3545(6)	3633.4(8)	32.6(6)
N(1)	3751(4)	3995(8)	3517.8(10)	34.8(8)
C(1)	−223(4)	6334(8)	4691.4(11)	30.9(8)
C(2)	−448(4)	8377(8)	4493.1(12)	31.9(8)
C(3)	573(4)	8686(7)	4219.8(11)	28.6(8)
C(4)	1560(4)	6812(7)	4221.3(10)	22.8(7)
C(5)	2779(4)	6534(7)	3974.2(10)	25.3(7)
C(6)	2582(4)	4533(7)	3695.2(10)	24.6(7)
C(7)	3749(6)	2182(13)	3233.1(15)	53.3(15)
C(8)	5146(7)	1800(14)	3080.2(19)	64.6(17)
C(9)	5120(8)	−92(15)	2781.5(18)	64.5(19)
S(2A)	4213(3)	9898(4)	5428.0(5)	31.7(4)
S(2B)	3410(20)	5820(40)	5843(5)	31(3)
O(2)	4214(3)	11219(7)	6374.0(9)	35.0(7)
N(2)	6524(4)	11068(9)	6488.9(11)	38.9(9)
C(10A)	2754(6)	8233(12)	5293.2(19)	27.8(13)
C(10B)	2470(50)	6680(90)	5473(9)	30(4)
C(11A)	2500(9)	6279(13)	5509(2)	31.7(12)
C(11B)	3030(50)	8700(80)	5313(13)	28(4)
C(12A)	3523(16)	6180(30)	5785(4)	34(2)
C(12B)	4260(60)	9650(100)	5487(12)	29(4)
C(13A)	4475(7)	7956(13)	5784.0(19)	24.9(10)
C(13B)	4530(40)	8280(80)	5763(11)	28(4)
C(14)	5673(4)	8408(8)	6032.1(11)	31.8(9)
C(15)	5387(4)	10377(8)	6311.1(10)	25.3(8)
C(16)	6442(6)	12801(13)	6783.3(15)	51.7(13)
C(17)	7826(8)	13442(16)	6922(2)	73(2)
C(18)	7722(9)	15264(16) 7228.5(19)	74(2)	

**Table 9.17:** Crystallographic and refinement data of compound 2.

Identification code	CCDC 1043812
Empirical formula	C <sub>24</sub> H <sub>22</sub> O <sub>4</sub> S <sub>4</sub>
Formula weight [g/mol]	502.66
Temperature [K]	100(2)
Wavelength [Å]	0.70073
Crystal system	Monoclinic
Space group	<i>P</i> 2 <sub>1</sub> /c
Unit cell dimensions	<i>a</i> = 22.091(9)Å; <i>α</i> = 90° <i>b</i> = 5.8824(19); <i>β</i> = 91.81(2)° <i>c</i> = 9.0102(11); <i>γ</i> = 90°
Volume [Å <sup>3</sup> ]	1170.3(6)
<i>Z</i>	2
Density (calculated) [Mg/m <sup>3</sup> ]	1.426
Absorption coefficient [mm <sup>-1</sup> ]	0.435
<i>F</i> (000)	524
Crystal size [mm <sup>3</sup> ]	0.49 × 0.40 × 0.16
Theta range for data collection [°]	1.84 to 30.00
Index ranges	−31 ≤ <i>h</i> ≤ 31, −8 ≤ <i>k</i> ≤ 8, −12 ≤ <i>l</i> ≤ 12
Reflections collected	15612
Independent reflections	3379 [ <i>R</i> (int) = 0.0992]
Completeness to theta = 30.00°	98.9%
Absorption correction	Semi-empirical from equivalents
Max. and min. transmission	0.6089 and 0.2957
Refinement method	Full-matrix least-squares on <i>F</i> <sup>2</sup>
Data / restraints / parameters	3379 / 0 / 146
Goodness-of-fit on <i>F</i> <sup>2</sup>	1.163
Final <i>R</i> indices [ <i>I</i> > 2σ( <i>I</i> )]	<i>R</i> <sub>1</sub> = 0.0962, <i>wR</i> <sub>2</sub> = 0.2322
<i>R</i> indices (all data)	<i>R</i> <sub>1</sub> = 0.1251, <i>wR</i> <sub>2</sub> = 0.2517
Largest diff. peak and hole [e·Å <sup>-3</sup> ]	1.995 and −0.606

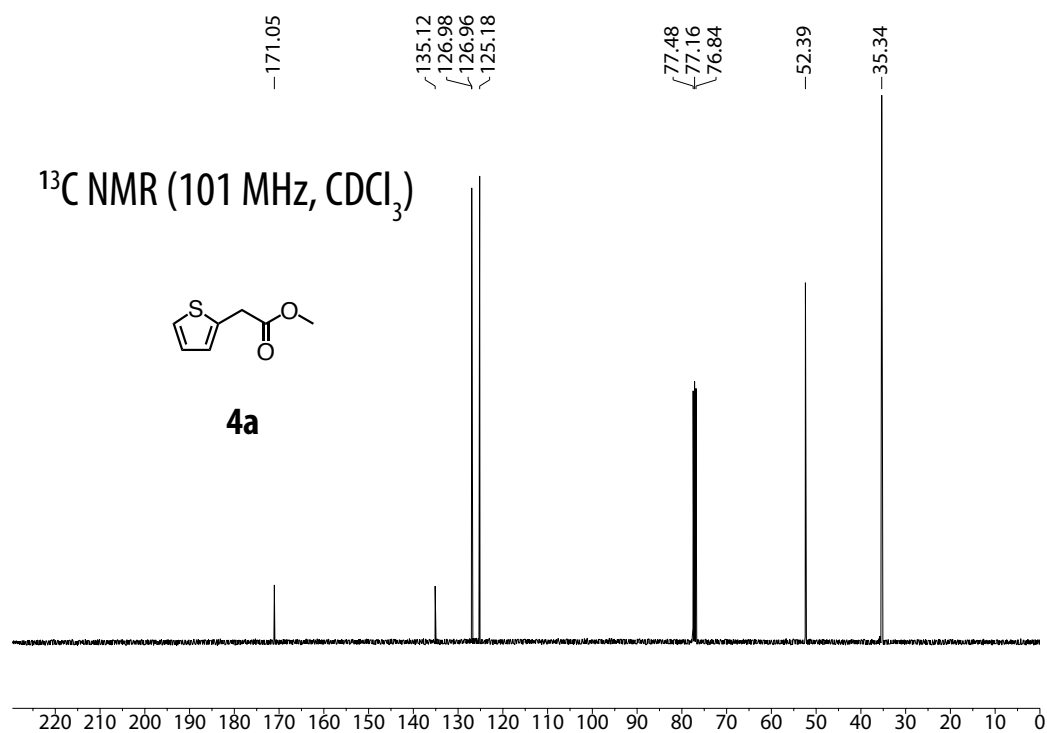
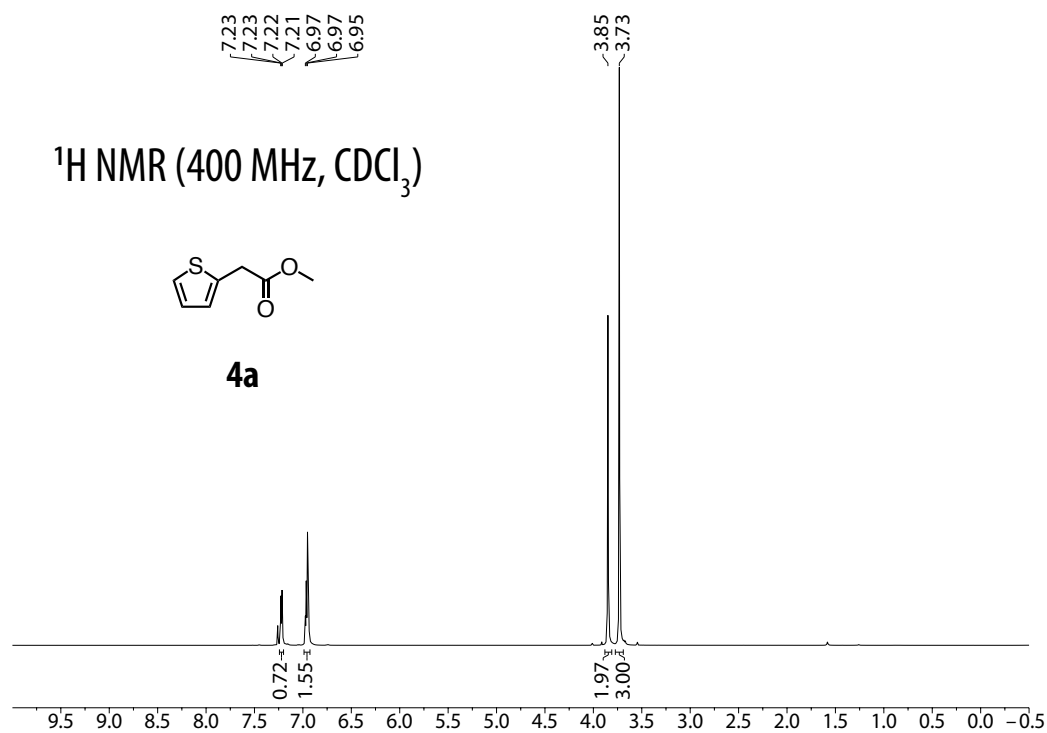
## 9.1. Crystallographic and Refinement Data

**Table 9.18:** Atomic coordinates ( $\times 10^4$ ) and equivalent isotropic displacement parameters ( $\text{\AA}^2 \times 10^3$ ) for **2**.  $U_{\text{eq}}$  is defined as one third of the trace of the orthogonalized  $U^{\text{ij}}$  tensor.

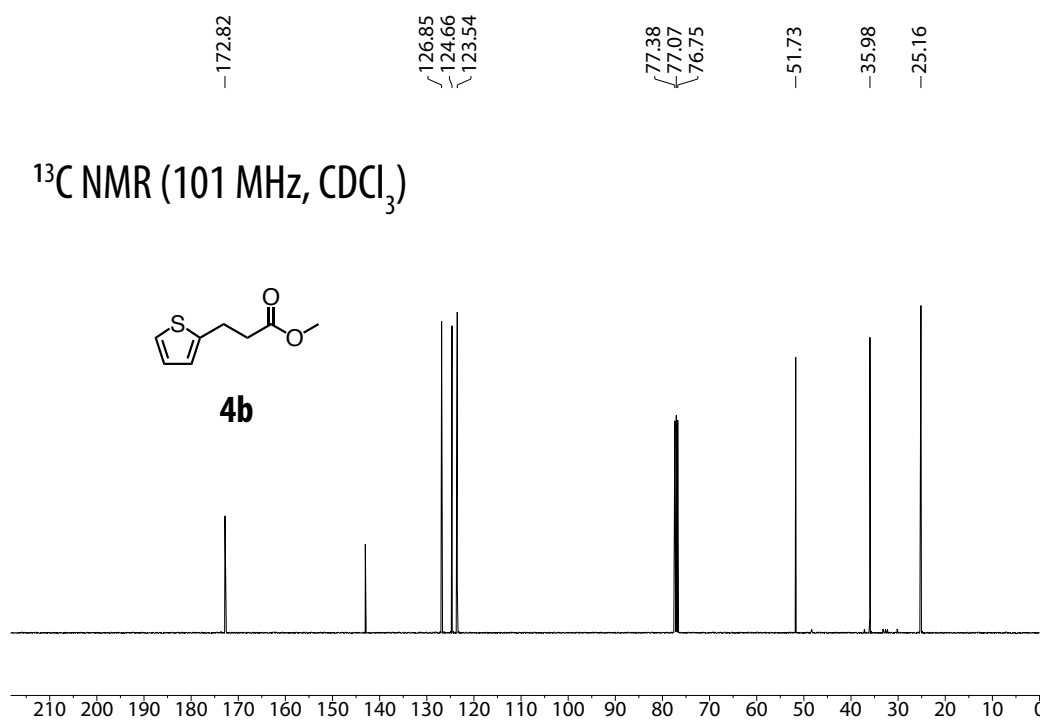
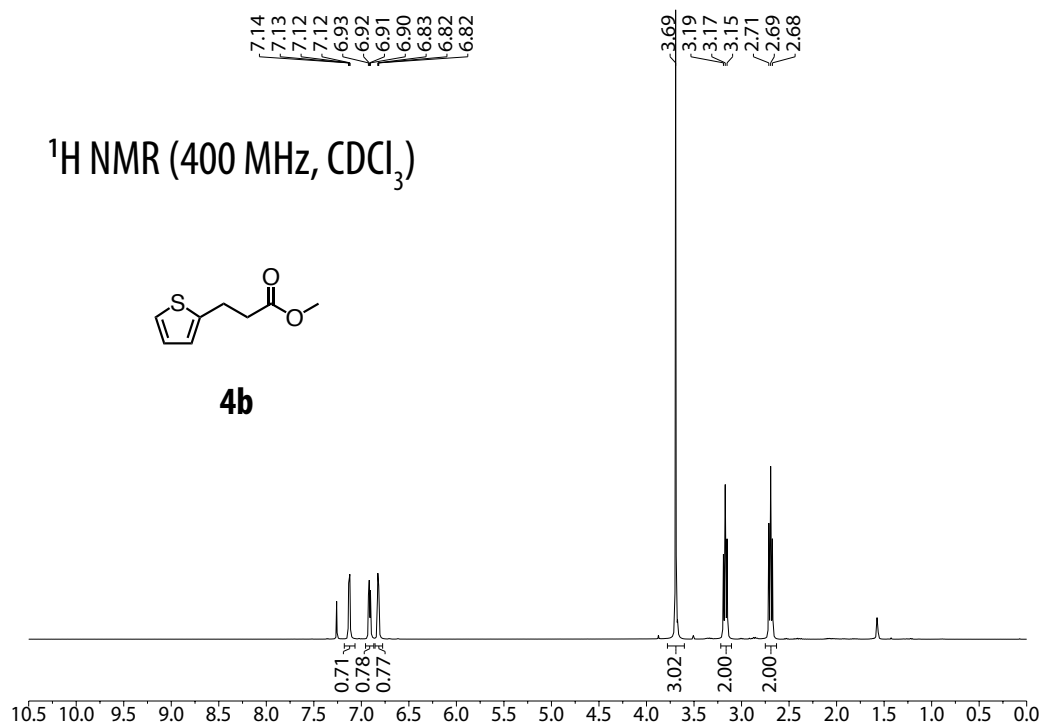
	$x$	$y$	$z$	$U_{\text{eq}}$
S(1)	1974(1)	3165(2)	4439(1) 29(1)	
S(2)	856(1)	6378(2)	923(1) 22(1)	
O(1)	4158(3)	−1548(10)	5994(6)	71(2)
O(2)	3848(2)	1727(7)	6941(4)	31(2)
C(1)	4631(3)	−177(12)	8274(7)	44(1)
C(2)	4203(2)	−90(10)	6941(6)	35(1)
C(3)	3409(2)	1918(9)	5723(5)	29(1)
C(4)	3076(2)	4140(10)	5961(5)	34(1)
C(5)	2632(2)	4720(8)	4721(5)	26(1)
C(6)	2666(2)	6439(9)	3715(6)	31(1)
C(7)	2155(2)	6537(9)	2712(6)	30(1)
C(8)	1739(2)	4863(8)	2959(5)	23(1)
C(9)	1163(2)	4413(8)	2184(5)	23(1)
C(10)	799(2)	2531(8)	2273(5)	22(1)
C(11)	271(2)	2643(8)	1329(5)	22(1)
C(12)	234(2)	4637(6)	531(4)	20(1)

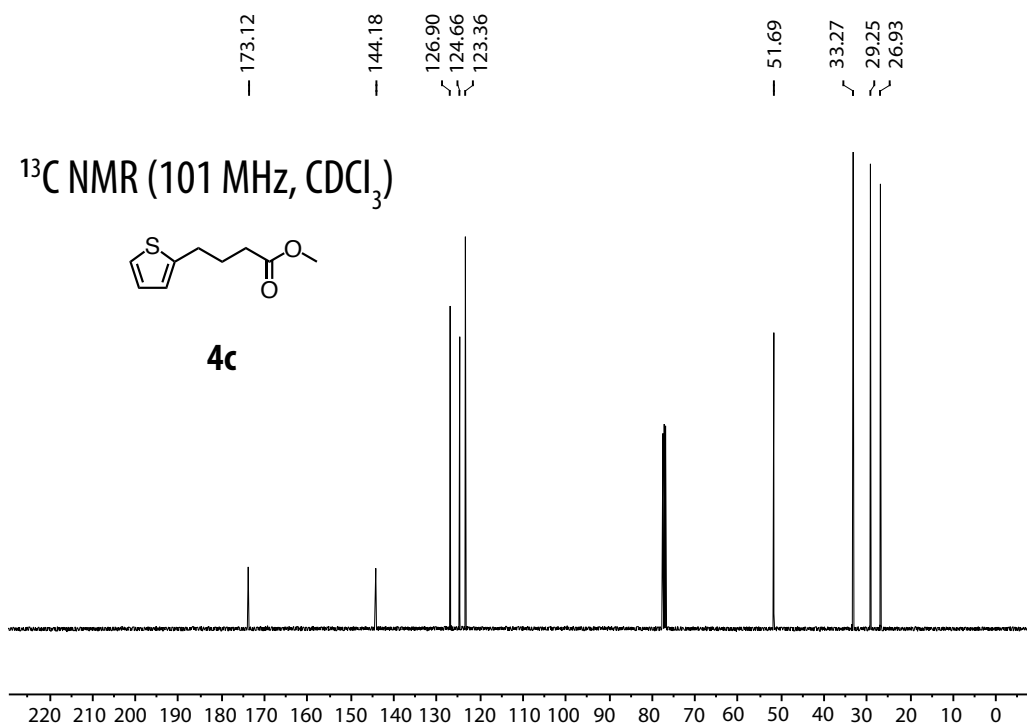
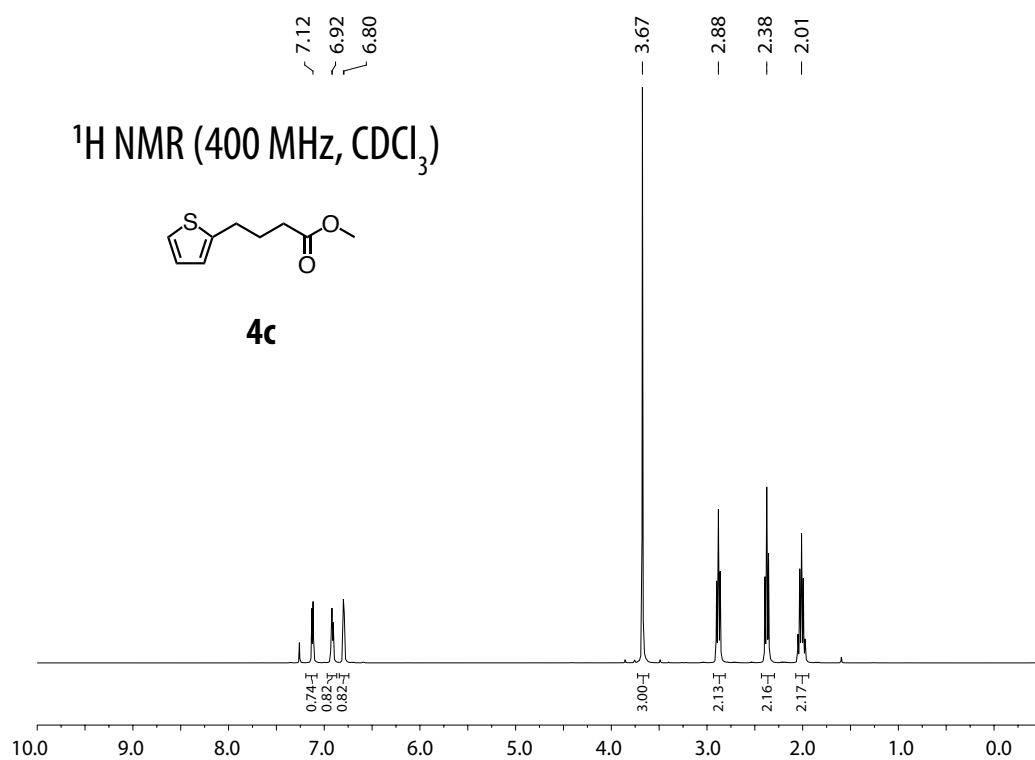
## 9.2 NMR Spectra

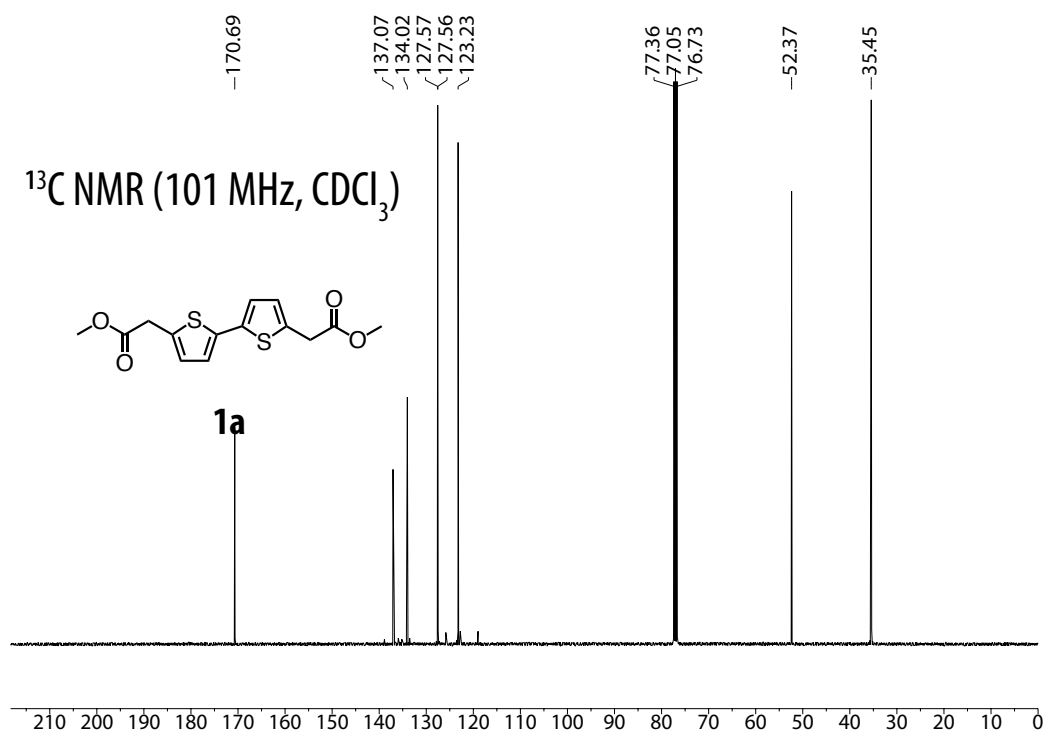
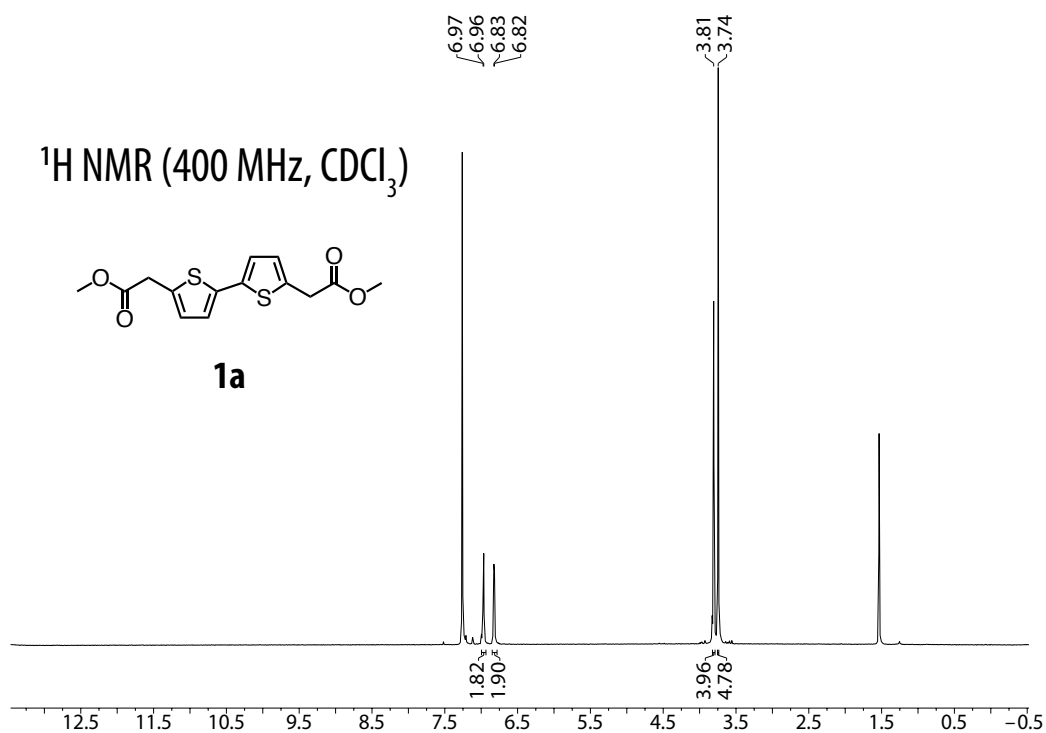
## 9.2.1 Bithiophenes with Hydrogen-Bonded Substituents

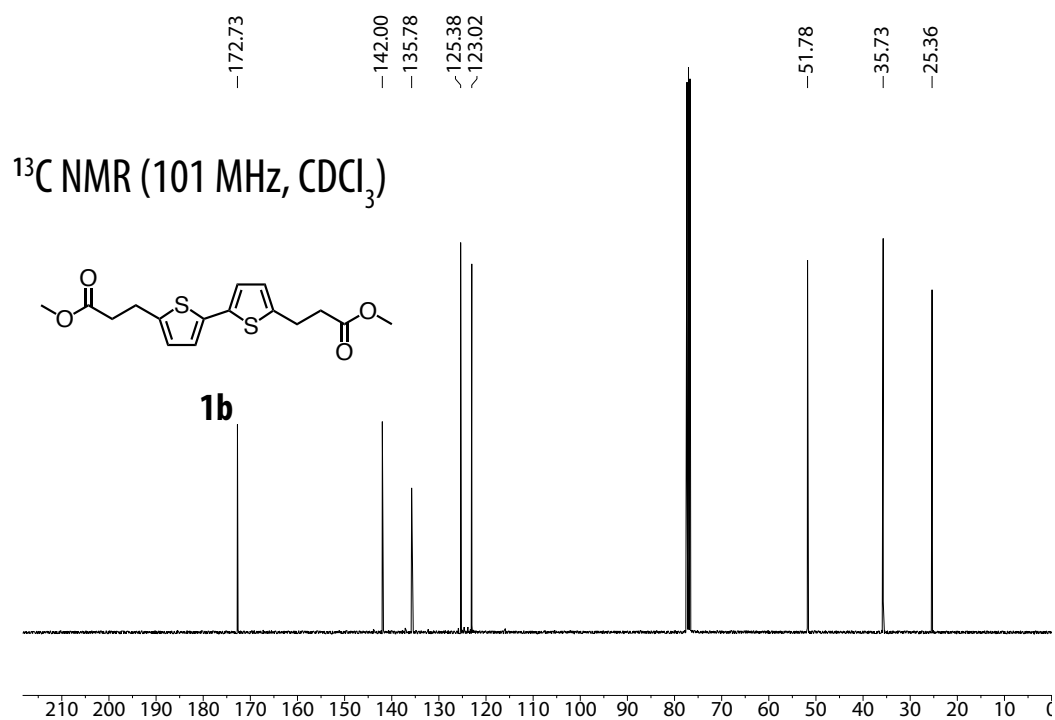
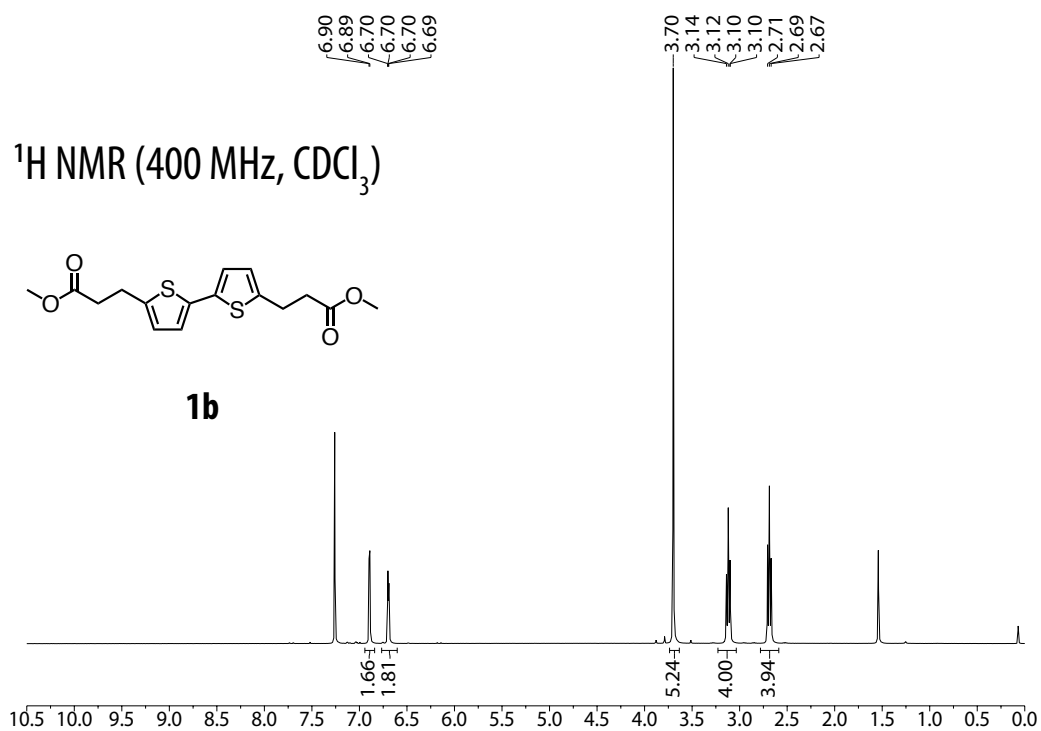


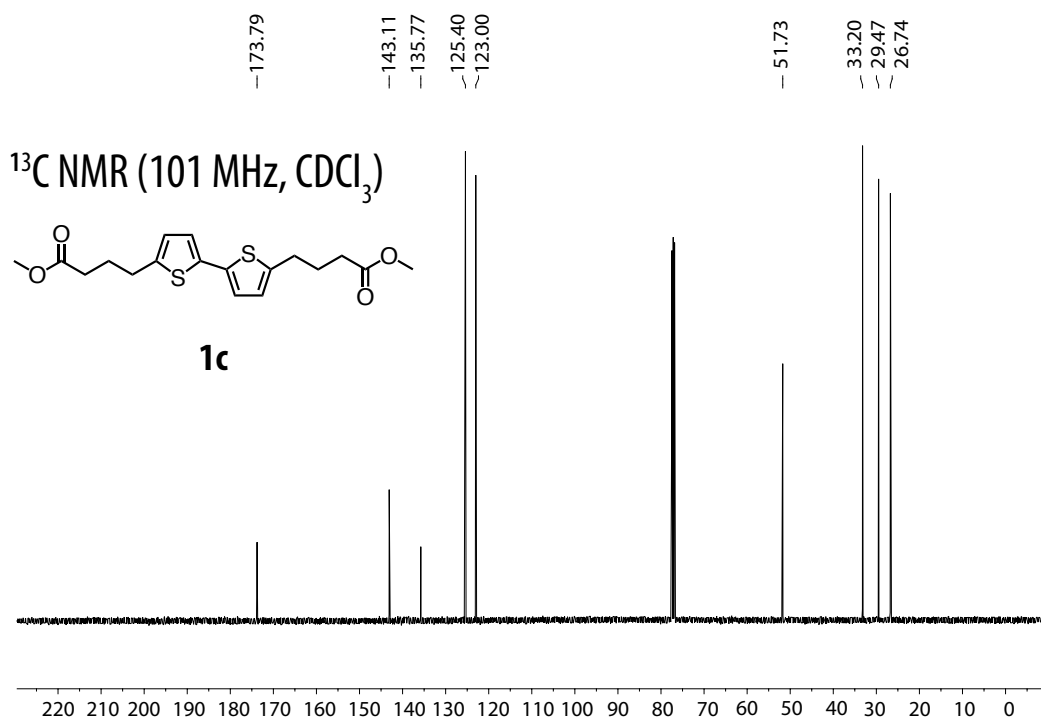
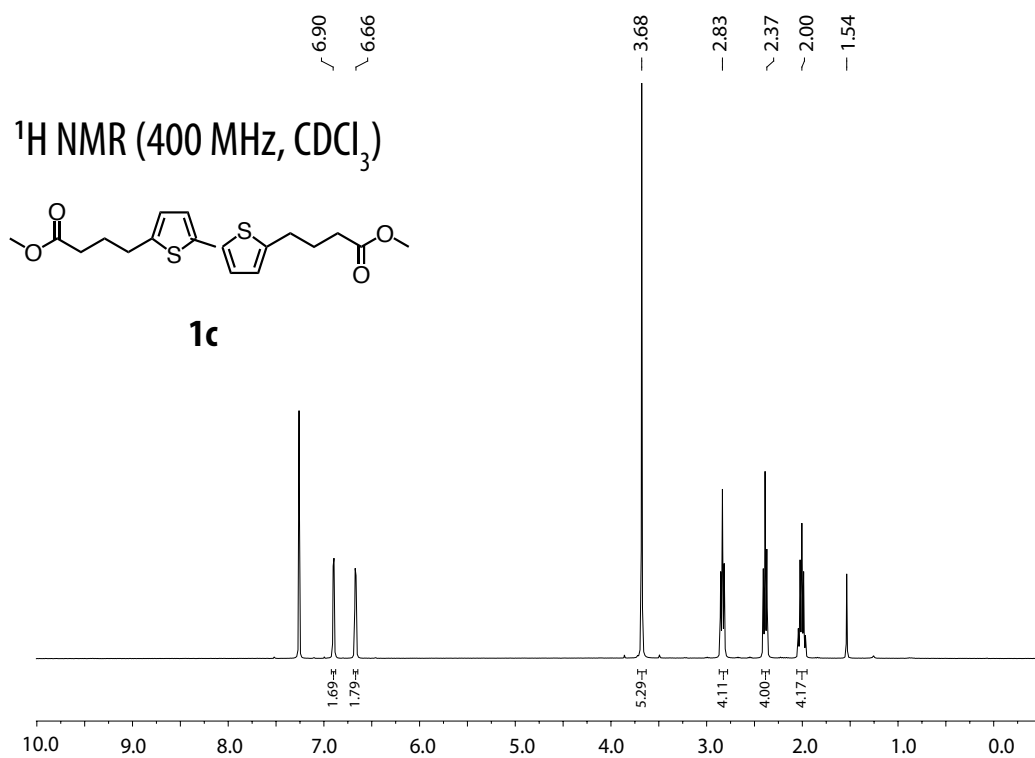


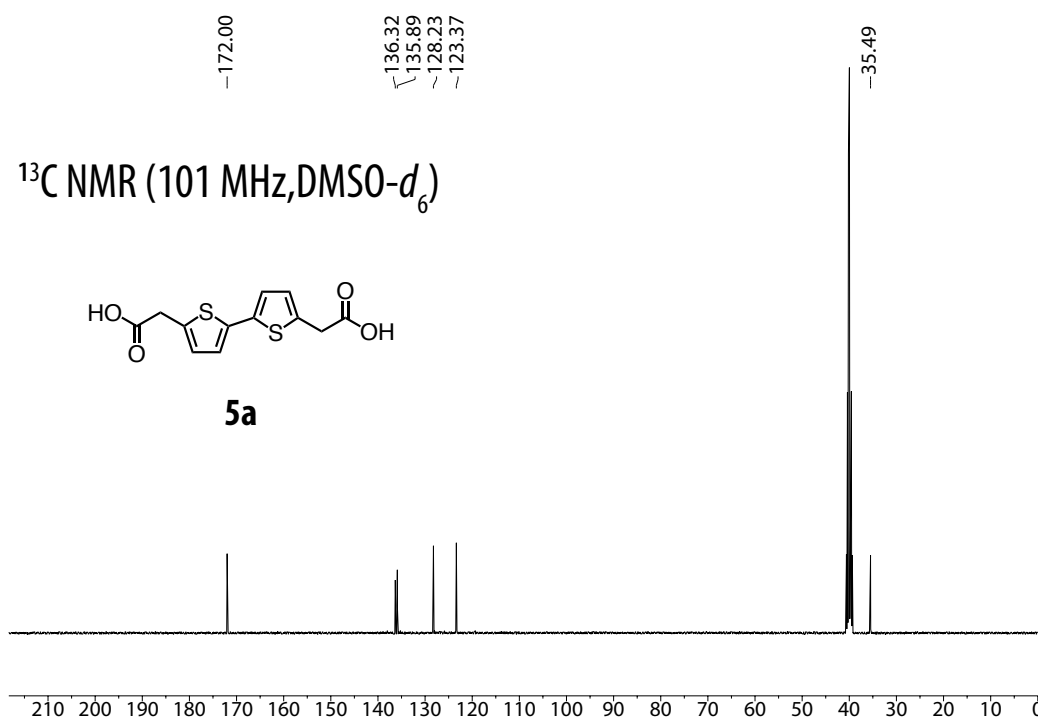
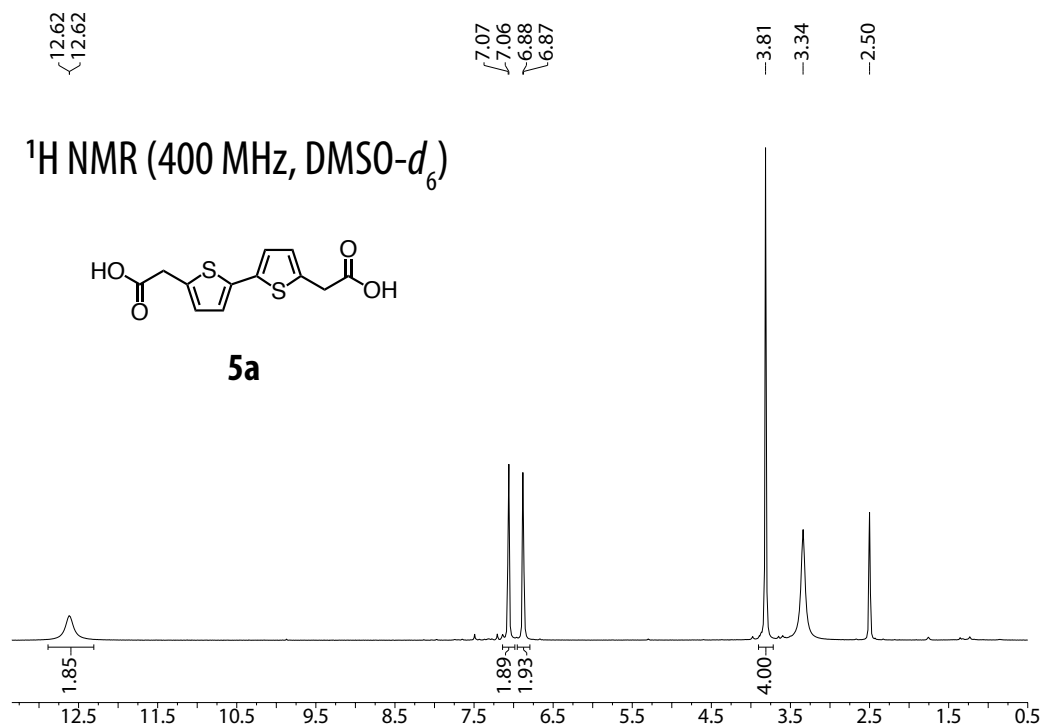


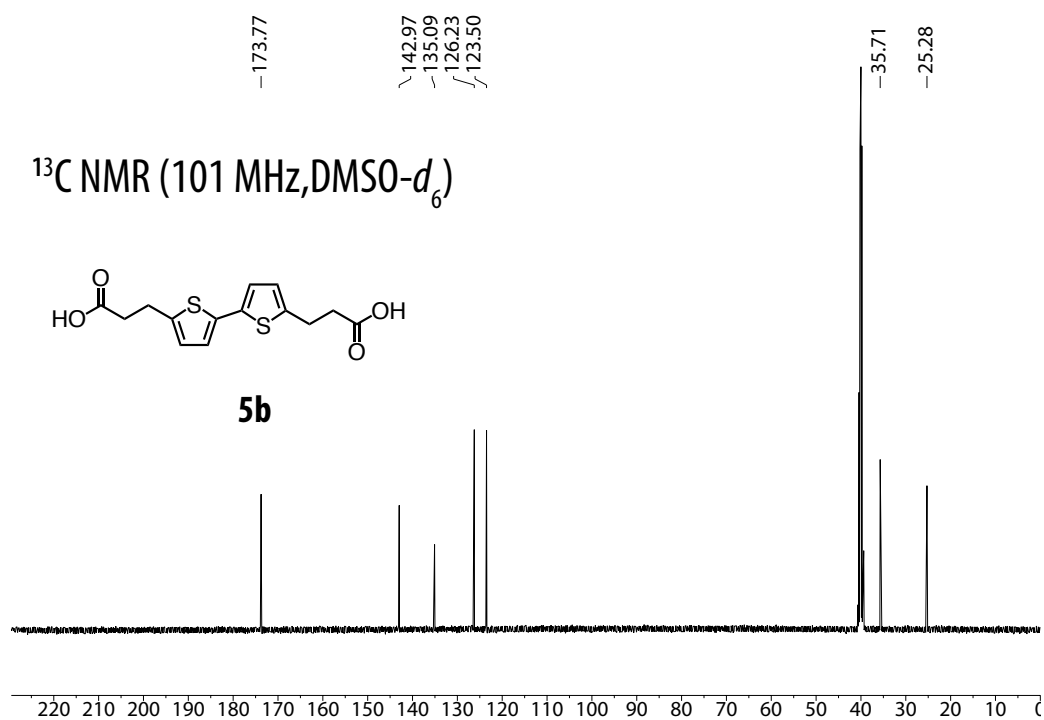
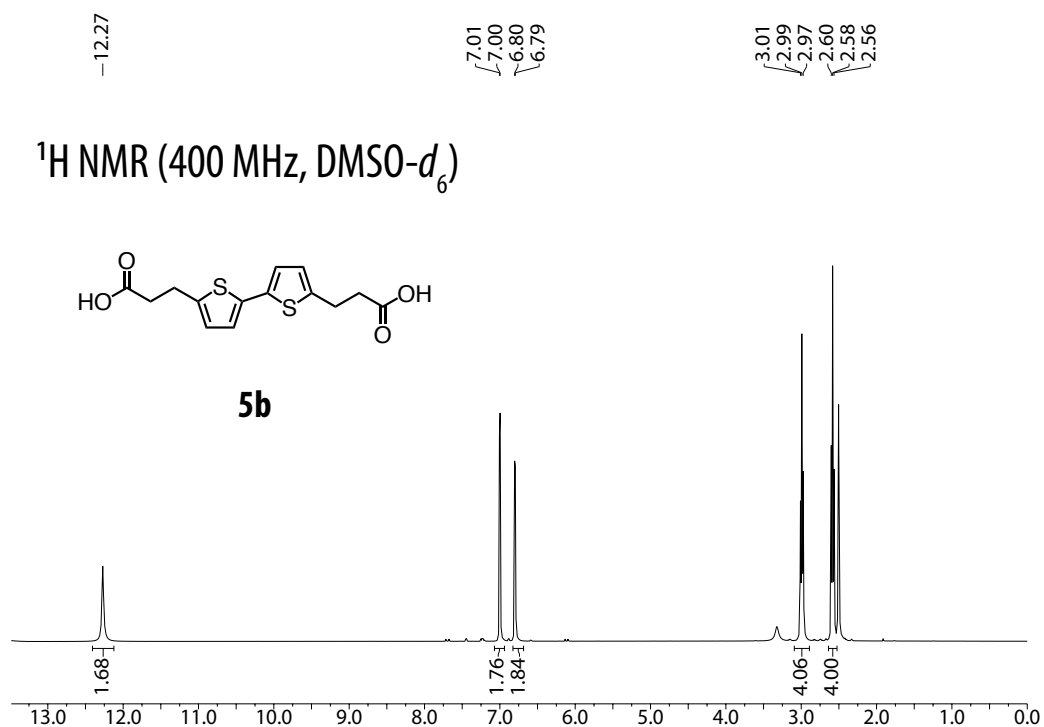


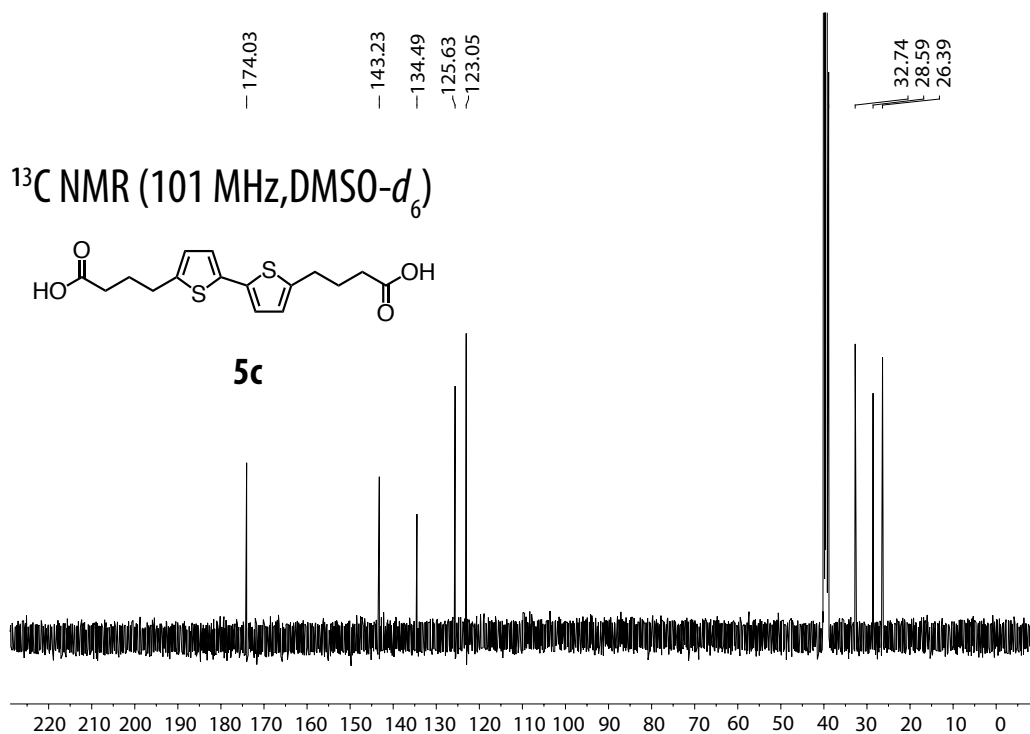
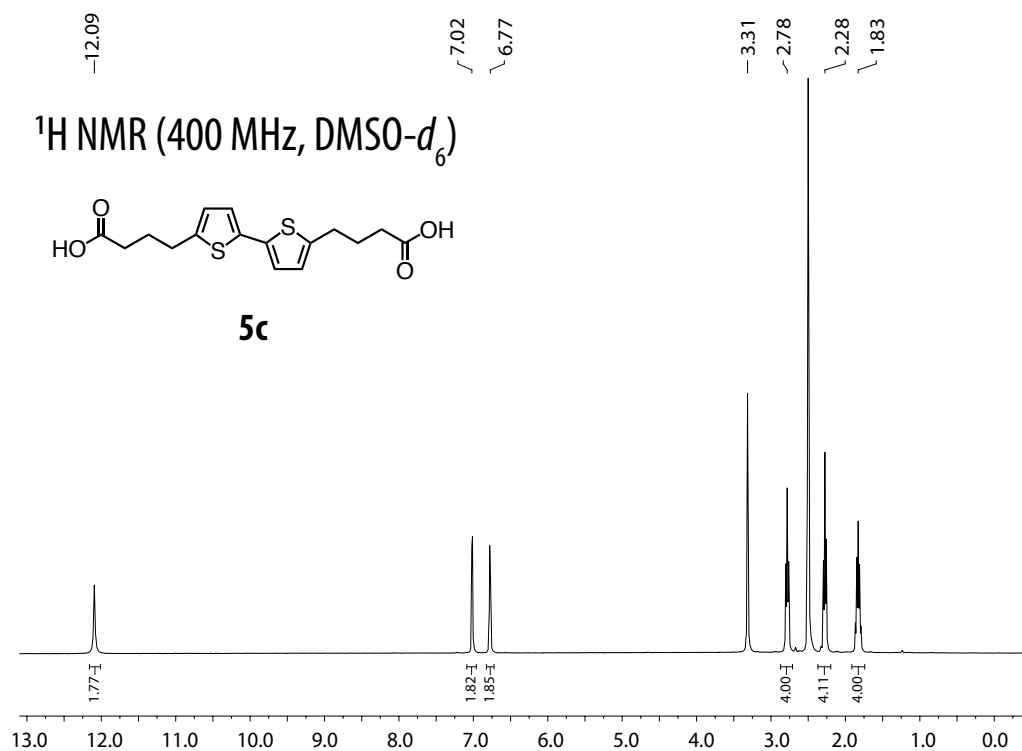




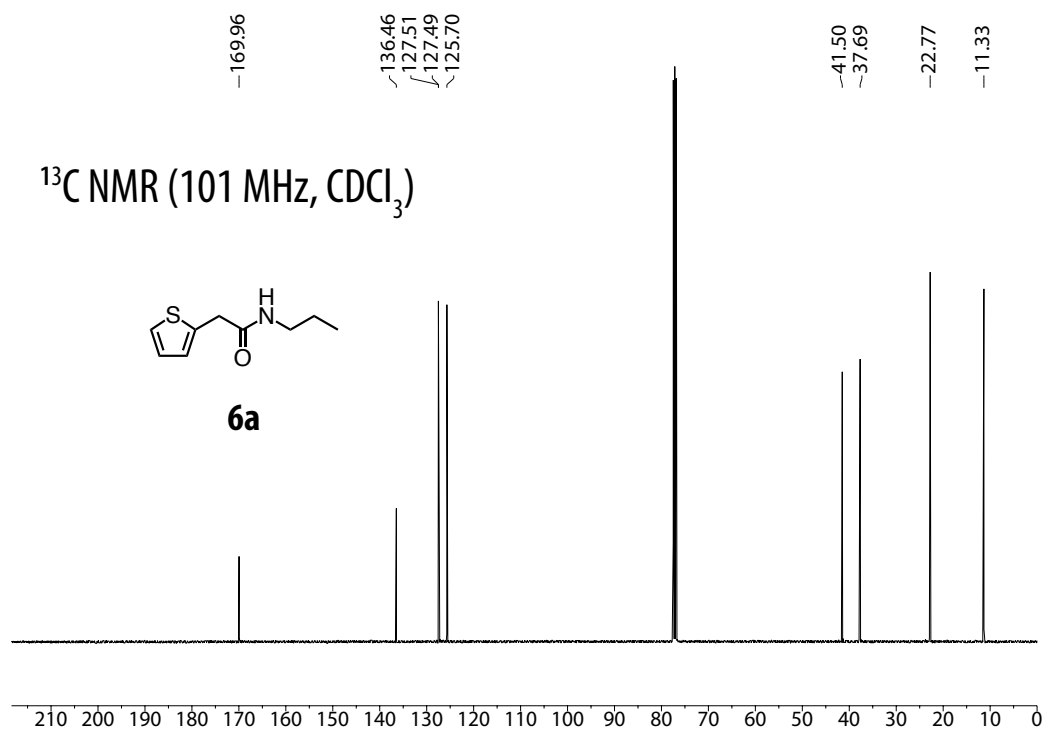
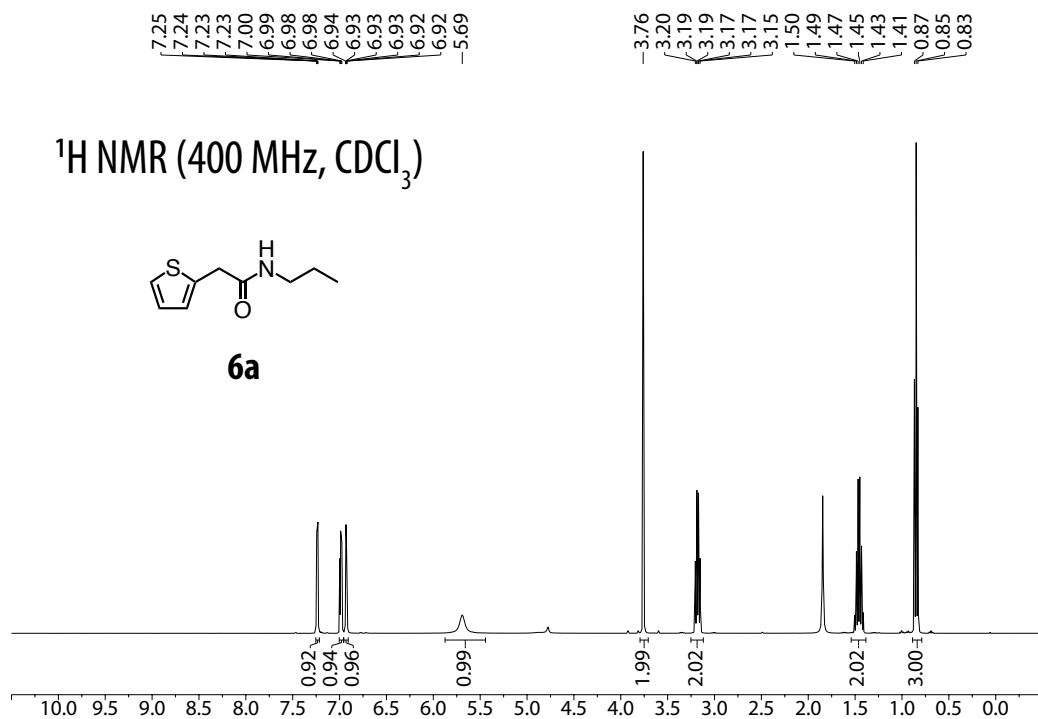


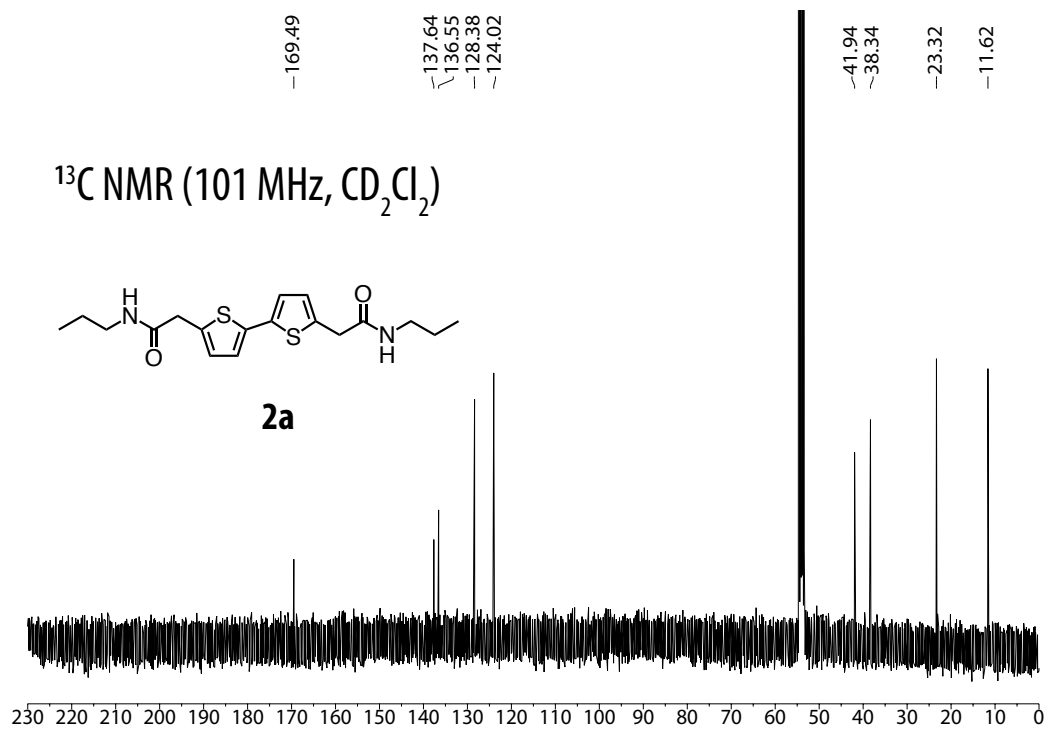
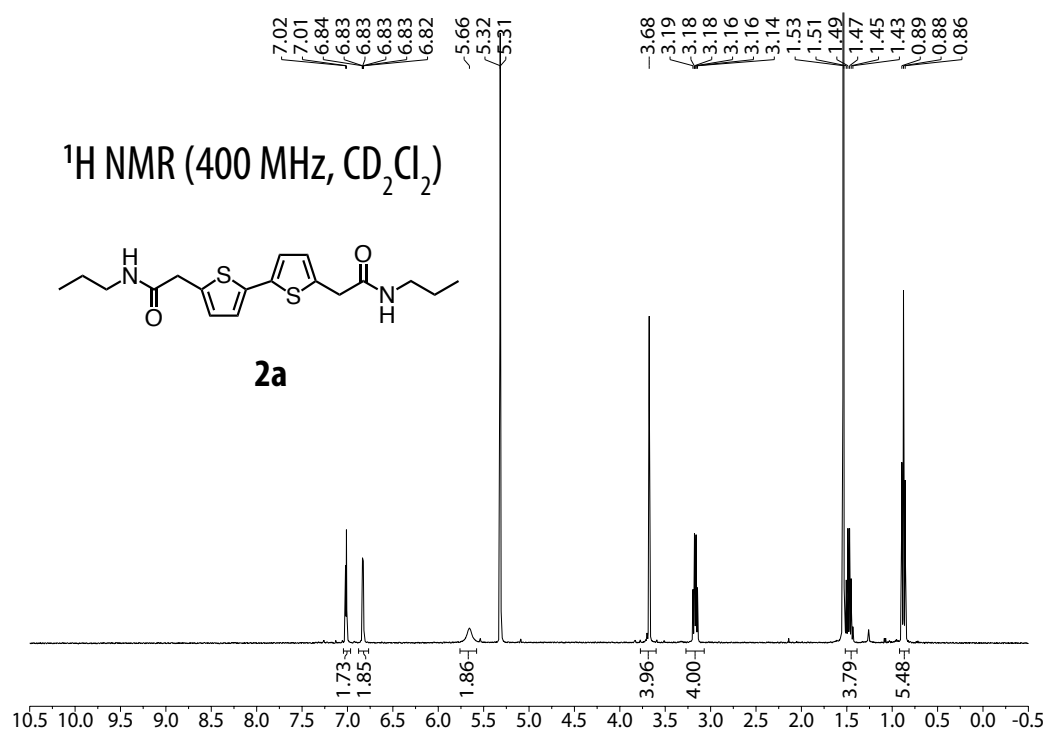


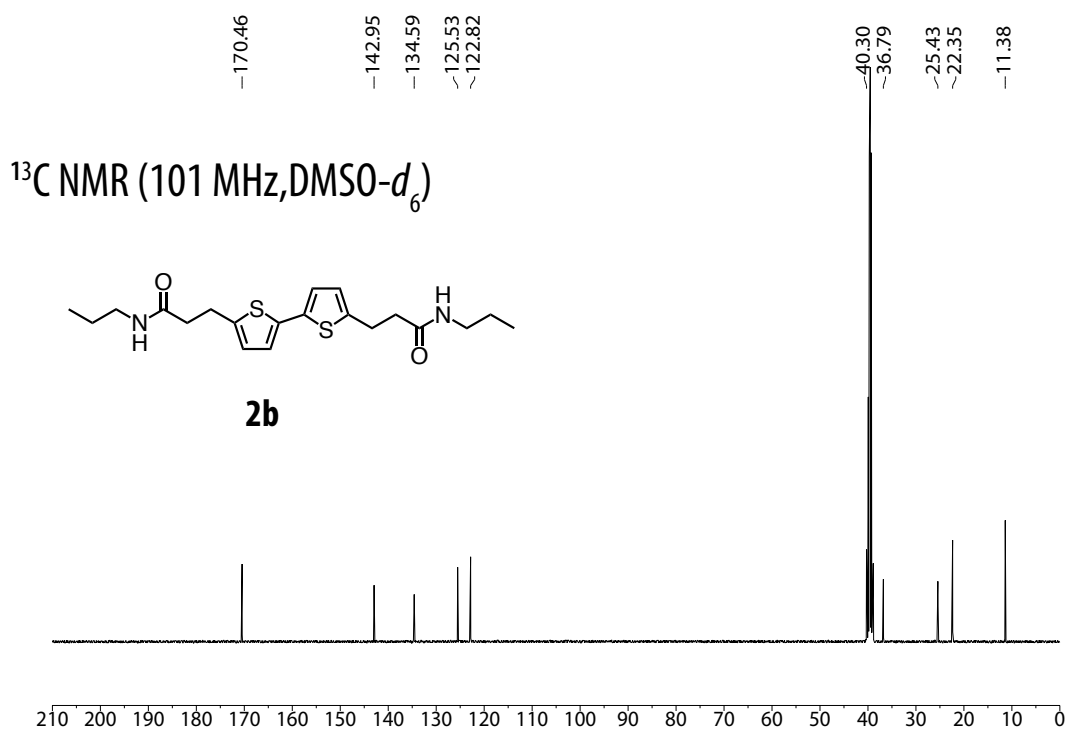
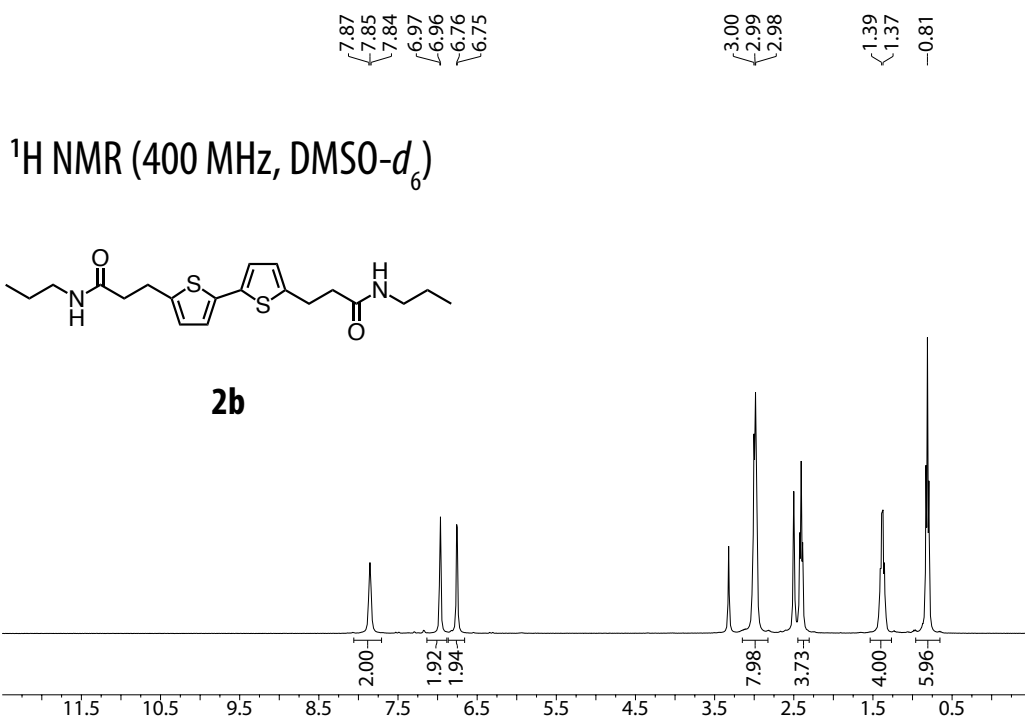


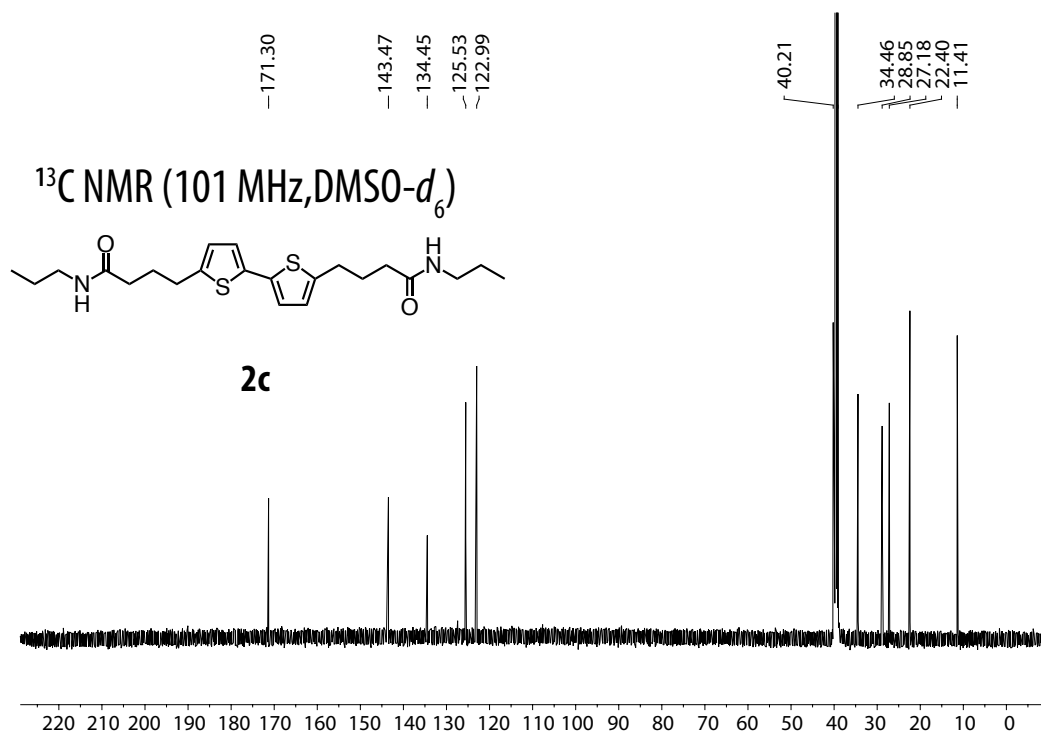
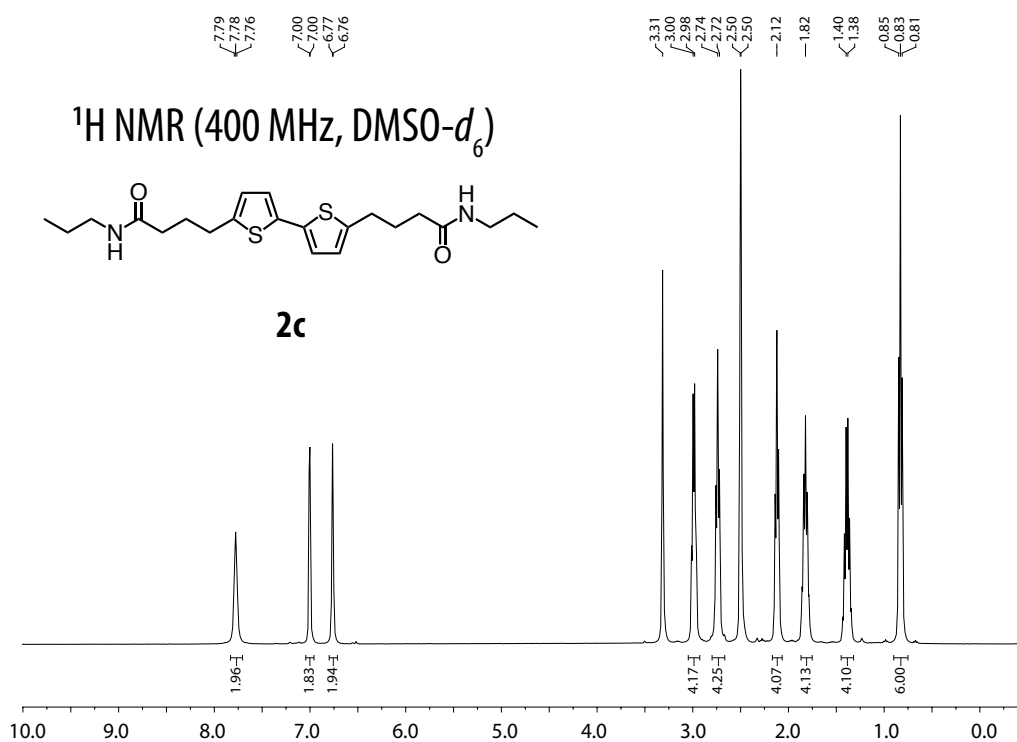




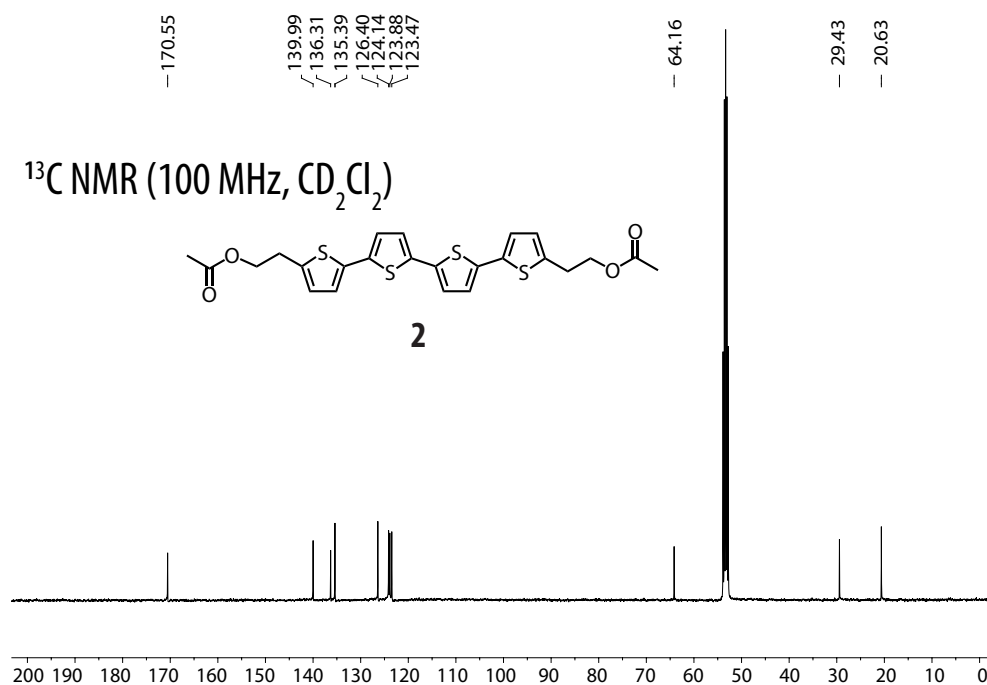
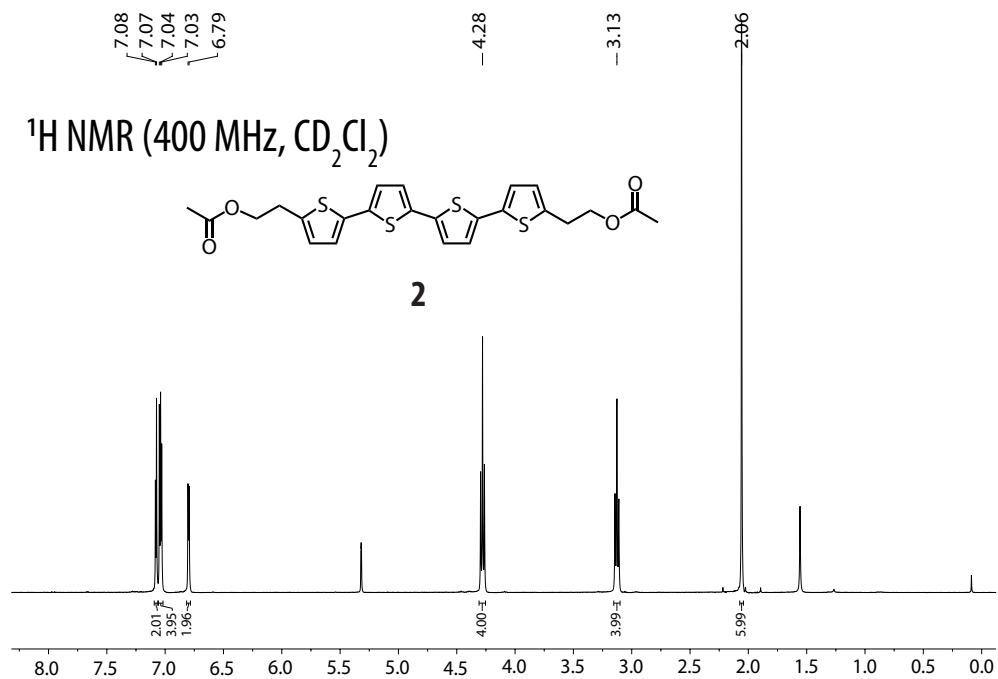




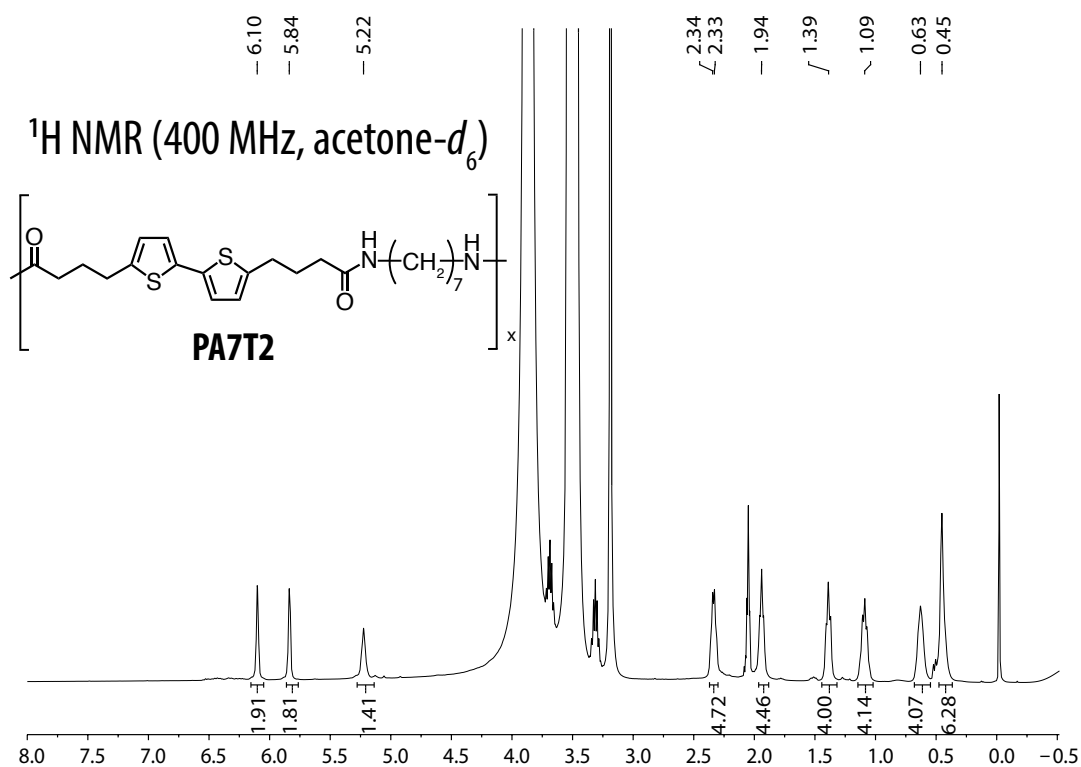
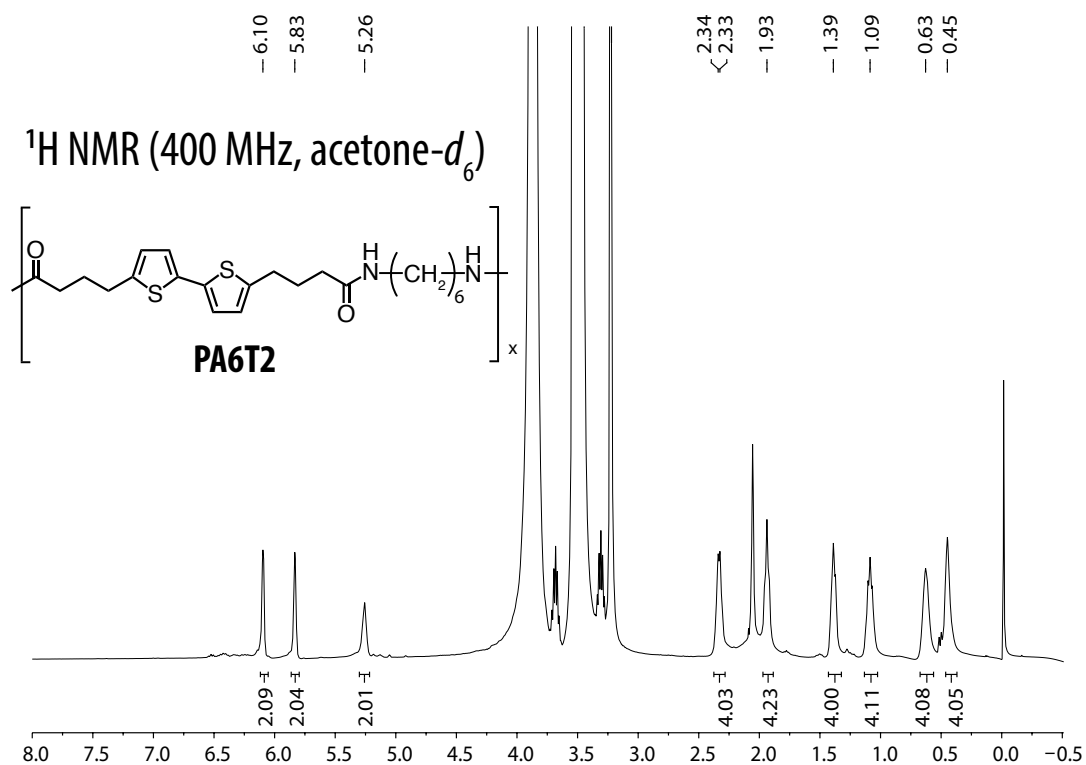


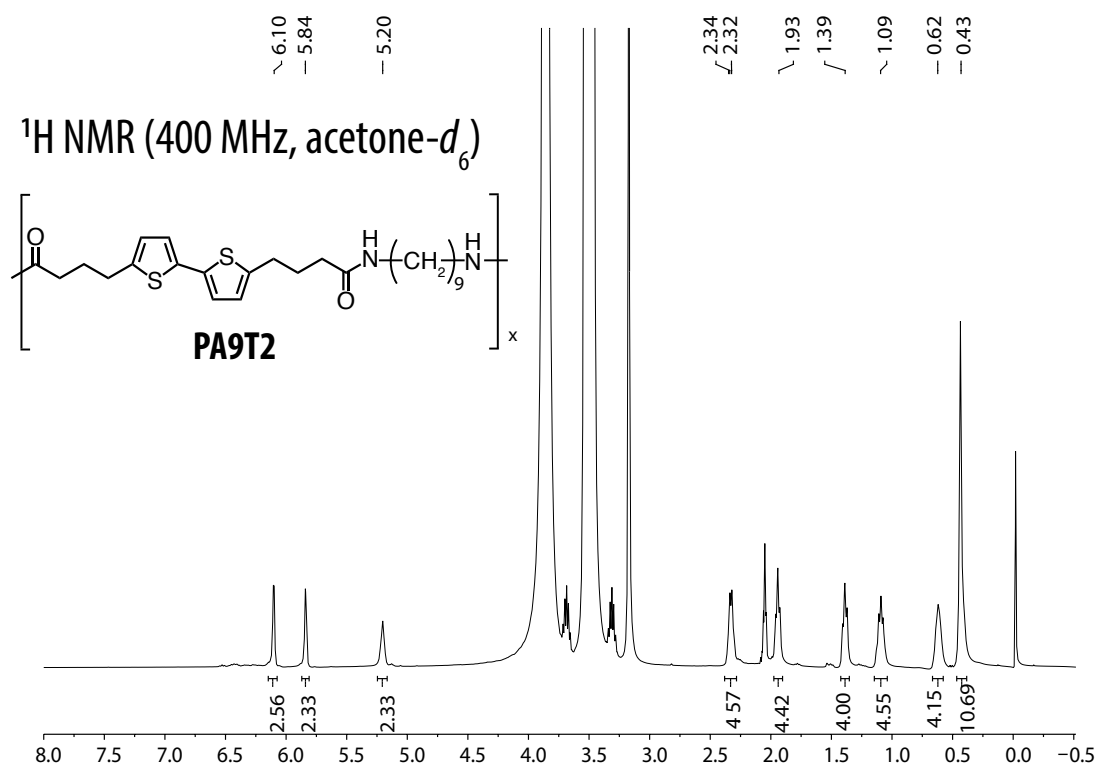
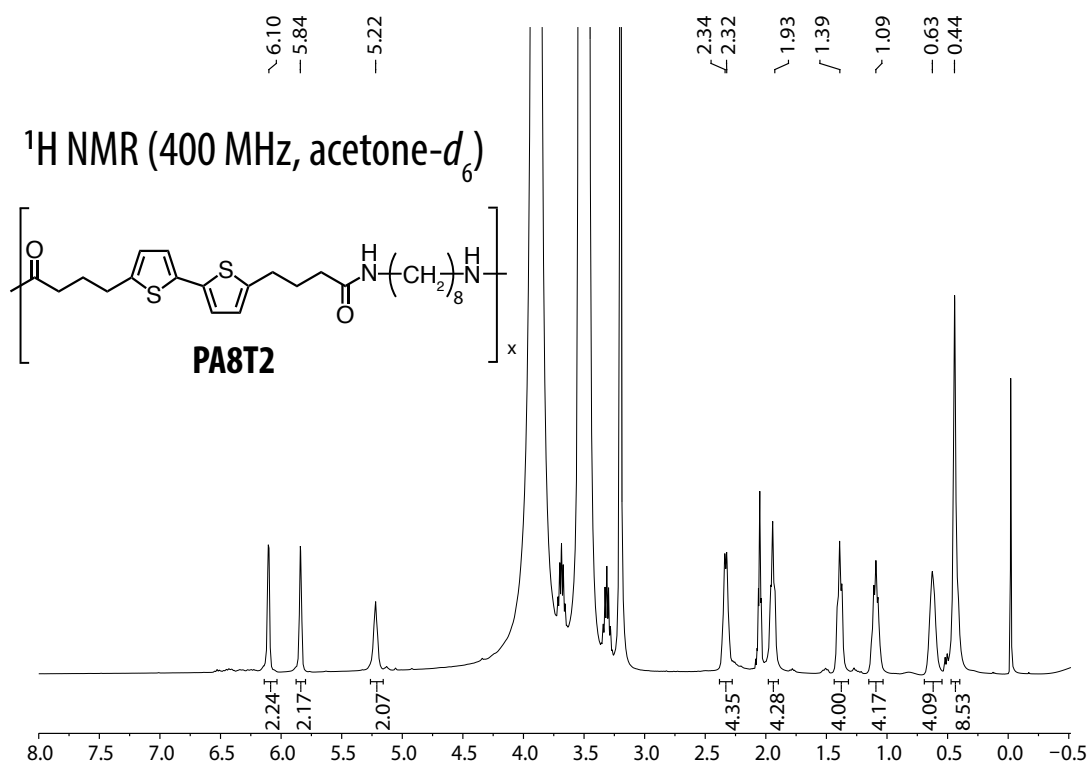


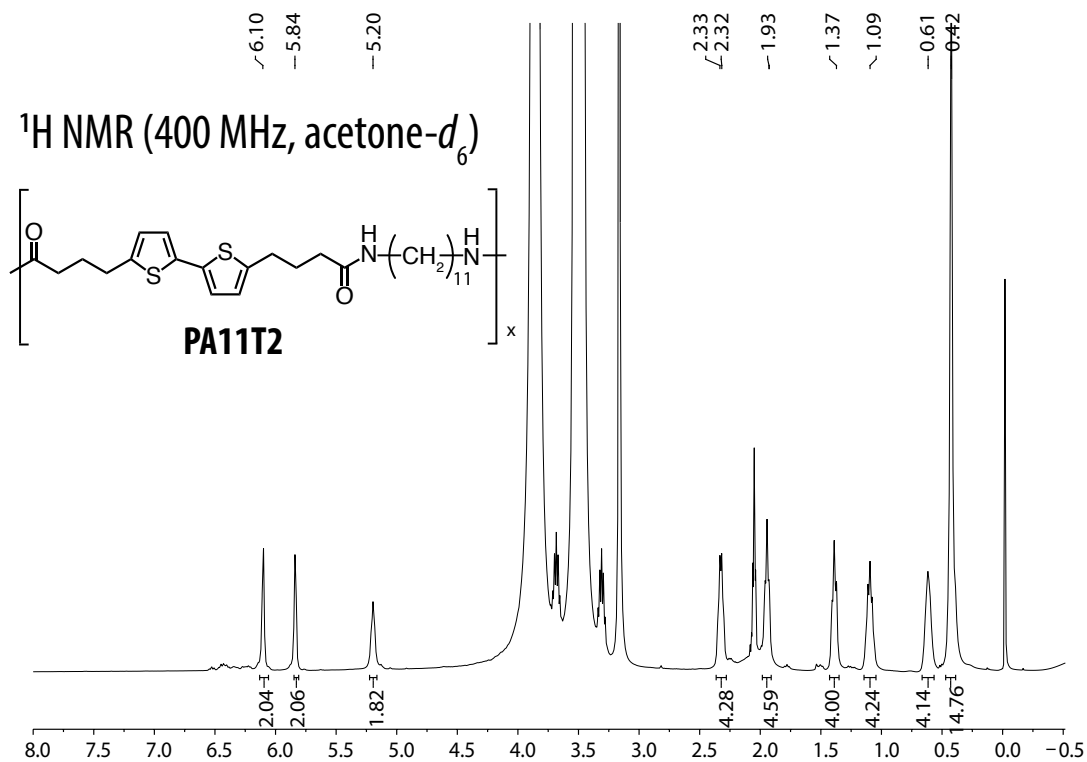
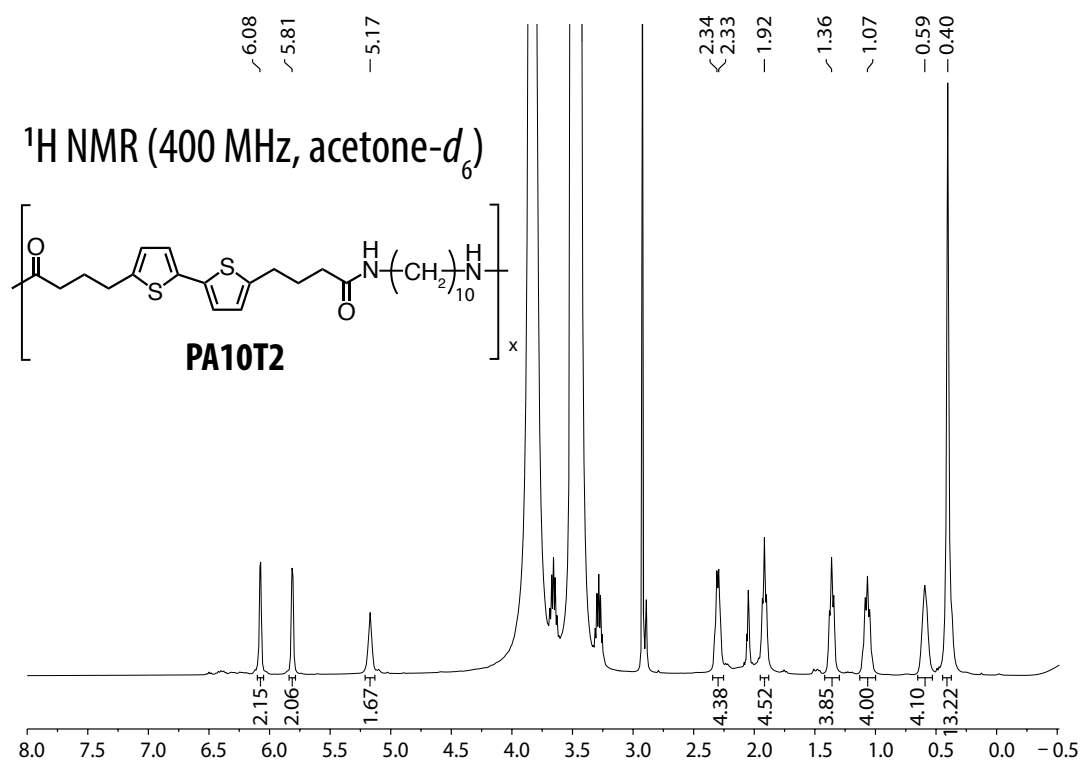
## 9.2.2 OFET Performance of a Hydrogen-Bonded Quaterthiophene



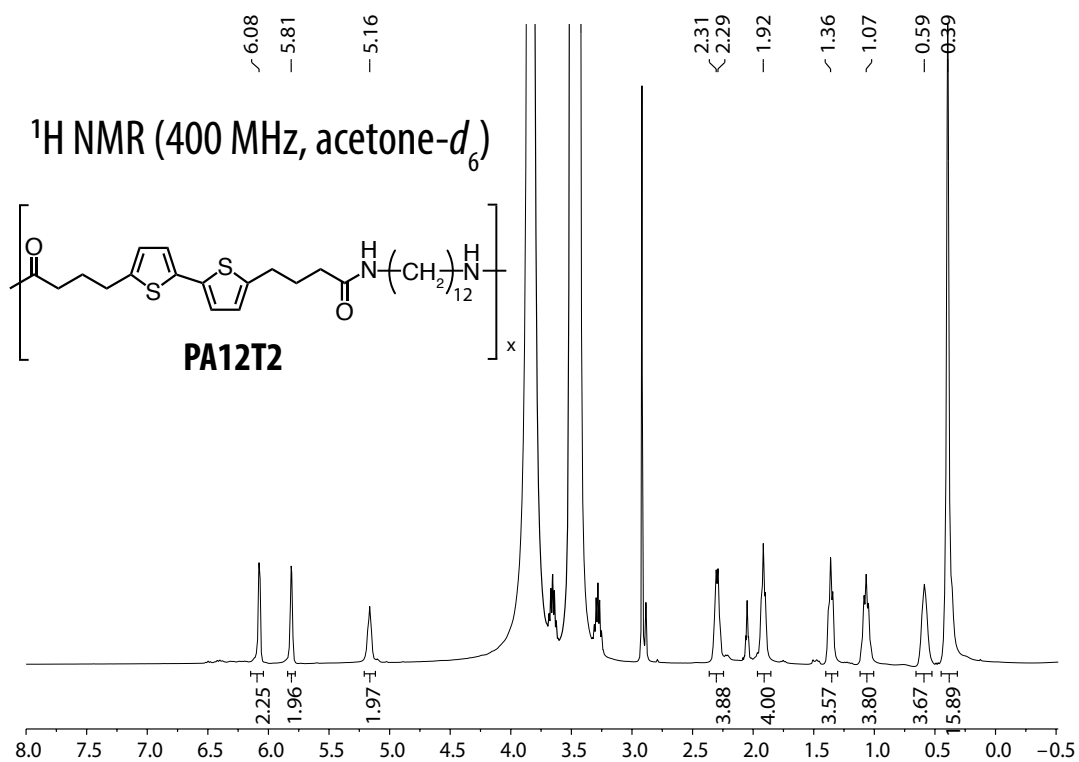
## 9.2.3 Engineering Polymers from Bithiophene-Containing Polyamides



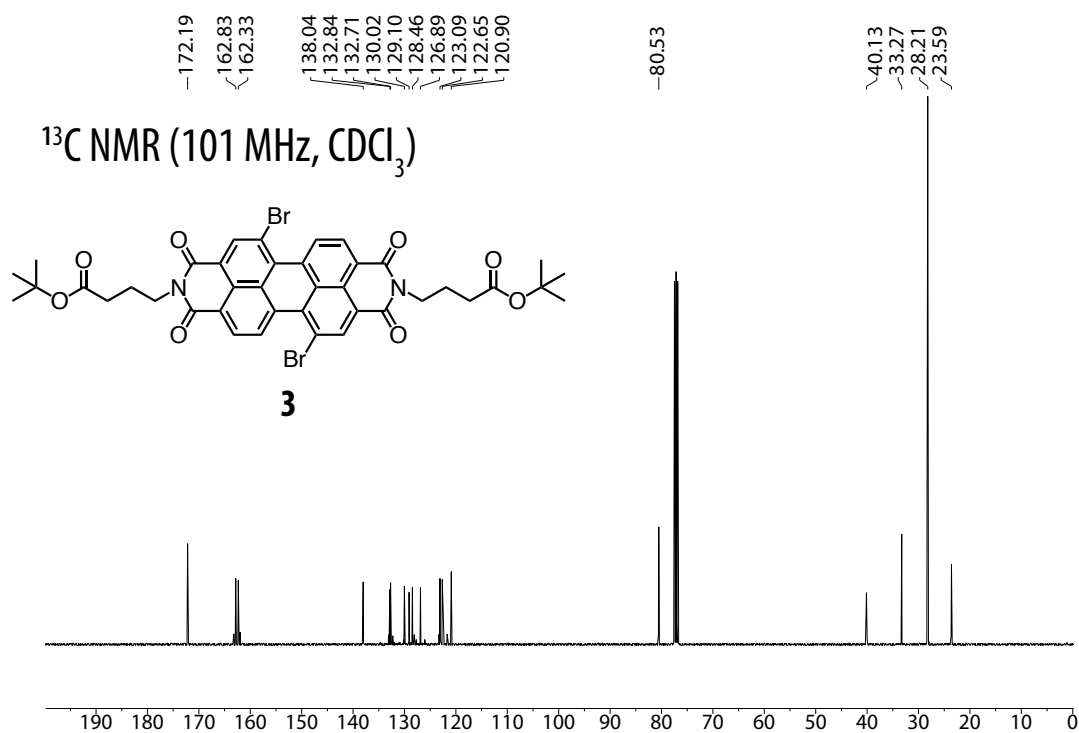
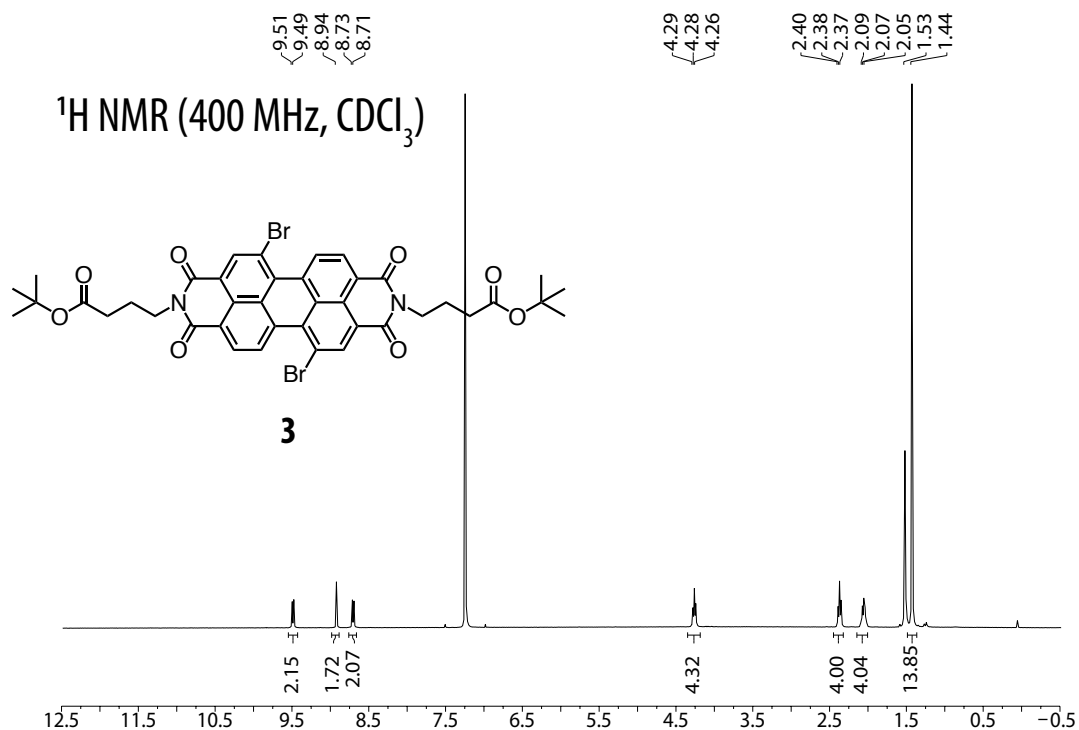


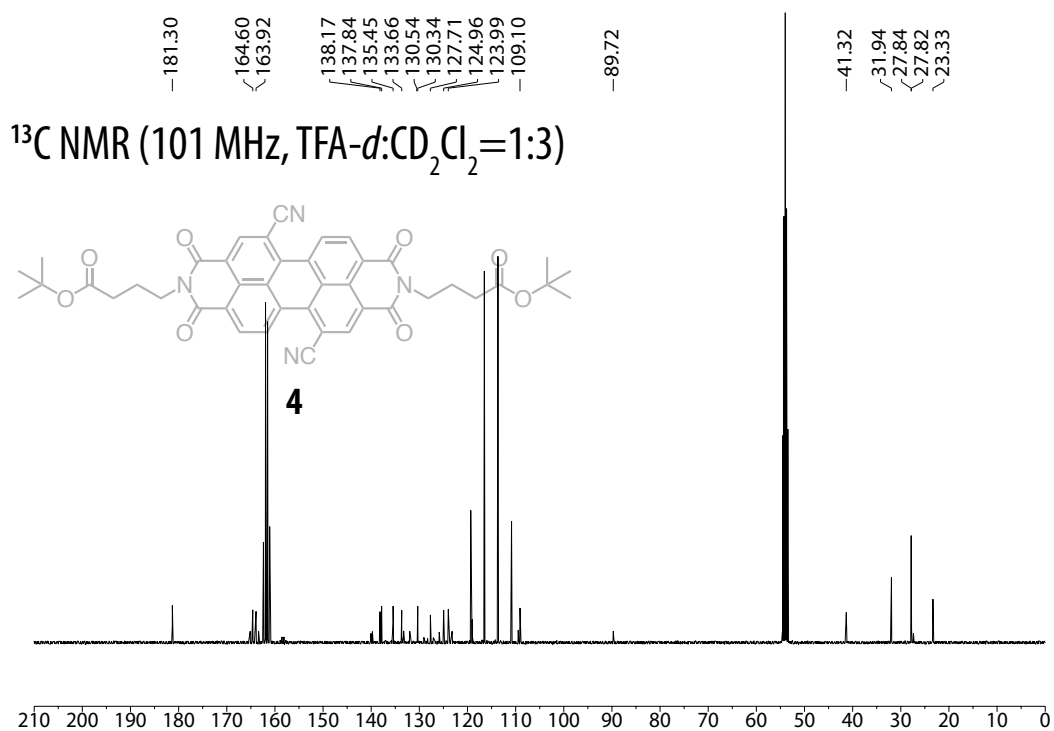
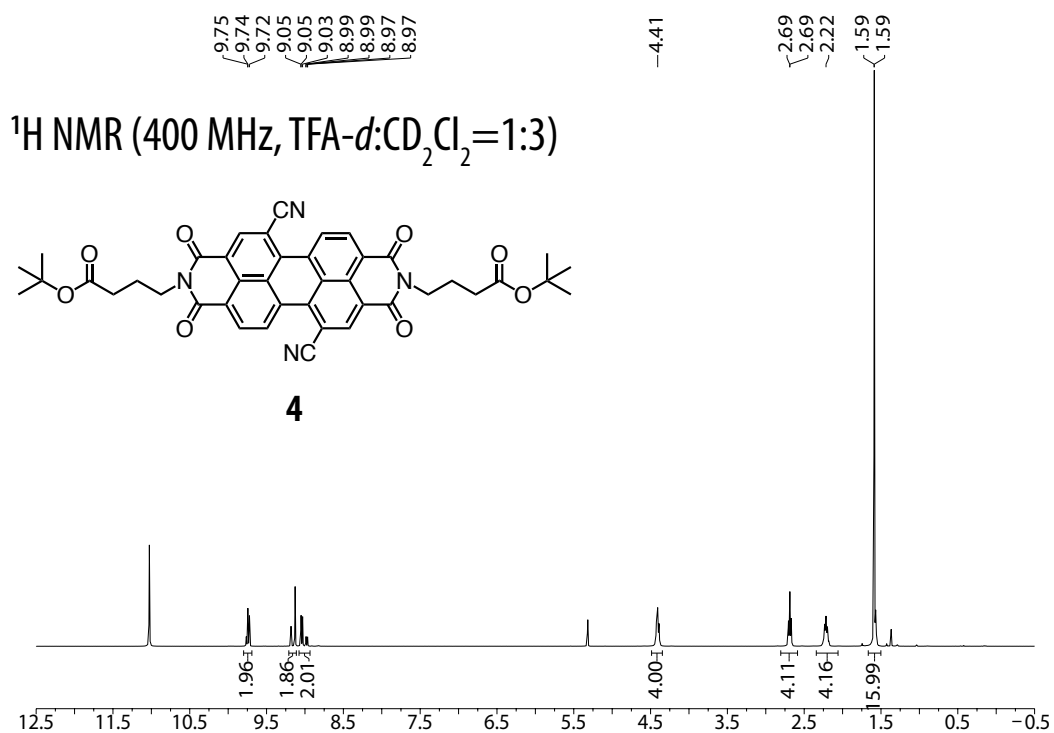


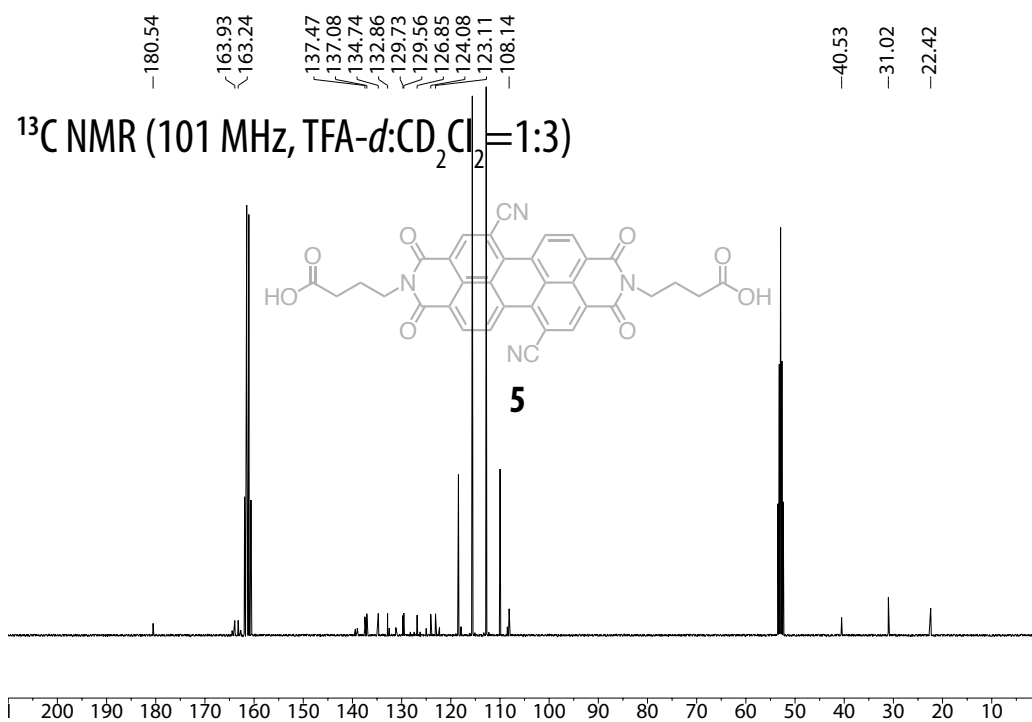
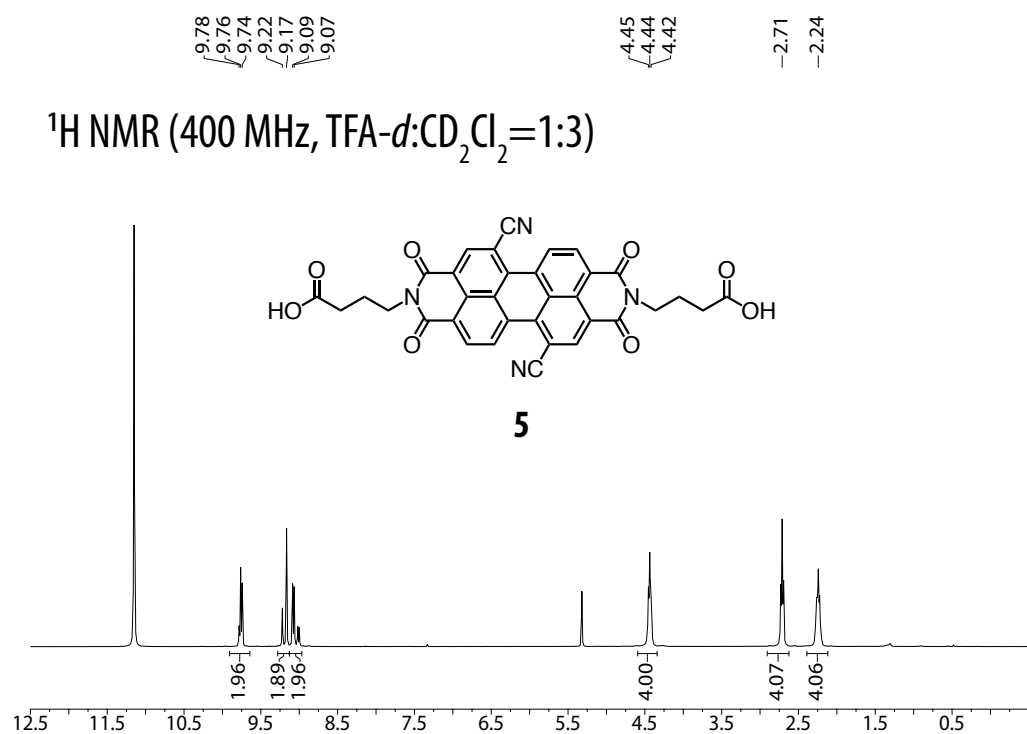


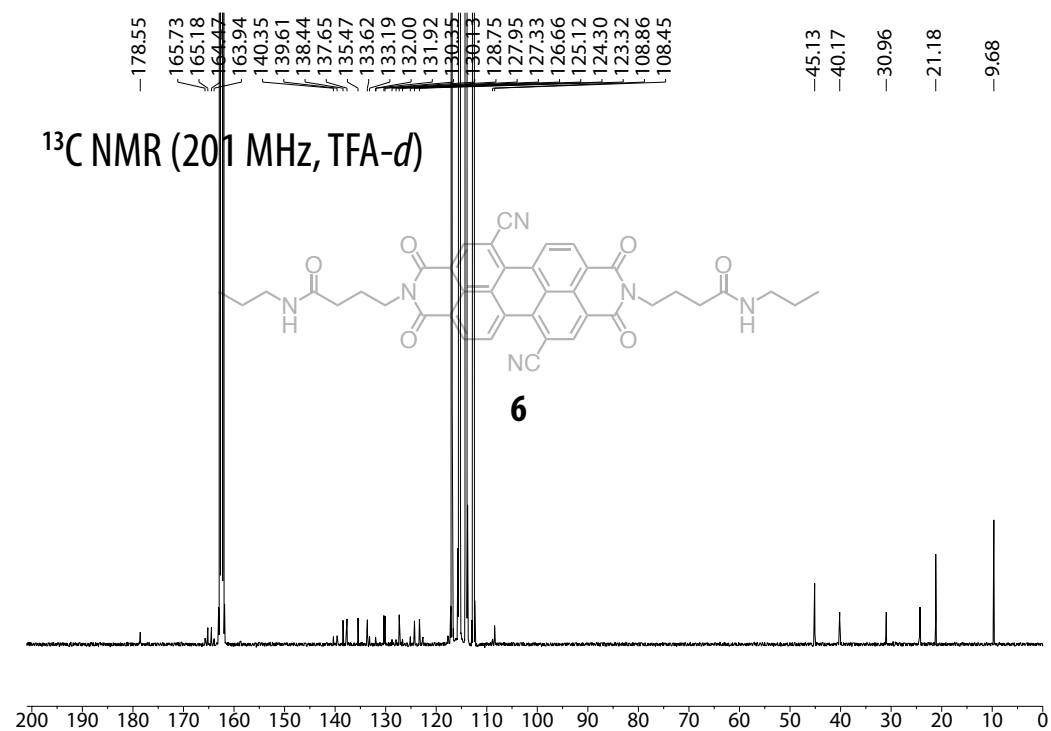
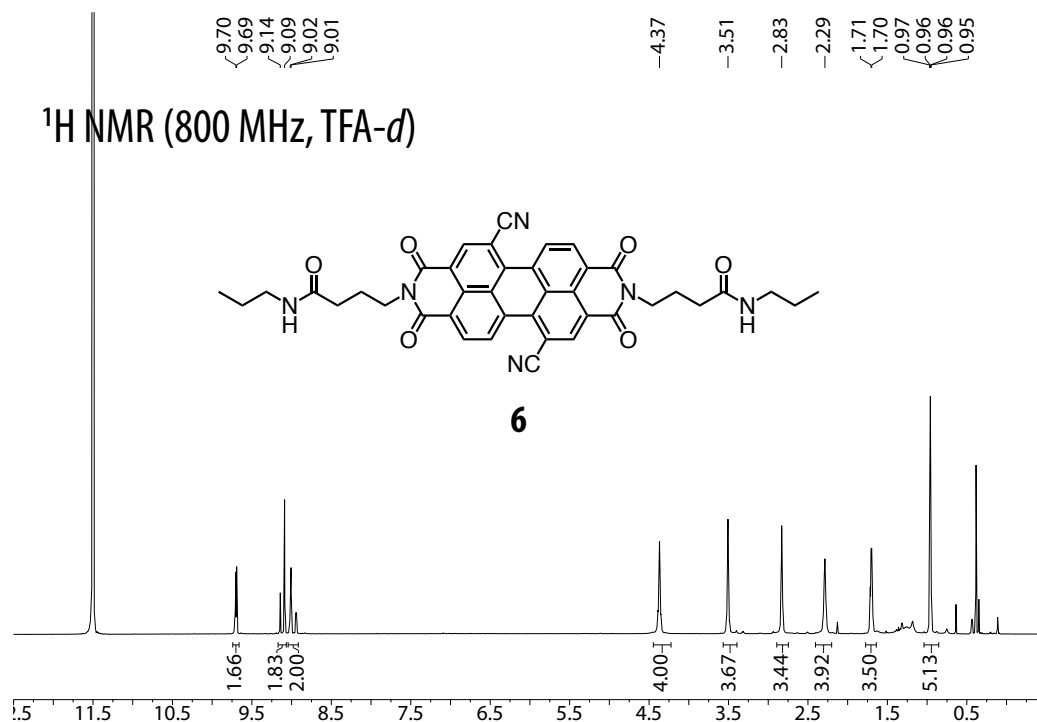


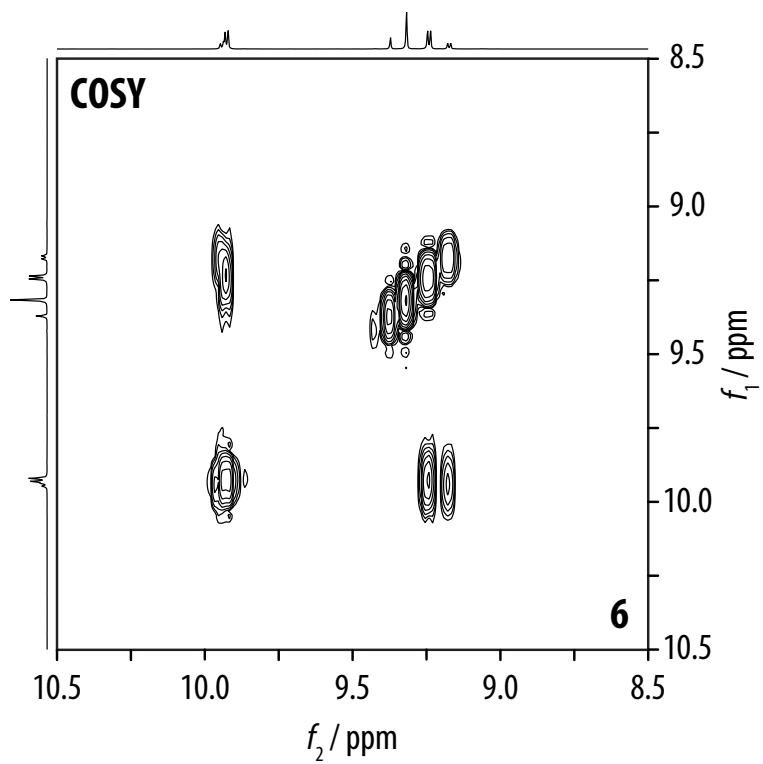
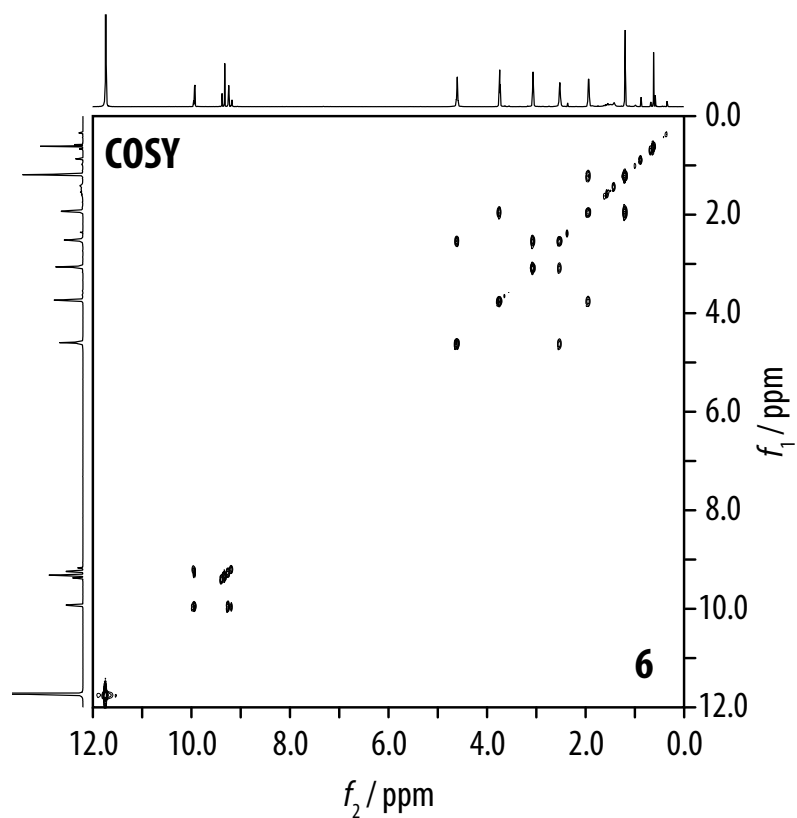
## 9.2.4 Semiaromatic Polyamides Containing Perylene Bisimide Repeat Units

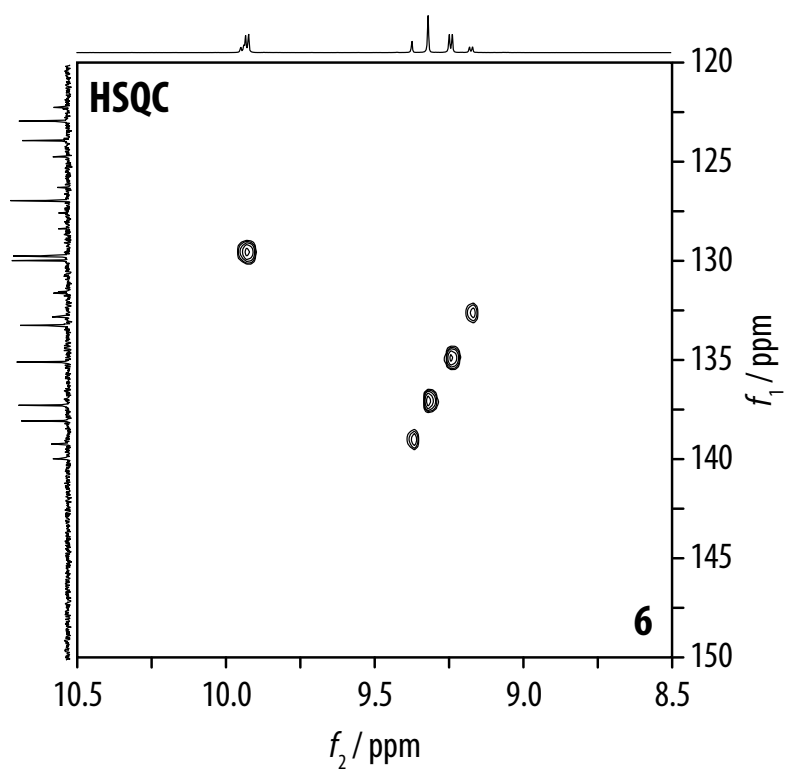
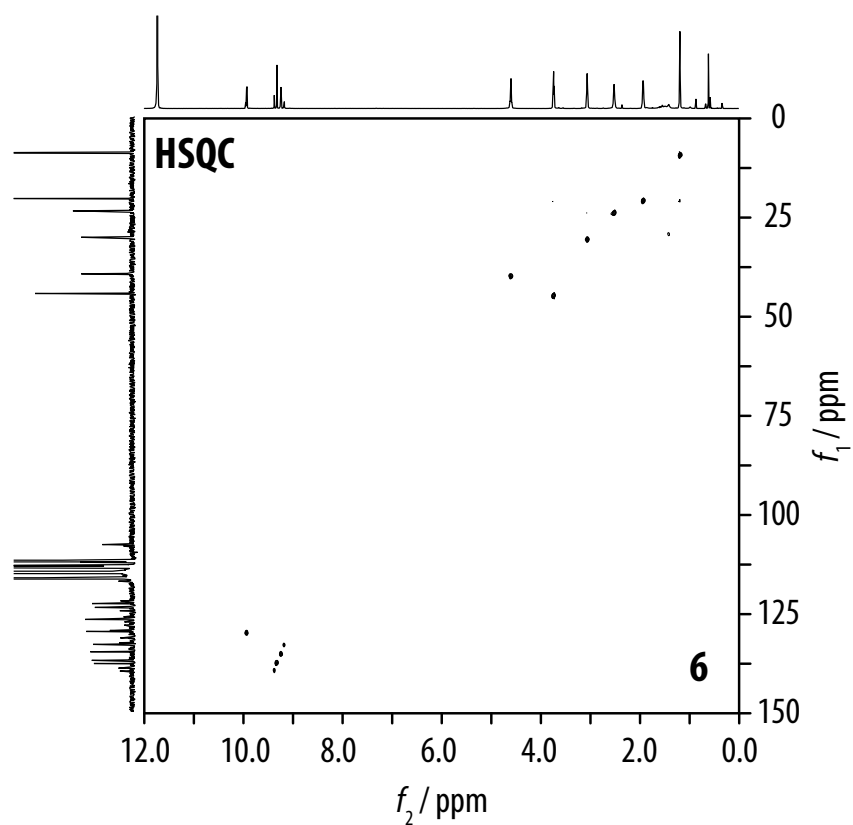


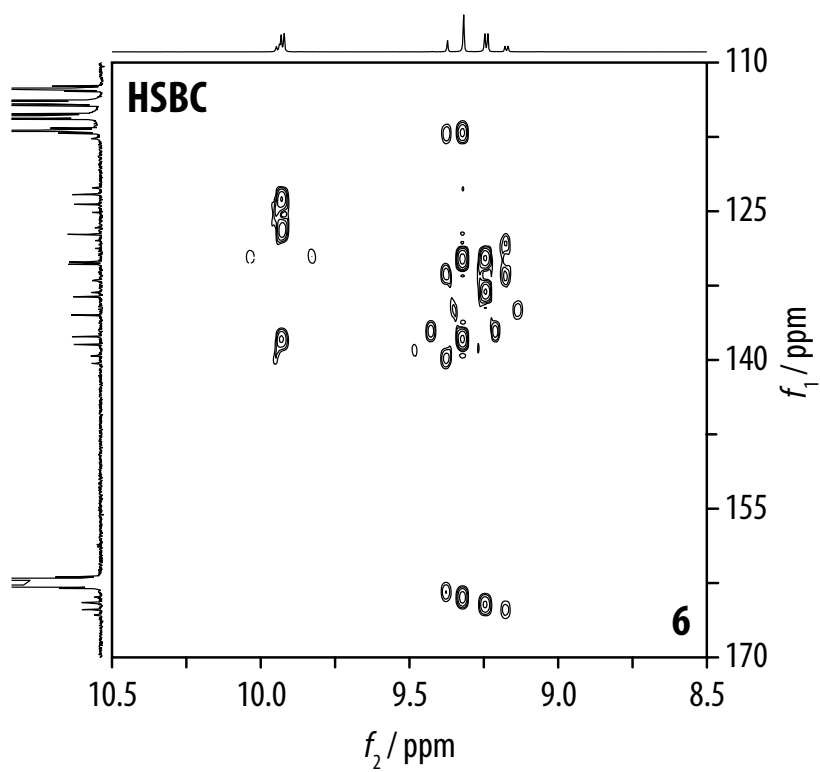
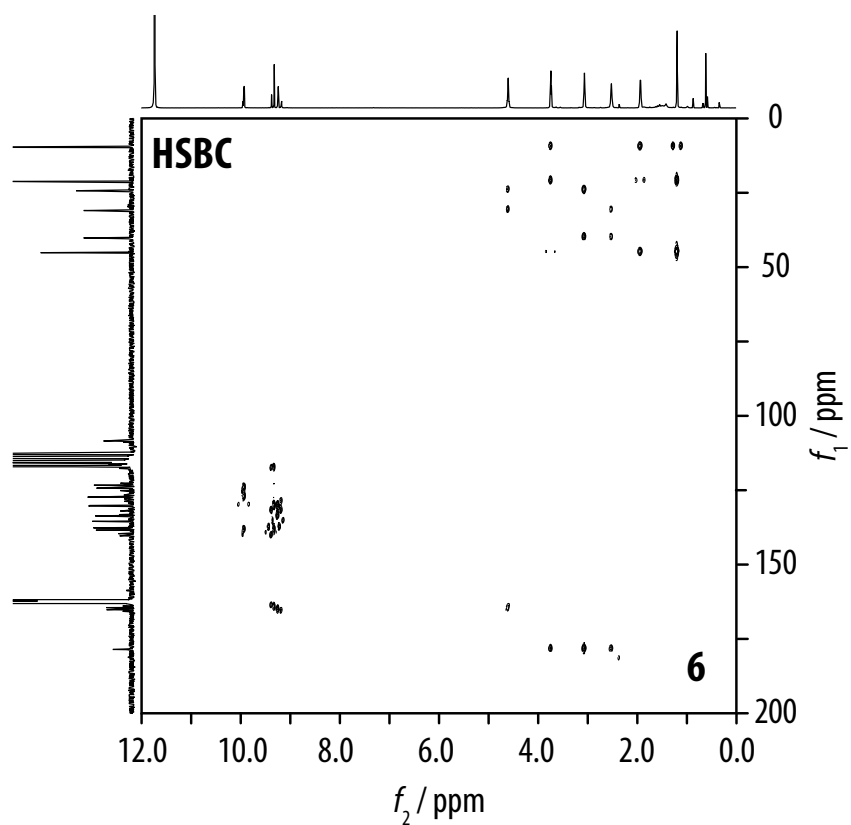




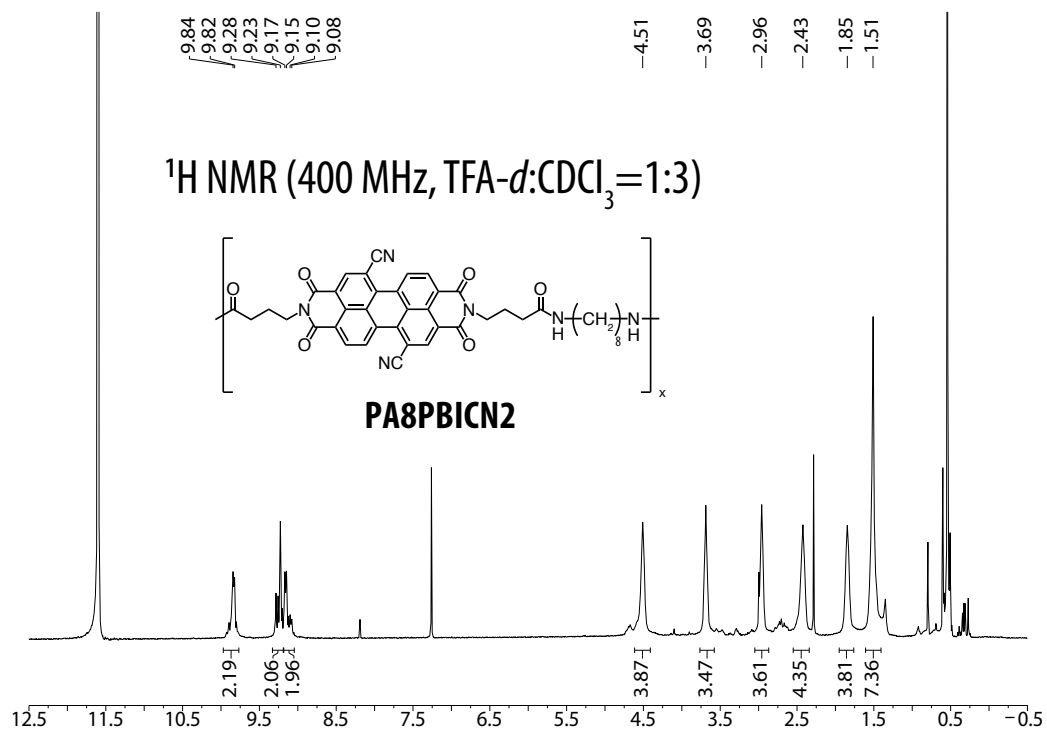
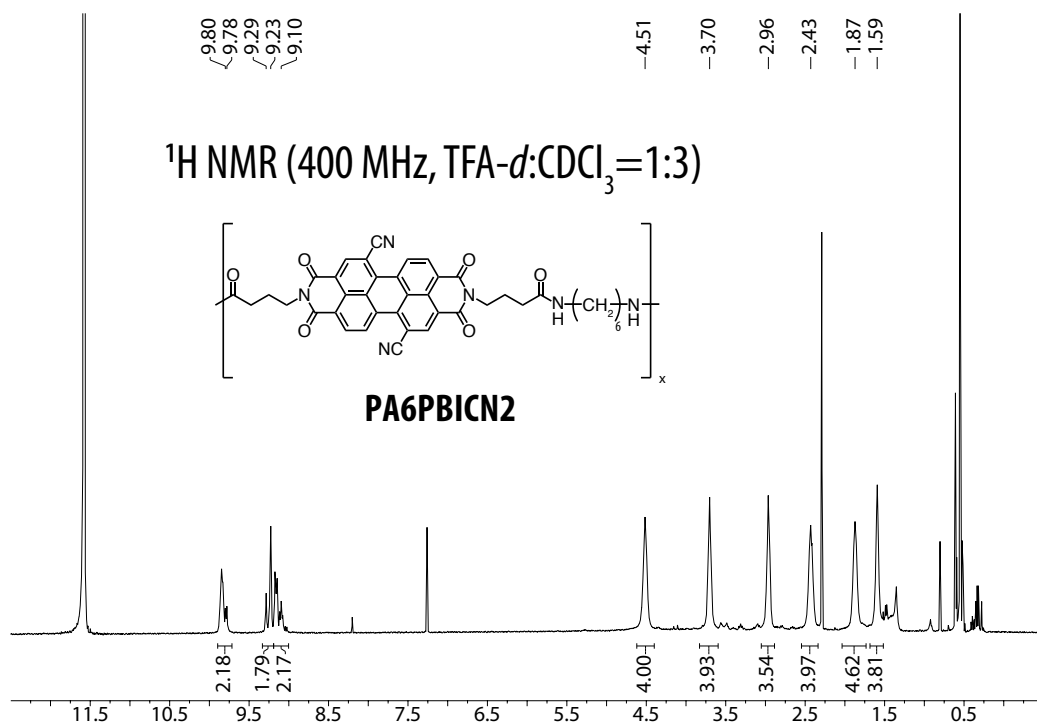


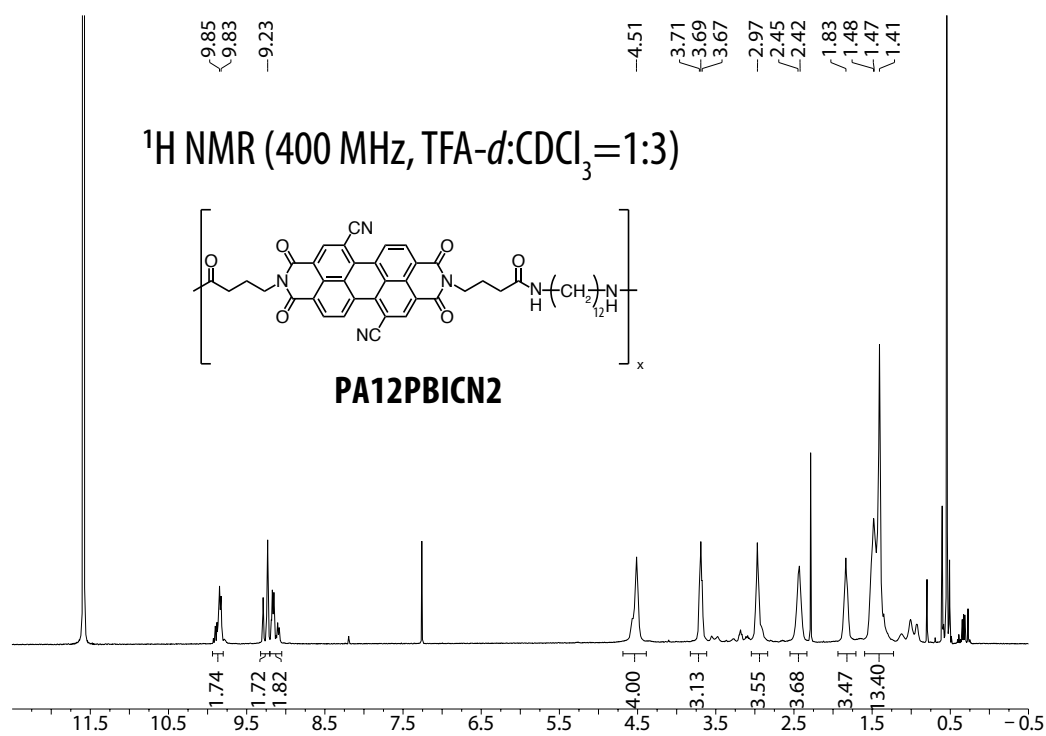
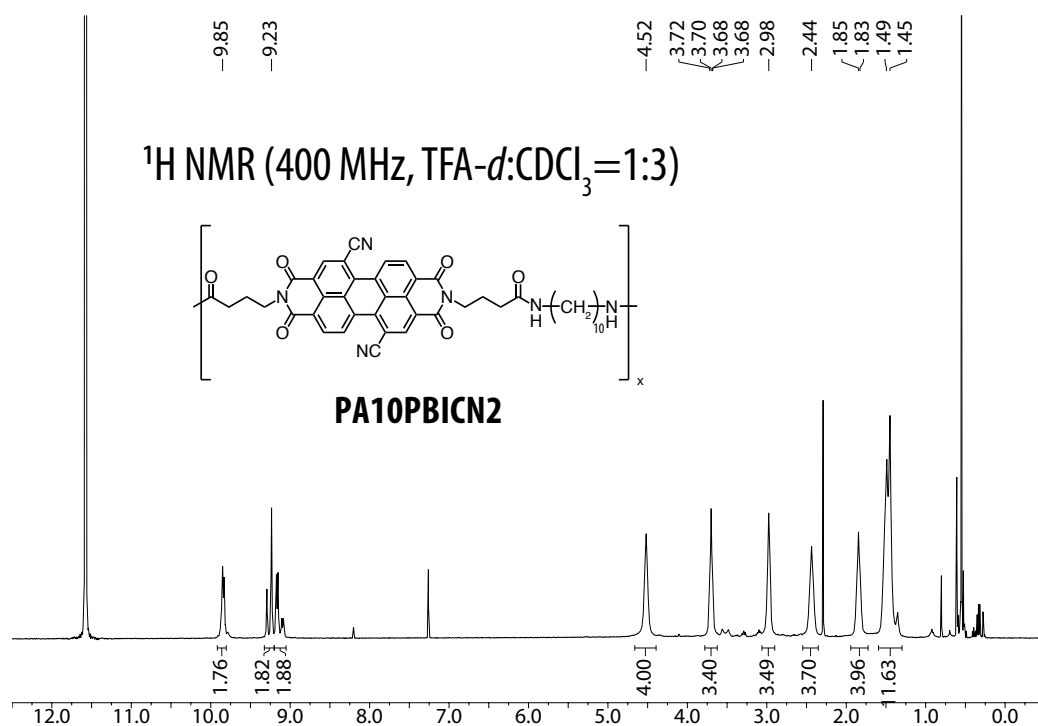












# List of Figures

1.1	<i>a)</i> In the course of last five decades, the number of transistors per chip has doubled every two years in line with Moore's law, while the increase in clock speed (how fast a microprocessor executes commands) slowed after 2004 because of the need to limit heat generation. <i>b)</i> Computers increase their performance and become smaller in size. Consequently, a new class of instruments has emerged about once every ten years. Figure adapted from ref. [5]. . . . .	1
1.2	Progress in organic semiconductor performance over a thirty-year period. Charge carrier mobility has improved by more than six orders of magnitude, exceeding the performance of amorphous silicon. The recent dramatic increase in the performance of donor-acceptor based systems is especially promising for future applications (* A special technique was used to align the material). Figure adapted from ref. [13]. . . . .	3
1.3	Schematic representation of <i>a)</i> the bonds ( $\sigma$ and $\pi$ ) and orbitals ( $sp^2$ and $p_z$ – coloured by blue and red, respectively), and the chemical structure of a benzene molecule and its <i>b)</i> molecular orbital diagram, illustrating the HOMO and LUMO energy levels along with the corresponding $p_z$ orbital representation. <i>c)</i> Molecular orbital diagrams of benzene, anthracene, pentacene and pentacene crystals. From benzene to pentacene, the HOMO–LUMO energy gap decreases with increasing extension of the $\pi$ -system. A band-like structure is generated in case of an organic crystal (e.g. pentacene) by further splitting of initial energy levels due to intermolecular (quadrupolar and dispersive) interactions. . . . .	4
1.4	Schematic illustration of intra-, intermolecular, and interdomain transport across different length scales. . . . .	5

- 1.5 Venkateshvaran et al. investigated the benefits of structural resilience for charge transport properties. *a*) Chemical structure of the **IDTBT** copolymer that was the focus of the work and the reference semicrystalline  $\pi$ -conjugated polymer system **PBTBT** ( $R = C_{12}H_{25}$ ). *b*) Molecular modeling of the backbone conformation of **IDTBT** and **PBTBT** (side chains and hydrogens omitted for clarity). *c*) The polymer backbone may be planarized under pressure if it exhibits significant torsion in as-deposited films. Thus, pressure-dependent Raman spectroscopy measurements were performed on **IDTBT** films. It was found that Raman intensity ratio between  $1542\text{ cm}^{-1}$  (ring stretching mode for **BT**) and  $1613\text{ cm}^{-1}$  (ring stretching mode for **IDT**) was independent of pressure, indicating a planar backbone. *d*) Calculated gas-phase torsion energies for **IDTBT** and **PBTBT**. For planar structures the potential minima are close to  $0^\circ$ ,  $180^\circ$  or both. Figure reproduced from ref. [40]. . . . . 6
- 1.6 Heeger et al. studied the field effect transistor performance of **PCDTPT** with different molecular weights. *a*) Top: chemical structure of **PCDTPT** ( $R = C_{16}H_{33}$ ); bottom left: scratching machine for nano-grooved  $\text{SiO}_2$ ; bottom right: resulting  $\text{SiO}_2$  after scratching. *b*) The mobility value and the value in parentheses represent mean and maximum values obtained from devices fabricated by slow drying. *c*) Temperature-dependent mobility values of 50, 160, 300 kDa materials. Figure reproduced from ref. [45]. . . . . 7
- 1.7 Mei et al. introduced siloxane-terminated side chains into an isoindigo-based semiconducting polymer and investigated the resulting structure-property relationships. *a*) Chemical structure of the isoindigo based polymer, where R stands for siloxane terminated side chains (**PII2T-Si**) or for a branched alkyl chain as a reference (**PII2T-Ref**). *b*) 2D grazing incidence X-ray scattering (GIXS) patterns of annealed **PII2T-Ref** and annealed **PII2T-Si**. *c*) Representative transfer curves for **PII2T-Ref** and **PII2T-Si**. Average hole mobilities up to  $2.0\text{ cm}^2\text{ V}^{-1}\text{ s}^{-1}$  were found for **PII2T-Si**, which is six times higher than **PII2T-Ref**. Figure adapted from ref. [22]. . . . . 8
- 1.8 Kang et al. designed **DPP**-based polymers with a side chain branching point far from the polymer backbone and reported their photophysical and structural features as well as their device performance. *a*) Chemical structure of **P-24-DPPDTSE** (reference compound) and **P-29-DPPDTS**. *b*) Out-of-plane diffraction spectra of **P-24-DPPDTSE** and **P-29-DPPDTS**. Inset: the corresponding in-plane diffraction patterns. *c*) Representative transfer curve for **P-29-DPPDTS**. Figure adapted from ref. [52]. . . . . 9

- 1.9 Noriega et al. carried out a systematic study on the relationship between microstructure and electrical properties in polymer semiconductors. *a*) Chemical structure of regioregular (**RR**) and regiorandom (**RRa**) **P3HT**. *b*) Electroluminescence spectra of films made from pure **RR**- and pure **RRa-P3HT**. *c*) Photoluminescence (dotted) and electroluminescence spectra of the blend films containing 90% **RRa-P3HT** and 10% **RR-P3HT**. Unlike the photoluminescence spectra, the electroluminescence spectra only exhibited emissions from **RR-P3HT** on application of a certain current. This finding showed that charges move and recombine in the more ordered regions of the blend. Figure reproduced from ref. [12]. . . . . 10
- 1.10 Müllen et al. described an alternating copolymer **CDT-BTZ**. *a*) Chemical structure of **CDT-BTZ** ( $R = C_{16}H_{33}$ ). *b*) X-ray diffraction patterns from **CDT-BTZ** with different molecular weight. *c*) Output and transfer characteristics for drop-cast annealed thin films **CDT-BTZ** with the highest  $M_n = 35$  kg/mol. Figure reproduced from ref. [63]. . . . . 11
- 1.11 Zhang et al. studied the molecular origin of high field-effect mobility in a **C<sub>16</sub>IDT-BT** copolymer. *a*) Chemical structure of **C<sub>16</sub>IDT-BT** ( $R = C_{16}H_{33}$ ). *b*) Top: the top-gate bottom-contact device configuration (TGBC) with the channel length 50  $\mu\text{m}$  and width 1 mm; bottom left: transfer curves in the linear and saturation regimes; bottom right: transfer curves from temperature-dependent transistor measurements. *c*) GIXS profile for **C<sub>16</sub>IDT-BT**, where broad arc patterns indicate a lack of longer-range crystalline order. Figure reproduced from ref. [42]. . . . . 12
- 1.12 Chung et al. prepared a new alternating copolymer, **PDPDBD**, and investigated its electronic properties. *a*) Chemical structure of **PDPDBD** ( $R_1 = 2\text{-ethylhexyl}$ ,  $R_2 = 2\text{-decyltetradecyl}$ ). *b*) Transfer curve of a FET from annealed **PDPDBD** (left). Temperature-dependent transfer characteristics, where the mobility is plotted as a function of the inverse temperature (right). *c*) 2D GIXS profiles for pristine (top left) and annealed **PPDBD** thin films (top right). Figure reproduced from ref. [70]. . . . . 12
- 1.13 Scatter plots of the angle versus distance for *a*) O–H...O and *b*) C–H...O illustrating the angular preference of strong hydrogen bonds above 160°. Figure adapted from ref. [91]. . . . . 15

- 1.14 Gilli et al. examined the correlation between the intramolecular O–H...O hydrogen bond distance and  $^1\text{H}$  NMR chemical shifts of the enolic proton  $\delta(\text{OH})$  in  $\beta$ -diketone enols. *a*) Classification of different molecules with  $\text{O}=\text{C}-\text{C}=\text{C}-\text{OH}$   $\beta$ -diketone enol groups; **I**  $\beta$ -diketone enols, **II**  $\beta$ -ketoesters, **III** 2-hydroxybenzoketones, **IV**  $\delta$ -diketone enols, **V**  $\alpha$ -keto-oximes. *b*) Top: The range of  $^1\text{H}$  NMR chemical shifts correspond to hydrogen bonds with different strengths. Bottom: A plot of  $\delta(\text{OH})$  versus distance  $d(\text{O}\cdots\text{O})$  shows that shortening of the bond distance is strongly correlated with the downfield shift of the enolic proton. Figure reproduced from refs. [103,109]. . . . . 17
- 1.15 Tovar et al. prepared quaterthiophenes substituted with tripeptide segments and investigated their performance in OFET devices. *a*) Molecular structure of **T4-R<sub>1</sub>R<sub>2</sub>R<sub>2</sub>** where R<sub>1</sub> and R<sub>2</sub> are chosen from glutamic acid (Glu), aspartic acid (Asp) and glycine (G), alanine (A), valine (V), or isoleucine (I). Solution-phase *b*) absorption, *c*) fluorescence and *d*) CD spectra of **T4ER<sub>2</sub>R<sub>2</sub>** demonstrate that **AA** and **GG** substituted molecules have the highest intermolecular electronic coupling, leading to most blue-shifted absorption, quenched emission and strong bisignate CD signal with a negative Cotton effect. *e*) Output characteristics of OFET devices with the **T4-DGG** as semiconducting layer yielded mobilities as high as  $0.02\text{ cm}^2\text{ V}^{-1}\text{ s}^{-1}$ . Figure reproduced from ref. [110]. . . . . 18
- 1.16 Stupp et al. employed a self-assembling hairpin-shaped **T6-M1** as a donor component in organic solar cells. *a*) Molecular structure of **T6-M1** (R = hexyl). *b*) Transmission electron microscopy (TEM) images of **T6-M1** showed bundles of nanofibers. *c*) Illustration of the nanostructural organization of **T6-M1** in the presence of PC<sub>71</sub>BM upon thermal annealing. Figure reproduced from refs. [116,119]. . . . . 19
- 1.17 Würthner et al. demonstrated crystal engineering approach using hydrogen bonding, resulting an enhanced device performance together with remarkable device stability. *a*) Molecular structure of **Cl<sub>8</sub>-PTCDI** *b*) Single crystal X-ray structure analysis revealed a twisted perylene backbone with a “brickwork” arrangement. *c*) Transfer curve of an OFET from **Cl<sub>8</sub>-PTCDI** showing mobilities as high as  $0.9\text{ cm}^2\text{ V}^{-1}\text{ s}^{-1}$  with excellent  $I_{\text{on}}/I_{\text{off}}$  ratios up to  $10^8$  in air. Figure reproduced from ref. [120]. . . . . 20
- 1.18 Głowacki et al. investigated the thin film transistor performance of organic pigments that had been widely used as toners for inkjet printing and were available at low-cost. *a*) Molecular structure of epindolidione and quinacridone. OFET devices fabricated from *b*) epindolidione and *c*) quinacridone resulted in mobilities of up to  $1.5$  and  $0.1\text{ cm}^2\text{ V}^{-1}\text{ s}^{-1}$  along with  $I_{\text{on}}/I_{\text{off}}$  ratios around  $10^7$  and  $10^4$ , respectively. Both were stable in air more than 140 days, as compared to their non-hydrogen-bonded acene analogues. Figure reproduced from ref. [122]. . . 20

- 1.19 Perepicka et al. exploited co-assembly of hydrogen donor and acceptor molecules through complementary hydrogen bonding and investigated the resulting electronic properties of the cocrystals. *a)* Molecular structure of diphenyldipyrrolopyridine (**DP-P2P**), which co-assembled with naphthalenetetracarboxydiimides (**NDI**) via triple hydrogen bonds. *b)* The single crystal X-ray structure of **DP-P2P:NDI-8<sub>1</sub>** displayed an alternating arrangement of dimerized donor and acceptor columns, marked with green and purple circles, respectively *c)* Transfer characteristics of single cocrystal OFET devices demonstrated ambipolar transport for **DP-P2P:NDI-8<sub>1</sub>** and **DP-P2P:NDI-CyHex**, while only unipolar n-type transport was observed for **DP-P2P:NDI-H<sub>2</sub>**. Figure reproduced from ref. [129]. 21
- 1.20 Zhang et al. investigated how urea-containing alkyl chains affect FET device performance. *a)* Molecular structure of diketopyrrolopyrrole-quaterthiophene (**DPP4T**) semiconducting polymer with urea-containing alkyl side chains in the molar ratios 1:30, 1:20, 1:10, 0:100. *b)* 2D GIXS profiles for annealed **pDPP4T-3** deposited on an OTS modified Si<sup>+</sup>/SiO<sub>2</sub> substrate exhibited a well-defined lamellar arrangement. *c)* Transfer and output curves from OFET devices fabricated from the thin films of **pDPP4T-3** using a bottom gate top contact configuration, after annealing. Figure reproduced from ref. [134]. . . . . 22
- 1.21 *a)* PA66 crystallizes in  $\alpha$  phase with the chains in an all-*trans* conformation, forming hydrogen-bonded sheets that are stacked along the *b*-axis. PA66 has a triclinic unit cell with lattice parameters  $a = 4.9 \text{ \AA}$ ,  $b = 5.4 \text{ \AA}$ ,  $c = 17.2 \text{ \AA}$ ,  $\alpha = 48.5^\circ$ ,  $\beta = 77^\circ$ ,  $\gamma = 63.5^\circ$ . *b)* Wide-angle X-Ray diffractograms of the “even-even” AABB-type polyamides PA66 and PA610, and the “even” AB-type polyamide, PA12. The wide-angle X-Ray diffraction (WAXD) patterns shown for PA66 and PA610 are characteristic of the  $\alpha$  phase, with two intense Bragg peaks at  $20.2^\circ$  and  $24^\circ$  associated with intrachain distances within and between the hydrogen-bonded sheets, respectively. The WAXD pattern for PA12, on the other hand, shows only a single strong reflection characteristic of the  $\gamma$  phase. *c)* By altering the crystallization conditions, PA6 may form the  $\alpha$  or  $\gamma$  phase, with the hydrogen-bonded chains are antiparallel and parallel, respectively. *d)* WAXD patterns at different temperatures showing the transition to pseudo-hexagonal packing on heating the  $\alpha$  phase of PA66. The transition temperature is referred to as the Brill temperature. *e)* AFM amplitude image of semicrystalline PA66 showing chain-folded crystalline lamellae, which in turn aggregate to form spherulites. Figure adapted from refs. [162,166–169]. . . . . 28

- 1.22 Crystal structure of poly(*p*-phenylene terephthalamide) (PPTA) based on X-ray diffraction studies. *a,b*) Northolt and Tadokoro proposed a monoclinic (pseudo-orthorhombic) unit cell with lattice parameters  $a = 7.87 \text{ \AA}$ ,  $b = 5.18 \text{ \AA}$ ,  $c = 12.9 \text{ \AA}$  and  $\gamma = 90^\circ$  containing two polymer chains. This structure is also known as modification I. *c*) Representation of a second PPTA polymorph viewed along the *c*-axis, known as modification II and may be obtained by using water as a coagulant. *d*) Equatorial and meridional WAXD scans of PPTA fibers. The presence of sharp Bragg peaks and the absence of a strong amorphous halo reflects the high crystallinity of the PPTA fibers. *e*) Schematic illustration of microfibrils and skin-core structure of PPTA fibers. Figure reproduced from refs. [178,179,182]. . . . . 29
- 1.23 Tashiro et al. studied the crystal structure and phase transition behavior of semiaromatic PA9T. *a*) IR spectra of amide A (top) and methylene regions (bottom) of PA9T recorded from 27 to 330 °C. The sharp and strong N–H stretching mode became weaker and shifted towards higher wavenumbers with increasing temperature, indicating a decrease in the concentration of hydrogen-bonded amide groups and a weakening of the hydrogen bond strength with increasing temperature. In addition, IR bands associated with the methylene units became weaker and broader with increasing temperature, indicating increased conformational disorder. *b,c*) Suggested crystal structure of PA9T derived from 2D WAXD patterns and computer modeling. The diffraction patterns were indexed assuming a orthorhombic unit cell with lattice parameters  $a = 4.95 \text{ \AA}$ ,  $b = 8.39 \text{ \AA}$ ,  $c = 38.6 \text{ \AA}$ . Figure reproduced from ref. [190]. . . . . 30
- 1.24 *a*) Chemical structure of semiaromatic polyamide poly(hexamethylene terephthalamide-co-isophthalamide) (PA6TI) prepared by the copolymerization of rigid terephthalic acid (T) and isophthalic acid (I) monomers with hexamethylene diamine. *b*) Crystal structure of PA6TI determined from selected-area electron diffraction of an oriented PA6TI thin film. The observed reflections were indexed using triclinic unit cell with lattice parameters  $a = 5.02 \text{ \AA}$ ,  $b = 5.4 \text{ \AA}$ ,  $c = 16.4 \text{ \AA}$ ,  $\alpha = 50.5^\circ$ ,  $\beta = 79^\circ$ ,  $\gamma = 94^\circ$ . *c*) The 1D SAXS correlation function was used to estimate the lamellar thickness (*l*) and long period (*L*) of the PA6TI, under the assumption of two-phase model (insert). *d*) AFM amplitude images of PA6TI revealed well-defined spherulitic textures similar to those in aliphatic PA66. Figure reproduced from refs. [168,198,199]. . . . . 31



1.25	Frauenrath et al. reported the efficient formation of random copolymers by transamidation during melt compounding of semicrystalline semiaromatic polyamides and certain semicrystalline aliphatic polyamides. <i>a)</i> MALDI-TOF mass spectra of the PA6TI blended with 50 wt% PA610 in melt and in solution. The appearance of the new peaks (marked in red) in the melt-compounded spectra indicated efficient transamidation resulting in random copolymers <i>b)</i> Correlation lengths deduced from SAXS as a function of aliphatic polyamide reveal the lamellar thickness ( <i>l</i> ) to be similar for almost all the materials, while the long period ( <i>L</i> ) varies somewhat. <i>c)</i> Nomarski differential interference contrast images of the PA6TI-PA12 blends showed phase separated domains. Figure reproduced from ref. [168]. . . . .	32
2.1	Structures of the bithiophene derivatives functionalized with ester or amide groups investigated in this work. . . . .	41
2.2	Ball-and-stick representations of the single-crystal X-ray structure of <b>6a</b> (CCDC 1951223). The crystal contained eight molecules of <b>6a</b> per orthorhombic unit cell <i>Pca</i> 2 <sub>1</sub> , with the lattice parameters <i>a</i> = 9.48958(16) Å, <i>b</i> = 5.37710(10) Å, <i>c</i> = 38.1047(6) Å, and $\alpha = \beta = \gamma = 90^\circ$ . <i>a, b)</i> Unit cell representation of <b>6a</b> along crystallographic <i>b</i> -axis and <i>a</i> -axis, respectively. Along the crystallographic <i>a</i> -axis, the adjacent thienyl cores arranged in edge-to-face arrangement, exhibiting intermolecular C...S and C...C close contacts of 3.460 and 3.923 Å within the close pairs, respectively. The amide groups in side chains organized almost orthogonal by an angle of 86.9° to the thienyl plane, with two different hydrogen bonding distances of 2.867 and 2.906 Å (all hydrogen atoms except those that participate in hydrogen bonding have been omitted for clarity). . . . .	43
2.3	Representative polarized optical microscopy images of <i>a-c)</i> bithiophene diesters <b>1a-c</b> , and <i>d-f)</i> bithiophene diamides <b>2a-c</b> using polarized optical under cross polarizers. . . . .	44
2.4	Ball-and-stick representations of the single-crystal X-ray structures of the bithiophene diesters <b>1a-c</b> . Unit cells and short contacts of <i>a, b)</i> <b>1a</b> (CCDC 1951216), <i>c, d)</i> <b>1b</b> (CCDC 1951217), and <i>e, f)</i> <b>1c</b> (CCDC 1951218). . . . .	45
2.5	Ball-and-stick representations of the single-crystal X-ray structures of the bithiophene diamides <b>2a-c</b> . Unit cells, and short contacts of <i>a, b)</i> <b>2a</b> (CCDC 1951219), <i>c, d)</i> <b>2b</b> (CCDC 1951220), and <i>e, f)</i> <b>2c</b> (CCDC 1951221). Hydrogen bonds observed in the bithiophene diamides <b>2a-c</b> are marked with blue dashed lines. . . . .	46

- 2.6 Ball-and-stick representation of the ill-defined single-crystal X-ray structure of **2c** *a*) viewed along the crystallographic *c*-axis and *b*) the *a*-axis, at 100 K with lattice parameters  $a = 22.3869(15) \text{ \AA}$ ,  $b = 25.7597(16) \text{ \AA}$ ,  $c = 30.9609(16) \text{ \AA}$ ,  $\alpha = 96.751(5)^\circ$ ,  $\beta = 95.932(5)^\circ$ , and  $\gamma = 108.448(6)^\circ$  (all hydrogen atoms have been omitted for clarity). . . . . 47
- 2.7 Bithiophene packing of *a*–*c*) diesters **1a–c** and *d*–*f*) diamides **2a–c**. Hydrogen bonding patterns observed in bithiophene diamides **2a–c** are marked with dashed lines. Hydrogen bonding (D–H···A) and herringbone angles are marked in blue and red colors, respectively. . . . . 49
- 2.8 Solid-state IR spectra of the amide A and the amide I and II regions of bithiophene diamides **2a–c**. . . . . 50
- 2.9 Ball-and-stick representations of the single-crystal X-ray structure of **DHT2** (CCDC 1951222). Single-crystals of **DHT2** were grown from a solution in ethanol at  $-5^\circ\text{C}$  by slow evaporation. **DHT2** crystallized in the triclinic space group  $P\bar{1}$ , with the lattice parameters  $a = 5.7717(6) \text{ \AA}$ ,  $b = 7.7801(9) \text{ \AA}$ ,  $c = 22.363(2) \text{ \AA}$ ,  $\alpha = 99.154(9)^\circ$ ,  $\beta = 91.780(9)^\circ$ , and  $\gamma = 105.885(10)^\circ$ . *a*) The unit cell of **DHT2** viewed along the crystallographic *a*-axis, contained two independent molecules of **DHT2**. *b*) The interlayer distance was  $3.547 \text{ \AA}$ , between parallel-displaced neighboring molecules. *c*) Illustration of C···C, C···S, and S···S close contacts of  $3.431$ ,  $3.849$ , and  $3.697 \text{ \AA}$ , respectively, between parallel-displaced neighboring molecules. The molecular axis of the bithiophene was tilted by  $66.17^\circ$  with respect to the layer normal. Furthermore, each hexyl substituent was almost in an all-*trans* conformation and tilted differently with respect to the bithiophene core ( $5.23^\circ$  or  $67.83^\circ$ ). *d*) Illustration of the pitch angle and *e*) the roll angle of **DHT2** (all hydrogen atoms have been omitted for clarity). . . . . 53
- 2.10 Illustration of *a*–*c*) pitch angles, and *d*–*f*) roll angles of bithiophene diesters **1a–c**. 54
- 2.11 Illustration of *a*–*c*) pitch angles, and *d*–*f*) roll angles of bithiophene diamides **2a–c**. 54

2.12	Thermogravimetric analysis (TGA) scans of bithiophene <i>a</i> ) diesters <b>1a–c</b> , diacids <b>5a–c</b> , and <i>b</i> ) diamides <b>2a–c</b> , as well as alkyl substituted <b>DHT2</b> . <i>c,d</i> ) Decomposition, $T_d$ , and melting temperatures, $T_m$ , of the bithiophene diesters <b>1a–c</b> , dicarboxylic acids <b>5a–c</b> , and diamides <b>2a–c</b> as a function of the spacer length. <i>e</i> ) Normalized solution-phase UV-vis and fluorescence spectra (excitation at 325 nm) of the different bithiophene derivatives in DMSO ( $c = 0.01$ mmol/L). <i>f</i> ) Normalized UV-vis spectra of solid thin films of the different bithiophene derivatives, prepared by spin-coating onto quartz substrates. <i>g</i> ) Plot of maximum absorption wavelengths in the solid-state absorption spectra as a function of volume per bithiophene, <i>h</i> ) pitch, and <i>i</i> ) roll angles. Full symbols denote a herringbone packing, while empty symbols indicate a parallel-displaced $\pi$ - $\pi$ stacked arrangement of the bithiophene cores. . . . .	55
3.1	Molecular structures of the quaterthiophene bisacetamide <b>1</b> and the corresponding diacetate <b>2</b> investigated in this work. . . . .	61
3.2	<i>a</i> ) The amide A, and <i>b</i> ) amide I and II regions of the solid-state infrared (IR) spectra of <b>1</b> revealed strongly, resonance-enhanced amide hydrogen bonding at room temperature with absorption bands at around 3280, 1636, and 1550 $\text{cm}^{-1}$ , respectively. <i>c</i> ) By increasing the temperature, these bands were shifted to higher (for amide A and I) and lower (for amide II) wavenumbers. . . . .	62
3.3	Ball-and-stick representations of the single-crystal X-ray structure of <i>a</i> ) quaterthiophene diacetamide <b>1</b> (CCDC 976399) viewed along the crystallographic [110] axis, and <i>b</i> ) quaterthiophene diacetate <b>2</b> (CCDC 1043812) viewed along the <i>c</i> -axis, with <i>c,d</i> ) an illustration of the C $\cdots$ C, C $\cdots$ S, and S $\cdots$ S short contacts between edge-to-face and parallel-displaced neighboring pairs of <b>1</b> and <b>2</b> (all hydrogen atoms except the amide hydrogens omitted for clarity). . . . .	63
3.4	Representative examples for DORI = 0.5 isovalues for two pairs of molecules in the crystal structure of <b>1</b> . The surfaces are color-coded according to the values of the function $\text{sgn}(\lambda_2)\rho$ in the $-0.01$ to $0.01$ a.u. range, where $\lambda_2$ is the second isovalue of the electron density Hessian and $\rho$ is the electron density. The compactness index was computed as integral of the electron density over the intermolecular regions. . . . .	66
3.5	Top views onto the herringbone packing of the quaterthiophene cores in <i>a</i> ) <b>1</b> , in comparison to <i>b</i> ) <b>2</b> , <i>c</i> ) LT, <sup>255</sup> $\alpha$ -4T, <i>d</i> ) DM4T, <sup>291</sup> and <i>e</i> ) DH4T <sup>292</sup> (all hydrogen atoms and side chains omitted for clarity). The numbers and line widths represent the computed density overlap regions indicator (DORI) values of quaterthiophene pairs. . . . .	67

- 3.6 Atomic force microscopy (AFM) height images of thin films of **1** vapor-deposited onto *a,b*) Si<sup>+</sup>/SiO<sub>2</sub> or *d,e*) OTS-treated Si<sup>+</sup>/SiO<sub>2</sub> substrates, as well as *c,f*) height profiles obtained from *b,e*). Figure adapted from ref. [296]. . . . . 68
- 3.7 *a*) Atomic force microscopy (AFM) height images of films of **2** vapor-deposited onto OTS-treated substrates at  $T_S \approx 120$  °C. Thermal properties of **1** and **2** were characterized by *b*) thermogravimetric analysis (TGA) and *c*) differential scanning calorimetry (DSC). TGA scans indicated the main decomposition temperatures of both compounds to be above 300 °C. DSC heating and cooling scans of **2** showed multiple thermal transitions, suggesting the presence of different phases on heating, while **1** showed only single melting and cooling transitions. *d-f*) Atomic force microscopy (AFM) height images of films of **2** vapor-deposited onto OTS-treated substrates at temperatures of 40 °C. . . . . 69
- 3.8 *a*) Optical micrograph of a bottom-gate top-contact OFET device with a channel length  $L = 5$  μm and width  $W = 50$  μm fabricated from a thin film of **1** on SiO<sub>2</sub> at  $T_S \approx 120$  °C. The bright yellow areas are the Au source and drain electrodes. Representative examples of *b,c*) a directly measured output and transfer curves (measured in the forward and reverse directions) for the bottom-gate top-contact transistors fabricated from films of **1** and **2** on a bare or an OTS-treated SiO<sub>2</sub> substrate; devices with a channel length *d-f*)  $L = 5$  μm, *g-i*) 10 μm, and *j-l*) 20 μm. 71
- 4.1 *a*) Representative <sup>1</sup>H NMR spectra for **PA6T2** in non-deuterated HFIP with acetone-*d*<sub>6</sub> as the internal standard showed the expected proton signals, including those of the amide protons. The <sup>1</sup>H NMR chemical shifts in the range of 5.8–6.1 ppm originated from the two chemically different thiophene protons, whereas the aliphatic protons of the diamine and the spacer gave rise to six distinct peaks below 2.5 ppm. *b*) From the cross-peaks observed in <sup>1</sup>H–<sup>1</sup>H COSY experiments, the peaks at 2.33, 0.65, 0.45 ppm were attributed to the aliphatic protons of the diamine, while the peaks at 1.94, 1.39, 1.09 ppm corresponded to the protons of the propylene spacer. Distinct amide protons were also observed at around 5.2 ppm. *c*) Expanded view of the dashed area of the full spectrum in *b*). 79
- 4.2 *a*) Results from thermogravimetric analysis (TGA) scans of **PA $n$ T2** indicated a main decomposition temperature above 300 °C. *b*) Successive dynamic scanning calorimetry (DSC) cooling and heating scans from **PA $n$ T2** ( $n = 6$ –12) at 10 °C/min. Melting of **PA $n$ T2** with even  $n$  was characterized by multiple melting endotherms, whereas only a single endotherm was observed for odd  $n$ . *c*) The corresponding melting ( $T_m$ ) and crystallization temperatures ( $T_c$ ) showed a global decrease with increasing  $n$  but were reduced for odd  $n$  with respect to the values obtained for adjacent even  $n$ . *d*) DSC heating scans at 10 °C/min from **PA $n$ T2** with even  $n$  after isothermal crystallization from the melt at the specified temperatures. . . 80

- 4.3 *a, b*) Solid-state IR spectra of the bithiophene dibutyric acid **T2**, model compound **T2a** and the resulting polyamides **PA $n$ T2**. After polycondensation, the C=O stretching vibration of the free carboxylic acid was replaced by the amide A, I, and II bands of the amide functions. *c*) Wide-angle X-Ray diffraction (WAXD) patterns from the as-synthesized (powder) and *d*) isothermally crystallized (bulk) specimens recorded at room temperature in reflection and transmission, respectively. *e*) Deconvoluted WAXD pattern of **PA $n$ T2** allowed roughly to estimate degree of crystallinity by distinguishing the Bragg peaks from the amorphous halo. The inset showed the 2D WAXD pattern of the polyamides, suggesting absence of the preferential orientation of the crystallites. *f*) Degree of crystallinity for **PA $n$ T2** estimated from deconvolution of the WAXD profiles. Spacings corresponding to the lowest angle Bragg reflections from the WAXD patterns of the melt-crystallized polyamides shown as a function of  $n$ . . . . . 82
- 4.4 *a*) Molecular structure of the bithiophene diamide model compound **T2a**. *b*) Ball-and-stick representations of the single-crystal X-ray structure of **T2a** viewed along the *ab*-plane, showing the presence of both N–H...O=C hydrogen bonds and the parallel-displaced  $\pi$ -stacked arrangement of the bithiophene units with *c*) a hydrogen bonding distance (H...O) of 2.0 Å and a bithiophene interlayer distance of 3.6 Å. *d*) C...S and C...C and S...S close contacts between parallel-displaced pairs of bithiophenes (all hydrogen atoms except those that participate in hydrogen bonding have been omitted for clarity). . . . . 83
- 4.5 *a*) Model structure for **PA $n$ T2** with even  $n$ , shown here for  $n = 8$ , assuming a triclinic  $P\bar{1}$  space group with the  $c$ -axis parallel to the axes of the main methyl sub-chain. *b*) Selected area electron diffraction (SAED) pattern from an oriented film of **PA8T2**. *c*) Comparison of the experimental WAXD data for a melt crystallized film of **PA8T2** with a simulated WAXD powder pattern from the structure in *a*) with lattice parameters  $a = 5.10$  Å,  $b = 5.68$  Å,  $c = 30.61$  Å,  $\alpha = 60.40^\circ$ ,  $\beta = 71.24^\circ$ ,  $\gamma = 109.68^\circ$  derived from the SAED pattern. . . . . 84
- 4.6 *a*) Estimation of the lamellar thickness ( $L_c$ ) and lamellar long period ( $L_p$ ) from the small-angle X-Ray scattering (SAXS) correlation function for even  $n$ , assuming a two-phase model. *b*) Estimated  $L_c$  and  $L_p$  for the even polyamides along with  $L_a$ , the thickness of the corresponding amorphous layer, taken to be equal to  $L_p - L_c$ . *c*) Degree of crystallinity for **PA $n$ T2** estimated from the SAXS measurements (even  $n$  only). *d*) Atomic force microscopy (AFM) intermittent contact mode height image the local lamellar structure in a film of **PA8T2** isothermally crystallized from the melt at 176 °C. The white markers are separated by 10 nm. *e*) Schematic representation of the lamellar morphology of **PA8T2**. . . . . 85

- 4.7 Selected area electron diffraction (SAED) from an oriented film of **PA7T2** prepared at about 140 °C. Approximate  $d$ -spacings corresponding to the visible reflections are also indicated. The layer lines corresponded to the axial spacing of the methyl groups, and hence did not provide a direct indication of the unit cell dimensions. However, *b*) oriented films of **PA7T2** prepared at about 130 °C and in which the equatorial reflections were less well-resolved, showed additional meridional reflections. The spacings of these reflections suggested a repeat distance in the orientation direction of approximately 55 Å, implying the spacing given in Figure 4.3*f* for  $n = 7$  to correspond to the (002) planes in the oriented films, and a putative (100) spacing of about 43 Å, which was significantly greater than the lamellar thicknesses observed for even  $n$ . It was hence tentatively concluded based on these results that specimens of **PA $n$ T2** melt-crystallized under quiescent conditions showed more limited three-dimensional order when  $n$  was odd. . . . . 86
- 4.8 Typical load-displacement curves with the residual imprint (inset) from nanoindentation measurements on the **PA $n$ T2**, industrial-grade PA610, and PA6TI specimens. . . . . 87
- 4.9 *a*) Instrumented hardness ( $H_{IT}$ ) and *b*) Melting enthalpy of the specimens hot-pressed at their melting maxima. *c*) elastic modulus from the indentation measurements,  $E_{IT}$ , and from dynamic mechanical analysis,  $E'$ , of **PA $n$ T2** as a function of  $n$ . For comparison, the moduli of industrial-grade PA610 and PA6TI were shown as a broad range, representing the results obtained from nanoindentation and DMA. . . . . 88
- 4.10 *a*) Normalized UV-vis absorption spectra of **PA6T2** compared with those of the model compound **T2a** from solutions (solid lines) and spin-coated thin films on a quartz substrate (dashed lines). *b*) Absorption spectra of the **PA6T2** before and after irradiation for several minutes at 317 nm, showing the photo-bleaching effect. *c*) Transient change in conductivity of **T2a**, **PA6T2** and **PA12T2** on irradiation with a 10 ns electron pulse normalized by the irradiation dose,  $D$ . 89
- 4.11 Orbital energy levels of 4,4'-(2,2'-bithiophene-5,5'-diyl)bis(*N*-methylbutanamide) were obtained by density functional theory (DFT) (B97-3/def2-SV(P)) calculations. The methyl diamide bithiophene was used as proxy for **PA $n$ T2** instead of model compound **T2a** to reduce the calculation time. . . . . 89
- 5.1  $^1\text{H}$  NMR spectrum (600 MHz, calibrated with 4,4-dimethyl-4-silapentane-1-sulfonic acid) of **2** in conc.  $\text{D}_2\text{SO}_4$  indicating the presence of the 1,7-dibromo, 1,6-dibromo, and 1,7,6-tribromo perylene bisimide regioisomers. . . . . 96

5.2	Solid-state IR spectra of the of the dicyanoperylene bisimide-containing polyamides <b>PA<math>n</math>PBICN2</b> . <i>a</i> ) The formation of amide bonds was confirmed from comparison of the solid-state IR spectra of the polyamides <b>PA<math>n</math>PBICN2</b> with that of compounds <b>5</b> and <b>6</b> . <i>b</i> ) The characteristic amide A <i>c</i> ) and amide I and II bands (blue) appeared after polycondensation, along with the C=O stretching vibrations of the perylene bisimide core (red). . . . .	98
5.3	<i>a</i> ) Wide angle X-Ray diffraction (WAXD) patterns of the as-synthesized <b>PA<math>n</math>PBICN2</b> ( $n = 6, 8, 10, 12$ ) powders were recorded at room temperature in transmission mode, along with the corresponding 2D patterns (insets). Deconvolution of these patterns was used to separate the amorphous background from the Bragg peaks. <i>b</i> ) Systematic increase in the $d$ -spacings corresponding to the lowest angle peaks in the WAXD patterns with increasing $n$ from 19.5 to 23.5 Å (inset: corresponding Bragg peaks). <i>c</i> ) Estimated crystallinity index as a function of $n$ based on the deconvolution of the WAXD patterns, together with the corresponding long period ( $L_p$ ) estimated from small-angle X-ray scattering (SAXS) measurements. . . . .	99
5.4	<i>a</i> ) Model structure for <b>PA6PBICN2</b> assuming a triclinic unit cell with the $c$ -axis parallel to the polymer backbone. <i>b</i> ) Simulated WAXD powder pattern from the structure in <i>a</i> ) in comparison with a fitting of the experimental WAXD peaks in Figure 5.3 <i>a</i> . . . . .	100
5.5	<i>a</i> ) Thermogravimetric analysis (TGA) scans of <b>PA<math>n</math>PBICN2</b> ( $n = 6, 8, 10, 12$ ) as well as <b>5</b> and <b>6</b> performed at heating rate of 10 °C/min under nitrogen atmosphere. <i>b</i> ) Differential scanning calorimetry (DSC) heating and cooling runs of <b>PA<math>n</math>PBICN2</b> ( $n = 6, 8, 10, 12$ ) confirmed the absence of any significant thermal transistions before the degradation onset temperature of 300 °C. <i>c</i> ) The shear modulus, $G$ , of <b>PA<math>n</math>PBICN2</b> as a function of $n$ calculated from dynamic mechanical analysis measurements (shear mode, 1 Hz at room temperature). Representative values from the commercially available polyamides PA610 and PA6TI are shown for comparison. . . . .	101
5.6	Normalized UV-vis (solution-phase and thin film) absorption and solution-phase fluorescence spectra of <i>a</i> ) model compound <b>6</b> and <i>b</i> ) <b>PA6PBICN2</b> . The solution-phase spectra were obtained from TFA solutions (black: absorption spectra, $c = 10^{-4}$ mol/L; red: fluorescence spectra ( $c = 10^{-6}$ mol/L), while thin film spectra were obtained from spin-coated thin films on quartz substrates (blue). The inset shows the corresponding specimens under UV light (254 nm). <i>c</i> ) The change in conductivity on irradiation with a 10 ns electron pulse for <b>PA<math>n</math>PBICN2</b> ( $n = 6, 8, 10, 12$ ) and model compound <b>6</b> , measured by time-resolved microwave conductivity. . . . .	102

## List of Figures

---

- 7.1 Representative illustration for determination of pitch and roll angles showing the definition of the bithiophene short and long axis. . . . . 119
- 7.2 Illustration of packing arrangement of bithiophenes within a layer. The yellow cloud illustrates the van der Waals surface of the corresponding bithiophenes. . 120



# List of Tables

1.1	Hydrogen bond strength can be divided into three categories, namely strong, moderate and weak based on their nature and geometrical parameters. Data adapted from ref. [98]. . . . .	16
1.2	Thermomechanical properties of aliphatic, semiaromatic polyamides (poly( <i>m</i> -xylene adipamide) (MXD6), PA6TI) and aramids (Nomex <sup>®</sup> , Kevlar <sup>®</sup> ) with steel as a reference. The values for the tensile strength ( $\sigma_{\max}$ ), stiffness ( $E$ ), and elongation at break ( $\epsilon_b$ ) may vary depending on processing conditions. Data from refs. [198,199,206–209] . . . . .	33
2.1	Comparison of the single-crystal structures of bithiophene diesters <b>1a–c</b> and bithiophene diamides <b>2a–c</b> . . . . .	48
2.2	Hydrogen bonds observed in single-crystals of the bithiophene diamides <b>2a–c</b> . Symmetry transformations used to generate equivalent atoms: <sup>1</sup> $+x, 1/2-y, -1/2+z$ ; <sup>2</sup> $x, -1+y, +z$ ; <sup>3</sup> $-1+x, -1+y, z$ . . . . .	50
2.3	Detailed comparison of the crystal structures of $\alpha$ -T2, measured at 133 K <sup>267</sup> and 173 K, <sup>268</sup> and bithiophenes with terminal alkyl side chains, $\alpha, \omega$ -dimethylbithiophene ( <b>DMT2</b> ) <sup>266</sup> and $\alpha, \omega$ -dihexylbithiophene ( <b>DHT2</b> ). . . . .	52
2.4	Decomposition temperatures $T_d$ , (from TGA, at 5 wt% mass loss), melting temperatures $T_m$ , and the absorption and emission maxima, $\lambda_a^{\max}$ and $\lambda_e^{\max}$ , respectively, from UV-vis and fluorescence spectroscopy. . . . .	53
3.1	Comparison of the crystal structure of <b>1</b> (CCDC 976399) with the structures of the quaterthiophene diacetate <b>2</b> (CCDC 1043812), the low temperature polymorph of $\alpha$ -4T, <sup>255</sup> $\alpha, \omega$ -dimethylquaterthiophene (DM4T), <sup>291</sup> and $\alpha, \omega$ -dihexylquaterthiophene (DH4T). <sup>292</sup> . . . . .	64
3.2	Hydrogen bonds observed in single crystals of <b>1</b> . Symmetry transformations used to generate equivalent atoms: <sup>1</sup> $-x+1, -y, -z$ ; <sup>2</sup> $-x+2, -y+1, -z$ ; <sup>3</sup> $x-1, y-1, z$ . . .	65

## List of Tables

3.3	Average and maximum mobilities $\mu$ , $I_{\text{on}}/I_{\text{off}}$ , and threshold voltages $V_T$ of bottom-gate ( $\text{Si}^+$ ) top-contact (Au) OFETs with $W/L = 10$ ; entries <b>1–3</b> : variation of channel length for devices of <b>1</b> on bare and; entries <b>4–6</b> : OTS-treated $\text{SiO}_2$ substrates at $T_S = 120^\circ\text{C}$ ; entries <b>7–9</b> : variation of channel length for devices of <b>2</b> on OTS-treated $\text{SiO}_2$ substrates at $T_S = 40^\circ\text{C}$ . All devices were measured in inert atmosphere. The reported device characteristics were averaged out over three to five devices from two different batches. . . . .	70
4.1	Yields, molecular weights ( $M_n$ , $M_w$ ), and dispersities of ( $\bar{D}$ ) obtained from gel permeation chromatography of the bithiophene-containing polyamides <b>PAnT2</b> . . . . .	78
4.2	The exact positions and full-width at half maximums (FWHMs) of the characteristic IR vibrations, including the amide A, I, and II, and asymmetric / symmetric $\text{CH}_2$ peaks, for all the bithiophene-containing polyamides <b>PAnT2</b> and the model compound <b>T2a</b> . . . . .	81
5.1	Yields, number and molecular weights ( $M_n$ , $M_w$ , and dispersities ( $\bar{D}$ ) obtained from gel permeation chromatography of the dicyanoperylene bisimide-containing polyamides <b>PAnPBICN2</b> . . . . .	97
7.1	Values that were used for calculation of volume per bithiophenes, where $a, b$ represented the both crystallographic planes in which the bithiophenes were arranged in a layer; $\alpha$ is the angle between those crystallographic axes, $d$ is the distance between planes of the bithiophene's outermost carbons within a layer. . . . .	120
9.1	Crystallographic and refinement data of compound <b>1a</b> . . . . .	156
9.2	Atomic coordinates ( $\times 10^4$ ) and equivalent isotropic displacement parameters ( $\text{\AA}^2 \times 10^3$ ) for <b>1a</b> . $U_{\text{eq}}$ is defined as one third of the trace of the orthogonalized $U^{\text{ij}}$ tensor. . . . .	157
9.3	Crystallographic and refinement data of compound <b>1b</b> . . . . .	158
9.4	Atomic coordinates ( $\times 10^4$ ) and equivalent isotropic displacement parameters ( $\text{\AA}^2 \times 10^3$ ) for <b>1b</b> . $U_{\text{eq}}$ is defined as one third of the trace of the orthogonalized $U^{\text{ij}}$ tensor. . . . .	159
9.5	Crystallographic and refinement data of compound <b>1c</b> . . . . .	160
9.6	Atomic coordinates ( $\times 10^4$ ) and equivalent isotropic displacement parameters ( $\text{\AA}^2 \times 10^3$ ) for <b>1c</b> . $U_{\text{eq}}$ is defined as one third of the trace of the orthogonalized $U^{\text{ij}}$ tensor. . . . .	161

9.7	Crystallographic and refinement data of compound <b>2a</b> . . . . .	162
9.8	Atomic coordinates ( $\times 10^4$ ) and equivalent isotropic displacement parameters ( $\text{\AA}^2 \times 10^3$ ) for <b>2a</b> . $U_{\text{eq}}$ is defined as one third of the trace of the orthogonalized $U^{\text{ij}}$ tensor. . . . .	163
9.9	Crystallographic and refinement data of compound <b>2b</b> . . . . .	164
9.10	Atomic coordinates ( $\times 10^4$ ) and equivalent isotropic displacement parameters ( $\text{\AA}^2 \times 10^3$ ) for <b>2b</b> . $U_{\text{eq}}$ is defined as one third of the trace of the orthogonalized $U^{\text{ij}}$ tensor. . . . .	165
9.11	Crystallographic and refinement data of compound <b>2c</b> . . . . .	166
9.12	Atomic coordinates ( $\times 10^4$ ) and equivalent isotropic displacement parameters ( $\text{\AA}^2 \times 10^3$ ) for <b>2c</b> . $U_{\text{eq}}$ is defined as one third of the trace of the orthogonalized $U^{\text{ij}}$ tensor. . . . .	167
9.13	Crystallographic and refinement data of compound <b>DHT2</b> . . . . .	168
9.14	Atomic coordinates ( $\times 10^4$ ) and equivalent isotropic displacement parameters ( $\text{\AA}^2 \times 10^3$ ) for <b>DHT2</b> . $U_{\text{eq}}$ is defined as one third of the trace of the orthogonalized $U^{\text{ij}}$ tensor. . . . .	169
9.15	Crystallographic and refinement data of compound <b>6a</b> . . . . .	170
9.16	Atomic coordinates ( $\times 10^4$ ) and equivalent isotropic displacement parameters ( $\text{\AA}^2 \times 10^3$ ) for <b>6a</b> . $U_{\text{eq}}$ is defined as one third of the trace of the orthogonalized $U^{\text{ij}}$ tensor. . . . .	171
9.17	Crystallographic and refinement data of compound <b>2</b> . . . . .	172
9.18	Atomic coordinates ( $\times 10^4$ ) and equivalent isotropic displacement parameters ( $\text{\AA}^2 \times 10^3$ ) for <b>2</b> . $U_{\text{eq}}$ is defined as one third of the trace of the orthogonalized $U^{\text{ij}}$ tensor. . . . .	173



## List of Schemes

- 1.1 Illustrative examples for the synthesis of AB- and AABB-type polyamides. *a)* Generally aliphatic AB-type polyamides can be prepared by ring opening polymerization of lactams. For example, PA6 can be synthesized starting from  $\epsilon$ -caprolactam with water as a nucleophile. *b)* Synthetic scheme for the polycondensation of PA66 starting from adipic acid and hexamethylene diamine. This is a general scheme for AABB-type polyamides that can be used for preparation of aliphatic, semiaromatic or fully aromatic polyamides. . . . . 24
- 1.2 General synthetic scheme of melt and solution-phase polycondensations. *a)* Melt polycondensation between two bifunctional monomers at high temperatures through “Nylon salt” formation, which enables control over the stoichiometry, is typically used for preparation of aliphatic polyamides. Solution-phase polycondensation, which is preferred for synthesis of semiaromatic and aromatic polyamides, can be divided into low-temperature or direct polycondensation carried out in either the presence or absence of phosphites and inorganic salts. For instance, *b)* Kevlar® and Nomex® were synthesized by low-temperature polycondensations starting from monomers *p*-phenylene diamine, terephthaloyl chloride and *m*-phenylene diamine isophthaloyl chloride, respectively. *Reagents and conditions:* *i)* triethylamine, inorganic salts (LiCl, CaCl<sub>2</sub>), NMP, < 0 °C. *c)* The direct solution polycondensation of diacid and diamine monomers is carried out at higher temperatures using triphenyl phosphite (TPP). This polycondensation is also known as Yamazaki-Higashi polycondensations. *Reagents and conditions:* *ii)* TPP, inorganic salt (LiCl, CaCl<sub>2</sub>), NMP/pyridine, 120 °C. *d)* The active ester polycondensation route has the advantage that additional additives (inorganic salts, catalysts) are not required. *Reagents and conditions:* *iii)* HMPA or DMSO 30–120 °C. . . . . 25
- 2.1 Synthesis of bithiophene diesters **1a–c** and bithiophene diamides **2a–c**. *Reagents and conditions:* *a)* H<sub>2</sub>SO<sub>4</sub> (96%, cat.), MeOH, reflux, 8 h, 97% yield; *b)* Pd(OAc)<sub>2</sub>, TFA, DMSO, 60 °C, 48 h, 26% yield; *c)* AgF, (C<sub>6</sub>H<sub>5</sub>CN)<sub>2</sub>PdCl<sub>2</sub>, DMSO, 85 °C, 14 h, 60% yield; *d)* LiOH, THF/H<sub>2</sub>O, reflux, 8 h, 95% yield; *e)* EDCI, HOBt, DIPEA, propylamine, room temperature, 12 h, 87% yield; *f)* propylamine, 1 h, 91% yield; *g)* Pd(OAc)<sub>2</sub>, TFA, DMSO, 60 °C, 48 h, 34% yield. . . . . 42

## List of Schemes

---

- 3.1 Two-step synthesis of quaterthiophene bisacetate **2**. *Reagents and conditions:* a) acetic anhydride, triethylamine, cat. amount of 4-(*N,N'*-dimethylamino)pyridine (DMAP), DCM, room temperature, 30 min, quantitative yield; b) *N*-bromosuccinimide, acetic acid, DCM, room temperature, 3 h, 97% yield; c) 5,5-Bis(tributylstannyl)-2,2-bithiophene, Pd(PPh<sub>3</sub>)<sub>4</sub>, dry DME, 80 °C, 12 h, 55% yield. . . . . 62
- 4.1 Synthesis of semiaromatic polyamides **PA<sub>n</sub>T2** by solution-phase polycondensation using Yamazaki-Higashi conditions. *Reagents and conditions:* a) triphenylphosphite (TPP), LiCl, NMP/pyridine (4:1), 120 °C, 4 h, 86–91%. . . . . 78
- 5.1 Synthesis of the dicyanoperylene bisimide *N,N'*-dibutanoic acid **5** and the corresponding diamide model compound **6**. *Reagents and conditions:* a) Br<sub>2</sub>, cat. amount of I<sub>2</sub>, conc. H<sub>2</sub>SO<sub>4</sub> (96%), 85 °C, 3 d, 97% yield; b) 4-aminobutyric acid *tert*-butyl ester hydrochloride, Zn(OAc)<sub>2</sub>, quinoline, 100 °C, 16 h, 79% yield; c) Zn(CN)<sub>2</sub>, Pd<sub>2</sub>(dba)<sub>3</sub>, dppf, dioxane, 95 °C, 48 h, 40% yield; d) CHCl<sub>3</sub>, TFA, reflux, 15 h, 96% yield; e) chlorendic hydroxyimide, DIC, propylamine, DMF/THF, 50 °C, 28 h, 84% yield. . . . . 95
- 5.2 Synthesis of dicyanoperylene bisimide-containing polyamides **PA<sub>n</sub>PBICN2**. *Reagents and conditions:* a) Chlorendic hydroxyimide, DIC, DMF, 50 °C, 14 h, b) DMSO, 120 °C, 2 d, 85–92%. . . . . 97

# Curriculum Vitae

## Personal Information

---

Name	Bilal Özen
Email	bilal.ozen@epfl.ch
Date of Birth	June 8, 1988, in Izmir, Turkey
Marital Status	Married, one child

## Education

---

2014 – present	Ph.D. Candidate in Materials Science and Engineering at École Polytechnique Fédérale de Lausanne (EPFL), Switzerland
2009 – 2014	B.Sc. & M.Sc. in Chemistry at University of Berne, Switzerland

## Professional Experience

---

since 2014	Ph.D. thesis in the group of Prof. H. Frauenrath at the Institute of Materials at EPFL, Lausanne, Switzerland.
2014	Research Associate (5 months) at University of Berne, Switzerland; research in the group of Prof. S. Decurtins.
2013	Master Thesis Student (11 months) at University of Berne, Switzerland; research in the group of Prof. S. Decurtins on "Benzodifuran-based Organic Dyes for Application in Dye-Sensitized Solar Cells".
2012	Bachelor Thesis and Research Assistant (5 months) at University of Berne, Switzerland; research in the group of Prof. S. Decurtins.

## Teaching Experience and Student Supervision

---

since 2015	Teaching assistant for "Organic Electronic Materials – Synthesis, Properties, and Applications (MSE 486)" M.Sc. level class given by Prof. H. Frauenrath; preparation of parts of the course content and exercise supervision.
2016 Spring	Supervision of Internship Student, Arvinth Sekar, Chemistry and Chemical Engineering, EPFL.

## List of Publications

---

- "Structure-Property Relationships in Bithiophenes with Hydrogen-Bonded Substituents" **Özen, B.**; Tirani, F. F.; Schenk, K.; Scopelliti, R.; Frauenrath, H., to be submitted.
- "Semiaromatic Polyamides with Enhanced Electron Mobility" **Özen, B.**; Candau, N.; Temiz, C.; Grozema, F. C.; Stoclet, G.; Plummer, C. J. G.; Frauenrath, H., to be submitted.
- "Synthesis and Characterization of Semiaromatic Polyamides with U-turn Repeating Units" Cretenoud, J.; **Özen, B.**; Baudat, E.; Tirani, F. F.; Scopelliti, R.; Plummer, C. J. G.; Frauenrath, H., to be submitted.
- "Crystallation and OFET Performance of a Hydrogen-Bonded Quaterthiophene Diacetamide" Gebers, J.\*; **Özen, B.\***; Hartmann, L.; Schaer, M.; Suárez, S.; Bugnon, P.; Scopelliti, R.; Steinrück, H.-G.; Konovalov, O.; Magerl, A.; Brinkmann, M.; Petraglia, R.; de Silva, P.; Corminboeuf, C.; Frauenrath, H., *Chemistry – A European Journal* **2020** (\* equally contributed). DOI: 10.1002/chem.201904562.
- "Engineering Polymers with Improved Charge Transport Properties from Bithiophene-Containing Polyamides" **Özen, B.**; Candau, N.; Temiz, C.; Grozema, F. C.; Tirani, F. F.; Scopelliti, R.; Chenal, J.-M.; Plummer, C. J. G.; Frauenrath, H. *J. Mater. Chem. C* **2020**, *8*, 6281–6292.
- "Synthesis and Characterization of Semiaromatic Polyamides Comprising Benzofurobenzofuran Repeating units" Cretenoud, J.; **Özen, B.**; Schmaltz, T.; Görl, D.; Fabrizio, A.; Corminboeuf, C.; Tirani, F. F.; Scopelliti, R.; Frauenrath, H. *Polym. Chem.* **2017**, *8*, 2197–2209.
- "Directed Metalation Cascade to Access Highly Functionalized Thieno[2,3-*f*]benzofuran and Exploration as Building Blocks for Organic Electronics" Aeschi Y.; Li H., Cao, Z.; Chen, S.; Amacher, A.; Bieri, N.; **Özen, B.**; Hauser, J.; Decurtins, S.; Tan, S.; Liu, S.-X. *Org. Lett.* **2013**, *15*, 5586–5589.



## List of Presentations

---

- “Semiaromatic Polyamides Comprising Bithiophene Segments” **B. Özen**, N. Candau, C. J. G. Plummer, H. Frauenrath; poster presentation at Polycoll Meeting **2018**, Lausanne, Switzerland; and at Swiss Chemical Society (SCS) Fall Meeting **2017**.
- “Crystal Structure, Thin Film Morphology, and OFET Performance of a Hydrogen-Bonded Quaterthiophene” **B. Özen**, J. Gebers, L. Hartmann, M. Schaer, H. Frauenrath; poster presentation at International Conference on Organic Electronics (ICOE) **2016**, Bratislava, Slovakia and at Conjugated Oligomers and Polymers (KOPO) **2015**, Würzburg, Germany.
- “Synthesis of a Hydrogen-Bonded Quaterthiophene and its Use in Organic Field-Effect Transistors” **B. Özen**, J. Gebers, L. Hartmann, M. Schaer, H. Frauenrath; poster presentation at Swiss Chemical Society (SCS) Fall Meeting **2015**, Lausanne, Switzerland.

## Language Skills

---

Türkisch	native
English	fluent
German	fluent
Schwyzerdütsch	basic
French	basic